Stony Brook University

Study of Factors Affecting Amylin Fibril Formation and the Characterization of a Protein which Prevents Amyloidogenesis

A Dissertation Presented

by

Ruchi Gupta

to

The Graduate School

In Partial Fulfillment of Requirements

for the Degree of

Doctor of Philosophy

in

Chemistry

Stony Brook University

August 2008

Stony Brook University

The Graduate School

Ruchi Gupta

We, the dissertation committee for the above candidate for the

Doctor of Philosophy degree, hereby recommend acceptance of this dissertation.

Daniel P. Raleigh, Thesis Advisor

Professor at Department of Chemistry, Stony Brook

Peter J. Tonge, Chairperson of Defense

Professor at Department of Chemistry, Stony Brook

Carlos Simmerling, Third Member

Associate Professor at Department of Chemistry, Stony Brook

Thomas P. Sakmar, Fourth Member

Richard M, and Isabel P. Furlaud Professor, Rockefeller University

Suzanne Scarlata, Outside Member

Professor at Department of Physiology and Biophysics, Stony Brook

This dissertation is accepted by the Graduate School

Lawrence Martin

Dean of the Graduate School

Abstract of Dissertation

Study of Factors Affecting Amylin Fibril Formation and the Characterization of a Protein which Prevents Amyloidogenesis

by

Ruchi Gupta

Doctor of Philosophy

in

Chemistry

Stony Brook University

2008

Amyloid fibril formation has been implicated in approximately 25 different diseases including Type 2 diabetes, Alzheimer's disease and Parkinson's disease. The proteins involved in each of these diseases show no sequence or structural homology. The proteins like Amylin associated with Type 2 diabetes and Aβ involved in Alzheimer's disease are natively unstructured. The aggregation of these proteins initially involves a structural rearrangement of monomers to form the nucleus, which then serves as a template for the addition of monomers/oligomers for fibril growth. The rates of nucleus formation as well as the growth of fibrils vary from peptide to peptide and depend on the conditions used.

The kinetics of the nucleation phase and the growth phase of Amylin were studied as a function of temperature and co-solvent type and concentration. The log of the apparent rate of growth of fibrils increases linearly with temperature and follows

Arrhenius behaviour. The activation energy barrier calculated from the temperature studies was found to be sensitive to the nature and amount of the co-solvent used. The activation barrier was higher in DMSO as compared to HFIP. The rate of both nucleation and elongation increased as the concentration of helix inducing solvent, HFIP, was increased. On the other hand, increasing the amount of a denaturing solvent like DMSO decreased the rate of nucleation and growth. Changes in the concentration of the peptide in the reaction mixture, however, did not significantly affect the nucleation time over a 17-fold increase in concentration. The velocity of growth phase was a linear function of the amount of Amylin, consistent with the fibril growth being first order.

A collaboration was initiated with Prof. Zanni at University of Wisconsin to use 2DIR to study amyloid formation by Amylin. The data is consistent with a zipper mechanism for conversion of Amylin monomers into amyloid fibrils. Residues 17-27 initiate β-sheet formation, which initially extends towards the N-terminus to include the fragment containing Ala13 and Ala8 followed by development of structure in the C-terminal region. In a collaborative effort with Prof. Sakmar's lab at Rockefeller University, we discovered that the human protein, Calnuc, inhibits aggregation and disassociates fibrillar deposits of Amylin and Aβ42, which is the causative agent of amyloid formation in Alzheimer's disease. Calnuc displayed potentially important therapeutic characteristics including inhibiting amyloid formation at any stage of aggregation and dissolving fibrillar deposits. The disaggregated Aβ42 species resulting after incubation with Calnuc was found to be non-toxic in cell based assays with PC12 cells and the activity was lost in the presence of physiological levels of Calcium. The functional efficacy of Calnuc was however shown to be calcium dependent. A calcium

insensitive mutant was designed which was shown to inhibit and disaggregate fibrils even in the presence of high concentrations of calcium.

Table of Contents

List of Figures

List of Tables

List of Symbols and Abbreviations

μL	microliter
μM	micromolar
LcrV	Low calcium response V
2D IR	2-dimensional infrared spectroscopy
His	Histidine
ΔC_p^o	Heat capacity change upon folding
ΔG^o	Standard Gibbs free energy change of unfolding
ΔH^o	Standard enthalpy change of unfolding
ΔS^o	Standard entropy change of unfolding
Aβ40	Amyloid beta 1-40
Aβ42	Amyloid beta 1-42
Ala	Alanine
APP	Amyloid precursor protein
Arg	Arginine
AUC	Analytical Ultracentrifugation
BACE-1	Beta-site APP cleaving enzyme-1
BSA	bovine serum albumin
CD	Circular Dichroism
Cox-1	Cyclooxygenase-1
Cox-2	Cyclooxygenase-2
CT	C-terminal
Cys	Cystine
D	Diffusion coefficient
Da	Dalton
DDI	distilled deionized water
DMSO	dimethylsulfoxide
E_a	activation energy
EDTA	ethylene diamine tetraacetic acid
EFRH	Glutamic acid Phenylalanine Arginine Histidine

ER	Endoplasmic Reticulum
ESI	Electrospray Ionization
et al.	et alii (and others)
FAP	Familial amyloidotic polyneuropathy
Fmoc	Fluorenylmethyloxycarbonyl
GTPase	Guanosine 5' Triphosphatase
HCl	hydrochloric acid
Hepes	4-(2-hydroxyethyl)piperazine-1-ethanesulfonic acid
HFIP	hexafluoroisopropanol
hIAPP	Human islet amyloid polypeptide
HPLC	High pressure liquid chromatography
Hsps	heat shock proteins
hIAPP	human Islet amyloid polypeptide
IDE	Insulin degrading enzyme
IPTG	Isopropyl-beta-D-thiogalactopyranoside
K	Kelvin
Kb	kilobase
kbp	kilobase pair
kcal	kilocalories
kDa	kilo-Daltons
k_m	maximum rate constant
kV	kilovolts
LRP	Lipoprotein receptor-related protein
Lys	Lysine
M	molar
m	Slope of ΔG^o versus denaturant concentration
mAbs	Monoclonal Antibodies
MALDI-TOF	Matrix-assisted laser desorption/ionization-time of flight
MESNA	Sodium 2-mercaptoethanesulfonate
ml	milliliter

mM	millimolar
mRNA	messenger ribonucleic acid
MTT	(3-(4,5-Dimethylthiazol-2-yl)-2,5-diphenyltetrazolium bromide
Na_2HPO_4	sodium hydrogen phosphate
NaCl	sodium chloride
NaOH	sodium hydroxide
NEP	Neprilysin
Ni-NTA	Nickel-nitrilotriacetic acid
nm	nanometer
NMR	Nuclear Magnetic Resonance
NP-61	Neuropharma-61
NUCB1	Nucleobindin1 (Calnuc)
NUCB2	Nucleobindin2 (Calnull)
OD	optical density
p67	plasmid67
PAL-PEG	4-(4-hydroxymethyl-3-methoxyphenoxy)- butyric acid polyethylene glycol
PC1/3	prohormone convertase1/3
PC2	prohormone convertase2
PCR	Polymerase chain reaction
PMSF	Phenylmethylsulfonylfloride
proIAPP	processed Islet Amyloid Polypeptide
PrP^c	cellular prion protein
PrP^{sc}	scrapie prion protein
PTPs	Protein tyrosine phosphatases
Rpm	revolutions per minute
SDS-PAGE	sodium dodecyl sulfate polyacrylamide gel electrophoresis
Ser	Serine
SH2	Src homology domain 2

sHsps	small heat shock proteins
TEM	Transmission electron microscopy
TFA	trifluoroacetic acid
Thio-T	thioflavin-T
T_m	Transition melting point
Tris-base	tris(hydroxymethyl)aminomethane
TTR	transthyretin
Tyr	tyrosine
UV/VIS	Ultraviolet/Visible
v/v	volume by volume
Y.enterocolitica	*Yersinia enterocolitica*
Y.pestis	*Yersinia pestis*
Y.pseudotuberculosis	*Yersinia pseudotuberculosis*
Yop	Yersinia outer protein
Yops	Yersinia outer proteins
YopH-CT	Yersinia outer protein-C-terminus
YopH-NT	Yersinia outer protein-N-terminus
R	radial distance
C_r	concentration of macrosolute at any radial distance
C_{r0}	concentration of the macrosolute at the reference radial distance
υ	partial specific volume
ω	angular velocity
ρ	density
R	gas constant
T	absolute temperature
k_B	Boltzmann's constant
$\acute{\eta}$	solvent viscosity
R_h	hydrodynamic radius
A	prefactor
D	diffusion coefficient

Acknowledgments

This thesis is dedicated to my parents, my aunt Anju Gupta and my grand father Mr. S.L. Aggarwal. Through out this journey of Ph.D., my family formed my backbone inspiring me at every stage of the work. My mom, specially, was there to share every failure and every success that I encountered. I salute her curiosity and patience in discussing the experiments and showing interest in an area which was far beyond her specialization. I also owe a fair share of the credit to my friends specially Daniel Amarante and Neeraj Kapoor in helping me put this work together and being there for me whenever I faltered. The knowledge and the training gained from this work came from lessons learned during discussions with my esteemed advisor, Prof Daniel P. Raleigh, who continuously encouraged me and supported me in trying new experiments. I also want to thank Prof. Sakmar for allowing me to work in his lab and starting a project which was completely unrelated to the research domain of his lab. Lastly I am thankful to all my lab mates and my undergrad Trish Burua for providing a friendly and conducive environment of learning and growth.

List of Publications

Marek, P., **Gupta, R.**, Raleigh, D.P. (2008). The Fluorescent Amino Acid *p*-Cyanophenylalanine Provides an Intrinsic Probe of Amyloid Formation. *Chem. BioChem*, *Comm. in press*.

Marek, P., Abedini, A., Song, B., Kanungo, M., Johnson, M., **Gupta, R.,** Zaman, W., Wong, S.S. and Raleigh, D.P. (2007). Aromatic interactions are not required for amyloid fibril formation by islet amyloid polypeptide but do influence the rate of fibril formation and fibril morphology. *Biochemistry* 46, 3255-3261.

Li Y., **Gupta R.**, Cho J., Raleigh D.P. (2007). Mutational analysis of the folding transition state of the C-terminal domain of ribosomal protein L9: a protein with an unusual beta-sheet topology. *Biochemistry* 46, 1013-1021.

Shim, S., **Gupta, R.,** Ling, Y. L., Strasfeld, D.B., Raleigh, D.P. and Zanni, M.T. Residue-specific structural information on the folding of amylin using 2D IR spectroscopy. *Submitted to PNAS.*

Gupta, R., Kapoor, N., Sakmar, T. and Raleigh, D. P. (2008). A simple method for the rapid and reproducible production of homogeneous fibrils of Aβ peptide. *To be submitted.*

Gupta, R. and Raleigh, D. P. Energetics of Amyloid Formation by the Natively Unfolded Islet Amyloid Polypeptide. *To be submitted.*

Kapoor, N., **Gupta, R.,** Menon, S., Raleigh, D. P. and Sakmar, T. P. Biophysical studies of human protein Calnuc. *To be submitted.*

Gupta, R. and Raleigh, D. P. Nature and amount of organic solvent affects amyloidogenesis of human IAPP. *To be submitted.*

Patent Disclosure

Marek, P., **Gupta, R.,** Meng, F. and Raleigh, D. P. (2008). Use of the Fluorescent Amino Acid *p*-Cyanophenylalanine as an Intrinsic Probe of Amyloid Formation. Stony Brook University.

Pending Patent

Gupta, R., Kapoor, N., Raleigh, D. P. and Sakmar, T. Discovery of a novel protein for prevention of Amyloidogenesis. Rockefeller University.

Chapter 1. Introduction

1.1 Amyloidogenesis

1.1.1. Amyloid fibrils and their properties

Aggregation has always been an issue of concern for biochemists dealing with proteins. It is either associated with the loss of precious protein samples or the loss of functionality of the protein in the assay. However, a special class of non-amorphous highly ordered filamentous aggregates called amyloid fibrils have attracted attention for being associated with many commonly occurring diseases. These proteinaceous amyloid deposits range from few nanometers to several microns in size and are composed of parallel or anti-parallel β-strands arranged in a cross-β sheet structure (Fig.1). The formation of this insoluble fibrous material by a usually soluble protein can result in cell death. This outcome may either be due to the toxicity of the aggregating species or the decrease in the amount of soluble protein that is available for performing its physiological function. The discovery that a large number of proteins can be induced to aggregate or form amyloid clearly shows that evolution has not always selected against this phenomenon. Indeed, recent research reveals that some amyloid structures can help in achieving diverse biological functions apart from being associated with diseases (Chiti et al 2006). For example, experimental results have shown that amyloid formation by

cytoplasmic polyadenylation element-binding proteins may be crucial for maintaining long term memory (Si et al. 2003). The aggregation of prion protein Ure2p in *Saccharomyces cerevisiae* activates expression of a series of genes involved in uptake of poor nitrogen sources. Amyloid-like prions also exhibit self-perpetuating, infectious and inheritable non-Mendelian genetic trait. (Chien et al. 2004).

Natively unfolded proteins, few molten globules and some denatured monomers tend to aggregate into a fibrillar β-sheet structure. This process of amyloidogenesis has been shown to play a crucial role in diseases like Alzheimer's, Parkinson's, Huntington's, Transmissible encephalopathy syndrome, Creutzfeldt-Jacob disorder, etc (Selkoe et al. 2003, Rochet et al. 2000). Most of these diseases involve a mutated, unfolded or a miscleaved version of the mature peptide like Aβ in Alzheimer's disease. Amyloid formation in Type-2 diabetes, on the other hand is associated itself with the aggregation of wt IAPP and partially processed forms of proIAPP. Despite the absence of any sequence or structural homology between these distinct classes of aggregating proteins, the pathway for the formation of the insoluble amyloid fibrils is believed to be similar. (Harrison et al. 2007). All amyloidogenic peptides form soluble oligomeric intermediates, which then form pre-fibrillar aggregates called protofilaments ranging from 2-5 nm in diameter (Serpell et al. 2000). About two to six of these protofilaments further coalesce and twist together to form fibrils that are 7-13 nm in width.

The formation of amyloid fibrils by a wide variety of sequences highlights the role of the main chain as the major determinant of the β-sheet framework. The interaction of different side chains with each other and with the solvent molecules dictates the details of this fibrillar architecture. Structural analysis of the fibrils elucidates the stabilizing role

of hydrophobic interactions of these side chains running along the fibril axis. Irrespective of the final morphology, all amyloid fibrils can bind to dyes like Thioflavin-T and Congo red (Naiki et al. 1989).

1.1.2. Amylin aggregation in Type 2 Diabetes

Eugene L Opie, in 1901, first described the association of a hyaline staining substance with diabetes mellitus (Opie 1901). This hyaline staining material was independently shown by Westermark and Cooper in 1987 to be a 37 amino acid long polypeptide called Amylin or Islet Amyloid Polypeptide (IAPP) (Westermark and Wernstedt 1987, Cooper and Willis 1987) (Fig. 2). Amylin is co-synthesized and co-packaged with insulin. Amylin and insulin are co-secreted from beta cells in response to increased plasma glucose levels. Amylin is expressed as a 89 amino acid precursor peptide which is processed by the convertases PC2 and PC1/3, resulting in the generation of the functional 37-residue hormone (Kahn et al. 1990, Fehmann et al. 1990) (Fig. 3). Amylin along with insulin and glucagon regulates glucose homeostasis in the body. It inhibits gastric emptying and controls the rate of meal derived glucose (Badman et al. 1996). The aggregation of Amylin results in the loss of β cell mass and function leading to impaired glucose metabolism (Hayden et al. 2001), a characteristic symptom of Type 2 diabetes.

On an average 70-90% of Type 2 diabetic patients show amyloid deposition in islet cells (Ohsawa et al. 1992, Rocken et al. 1992, Clark et al. 1990, Maloy et al. 1981). These proteinaceous deposits range in size from a few nanometers to a few microns. The association of soluble monomeric Amylin to form insoluble fibrillar deposits triggers

cell death in β-cells. Healthy humans generally maintain fasting plasma levels of Amylin varying from 4-25 pmol/L and a clearance rate of 6.2 ml/kg per min, which is much lower than that for insulin (Hartter et al. 1991). Amylin is a natively unfolded neuroendocrine hormone that regulates food intake and fat storage. Amylin also has a very important glucomodulatory role of suppressing glucagon secretion and inhibiting gastric emptying (Harrison et al. 2007). These four functions of Amylin allow for both exogenous and endogenous modulation of the rate of glucose appearance in the blood. In addition, Amylin also inhibits gastric acid, bile and pancreatic enzyme secretion. Thus, Amylin together with insulin constitutes an essential glucoregulatory cascade.

The aggregation of Amylin into amyloid deposits in Type-2 diabetes results in the loss of β-cells (Fig. 4). The extent of correlation between the amount of amyloid formation with the severity of Type 2 diabetes has not been precisely deciphered, however, the role of Amylin in diabetes cannot be undermined (Phillips et al. 2006). Hence, in order to understand diabetes and its complications, there has been renewed interest in studying other pathways associated with insulin depletion and loss of β-cells. Since Amylin and insulin are co-secreted, it is worthwhile to explore the role of Amylin in modulation of insulin levels. Administration of Pramlintide, an analog of Amylin, with insulin has been shown to more effectively regulate the levels of insulin in both Type-1 and Type-2 diabetes patients (Edelman 2008). Also, apart from toxic fibrillar deposits, the loss of Amylin in aggregation might result in decreased levels of functional Amylin leading to disruption of glucose homeostasis in the body.

The occurrence of such fibrillar deposits in patients suffering from amyloidogenic diseases led to the idea of fibrils being the causative agents behind these diseases.

However, recent findings have emphasized the possibility of prefibrillar species, specially the low molecular weight oligomers and protofibrils as being the real pathogenic entities (Kayed et al. 2003) (Fig. 5). These prefibrillar aggregates can evidently be either toxic to cells or perturb the cellular functioning, particularly in the case of neuropathic diseases. Thus, in the case of Type-2 diabetes which involves the loss of β-cell mass, it might be worthwhile to explore the role of Amylin aggregates in this depletion and the consequences on insulin secretion, regulation and function. The question that still remains unanswered is what initiates this process of amyloid formation in diabetic patients.

1.1.3. Aβ aggregation in Alzheimer's disease

Alzheimer's disease is generally characterized by progressive loss of memory and cognitive skills attributed to neuronal cell death (Alzheimer A. 1906). It currently affects more than 24 million people worldwide with 4.6 million new cases each year. However, the pathways involved in causing neuronal cell death are not well understood. Neurotoxic SDS-stable oligomers, spherical aggregates and chain-like aggregates have been shown to inhibit hippocampal long-term potentiation (Lambert et al. 1998, Hoshi et al. 2003), impair synaptic functions and disrupt cognition and learning behaviour in rats (Walsh et al. 2002, White et al. 2005, Hartley et al. 1999, Cleary et al. 2005, Lesne et al. 2006). There is also one unsubstantiated report about the involvement of G-protein modulation in causing neurotoxicity related to Aβ (Rymer and Good 2001). It was further detected that under physiological conditions the metabolism in the brain results in production of low quantities of Aβ (Klein et al. 2001) (Fig. 6). Experimental evidence suggests that

abnormal Aβ accumulation triggers tau pathology (Gotz et al. 2001, Lewis et al. 2001) which then acts as a mediator of Aβ-induced neurotoxicity (Alexander et al. 2002). Aβ has been shown to induce abnormal tau phosphorylation (Busciglio et al. 1995, Greenberg et al. 1994) which is suggested to be the limiting factor in Aβ-induced neurotoxicity (Leschik et al. 2007).

Aβ40 and Aβ42 are the most common isoforms whose aggregation characterizes Alzheimer's disease (Fig. 7). These isoforms are generated from a transmembrane glycoprotein called Amyloid precursor protein (APP), through the successive proteolytic cleavage by β (BACE-1) and γ-secretases sequentially (Selkoe 1998, De Strooper et al. 2000). Depending on the point of cleavage of γ-secretase, Aβ40 and Aβ42 are generated of which Aβ42 is more amyloidogenic. Enhanced production of this highly fibrillogenic isoform results from mutations in APP and in presenilins 1 and 2 (catalytic core of γ-secretase) in early-onset Alzheimer's disease (Loo et al. 1993, Lorenzo et al. 1994, Pike et al. 1993, Howlett et al. 1995). Presenilin is a part of the active site of γ-secretase, which generates the C-terminus of Aβ (Bentahir et al. 2006, Kumar-Singh et al. 2006). In addition, transgenic mice expressing mutant human APP show a time-dependent increase in extracellular Aβ and development of Alzheimer's related neuropathological and behavioural changes (Irvine et al. 2008). Moreover, exposure of cultured neurons to synthetic Aβ solutions containing amyloid fibrils causes cell death. However, the size and number of deposits do not correlate with the severity of symptoms at the time of death (Terry et al. 1991, Lemere et al. 1996). Rather, there have been cases where prevalent deposits are accompanied by no or mild Alzheimer's disease and vice versa (Slow et al. 2005, Arrasate et al. 2004, Morgan et al. 2000). As an alternative, Teplow and others

have postulated that pre-fibrillar aggregates namely protofibrils, Aβ-derived diffusible deposits or Aβ oligomers are the toxic species in order to explain the disagreement between the amount of fibrils and severity of the disease (Lambert et al. 1998, Hoshi et al. 2003, Quist et al. 2005, Kayed et al. 2003). Experiments show that non-fibrillar aggregate preparations, regardless of their size and/or morphological distribution, are toxic to cultured cells/neurons (Lashuel et al. 2002). In recent studies, anti-oligomeric antibodies which do not recognize monomeric or fibrillar Aβ showed abundant anti-oligomer reactivity in soluble extracts of Alzheimer's disease brain but not in the age-matched controls (Georganopoulou et al. 2005). In a separate experiment, a fibroblast cell line that was genetically modified to express mutant human APP produced a significant amount of SDS-stable dimers, trimers and tetramers (Podlisny et al. 1995, Walsh et al. 2002). These oligomers impair complex learned behaviour in rats (Cleary et al. 2005) and reduce the density of dendritic spines in cultured hippocampal neurons (Calabrese et al. 2007, Shankar et al. 2007). Thus removal or neutralization of such toxic species is an attractive therapeutic strategy.

1.1.4. Amyloidogenesis as relevant to other diseases

Apart from Type 2 Diabetes and Alzheimer's disease, amyloid aggregation is a characteristic feature of several other widespread diseases. One amongst them is the neurodegenerative Parkinson's disease that impairs movement. Normally, neurons from the substantia nigra pars compacta project axons that release dopamine in synapses on interneurons in the striatum. However, the death of neurons containing dopamine results in the failure to complete this circuit causing an inability to co-ordinate movement (Braak

et al. 2003). The death of neurons has been attributed to the aggregation of natively unfolded α-synuclein in Lewy bodies. The unaggregated α-synuclein in the presynaptic nerve terminals generally associates with synaptic vesicle membrane and inhibits neurotransmitter release (Larsen et al. 2006). However, the oligomers of α-synuclein formed during its aggregation have been proven to be toxic to the dopaminergic human neuroblastoma cells (El-Agnaf et al. 1998). The role of α-synuclein in Parkinson's disease was further confirmed when increased human α-synuclein expression in transgenic flies (Feany et al. 2000) and mice (Masliah et al. 2000) resulted in loss of neuronal dysfunction and synaptic terminals.

Another amyloidogenesic disease is Familial amyloidotic polyneuropathy (FAP) commonly caused by deposition of transthyretin (TTR) amyloid around peripheral nerves (Huo et al. 2007). Amyloidogenic mutations in TTR lead to the dissociation of native tetramers into partially unfolded species that can subsequently self-assemble into amyloid fibrils (McCutchen et al. 1995, Colon et al. 1996, Kelly et al. 1997, Cardoso et al. 2002). These extensive endoneurial deposits result in axonal degeneration and neuronal loss which causes severe impairment of the autonomic nervous system (Sousa and Saraiva 2003, Benson 1989). Creutzfeldt-Jacob disease in humans is another example of neurodegenerative disorder, which involves conformational conversion of cellular isoform of prion protein, PrP^{c}, into amyloidogenic prion protein, PrP^{sc} (Suehiro 2007). Intracellular accumulation of PrP^{sc} significantly impairs cellular functions and causes neuronal cell death (Kovacs and Budka 2008). There are also a number of non-neurodegenerative disorders, which involve amyloid formation such as Type 2 diabetes,

rheumatoid arthritis, etc. Thus one common mechanism of aggregation when applied to several different proteins can disrupt discrete pathways, which results in various diseases.

1.2. Inhibition of Aggregation

1.2.1. Small Molecule Inhibitors

Initial research involving amyloid formation and disease aimed at understanding aggregation and finding small molecule inhibitors, which could be tested as potential drug leads. The process of amyloid formation can be inhibited either by binding of the inhibitors to the initial monomeric/oligomeric species and preventing it from further self-associating or by inhibiting the pathway that results in the production of amyloidogenic peptide (Fig. 8). Examples include molecules like alpha-d-Mannosylglycerate (Ryu et al. 2008), nitrogen appended N-alkylsulfonamide (Bergstrom et al. 2008) and a multimeric quinacrine conjugate (Dolphin et al. 2008) that have been reported as potential inhibitors of Aβ aggregation. The second category includes inhibitors like NP-61, which inhibit hydrolysis of acetylcholine and interfere with β-amyloid aggregation. These inhibitors have been shown to reduce the amyloid load in the brain and reverse the cognitive impairment (García-Palomero et al. 2008). Another target for inhibition of Aβ production are gamma secretases. The cleavage of APP by β-secretase generates a fragment, which when further cleaved by γ-secretase at its C-terminus results in Aβ which self-associates to form amyloid fibrils. The inhibitors of gamma secretases, like LY450139, aim at preventing Aβ production and its subsequent amyloidogenesis (Siemers et al. 2007).

1.2.2. Natural mechanisms of Amyloid inhibition

1.2.2.1 Chaperones and proteolytic enzymes

In the past decade, a new area in research on understanding Alzheimer's disease has focused on discovering proteins which keep amyloidogenic peptides from aggregating. Indeed, a significant number of heat shock proteins (Hsps) and small heat shock proteins (sHsps) have been shown to that inhibit aggregation of amyloidogenic peptides. Chaperones like Hsp's (heat-shock proteins) assist in the refolding of misfolded proteins while sHsp's (small heat-shock proteins) bind to the misfolded conformation and deliver it to Hsp's for refolding. Hsp104 inhibits the fibrillization of Sup35 prion conformers. Several members of sHsps like αB-crystallin, Hsp27, Hsp20 and HspB8 bind to Aβ40 and Aβ42 and completely inhibit the aggregation of Aβ40 into mature fibrils. Incubation of Aβ40 with these sHsps completely abolished the cerebrovascular toxicity (Wilhelmus et al. 2006, Wilhelmus et al.2006). The extracellular chaperone Clusterin has been shown to inhibit aggregation of prion protein, Aβ, and apolipoprotein C-II. Both Hsp70 and Clusterin are believed to bind to prefibrillar species and prevent the formation of amyloid. The stabilization of these protofibrillar species, however, proved to be toxic in the cell culture based MTT assay using SH-SY5Y cells (Yerbury et al. 2007, Oda et al. 1995). Another mechanism to decrease Aβ load in the brain is the proteolytic activity of Insulin Degrading Enzyme (IDE) and Neprilysin (NEP). IDE is a cytosolic protein that has been shown to degrade Aβ monomers. IDE hypo-function produces accumulation of β-amyloid peptide and induces glucose intolerance (Camberos et al. 2006, Shen et al. 2006). NEP is a plasma membrane protein with its catalytic site exposed extracellularly that targets Aβ diffuse deposits and neuritic plaques (Marr et al.

2004). The combined activity of these enzymes regulates the amount of Aβ species present in the brain. A third pathway of Aβ clearance operates through Low-density lipoprotein receptor-related protein (LRP). LRP is believed to either bind directly to Aβ or its chaperone complex with LRP ligands α2 Microglobulin or apolipoprotein E4. The binding to LRP triggers internalization of the complex to late endosomes after which they are either delivered to lysosomes for degradation or effluxed across the blood brain barrier (Ito et al 2007).

1.3. Current and future therapies for Amyloidosis

1.3.1. Type 2 Diabetes

Diabetes is most commonly associated with insulin resistance whereby insulin binding is unable to open up the glucose transporters. The glucose molecules are not able to enter into the cells as a source of energy resulting in a high blood sugar level. The failure of pancreatic β-cells to adapt insulin secretion in relation to insulin sensitivity can result in insulin resistance. This further leads to inappropriate insulin levels, impaired glucose intolerance and type 2 diabetes (Ahren and Pacini 2007). Thus most of the drugs administered to diabetic patients aim at reducing insulin resistance by either stimulating beta cells to release more insulin like Meglitinides or acting as insulin sensitizers like Thiazolidinediones, which promote skeletal muscle glucose uptake. Insulin injections are generally the last resort for patients whose blood glucose levels cannot be maintained by oral drugs.

To this date, drugs regulating insulin levels have helped diabetic patients in maintaining reasonable glucose levels under strict dietary restrictions. However, no drug

is available that can cure diabetes or prevent further complications. It is possible that other hormones along with insulin contribute to causing diabetes. It is known that glucose homeostasis in an organism involves insulin and hormones like glucagon and Amylin. As mentioned, diabetes is also associated with the deposition of fibrillar aggregates of Amylin in pancreas. These aggregates have been proven to be toxic to insulin secreting beta cells (Lorenzo et al. 1994). The loss of beta cells might contribute to the insulin resistance and decreased effectiveness of the administered drugs. Experiments have shown Amylin to be the neuroendocrine hormone responsible for satiation signaling in the brain (Reidelberger et al. 2004, Lutz 2006, Olsson et al. 2007, Osto et al. 2007). Thus loss of Amylin in aggregation has been postulated to be responsible for the association of obesity with diabetes. Recently, the FDA approved an analog of Amylin called pramlintide to be administered with insulin. Patients that have been taking pramlintide with insulin have shown better response to insulin regulating drugs (Combettes and Kargar 2007). Thus preventing Amylin aggregation and targeting the toxicity associated with the fibrillar aggregates might prove to be useful approaches in finding cures for diabetes.

1.3.2. Alzheimer's disease

2001 marked the completion of a century since Alois Alzheimer discovered Alzheimer's disease. However, no treatment is effective in preventing progression of this disease. The drugs administered can only delay the worsening of symptoms. The first class of drugs involves Cholinesterase inhibitors to target mild to moderate dementia. These molecules inhibit the breakdown of neurotransmitter, acetylcholine, and show only

a marginal improvement in cognitive function (Christensen and White 2007). Cholinesterase was demonstrated to be involved in development of amyloid plaques. The second class of drugs includes memantine, which selectively blocks the N-methyl-D-aspartate class of glutamate receptor. These receptors cause degeneration of neurons most susceptible in Alzheimer's disease (Irvine et al. 2008). Some of the drugs currently in clinical trials have been designed to β and γ-secretases that can prevent the cleavage of APP. The inhibition of these enzymes reduces the production of Aβ and hence slows down its aggrgation.

A number of other anti-amyloid therapies are also under development to either decrease the production of soluble Aβ monomers or to remove the soluble and deposited Aβ. The rationale behind the first approach is to reduce the available Aβ concentrations below the critical concentration required for the oligomerization of Aβ into toxic species. Small molecules are also being developed to up-regulate the enzymes involved in Aβ degradation. To remove both soluble and fibrillar Aβ, antibodies have been developed that recognize different Aβ assemblies and neutralize them by promoting microglial clearance or redistribution of Aβ to systemic circulation. This approach alleviated the memory impairment, reduced cerebral Aβ and decreased neuritic dystrophy in transgenic mouse models of Alzheimer's disease. However, 18 of 298 patients developed meningoencephalitis on immunization with these antibodies (Orgogozo et al. 2003).

1.4. Disaggregation of Amyloid Fibrils

Several years of research has shown that the process of amyloid aggregation is a key feature in many neurodegenerative diseases. Attempts have been made to search for

compounds which can result in disaggregation of these fibrillar deposits. Initial experiments showed that amyloid fibrils are stable against chemical and thermal denaturing agents and are not very sensitive to the effects of dilution. However several compounds were discovered to disaggregate amyloid plaques. Hyperforin, an acylphloroglucinol compound isolated from Hypericum perforatum, disaggregates and inhibits amyloid deposits in a dose and time-dependent manner. This prevented Aβ-induced neurotoxicity in hippocampal neurins and decreased behavioral impairments in rat models (Dinamarca et al. 2006). α-1-antitrypsin was successful at completely disaggregating fibrils when added in the molar ratio of 1:5 (Eriksson et al. 1995). 4'-iodo-4'-deoxydoxorubicin and tetracyclines were effective in disrupting TTR fibrils producing non-cytotoxic species (Cardoso et al. 2003). Treatment of Alzheimer's mice models with curcumin resulted in significant decrease in dystrophy size and reversal of structural changes in neuritis within seven days (Garcia-Alloza et al. 2007).

Immunotherapy approach for dissociating amyloid fibrils has shown some promising results as well. Anti-Aβ(1-11) antibody inhibited aggregation of Aβ42 and induced disaggregation of fibrils to non-filamentous, non-toxic species (Mamikonyan et al. 2007). The immunization of transgenic mice with Glu-Phe-Arg-His antigen presented on the surface of filamentous phage caused a reduction in the number of amyloid plaques in the brain (Frenkel et al. 2003). mAbs against Aβ(1-28) prevented Aβ aggregation and triggered the reversal of fibrils to non-toxic components (Solomon et al. 1997). A trifunctional fusion antibody that binds to human insulin receptor was engineered to mediate influx and efflux across the blood brain barrier and was found to be effective at disaggregating amyloid plagues (Boada et al. 2007). Though anti-Aβ immunotherapy has

shown promising results *in vitro* and in mice models, it unfortunately showed detrimental effects such as brain inflammation and microhemorrhage. To counteract this, a single chain antibody (scFv) gene was intracranially and intramuscularly delivered through adeno-associated virus vectors. The antibody effectively inhibited aggregation of Aβ and promoted disaggregation of preformed fibrils (Wang et al. 2007). Thus engineered biological agents can be functional at disaggregating amyloid fibrils, suggesting they can be a promising approach in designing effective treatments against amyloidosis.

1.5 Figures

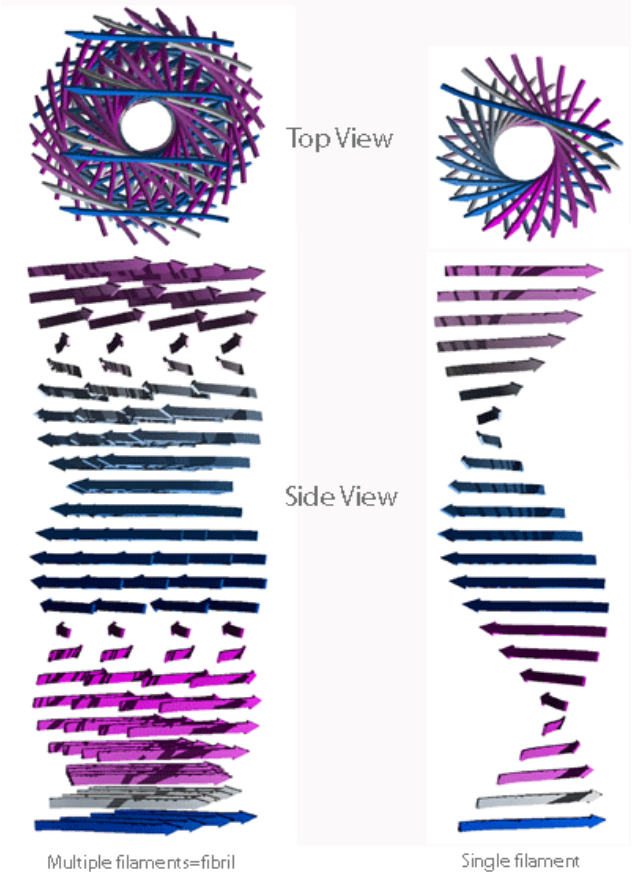

Figure 1. Structure of an amyloid fibril formed when insoluble protein aggregates. The arrows represent β-strands which are aligned into parallel β-sheets with a helical twist. *Picture courtesy of Louise Serpell, Sussex University.*

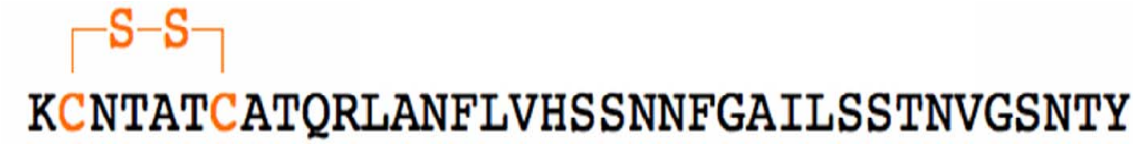

Figure 2. The amino acid sequence of processed hIAPP (or Amylin). The C-terminus of the 37 residue hormone is amidated and a disulfide bond is formed between Cys2 and Cys7.

Figure 3. Processing of proIAPP. The primary sequence of 67 residue proIAPP is shown. The N- and C-terminal flanking regions of proIAPP are shown in blue, and the mature IAPP sequence shown in black. Cleavage by PC-2 and PC-1/3 occurs at the sites indicated by arrows. The remaining residues at the C-terminus are removed by carboxypeptidase E and mature IAPP is formed by removal of Gly-49 at the C-terminus and amidation of the Tyr.

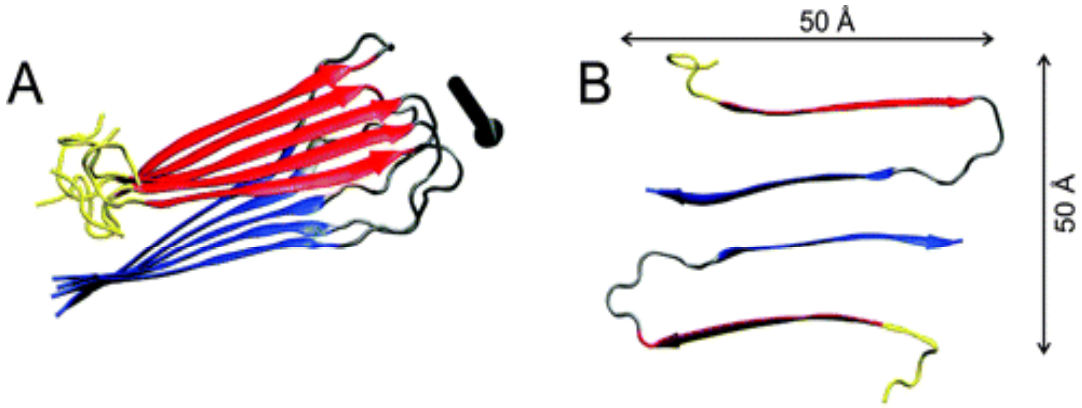

Figure 4. Model of structural arrangement of Amylin protofilaments from Solid state NMR structure (Luca et al. 2007). A) Ribbon diagram of one cross-molecular layer with N-terminus shown in red and C-terminus shown in blue. The black arrow indicates the axis of fibril growth. B) Arrangement of 2 Amylin molecules in the β-sheet structure in the cross-sectional view.

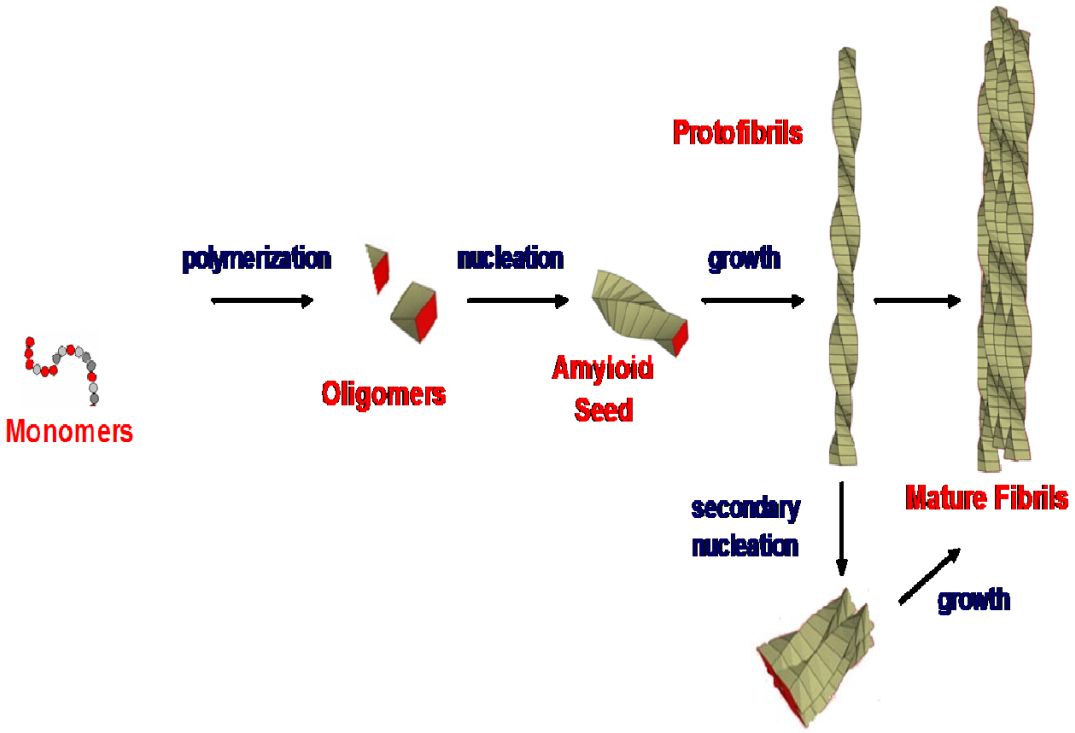

Figure 5. A schematic diagram proposing a model of steps involved towards amyloid formation. The association of monomers forms oligomeric species which then assemble to 'seed' rapid growth. Secondary nucleation is also observed which is dependent on the presence of fibrils, protofibrils and off-pathway steps such as formation of amorphous aggregates.

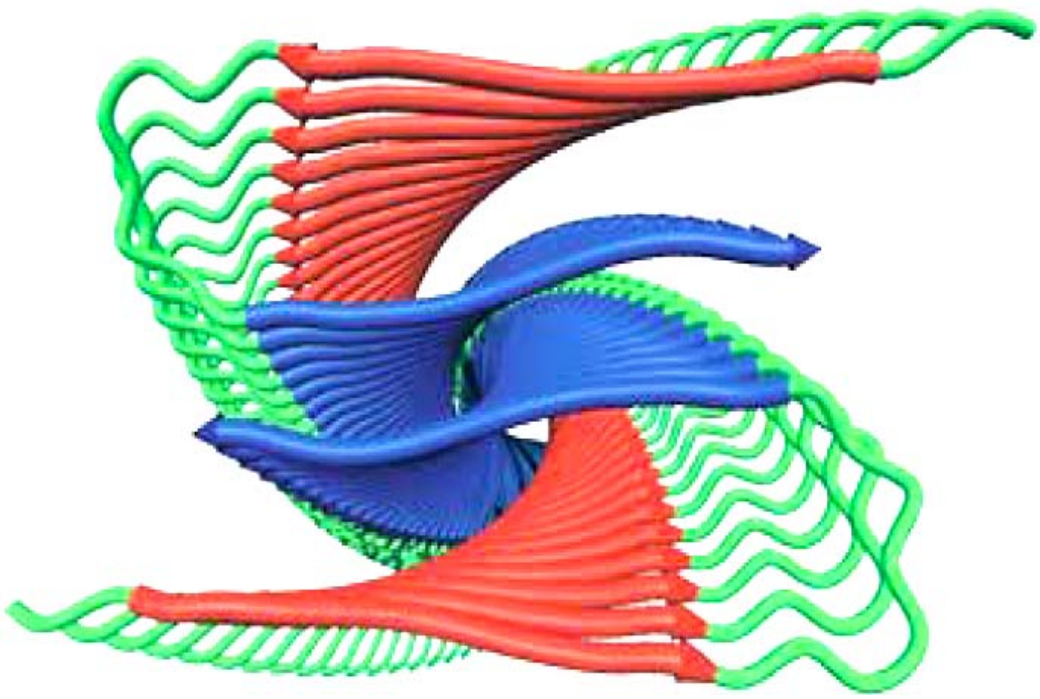

Figure 6. Cartoon representation of structure of full length Aβ40 fibrils based on the solid state NMR data (Petkova et al. 2006).

DAEFRHDSGYEVHHQKLVFFAEDVGSNKGAIIGLNVGGVV

DAEFRHDSGYEVHHQKLVFFAEDVGSNKGAIIGLNVGGVVIA

Figure 7. Amino acid sequence of Aβ40 (blue) and Aβ42 (green) generated from the cleavage of amyloid precursor protein.

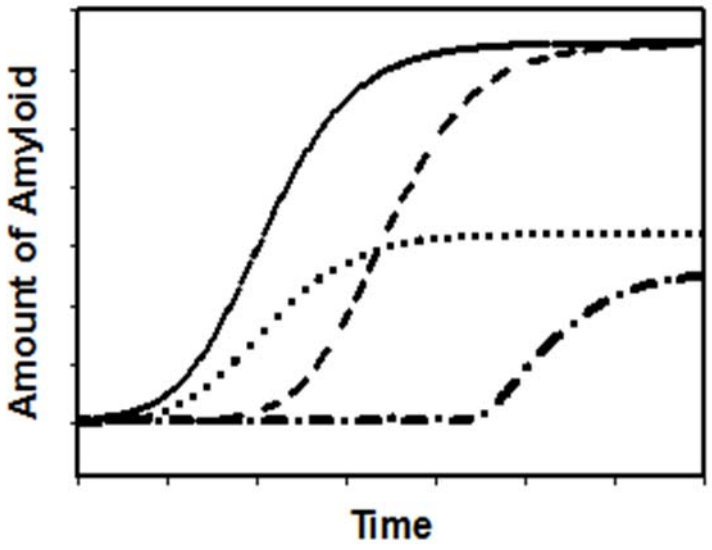

Figure 8. A schematic representation of the effect of different inhibitors on the kinetics of amyoid formation. The profile of an amyloidogenic protein is shown as a solid line. An inhibitor which reduces the production of amyloid but does not alter the lag phase leads to the dotted curve, while an inhibitor which lengthens the lag phase but does not prevent amyloid formation leads to the dashed curve. The result of adding an inhibitor which both lengthens the lag phase and reduces the amount of amyloid is indicated by the dotted-dashed line.

Chapter 2. Energetics of Amyloid Formation by the Natively Unfolded Islet Amyloid Polypeptide

2.1 Abstract

Amyloid formation has been implicated in a wide range of human diseases including Type 2 diabetes, Alzheimer's disease and Parkinson's disease. In Type 2 diabetes, the hormone Islet Amyloid Polypeptide (IAPP or Amylin) aggregates to form amyloid plagues in the pancreas. These deposits are toxic to the insulin producing β-cells and are believed to contribute to the pathology of the disease. The process of amyloidogenesis is believed to involve oligomer formation before fibrillization. These oligomers might contribute to cellular toxicity. However, the exact mechanism of amyloid formation is still under investigation. Here we report temperature dependent kinetic studies of IAPP amyloid formation. The rate of amyloid formation was investigated using thioflavin-T binding assays over the temperature range of 5 ^{o}C to 60 ^{o}C. Comparative studies were conducted of peptides initially solubilized in hexafloroisopropanol (HFIP) and DMSO and the respective activation parameters were determined. The activation parameters have been compared to other amyloidogenic systems of comparable size.

2.2 Introduction

IAPP, like the Aβ peptide of Alzheimer's disease, is "natively unfolded" in its monomeric state, which is a property it shares with a number of other important amyloidogenic polypeptides. The design of inhibitors of IAPP fibrillogenesis is an active area of research (Harrison et al. 2007). A detailed understanding of the self assembly process and the energetics of the various steps is an important for selecting potential species as drug targets. Unfortunately, relatively little is known about IAPP fibrillogenesis in comparison to the aggregation process of Aβ. To further understand the energetics governing this process, temperature dependent kinetic measurements have been used to characterize the fibril formation by IAPP.

In vitro studies of a large number of amyloidogenic systems indicate that the process of amyloid formation can be divided into two phenomenological steps (Merlini and Bellotti 2003). In the first step, the so-called lag phase, no fibrils are observed rather a "seed" or a critical nucleus is formed through association of monomers. The second step is the addition of soluble protein to the nucleus, which is rapid and energetically favorable, resulting in a rapid growth phase and finally into amyloid fibrils.

The formation of the nucleus is a complicated and potentially heterogeneous process. In addition, secondary nucleation can be important. Thus the fundamental steps which make up the lag phase are difficult to characterize. In contrast, the growth phase is normally a well-defined process involving addition of soluble protein to fibrillar ends. But even here complications can arise because of secondary nucleation. A number of experimental studies have indicated that the kinetics of fibril elongation is first order (Kusumoto et al. 1998). The elongation rate is a fundamental property of a fibrillogenesis

reaction and will vary from system to system depending on the solvent conditions such as pH, temperature, ionic strength and co-solvent composition. The kinetics of elongation phase of Aβ and insulin has been reported and apparent activation parameters have been determined by conducting temperature dependent studies. The value of $\Delta H^{\#}$ for Aβ has been reported to be 23.0 kcal/mol (Kusumoto et al. 1998) and 24.4 kcal/mol for Insulin at pH 2.0 (Knowles et al. 2007). The change in free energy of activation was computed to be 7.7 kcal/mol for Aβ and 8.0 kcal/mol for insulin at 293K. The similar energetics reflects that the growth of amyloid fibrils involves an activation barrier, which regulates the rate of elongation of fibrils during amyloid formation and suggests that similar processes may be involved.

2.3 Materials and Methods

2.3.1 Protein Synthesis and Purification

Wild type human IAPP (Amylin) was synthesized on a 0.25mmol scale using 9-fluornylmethoxycarbonyl (Fmoc) chemistry on an Applied Biosystems 433A Peptide Synthesizer. 5-(4'-Fmoc-aminomethyl-3',5-dimethoxyphenol) valeric acid (PAL-PEG) resin was used to generate an amidated C-terminus. Pseudoproline dipeptide derivatives were employed as described (Abedini and Raleigh 2005). Fmoc-protected pseudoproline (oxazolidine) dipeptide derivatives were purchased from Novabiochem. All other reagents were purchased from Advanced Chemtech, Fischer Scientific, PE Biosystems and Sigma. All solvents used were of A.C.S. grade. Standard Fmoc reaction cycles were used. The first residue added to the resin, pseudoproline dipeptide derivatives, all β-branched residues and all residues following the β-branched residue were double coupled.

The peptide was cleaved from the resin using standard trifluoroacetic acid (TFA) methods. The crude peptide was treated with 20% (v/v) acetic acid and lyophilized. The disulfide bond was formed via DMSO induced oxidation of the crude peptide. The oxidized peptide was purified via reverse-phase HPLC using a Vydac C-18 preparative column. A two-buffer system utilizing HCl as an ion-pairing agent was used for the purification. Buffer A consisted of 0.045% (v/v) HCl in distilled de-ionized (DDI) water. Buffer B consisted of 80% (v/v) acetonitrile, 20% (v/v) DDI water and 0.045% (v/v) HCl. The purity of the peptide was checked by HPLC and was 99%.

The purified peptide was analyzed by matrix-assisted laser desorption/ionization time-of-flight (MALDI-TOF) mass spectroscopy. The observed molecular weight was 3903.4Da and the expected molecular weight was 3903.3Da.

2.3.2 Fluorescence based kinetic assays

The kinetics of amyloid formation by Amylin were studied using Thioflavin-T fluorescence. All fluorescence measurements were done on a Jobin Yvon Horiba fluorescence spectrophotometer using an excitation wavelength of 450 nm and an emission wavelength of 485 nm. The emission and excitation slits were both set to 5 nm and a 1.0 cm cuvette was used. Experiments were performed by diluting a stock solution of peptide (1.58 mM for 2% studies and 3.16 mM for 1% studies) in HFIP or DMSO into 20 mM Tris-HCl buffer at pH 8.5 containing thioflavin-T. Each stock solution was filtered through a 0.45 μm pore size GHP Acrodisc syringe filter prior to the experiment to remove large aggregates. The final reaction mixture contained 32 μM peptide and 32 μM thioflavin-T at pH 8.5 at the desired temperature. All solutions were stirred during

the assay to maintain solution homogeneity. Temperature was controlled by a water bath and the temperature of the cell was calibrated using a thermocouple before each experiment.

2.3.3 Data Analysis

To calculate the kinetic parameters for elongation of fibrils, the data was fitted to a 5-parameter equation:

$$y(t) = y(t_0) + \frac{a}{\left[1 + e^{\left\{\frac{t_0 - t}{b}\right\}}\right]^c} \quad (1)$$

where, y(t) is the observed fluorescence at time t, b is related to the slope of the growth phase, a is the final fluorescence intensity and c is the lag phase. The function describes a sigmoidal curve for kinetics of fibril formation. The first derivative of the fit gave the apparent rate of fibril growth as a function of time. These apparent rate constants corresponding to the maximum growth rate were used for the Arrhenius analysis. The slope of the Arrhenius plot was used to evaluate the apparent activation energy barrier, E_a, for fibril growth. Since each reaction was performed under constant pressure and volume, $E_a = \Delta H^{\ddagger}$. The change in entropy for the process was estimated using the procedure described by (Kusumoto et al. 1998):

$$\Delta S^{\#} = R \ln\left(\frac{A}{\upsilon^{1/3} D}\right) \quad (2)$$

where, A is the prefactor whose value was obtained from the y-intercept of the Arrhenius plot. The reaction volume size $l = \upsilon^{1/3}$ was taken to be the order of the dimension of a

IAPP monomer ≈ 1nm. The diffusion coefficient, D, of the free monomer was calculated using $D = k_B T/6\pi\eta R_h$, where k_B is Boltzmann's constant, T is the absolute temperature, ή is the solvent viscosity and R_h is the hydrodynamic radius.

2.3.4 Circular Dichroism Spectroscopy

All CD experiments were performed using an Aviv 62A DS CD spectrophotometer. Far-UV CD spectra were recorded at the end of each kinetic run. Spectra were recorded over the wavelength range of 190-250nm at 1nm intervals with an averaging time of 3s using a 0.1cm path length cell. Background spectrum was subtracted from each of the collected data sets. Each spectrum obtained was an average of 3 scans.

2.3.5 Transmission Electron Microscopy

TEM was performed at the Microscopy imaging center at the State University of New York at Stony Brook. Samples were prepared by placing 15µl of solution onto formvar coated 300 mesh copper grids and counterstained with 2% aqueous uranyl acetate. Samples were viewed with a FEI Tecnai12 BioTwinG^2 transmission electron microscope at 80 kV. Digital images were acquired with an AMT XR-60 CCD Digital Camera System and compiled using Adobe Photoshop CS2.

2.4 Results

IAPP is extremely aggregation prone and it is difficult to prepare samples in an initially unaggregated state. A variety of protocols have been developed over the years. The most effective method involves dissolving the polypeptide in either HFIP or DMSO

and initiating fibril formation by diluting the stock solution into aqueous buffer (Higham et al. 2000). The residual co-solvent present in the reaction mixture can modulate the kinetics drastically and the magnitude of the effect depends on the type of co-solvent and its concentration. The lowest concentration of the co-solvent is clearly desirable. However, the amount is limited by the final concentration of IAPP needed in the reaction mixture and the solubility of IAPP in the organic solvent. The presence of even trace amounts of the co-solvent can have profound effects. The strategy used here is to conduct a series of experiments in which final concentrations of HFIP and DMSO are varied over a range and the values are extrapolated back to zero co-solvent concentration.

Fluorescence detected thioflavin-T binding assays are convenient and are commonly used to follow amyloid formation. The quantum yield of the dye increases in the fibril bound state and the dye appears to bind to almost all fibrils studied. The exact mode of binding is not understood but it is widely believed that it binds into the grooves on the surface of fibrils with the long axis of the dye, which is oriented perpendicular to the individual β-strands (Groenning et al. 2007). Thioflavin-T binding has been widely applied to IAPP and this methodology was utilized in the present work. All kinetic experiments were conducted using 32 μM thioflavin-T and 32 μM of peptide.

The kinetic profile of Amylin fibril formation shows a well-defined lag phase, which is also called the nucleation phase followed by a rapid growth phase. The growth of the amyloid fibrils is characterized by a rapid increase in the intensity of thioflavin-T fluorescence observed at 485nm. Experiments were conducted over a temperature range of 5^{o}C to 50^{o}C in solutions containing 1% HFIP, 2% HFIP, 1% DMSO, 1.5% DMSO, 2% DMSO (Fig. 2-3). Stock solutions were prepared so that the final peptide

concentration was the same in each experiment. Amyloid formation at each temperature was confirmed by TEM (Fig. 4-20) and Far UV CD spectroscopy (Fig. 21-23). The CD spectra collected at the end of each kinetic run were typical of those reported for IAPP fibrils and exhibited a characteristic minimum at 218nm. TEM images taken at the end of each kinetic run confirmed the presence of amyloid fibrils.

The rate of amyloid formation by Amylin is strongly pH dependent, particularly near neutral pH which reflects the titration of His-18 and the N-terminus in this pH region. This presents a significant complication since the pH of aqueous buffers can be temperature dependent as can the pK_a values of amino acid sidechains in proteins. IAPP contains one Lys, one Tyr and an Arg in addition to the aforementioned His. Conditions were chosen where minor temperature dependent changes in pH would not alter the observed kinetics. This necessitated working above the pK_a of the N-terminus and His-18 but below the pK_a of the other titratable sidechains. A series of control experiments were conducted in which the rate of aggregation was examined as a function of pH between pH 7.12 and pH 9 (Fig. 19, 20, 24-25). pH 8.5 proved to be a suitable compromise. Variations in pH between 8 and 9 had no significant effect on the observed kinetics with the lag phase varying by only 5% and the growth phase by 13%.

Each kinetic experiment was fitted to a 5-parameter sigmoidal function and the activation parameters were computed using the methodology of Teplow and Benedek (Kusumoto et al. 1998). The maximum rate of growth of fibrils (k_{max}) was derived from the fitted data at 32 μM total monomer concentration. The values of the log of k_{max} obtained at different temperatures showed an Arrhenius behaviour. The apparent activation energy, E_a, was determined from the slope of the curve. The entropic

contribution was estimated as described by Teplow and Benedek (Kusumoto et al. 1998). This analysis assumes that the mechanism of growth of fibrils involved addition of monomers to the growing fibril tips.

The kinetic analysis in 2% HFIP shows that both nucleation and growth require an activation barrier to proceed. The results shown in Figure-2 illustrate that as the temperature of the reaction is decreased, the lag phase increases and the growth rate slows. When the stock solution was made in DMSO and experiments were conducted with 2% DMSO as the final co-solvent concentration, the rate of aggregation was slower than observed for HFIP. The temperature dependent trends, however, were similar i.e. the lag phase increased at lower temperature and the growth rate decreased. The time needed to form the initial seeds increased considerably in the presence of DMSO. The rate of growth of the fibrils was also much slower in DMSO as compared to HFIP.

This behaviour can be understood by taking the nature of solvents into consideration. It has been suggested that the process of amyloid formation by Amylin involves formation of a helical intermediate (Williamson and Miranker 2007, Abedini and Raleigh unpublished). The co-solvent HFIP is known to induce helical structure. Thus the presence of HFIP will promote the formation of helical intermediate and its stabilization, resulting in the enhanced rate of amyloidogenesis. DMSO, on the other hand, is a denaturing solvent, which can impede the formation of structured intermediates and hence slow down the process of fibril formation. This is evident from the thermodynamic parameters obtained from the analysis of the temperature dependent kinetic data (Fig. 26). The enthalpy of activation computed for 2% HFIP was 6.5 kcal/mol and the estimated activation entropy was 2.4 kcal/mol at 293K (Table 1).

Aggregation of Amylin in 2% DMSO involved an activation energy of 18.2 kcal/mol with an associated entropy of activation of 12.9 kcal/mol at 293K (Table 1). The increase in activation barrier in the case of DMSO reflects the difficult in forming peptide peptide interactions in DMSO.

The above hypothesis was tested by studying the kinetics of Amylin fibrillization in lower percentages of the co-solvent. Since the presence of HFIP favors the aggregation of Amylin, reducing its concentration in the reaction mixture is expected to decelerate fibril formation. Figure-2 shows the data set for temperature dependent studies with 1% HFIP as the co-solvent. The rate of aggregation was slower in 1% HFIP as compared to 2% HFIP. Similar behaviour has been reported by Miranker and coworkers in their studies of the effect of varying HFIP concentration on fibril formation (Padrick and Miranker 2002). The activation energy barrier calculated for 1% HFIP was 9.7 kcal/mol in contrast to 6.5 kcal/mol observed in 2% HFIP.

Along the similar lines, reducing the amount of DMSO in the reaction mixture is expected to accelerate fibril formation. The temperature dependent kinetics data for 1% and 1.5% DMSO are shown in Fig. The data analysis for the growth phase gives an enthalpy of activation of 11.4 kcal/mol in 1% DMSO with an entropic contribution of 6.5 kcal/mol at 293K. The kinetics of Amylin aggregation in 1.5% DMSO revealed the enthalpy of activation to be 12.4 kcal/mol and entropy to be 11.2kcal/mol. The reduction in activation barrier on decreasing the concentration of DMSO supports the conjecture that DMSO interacts with Amylin and slows down the oligomerization of monomers into amyloid fibrils.

Table 1 summarizes the kinetic data for Amylin aggregation under all the conditions studied. The computed enthalpy of activation and the entropic contribution were used to evaluate the free energy of activation for growth of fibrils ($\Delta G^{\#}_{growth}$) under each co-solvent condition. $\Delta G^{\#}_{growth}$ was found to vary from 4.1 kcal/mol in 2% HFIP to 5.2 kcal/mol in 2% DMSO at 293K. Extrapolation of the data to Amylin aggregation under no co-solvent condition gives a $\Delta G^{\#}_{growth}$ value of around 5 kcal/mol. This value is significantly lower than that reported for aggregation of Aβ40 and insulin. $\Delta G^{\#}_{growth}$ documented for Aβ fibril formation is reported to be 7.7 kcal/mol and is 8.0 kcal/mol for insulin aggregation (Kusumoto et al. 1998, Knowles et al. 2007). The lower $\Delta G^{\#}_{growth}$ value highlights the greater tendency of unstructured Amylin monomers to rapidly associate into β-sheet fibrils as compared to other known amyloidogenic peptides.

2.5 Discussion

The kinetic studies on amyloidogenesis of wild type Amylin reported here reveal the temperature dependence of the rate of fibril formation. The log of the apparent rate of growth of fibrils increases linearly with the temperature following Arrhenius behaviour. Shortening of the lag phase was also observed as the temperature of the reaction was increased, which indicated that both the processes of nucleation and addition of the monomers/oligomers to form fibrils involves overcoming an activation energy barrier. This barrier is very sensitive to the nature and amount of the organic solvent present in the reaction.

Transition-state theory predicts (Kusumoto et al. 1998) that the growth of the fibrils by incorporation of the monomers is exponentially modulated by the Gibbs free energy of

the transition state between the native structure of the protein and its configuration in the fibrillar state. The plots and data summarized in Table 1 clearly show the convergence of data as the amount of organic co-solvent is decreased. Thus under the condition where no organic co-solvent is present, $\Delta G^{\#}_{growth}$ will be approximately 5.0 kcal/mol and the apparent activation energy will be around 10.5 kcal/mol. These values can be compared to the parameters derived for insulin and Aβ fibril formation. The activation energy observed for these amyloidogenic peptides is much larger than that observed for Amylin. The activation energy for Aβ40 was reported to be 23 kcal/mol and for insulin, it was 24.4 kcal/mol (Table-2) (Kusumoto et al. 1998, Knowles et al. 2007). This barrier is much larger when compared to the anticipated enthalpy of activation ~ 10.5 kcal/mol for Amylin with no organic co-solvent. $\Delta G^{\#}$ of activation for Aβ40 and insulin is on the order of 7.7 to 8 kcal/mol respectively. These values are significantly larger than for Amylin. This comparison sheds light on the fast aggregating behavior of Amylin as compared to other peptides. The presence of a smaller activation barrier for aggregation of Amylin confirms that Amylin has a relatively higher amyloidogenic propensity than Aβ and insulin. Small molecules that increase the activation barrier or decrease the entropy of the system might be promising therapeutic targets. The temperature dependent studies illustrated here present itself as a methodology of testing these leads for inhibition.

2.6 Figures

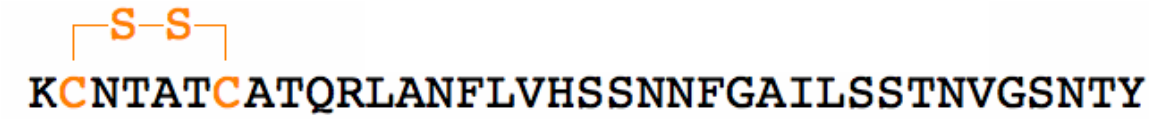

Figure 1. Amino acid sequence of processed Amylin (or Amylin). The C-terminus of the 37 residue hormone is amidated and a disulfide bond is formed between Cys2 and Cys7.

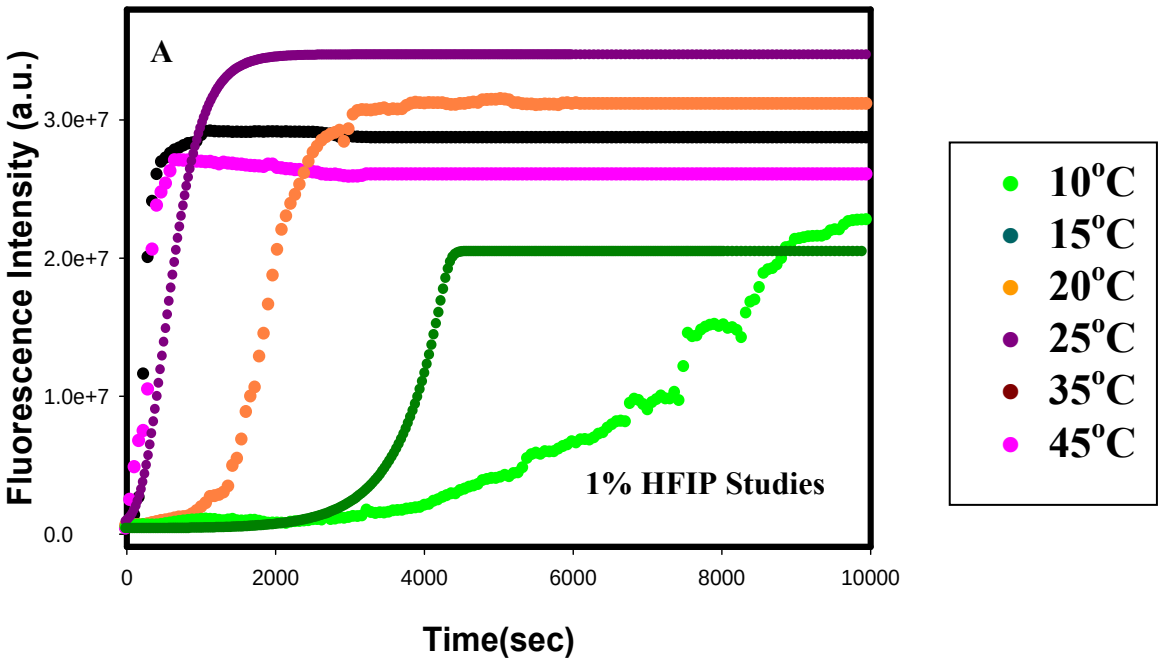
A
Fluorescence Intensity (a.u.)
3.0e+7
2.0e+7
1.0e+7
0.0
0
2000
4000
6000
8000
10000
Time(sec)
1% HFIP Studies
10°C
15°C
20°C
25°C
35°C
45°C

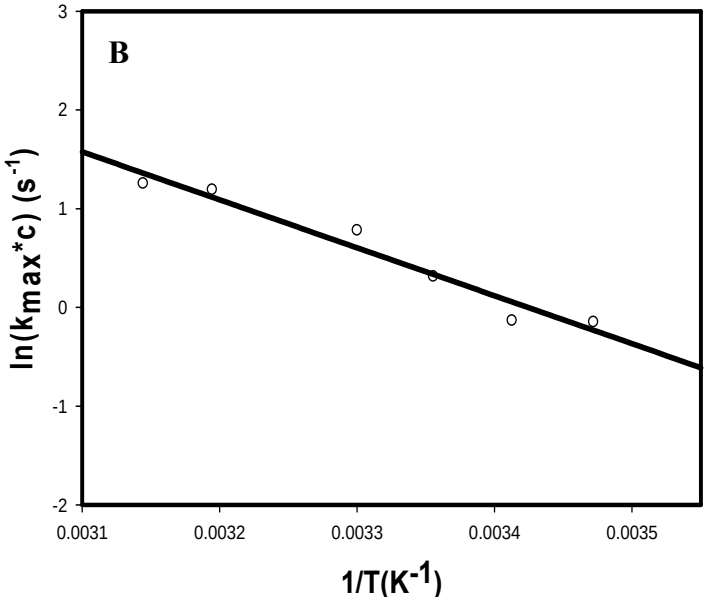
B
ln(kmax*c) (s-1)
3
2
1
0
-1
-2
0.0031
0.0032
0.0033
0.0034
0.0035
1/T(K-1)

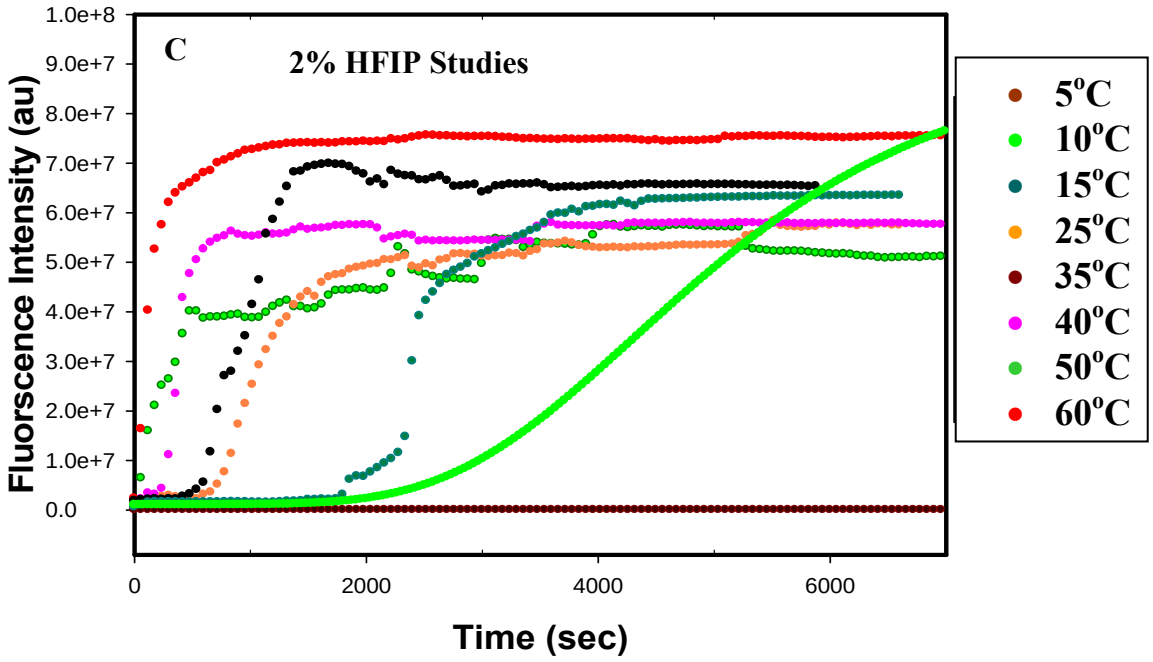

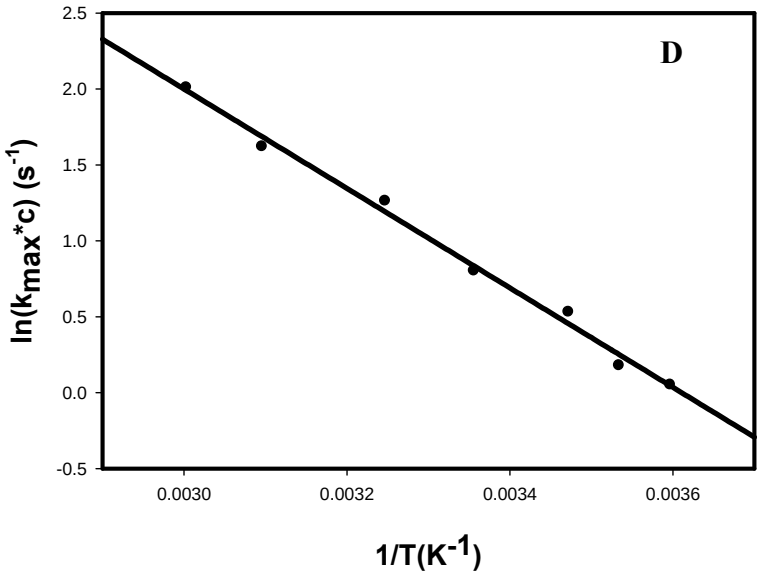

Figure 2. Temperature dependent kinetics of amyloid formation by Amylin with A) 1% HFIP, C) 2% HFIP as the organic co-solvent. The Arrhenius plots of k_{max} obtained from the fitted data at different temperature in B) 1% HFIP and D) 2% HFIP are shown.

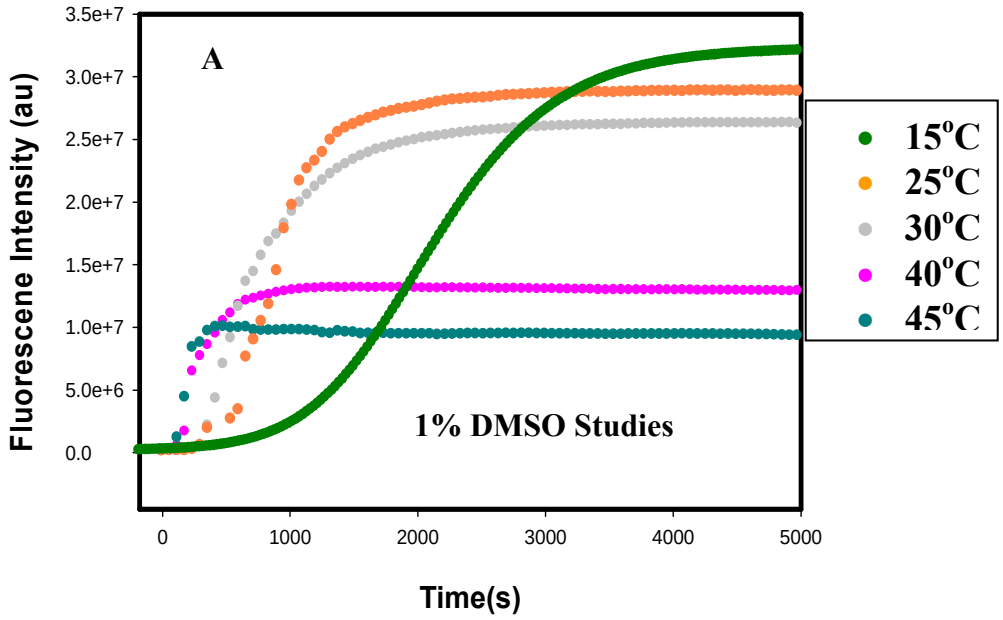
A
Fluorescene Intensity (au)
3.5e+7
3.0e+7
2.5e+7
2.0e+7
1.5e+7
1.0e+7
5.0e+6
0.0
0
1000
2000
3000
4000
5000
Time(s)
1% DMSO Studies
15°C
25°C
30°C
40°C
45°C

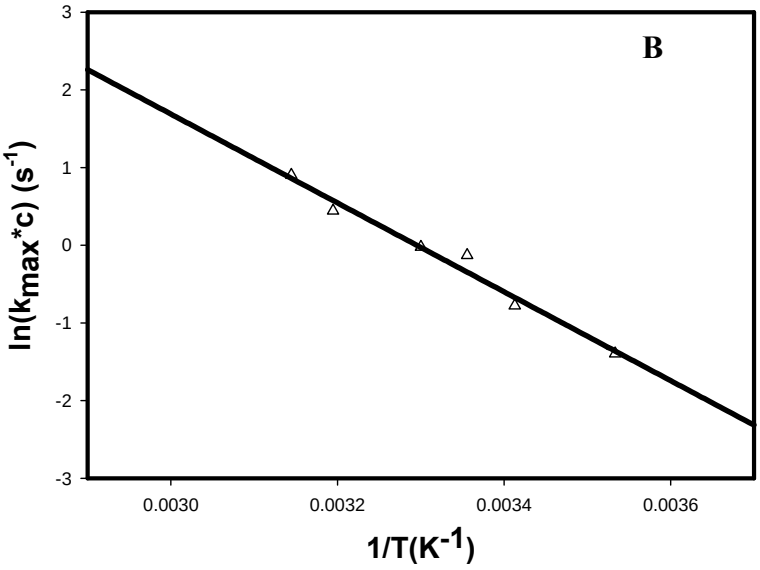
B
ln(kmax*c) (s-1)
3
2
1
0
-1
-2
-3
0.0030
0.0032
0.0034
0.0036
1/T(K-1)

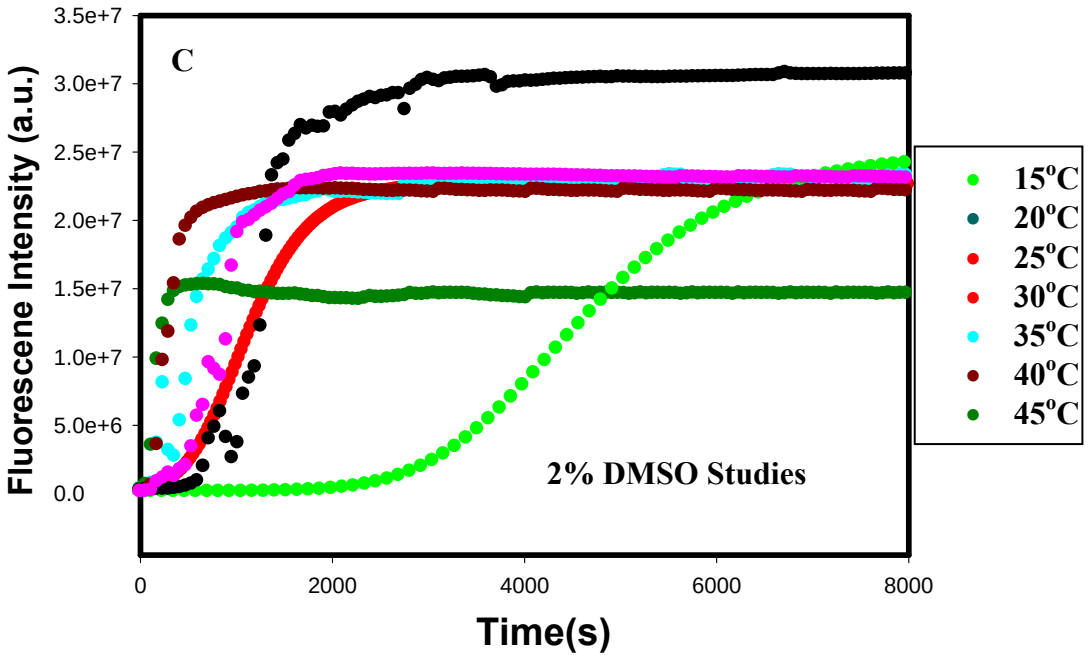
C
Fluorescene Intensity (a.u.)
3.5e+7
3.0e+7
2.5e+7
2.0e+7
1.5e+7
1.0e+7
5.0e+6
0.0
0
2000
4000
6000
8000
Time(s)
2% DMSO Studies
15°C
20°C
25°C
30°C
35°C
40°C
45°C

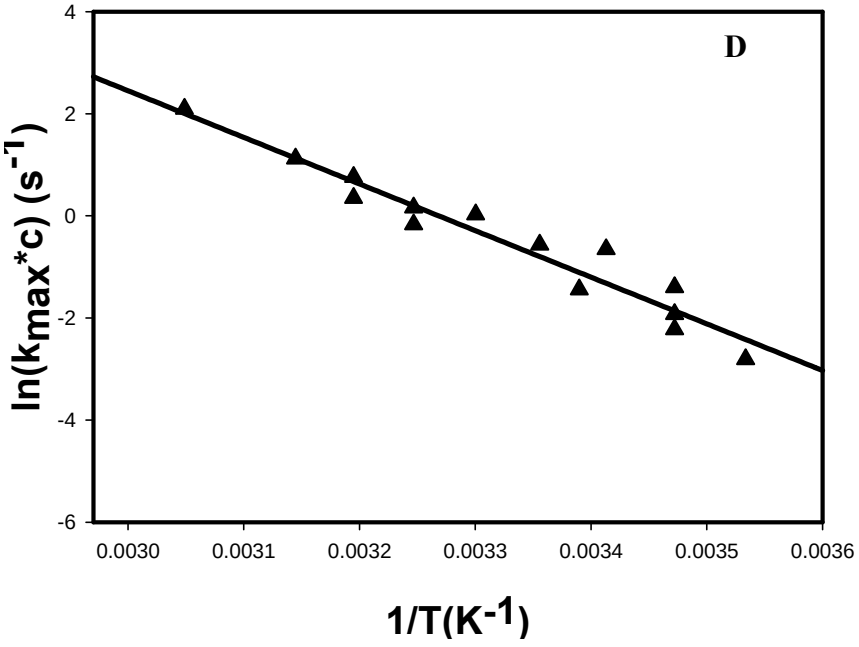
D
ln(kmax*c) (s-1)
4
2
0
-2
-4
-6
0.0030
0.0031
0.0032
0.0033
0.0034
0.0035
0.0036
1/T(K-1)

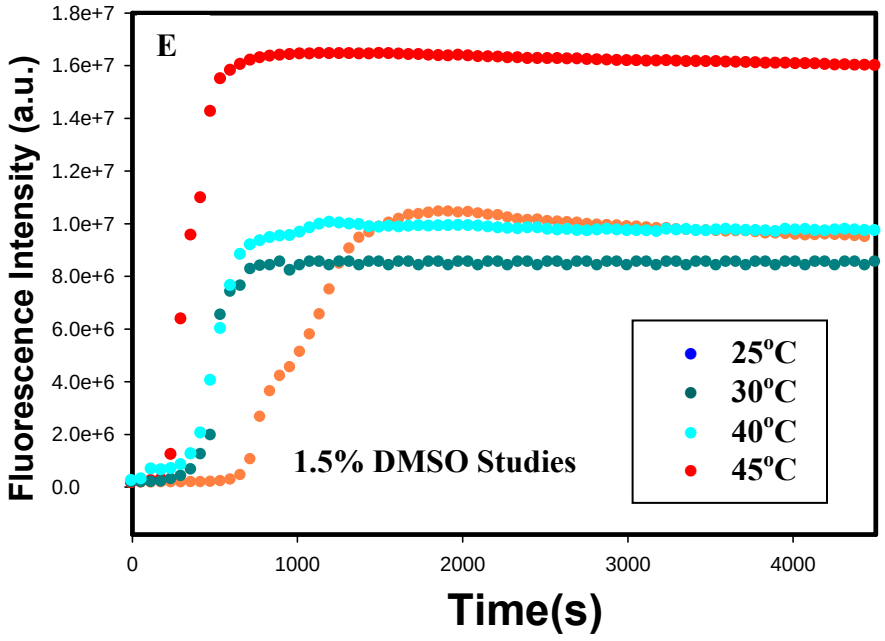

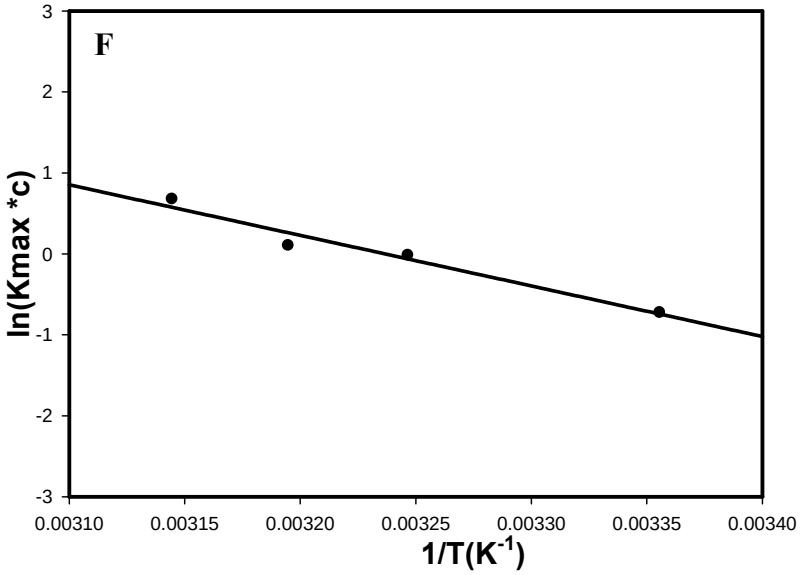

Figure 3. Temperature dependent kinetics of amyloid formation by Amylin with A) 1% DMSO, C) 2% HFIP, E) 1.5% DMSO as the organic co-solvent. The Arrhenius plots of kmax obtained from the fitted data at different temperature in B) 1% DMSO, D) 2% DMSO and F) 1.5% DMSO are shown.

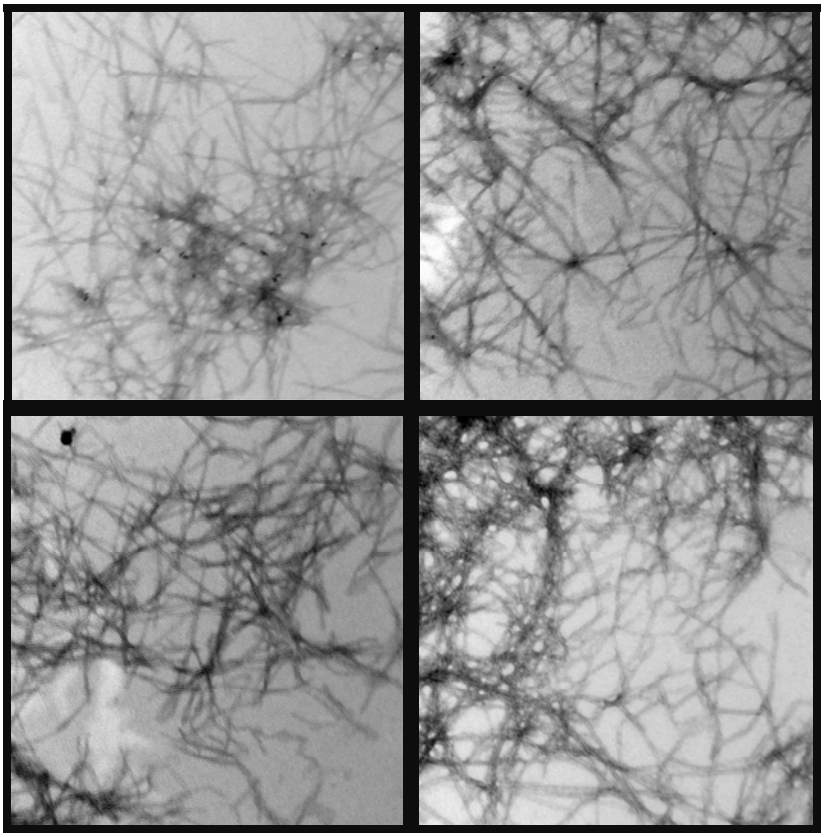

Figure 4. TEM images of 32μM Amylin fibrils formed in 1% DMSO co-solvent and 20mM Tris at pH 8.5 and 15^{o}C. The scale bar in the images is 100nm.

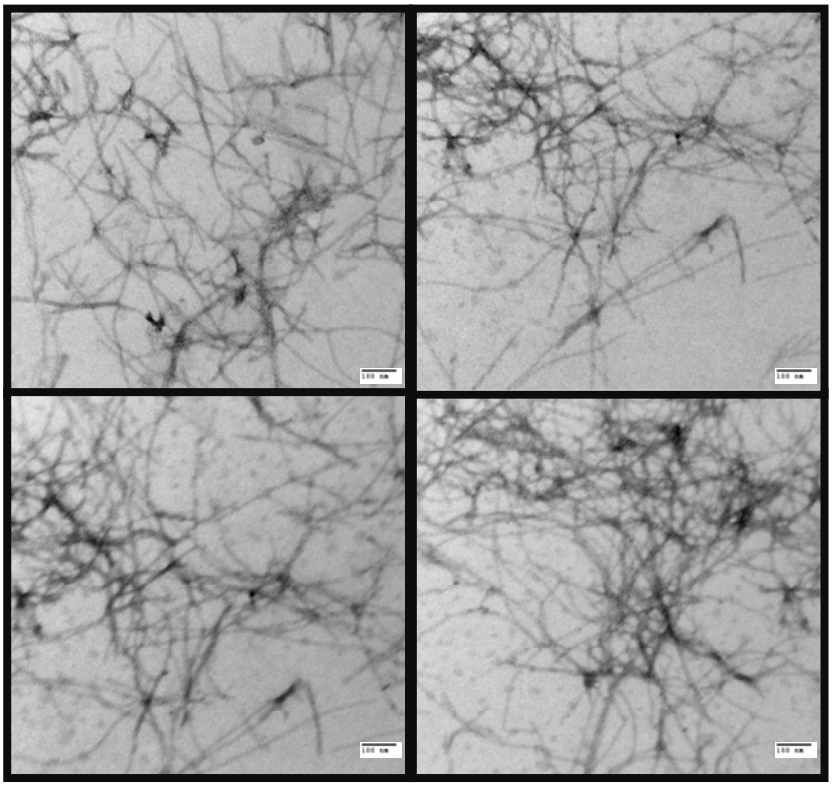

Figure 5. TEM images of 32μM Amylin fibrils formed in 1% DMSO co-solvent and 20mM Tris at pH 8.5 and 25^{o}C. The scale bar in the images is 100nm.

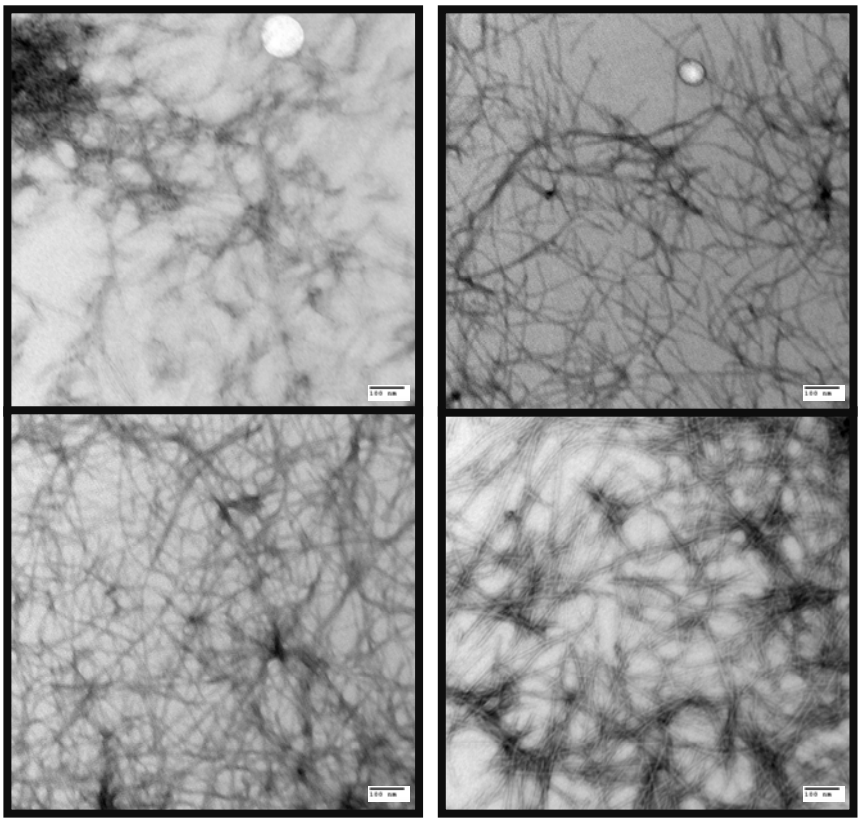

Figure 6. TEM images of 32μM Amylin fibrils formed in 1% DMSO co-solvent and 20mM Tris at pH 8.5 and 35^{o}C. The scale bar in the images is 100nm.

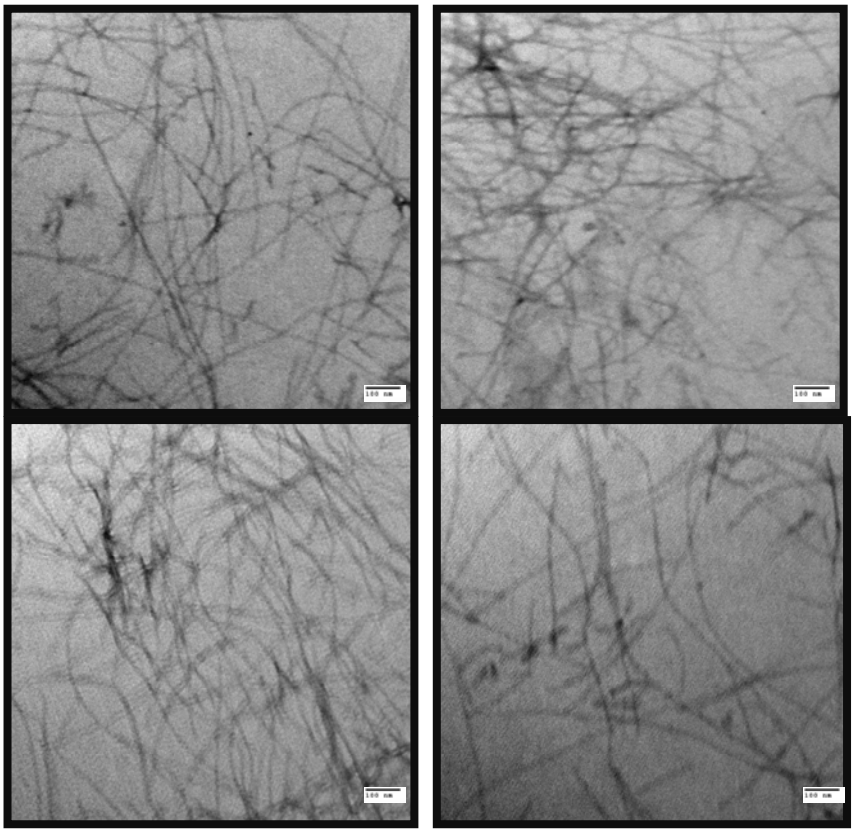

Figure 7. TEM images of 32μM Amylin fibrils formed in 1% DMSO co-solvent and 20mM Tris at pH 8.5 and 50^{o}C. The scale bar in the images is 100nm.

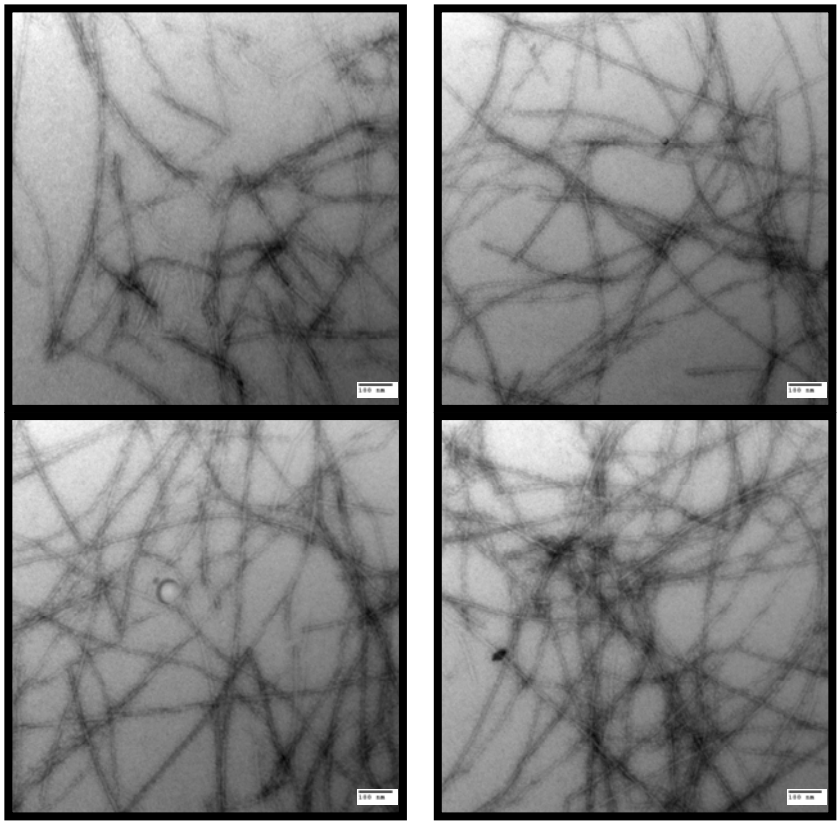

Figure 8. TEM images of 32μM Amylin fibrils formed in 2% DMSO co-solvent and 20mM Tris at pH 8.5 and 10^{o}C. The scale bar in the images is 100nm.

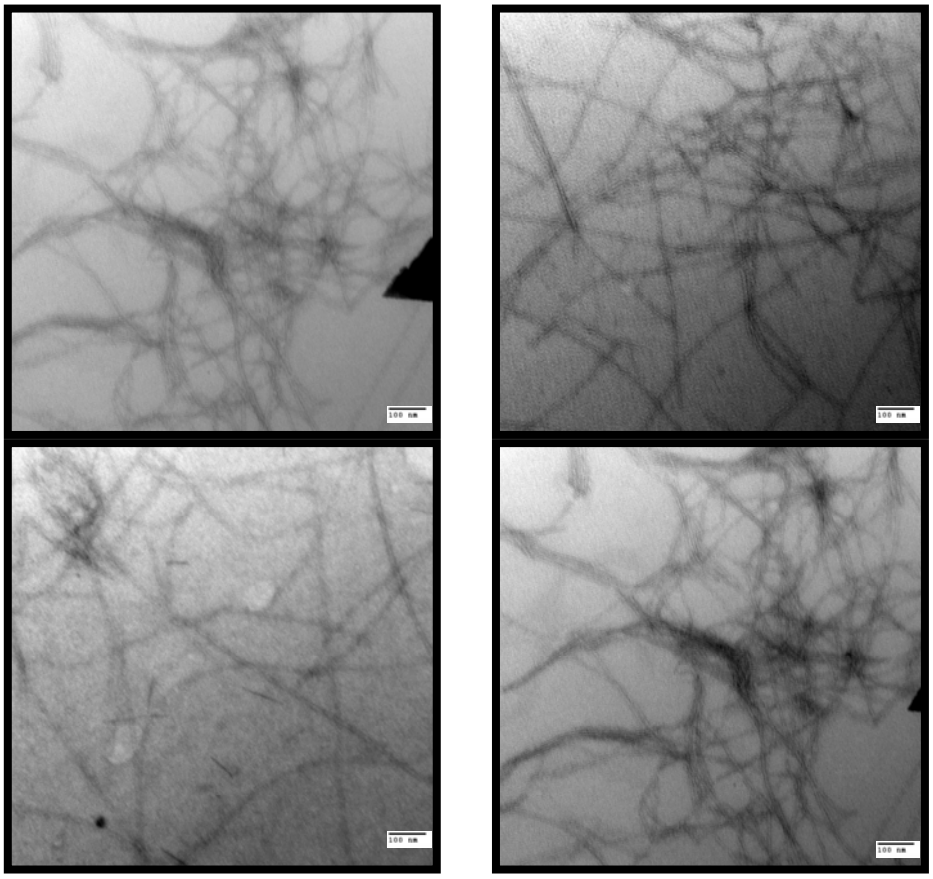

Figure 9. TEM images of 32μM Amylin fibrils formed in 2% DMSO co-solvent and 20mM Tris at pH 8.5 and 25^{o}C. The scale bar in the images is 100nm.

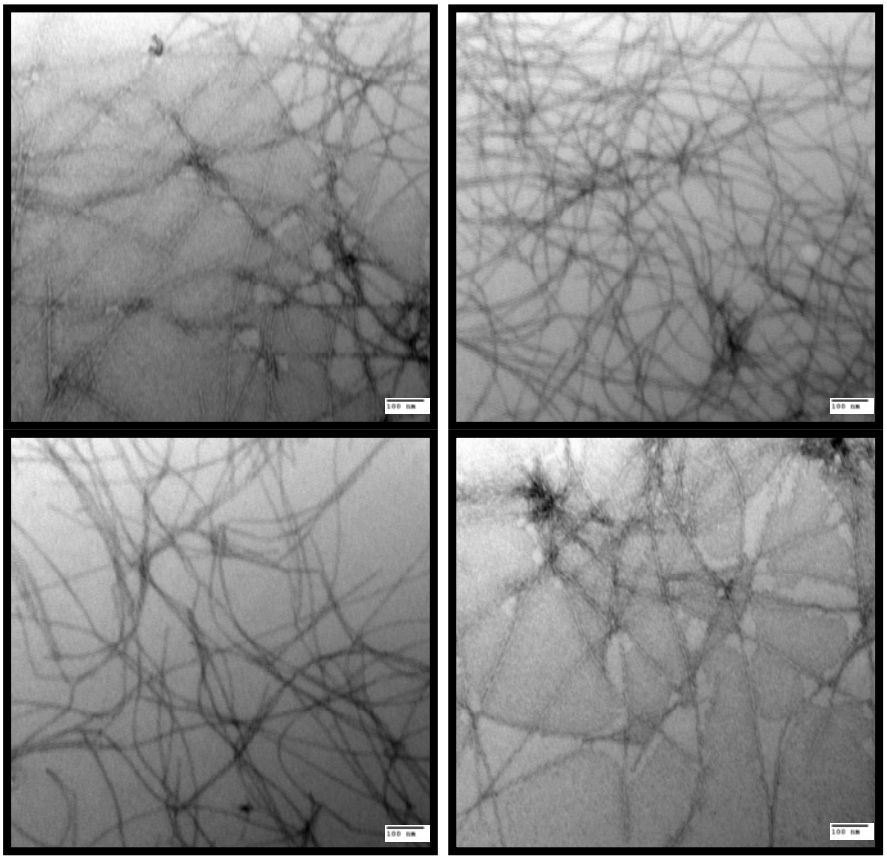

Figure 10. TEM images of 32μM Amylin fibrils formed in 2% DMSO co-solvent and 20mM Tris at pH 8.5 and 45^{o}C. The scale bar in the images is 100nm.

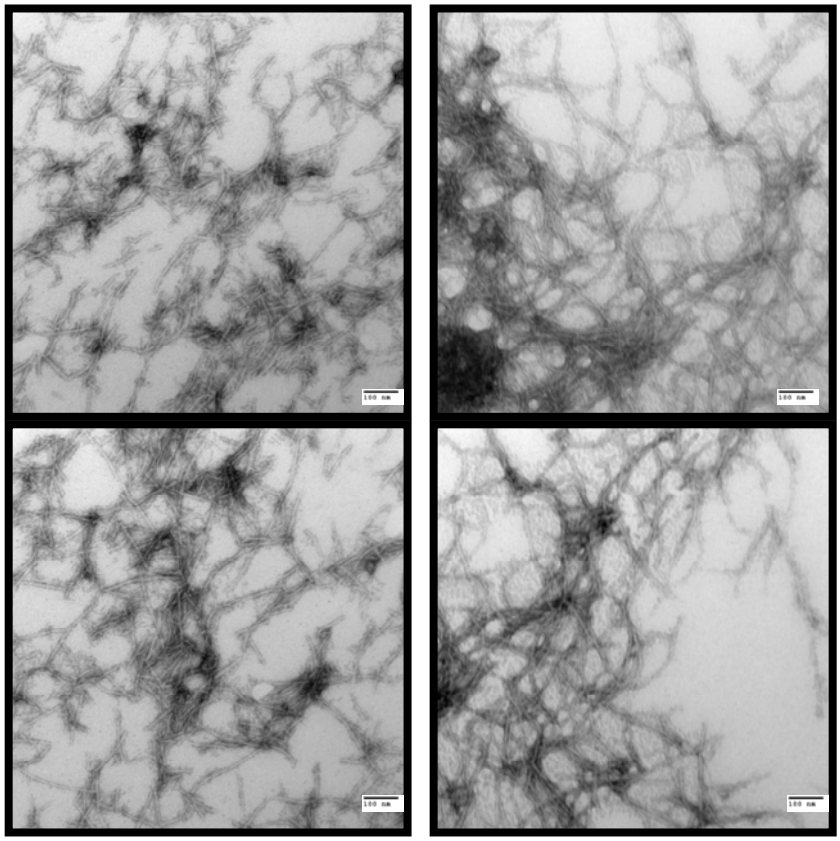

Figure 11. TEM images of 32μM Amylin fibrils formed in 1% HFIP co-solvent and 20mM Tris at pH 8.5 and 15^{o}C. The scale bar in the images is 100nm.

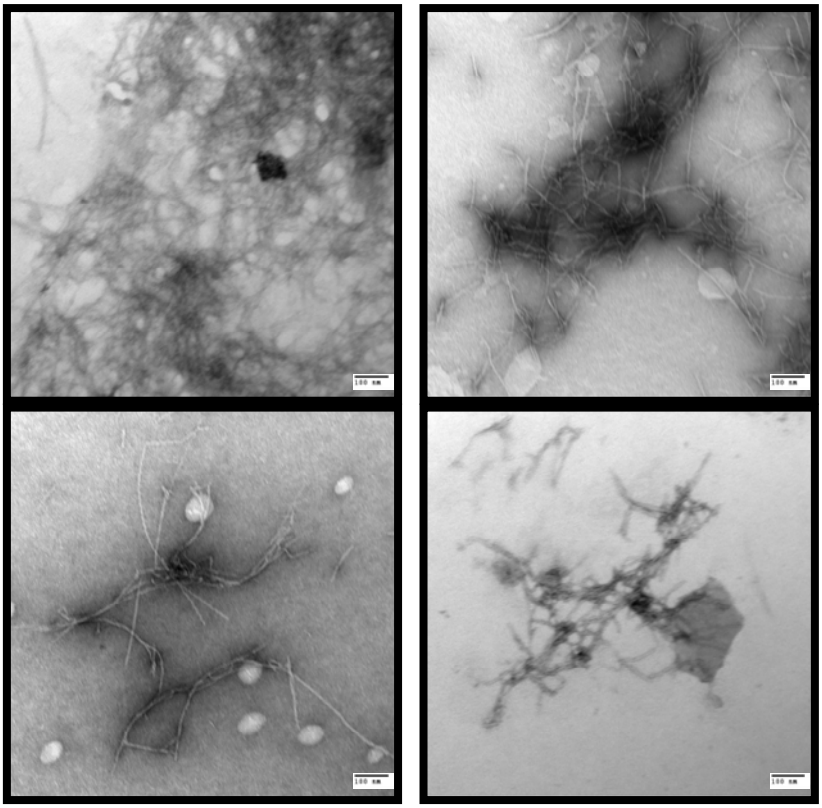

Figure 12. TEM images of 32μM Amylin fibrils formed in 1% HFIP co-solvent and 20mM Tris at pH 8.5 and 25^{o}C. The scale bar in the images is 100nm.

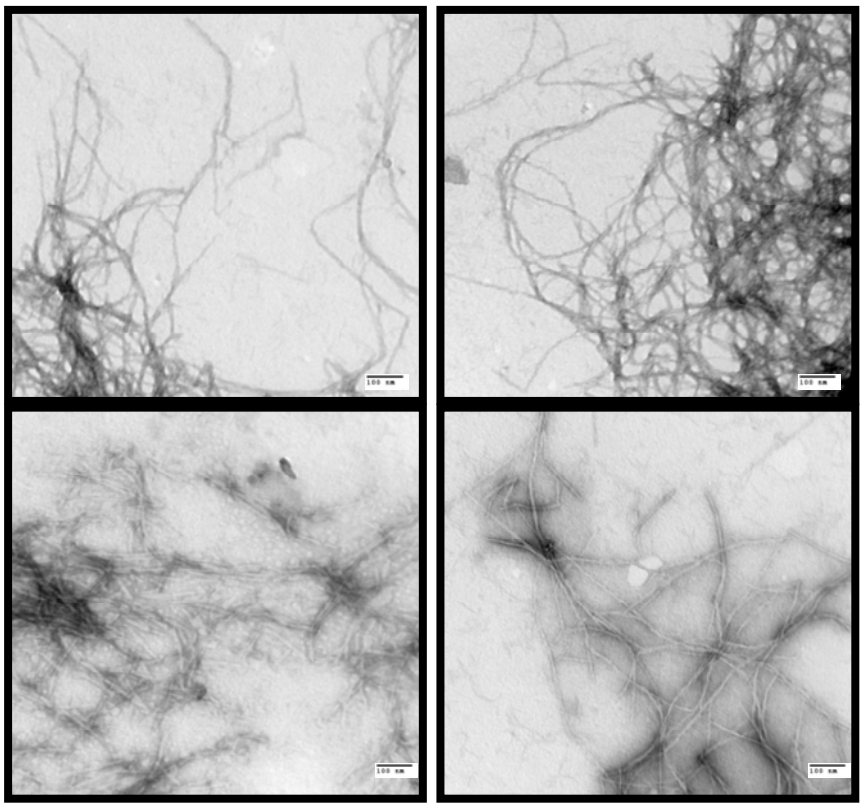

Figure 13. TEM images of 32μM Amylin fibrils formed in 1% HFIP co-solvent and 20mM Tris at pH 8.5 and 35^{o}C. The scale bar in the images is 100nm.

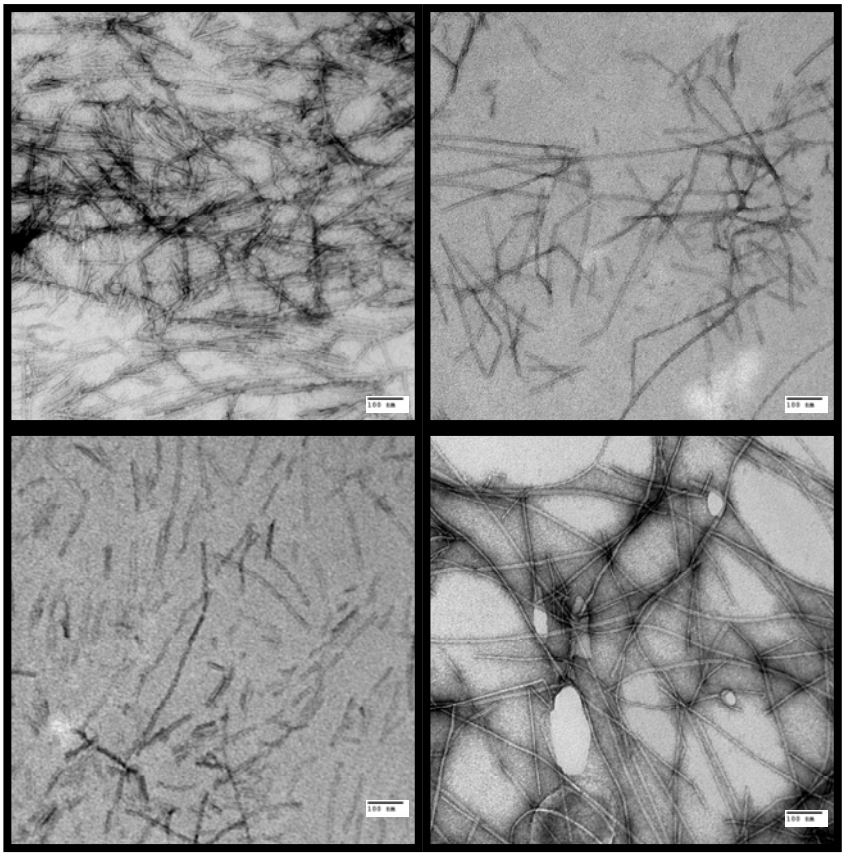

Figure 14. TEM images of 32μM Amylin fibrils formed in 2% HFIP co-solvent and 20mM Tris at pH 8.5 and 5^{o}C. The scale bar in the images is 100nm.

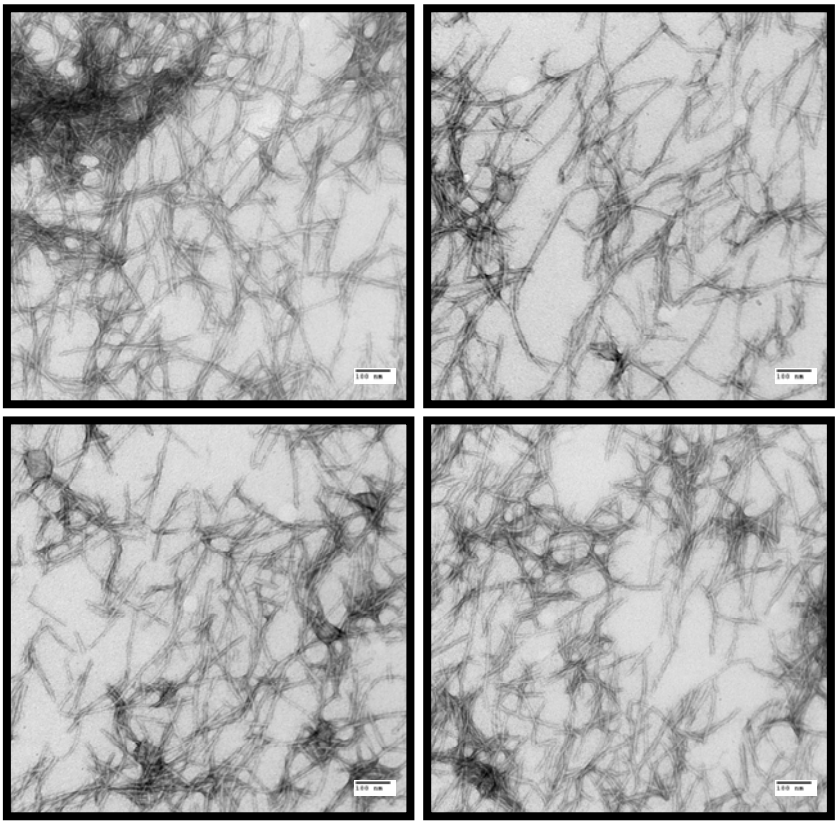

Figure 15. TEM images of 32μM Amylin fibrils formed in 2% HFIP co-solvent and 20mM Tris at pH 8.5 and 15^{o}C. The scale bar in the images is 100nm.

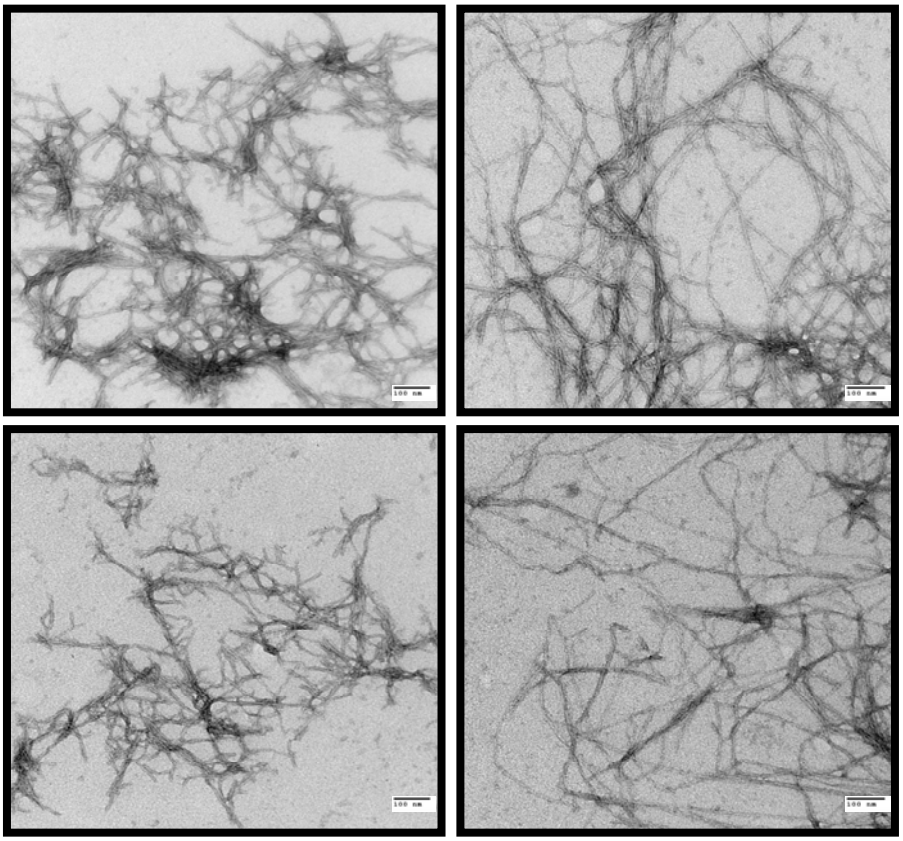

Figure 16. TEM images of 32μM Amylin fibrils formed in 2% HFIP co-solvent and 20mM Tris at pH 8.5 and 25^{o}C. The scale bar in the images is 100nm.

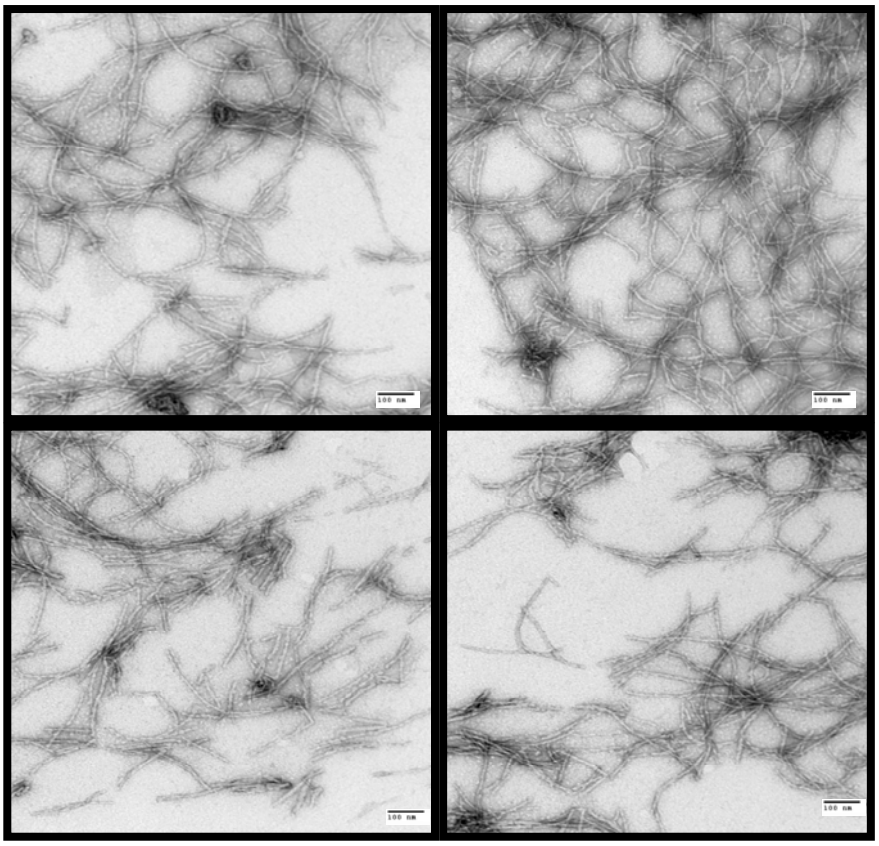

Figure 17. TEM images of 32μM Amylin fibrils formed in 2% HFIP co-solvent and 20mM Tris at pH 8.5 and 35^{o}C. The scale bar in the images is 100nm.

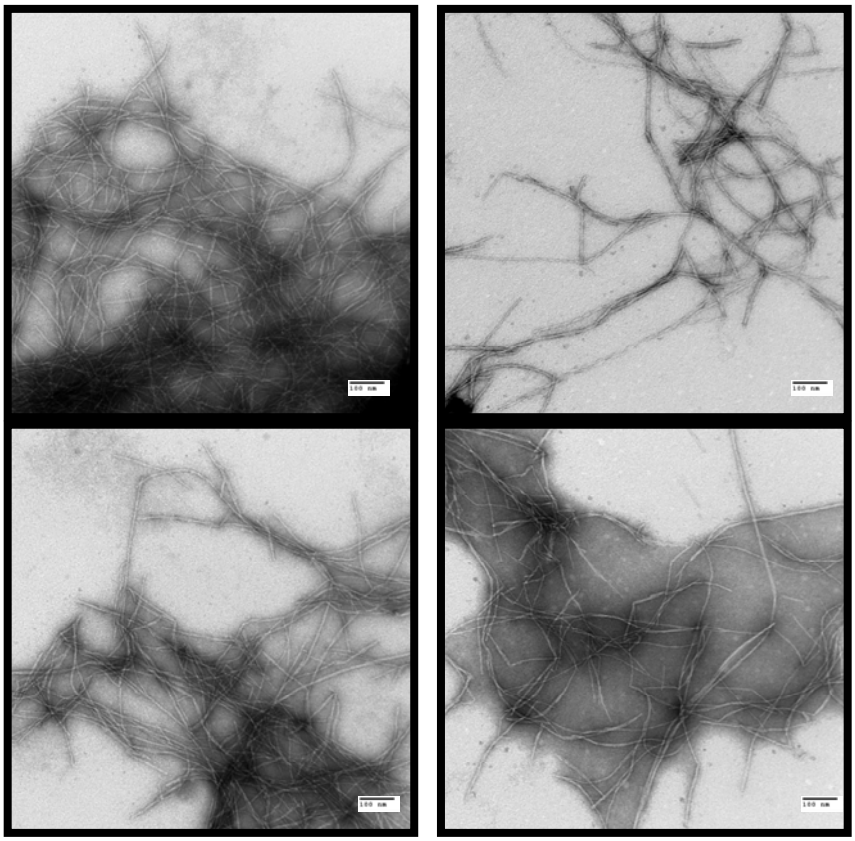

Figure 18. TEM images of 32μM Amylin fibrils formed in 2% HFIP co-solvent and 20mM Tris at pH 8.5 and 60^{o}C. The scale bar in the images is 100nm.

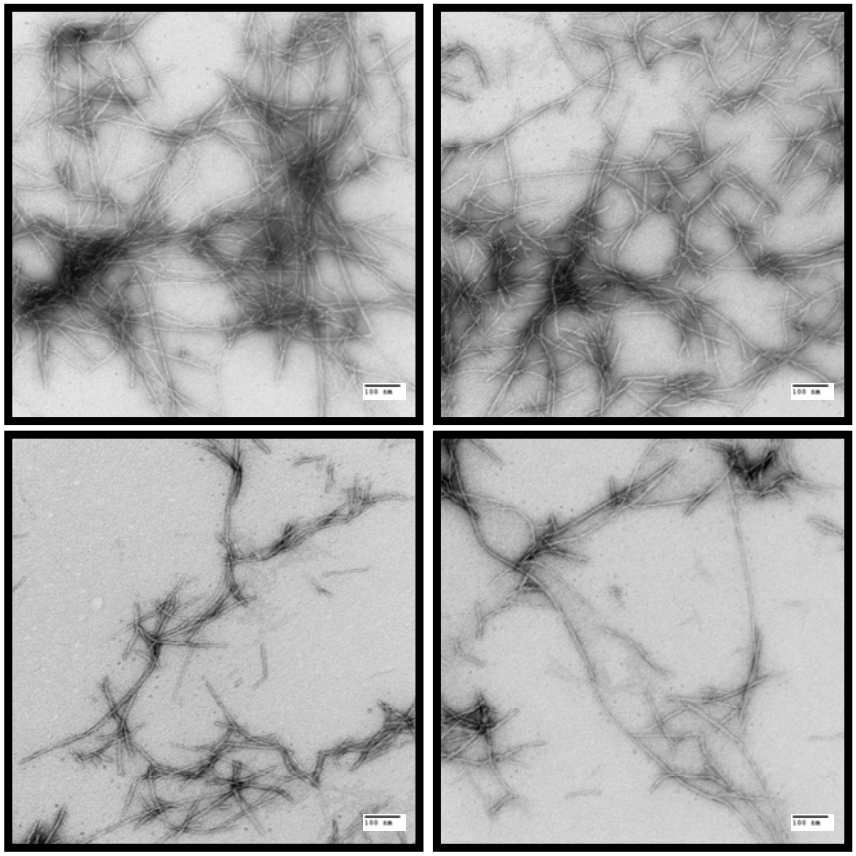

Figure 19. TEM images of 32μM Amylin fibrils formed in 2% HFIP co-solvent and 20mM Tris at pH 7.12 and 25^{o}C. The scale bar in the images is 100nm.

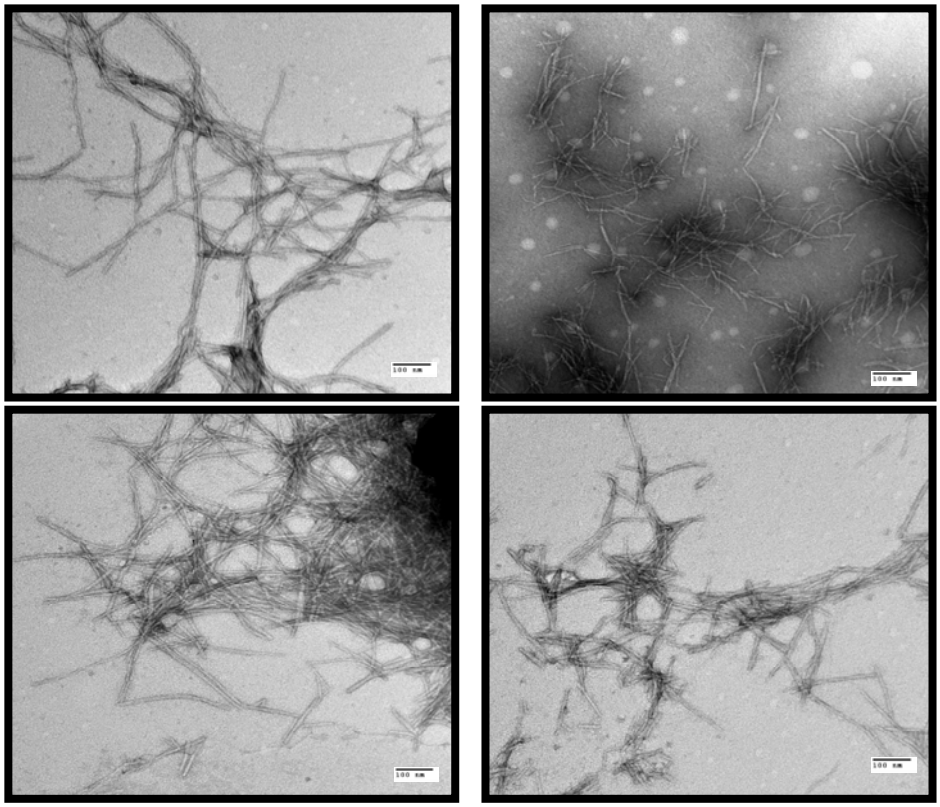

Figure 20. TEM images of 32μM Amylin fibrils formed in 2% HFIP co-solvent and 20mM Tris at pH 9.0 and 25^{o}C. The scale bar in the images is 100nm.

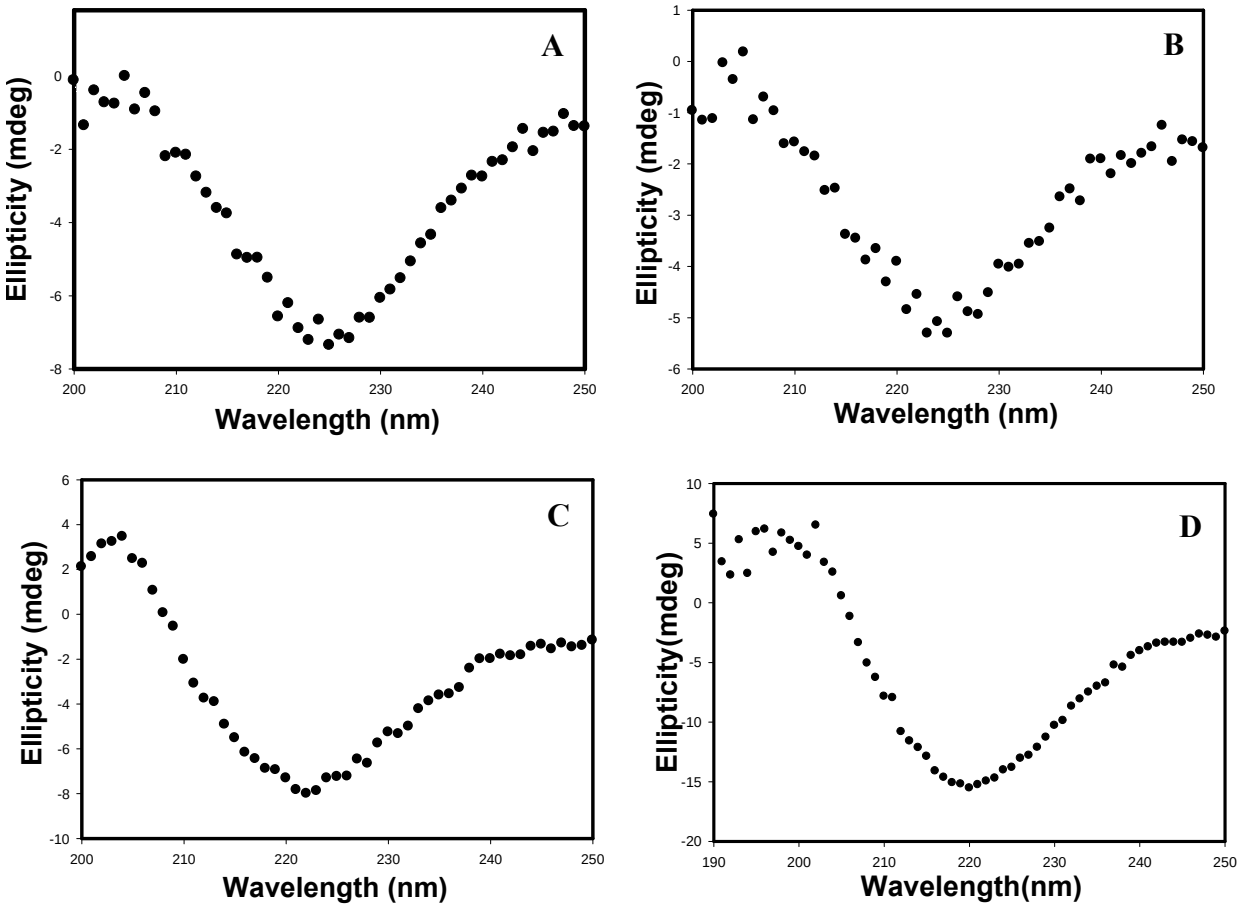

Figure 21. Circular dichroism (CD) data collected at the end of the kinetic run of amylin aggregation in 1% HFIP in 20mM Tris at pH 8.5 at 5^{o}C (A), 25^{o}C (B), 35^{o}C (C) and 45^{o}C (D).

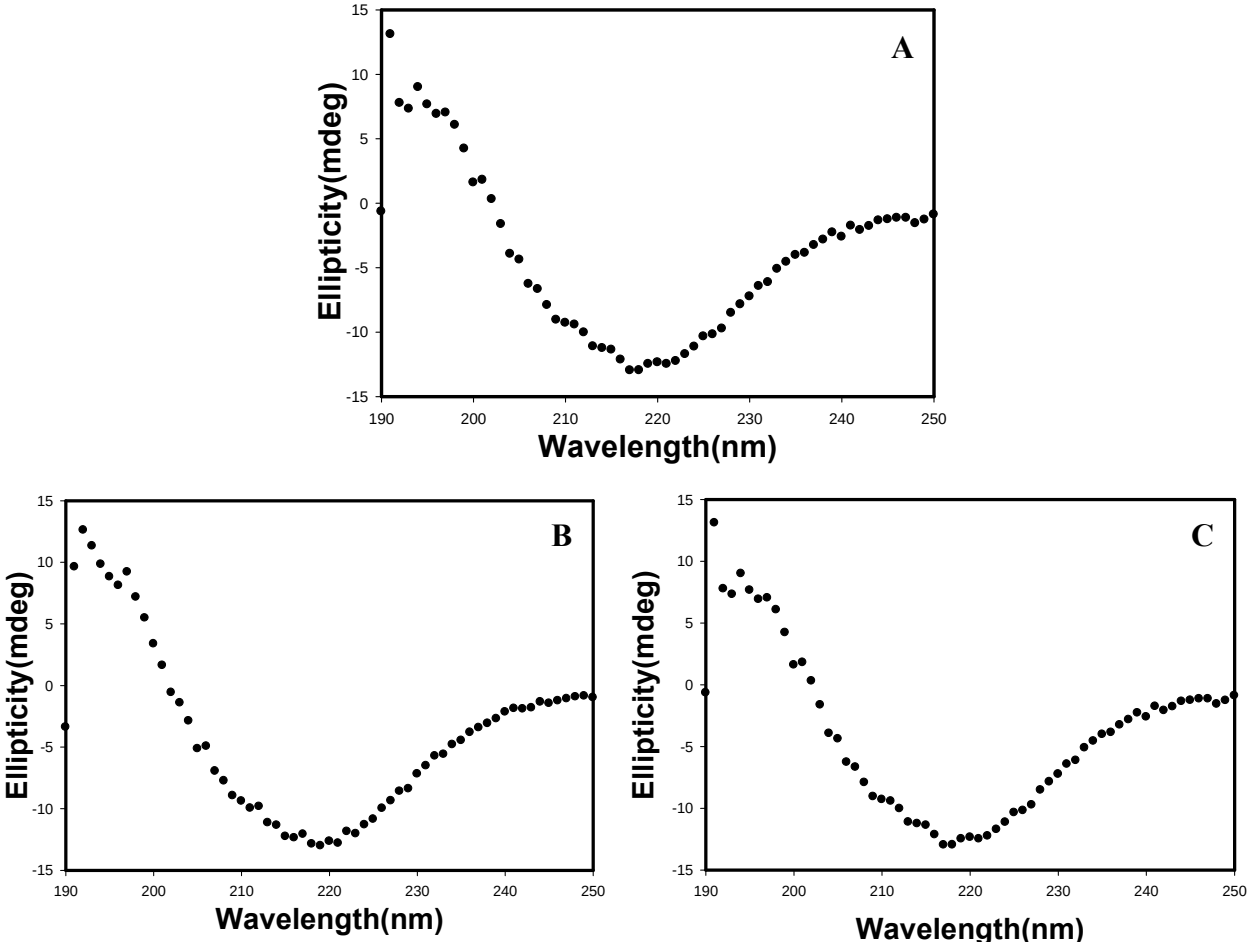

Figure 22. Circular dichroism (CD) data collected at the end of the kinetic run of amylin aggregation in 2% DMSO in 20mM Tris at pH 8.5 at 15^{o}C (A), 25^{o}C (B) and 45^{o}C (C).

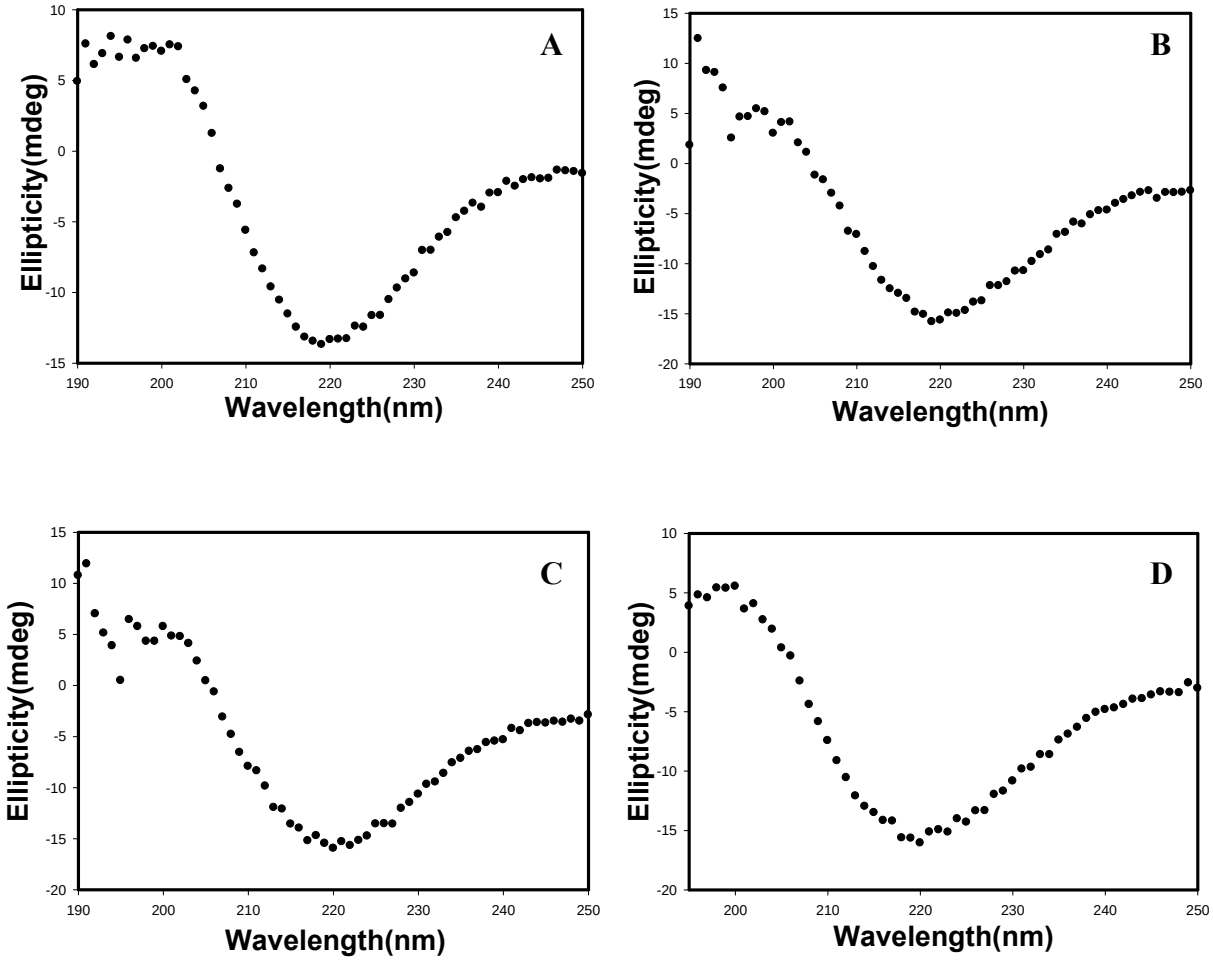

Figure 23. Circular dichroism (CD) data collected at the end of the kinetic run of amylin aggregation in 2% HFIP in 20mM Tris at pH 8.5 at 15^{o}C (A), 25^{o}C (B), 40^{o}C (C) and 60^{o}C (C).

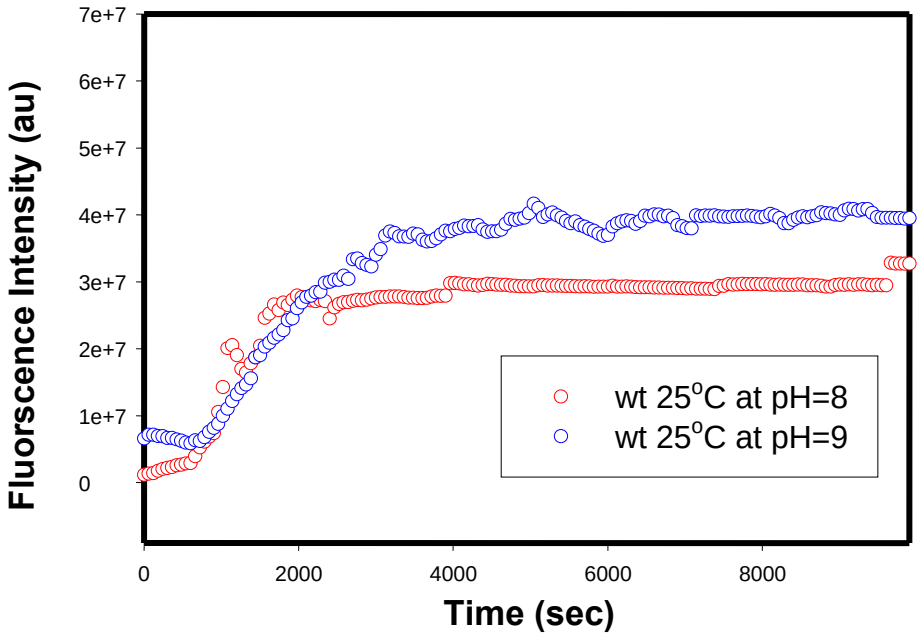

Figure 24. Kinetics of 32μM Amylin aggregation in 20mM Tris at pH 8.0 (red) and pH 9.0 (blue) at 25°C.

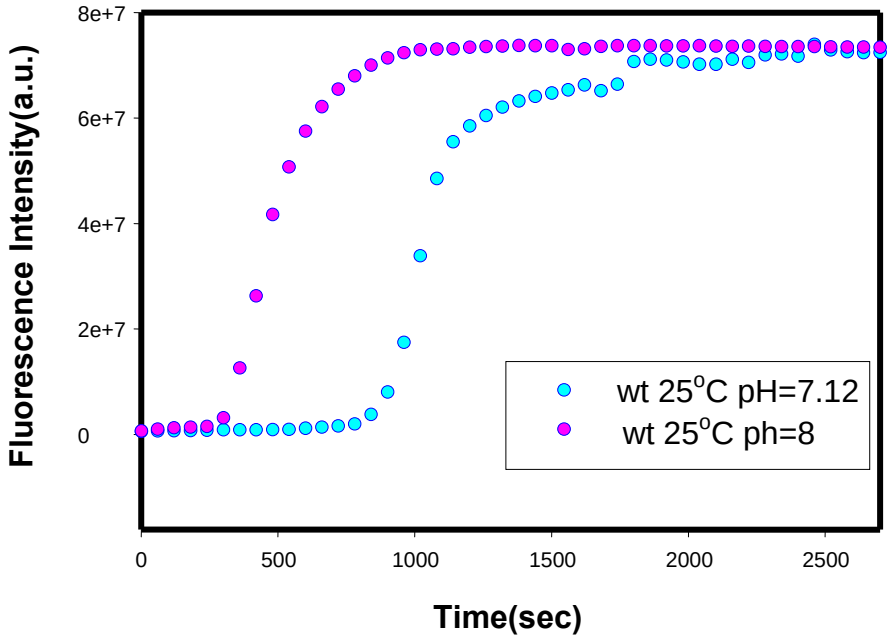

Figure 25. Kinetics of 32μM Amylin aggregation in 20mM Tris at pH 7.12 (blue) and pH 8.0 (purple) at 25°C.

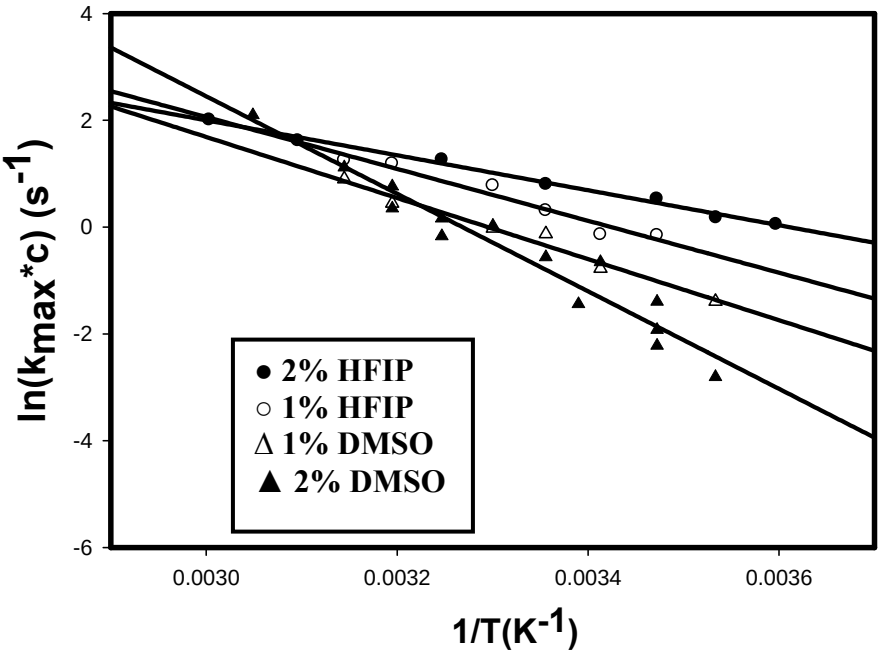

Figure 26. Comparison of the Arrhenius plots of k_{max} at different temperatures under varying amounts of different co-solvents.

2.7 Tables

Table 1. Thermodynamic parameters computed from kinetic reactions of amylin aggregation under different co-solvent conditions.

Peptide	Residues	E_a (kcal/mol)	$T\Delta S^{\#}$ (kcal/mol)	$\Delta G^{\#}$ (kcal/mol)
Amylin Stock in 2%HFIP	37	6.51	2.38	4.13
Amylin Stock in 1%HFIP	37	9.66	5.19	4.48
Amylin Stock in 2%DMSO	37	18.16	12.93	5.23
Amylin Stock in 1.5%DMSO	37	12.43	11.34	5.11
Amylin Stock in 1%DMSO	37	11.37	6.49	4.88
Aβ	40	23	15.62	7.68
Insulin (aqueous, pH 2.0)	57	24.4	16.41	7.99

Chapter 3. Factors Affecting the Rate of Aggregation of Human Islet Amyloid Polypeptide

3.1 Introduction

Amylin aggregation shows the characteristics of nucleation dependent polymerization, which suggests that an increase in the amount of secreted Amylin might trigger its aggregation. Further, it was found that Amylin levels are elevated in diabetic and insulin resistant obese patients (Ludvik et al. 1997). Thus to understand the importance of concentration on the fibrillization process, the kinetics of the aggregation process of Amylin was studied at different concentrations of total protein. The goal of the work described in this chapter is to examine environmental factors, which influence the rate of amyloid formation.

The kinetics of amyloidogenesis show a characteristic lag phase followed by a growth phase, detected through the binding of the dye, thioflavin-T. The lag phase is associated with the formation of nucleus, which serves as a seed for the growth of monomers into amyoid fibrils. The effect of increasing protein concentration was thus analyzed on growth phase as well as on the lag phase. The experiments were conducted using different co-solvents, like HFIP and DMSO, to check the generality of the results and because these co-solvents are often used to prepare stock solutions for biophysical studies. Further, the effect of increasing organic co-solvent concentration on the rate of

Amylin aggregation was also analyzed. Experiments done with increased amounts of thioflavin-T showed that dye binding also modulates the rate of aggregation. The results that were obtained from the concentration dependent studies suggested that increase in the expression levels of Amylin is not the factor that leads to initiation of amyloidogenesis. However, once nucleation is initiated, increased expression levels can accelerate the rate of Amylin aggregation by producing protein, which can bind to the preformed seeds. Hence the propensity of Amylin to aggregate in type 2 diabetic patients must involve some other factors which trigger the unfolded Amylin to associate and form nucleation seeds. Once these seeds are formed, the rate of formation of β-sheet fibrillar species is dictated by the concentration of monomers present.

3.2 Materials and Methods

3.2.1 Protein Synthesis and Purification

Wild type human IAPP (hIAPP) was synthesized on a 0.25mmol scale using 9-fluornylmethoxycarbonyl (Fmoc) chemistry on an Applied Biosystems 433A Peptide Synthesizer. 5-(4'-Fmoc-aminomethyl-3',5-dimethoxyphenol) valeric acid (PAL-PEG) resin was used to generate an amidated C-terminus. Pseudoproline dipeptide derivatives were employed as described (Abedini and Raleigh 2005). Fmoc-protected pseudoproline (oxazolidine) dipeptide derivatives were purchased from Novabiochem. All other reagents were purchased from Advanced Chemtech, Fischer Scientific, PE Biosystems and Sigma Aldrich. All solvents used were of A.C.S. grade. Standard Fmoc reaction cycles were used. The first residue added to the resin, pseudoproline dipeptide derivatives, all β-branched residues and all residues following the β-branched residue

were double coupled. The peptide was cleaved from the resin using standard trifluoroacetic acid (TFA) methods. The crude peptide was treated with 20% (v/v) acetic acid and lyophilized. The disulfide bond was formed via DMSO induced oxidation of the crude peptide. The oxidized peptide was purified via reverse-phase HPLC using a Vydac C-18 preparative column. A two-buffer system utilizing HCl as an ion-pairing agent was used for the purification. Buffer A consisted of 0.045% (v/v) HCl in distilled de-ionized (DDI) water. Buffer B consisted of 80% (v/v) acetonitrile, 20% (v/v) DDI water and 0.045% (v/v) HCl. The purity of the peptide was checked by HPLC and was calculated to be 99%.

The purified peptide was analyzed by matrix-assisted laser desorption/ionization time-of-flight (MALDI-TOF) mass spectroscopy. The observed molecular weight was 3903.4 Da and agreed well with the expected molecular weight of 3903.3 Da.

3.2.2 Fluorescence based kinetic assays

The kinetics of amyloid formation by Amylin was studied using thioflavin-T fluorescence. All fluorescence measurements were done on a Jobin Yvon Horiba fluorescence spectrophotometer using an excitation wavelength of 450 nm and an emission wavelength of 485 nm. The emission and excitation slits were both set to 5 nm and a 1.0 cm cuvette was used. Experiments were performed by diluting a stock solution of peptide (1.58 mM for 2% studies and 3.16 mM for 1% studies) in HFIP or DMSO into 20 mM Tris-HCl buffer at pH 8.5 containing thioflavin-T. The stock solutions of Amylin were made by weighing the calculated amount of peptide and the concentration was confirmed by measuring absorbance at 220nm. Each stock solution was filtered

through a 0.45 μm pore size GHP Acrodisc syringe filter prior to the experiment to remove large aggregates. The final reaction mixture contained 32 μM peptide and 32 μM thioflavin-T at pH 8.5 at the desired temperature. This pH was chosen to avoid changes in the aggregation rate caused by minor variations in pH since the rate of amyloid formation is not strongly pH dependent near that pH. All solutions were stirred during the assay to maintain solution homogeneity. Temperature was controlled by a water bath and the temperature of the cell was calibrated using a thermocouple before each experiment.

3.2.3 Transmission electron microscopy

Transmission Electron Microscopy (TEM) was performed at the Microscopy Imaging Center at the State University of New York at Stony Brook. Samples were prepared by placing 15μl of solution onto formvar coated 300 mesh copper grids and counterstained with 2% aqueous uranyl acetate. Samples were viewed with a FEI Tecnai12 BioTwinG^2 transmission electron microscope at 80 kV. Digital images were acquired with an AMT XR-60 CCD Digital Camera System and compiled using Adobe Photoshop CS2.

3.2.4 Data Analysis

To calculate the kinetic parameters for elongation of fibrils, the data was fitted to a 5-parameter equation (1):

$$y(t) = y(t_0) + \frac{a}{\left[1 + e^{\left\{\frac{t_0 - t}{b}\right\}}\right]^c} \qquad (1)$$

where, y(t) is the observed fluorescence at time t, b is the slope of the growth phase, a is the final fluorescence intensity and c is related to the lag phase. The function describes a sigmoidal curve for kinetics of fibril formation. The derivative of the fit gave the apparent rate of fibril growth as a function of time. The slope obtained from fitting the curve was converted into the molar reaction velocity using equation (2):

$$\nu_{t50} = \frac{[hIAPP]_{t=0}}{4b} \qquad (2)$$

where ν_{t50} is the velocity of the reaction in monomer units at t_{50} i.e. when 50% of the monomers have associated to form fibrils (Padrick and Miranker 2002), b is the slope of the growth phase obtained from fitting the data to 5-parameter sigmoidal equation (1). $[hIAPP]_{t=0}$ is the concentration of Amylin in the reaction mixture at the start of fibril formation reaction.

3.3 Results

The kinetics of fibril formation by Amylin shows a characteristic nucleation dependent polymerization (Padrick and Miranker 2002; Uversky and Fink 2004; Chiti and Dobson 2006). The monomers associate to form oligomers, which serve as a template for elongation of these prefibrillar species into fibrils. Nucleation dependent polymerization suggests that the rate of formation of the nucleus is a concentration dependent rate limiting process. To evaluate the nucleation dependent polymerization, in case of Amylin aggregation, the kinetics of amyloid formation were monitored using thioflavin-T based assays using varying concentrations of Amylin. Amylin, in aqueous solutions, has a very high tendency to aggregate owing to its high hydrophobic content. Stock solutions of Amylin are thus prepared in organic solvents like HFIP or DMSO. To

initiate amyloid formation, the stock solution is diluted into 20mM Tris buffer at pH 7.4. The kinetics of fibril formation was monitored through fluorescence spectroscopy using the emission of thioflavin-T. Thioflavin-T is believed to bind to the fibrillar structure, which results in the enhancement of its fluorescence intensity at 485nm (LeVine 1999). TEM images of samples withdrawn at the completion of the reaction were analyzed for the formation of long and extensive fibrils (Figs. 1c, 1d, 4-6, 7d, 7e, 9). Circular dichroism (CD) of these samples showed a β-sheet morphology characteristic of amyloid fibrils (Sunde et al. 1997).

When the concentration of Amylin in the reaction mixture was gradually increased from 7μM to 122μM, there was no significant change observed in the lag phase of the kinetics (Fig. 1a). The time required for the formation of the nucleus did not increase or decrease as the concentration of Amylin monomers was increased. The elongation phase, however, changed in response to the concentration of monomers. The rate of growth of fibrils increased linearly as the concentration of Amylin was increased, consistent with first order elongation of the fibrils. This analysis showed that the formation of the nucleus does not depend strongly on the number of monomers present in the reaction mixture. However, once the rate limiting step is accomplished, the conversion of oligomers/intermediates into amyloid fibrils is influenced by the concentration of monomers. The response of both lag phase and growth phase was found to be consistent when the solvent used for making Amylin stock solution was changed from HFIP to DMSO. Amylin prepared in a DMSO stock solution showed slower kinetics of fibrillization than observed with the HFIP stock solution (Fig. 2a). The lag phase was prolonged and the rate of growth phase was decreased. However, consistent

with the HFIP studies, no significant concentration dependence of the lag phase was observed. The amyloid fibril growth rate continued to increase with the concentration. The measured t_{50} for each of these reactions was not sensitive to the total concentration of protein. The average t_{50} value computed for Amylin in HFIP stock solution was 1021.5s (Fig. 1b). The reactions in DMSO showed a relatively higher average value of t_{50}, which was 3382.5s (Fig. 2b). The larger t_{50} value is associated with a longer lag phase and a slower growth phase. Comparison of the kinetics in HFIP and DMSO showed that the rate of nucleation of Amylin and its fibril growth are both much slower in DMSO than in HFIP.

The observation that the lag phase is independent of total peptide concentration in DMSO is potentially important. Miranker and co-workers have proposed a dispersed phase model to account for the lack of a strong concentration effect on the lag phase when HFIP was used as the co-solvent. HFIP is believed to be immiscible with aqueous medium and readily dissolves hydrophobic peptides. Thus it was proposed that hydrophobic Amylin would preferably exist in HFIP pockets dispersed in the aqueous buffer during the reaction. Hence, inspite of the increase in total Amylin concentration, the concentration of peptide in aqueous medium will remain almost constant. Since amyloidogenesis occurs in the aqueous phase, the observation that the lag phase does not change significantly with change in total protein concentration in the reaction might be explained by no change in Amylin concentration in aqueous phase. However, it is not clear what is exactly meant by the dispersed phase nor was it clear if the dispersed phase was in fact due to the presence of HFIP. HFIP may not be fully miscible in water and thus the dispersed phase could be an artifact of the use of HFIP. However, it is very

important to note that models, which do not require a “disperse phase”, can also explain the lack of concentration dependence. Our data obtained with DMSO suggests that these models should be considered for Amylin.

The results of concentration dependent studies bring forth several hypotheses to facilitate the understanding of the nucleation process in the lag phase. The first hypothesis suggests that the formation of oligomers associated with seeding requires a concentration lower than 7μM and thus the lag phase might be sensitive to the concentration below 7μM but would seem concentration independent at higher concentrations. The second hypothesis is that the nucleation process requires protein monomers to rearrange into a conformation, which can readily associate to form the seed. Thus the observed lag phase will correspond to the time needed for this structural rearrangement and would vary depending upon the sequence of the amyloidogenic peptide. Thirdly, the rate limiting step may involve structural rearrangements within an oligomeric intermediate. The hypothesis that a structural rearrangement is involved is further supported by the fact that Amylin aggregation occurs through a longer lag phase in DMSO as compared to HFIP (Fig. 2). TEM images of fibrils formed with different concentrations of Amylin in 2% DMSO are shown in Fig. 3-5. Time based CD studies have shown that the process of fibril formation by Amylin involves the formation of a helical intermediate, which over a period of time aggregates to form a characteristic β-sheet structure. HFIP by the nature of its interactions tends to stabilize the helical conformation where as DMSO has a destabilizing effect on forming helical secondary structure. Thus if this intermediate formation is associated with the lag phase, HFIP will assist Amylin in achieving the helical structure and DMSO will decelerate the rate of

formation of this conformation. The nucleus will be readily formed in HFIP while in the presence of DMSO, nucleus formation will require a longer lag time.

The analysis of the growth phase shows that the velocity of Amylin aggregation reaction varies linearly with the increase in the concentration from 7μM-122μM. The velocity at t_{50} versus concentration plot is a useful tool for helping to understand the nature of the growth phase. Figure 3 shows that the slope of the curve is noticeably larger in HFIP than in DMSO. In 2% HFIP, the rate of growth of fibrils is 1.66×10^{-3} s^{-1} in contrast to an observed rate of 2.16×10^{-4} s^{-1} in 2% DMSO as a co-solvent (Fig. 6). This suggests that even after formation of the nucleus, monomers do require some structural rearrangement before adding on to the fibril ends for growth. The relatively slower rate of the growth phase in DMSO is consistent with the denaturing nature on the monomers. The slower rate of the structural rearrangement results in a decreased rate of fibril elongation. The effect of diffusion on slower rates of fibril formation in DMSO can be ruled out because of the comparable viscosity of 2% DMSO and 2% HFIP. Further, the co-solvent variation studies confirmed the effect of co-solvent on structural rearrangement. When the same concentration of Amylin monomers was subjected to fibril formation at higher percentages of HFIP, the rate of fibrillization was much faster in 4% HFIP as compared to 1% HFIP (Fig. 7). The t_{50} values showed a linear decrease with lowering of HFIP concentration. The rate constants for fibril elongation and the velocity of fibril formation were observed to increase linearly with increasing percentage of HFIP. Similarly, the rate of Amylin aggregation was enhanced when the concentration of DMSO was decreased from 7% to 1% (Fig. 8). Thus the concentration dependent studies on Amylin hint towards a structural rearrangement associated with

amyloidogenesis. It also underscores and highlights the importance of the presence of a small amount of co-solvent and how it can modulate the kinetics of amyloid formation significantly. The environmental factors around the amyloidogenic peptide can trigger the aggregation of otherwise soluble monomers and can further modulate the rate of aggregation. Thus physiologically, a perturbation of the environment around these proteins in terms of concentration of other proteins or membrane disruption might be able to trigger the nucleation process leading to amyloidosis.

3.4 Discussion

Deciphering the mechanism of Amylin fibrillization is a key to designing effective inhibitors against amyloidosis. One of the most important questions in the field of amyloidogenesis is to understand the factors that trigger the aggregation of otherwise soluble proteins and peptides. The knowledge and understanding of the nucleation process lies at the heart of answering this question. The kinetics of amyloidogenic proteins show a characteristic lag phase. However, the kinetics gives no insight into the mechanism of initiation of this oligomerization. The concentration dependent studies suggest that an increase in the expression level leading to an increase in the amount of Amylin is not enough to initiate amyloidogenesis, however, it is important in modulating the rate of fibrillization. The nature of the co-solvent present during aggregation can also significantly affect the nucleation phase by effecting structural rearrangements involved in formation of the seed.

Thus designing inhibitors, which can bind to monomers or oligomers and prevent their structural rearrangement can probably prevent fibrillization. Recently, small heat

shock (sHsps) proteins have been shown to bind to the unfolded or misfolded state of the amyloidogenic proteins. sHsps bind to prefibrillar species and prevent the formation of amyloid fibrils (Wilhelmus et al. 2006a, Wilhelmus et al. 2006b). Inhibiting the initiation of fibril formation might be a promising strategy against amyloidosis. Thus understanding the assembly involved in nucleation and the process of growth can give insights into the initiation and progression of amyloidogenic diseases and open avenues for new drug targets.

3.5 Figures

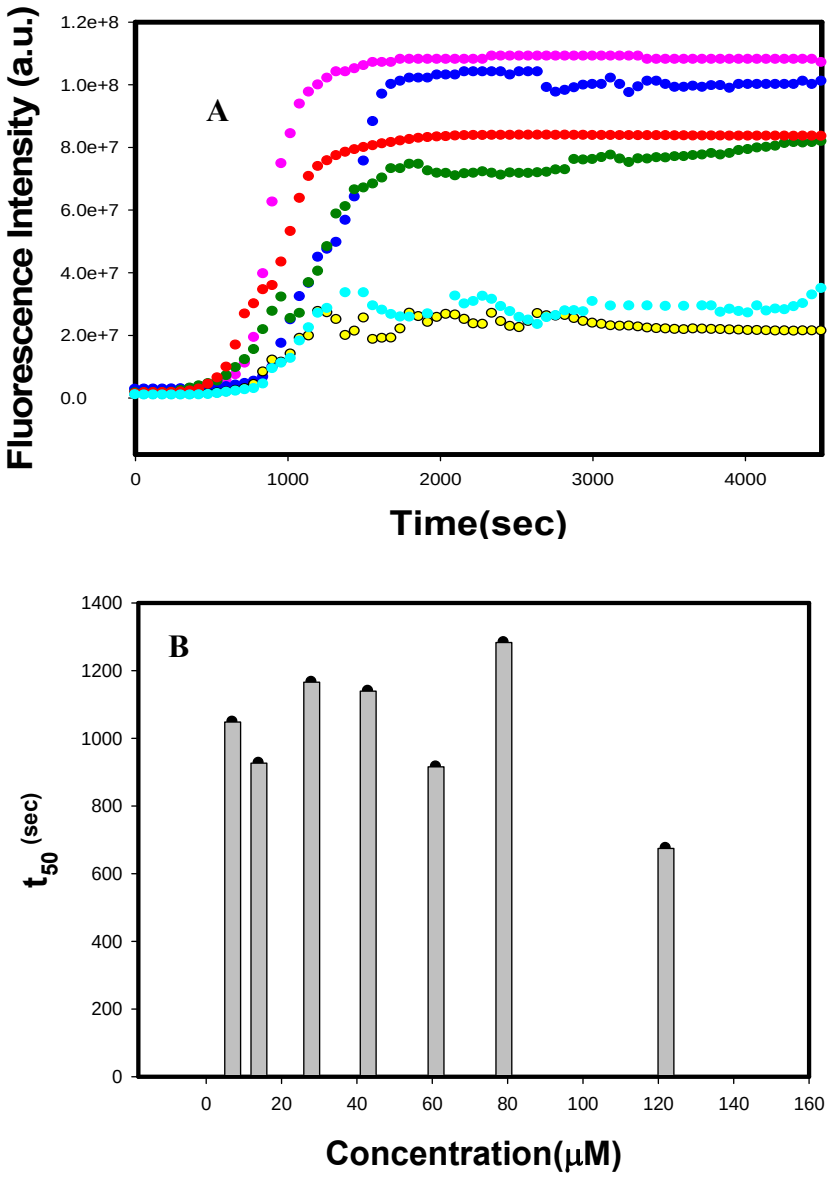

Figure 1. A) Concentration dependent aggregation of Amylin in 2% HFIP and 20mM Tris at pH 7.4 and 25°C. The different concentrations studied are 7μM (cyan), 14μM (yellow), 43μM (green), 61μM (blue), 79μM (red) and 122μM (pink). B) Plot of t_{50} values at various concentrations show no systematic increase or decrease as the concentration of Amylin is increased. t_{50} represent the time needed for 50% of the monomers to associate into fibrils.

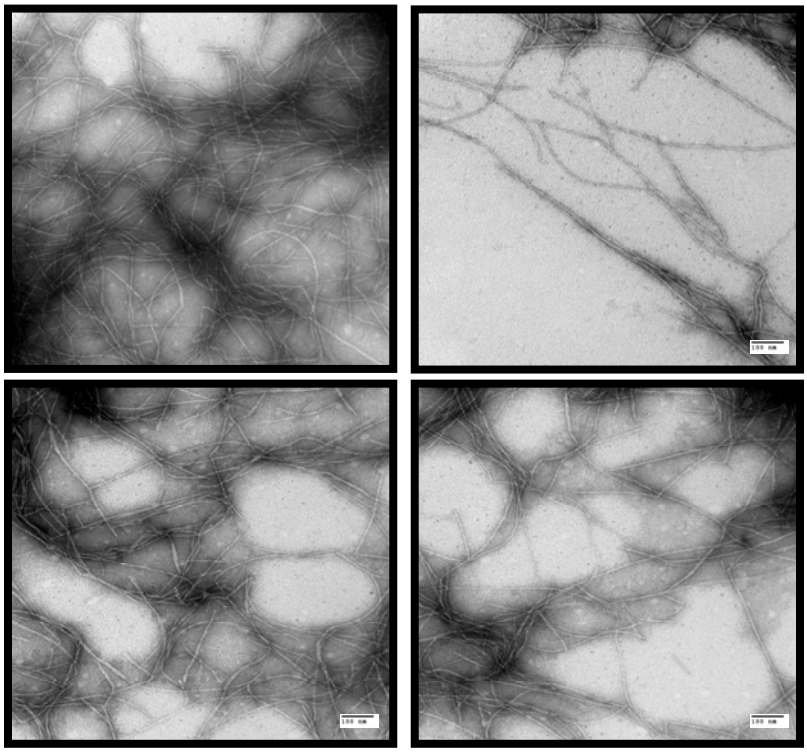

Figure 1c. Transmission electron microscopy (TEM) images of 14μM Amylin fibrils formed in 2% HFIP co-solvent and 20mM Tris at pH 7.4 and 25^{o}C. The scale bar in the images is 100nm.

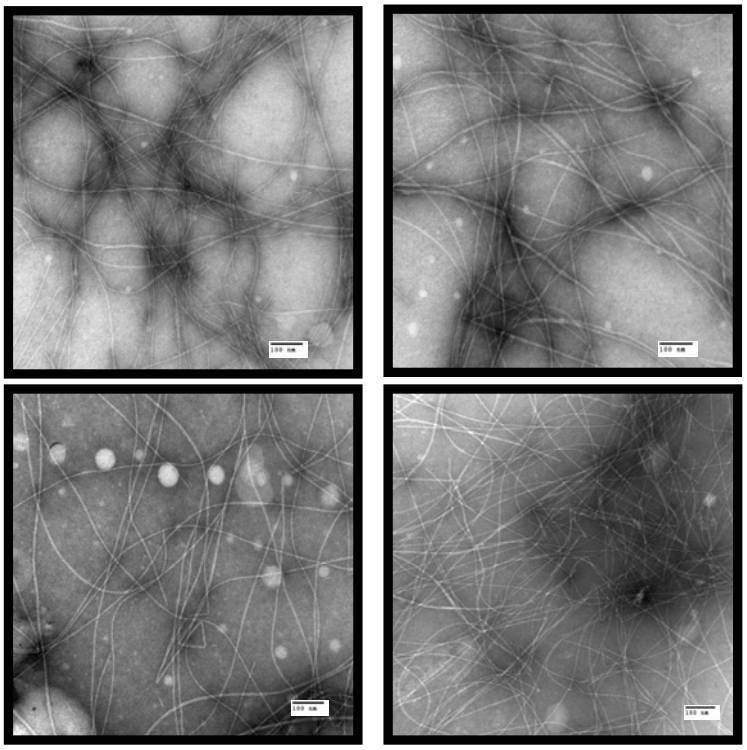

Figure 1d. Transmission electron microscopy (TEM) images of 32μM Amylin fibrils formed in 2% HFIP co-solvent and 20mM Tris at pH 7.4 and 25^{o}C. The scale bar in the images is 100nm.

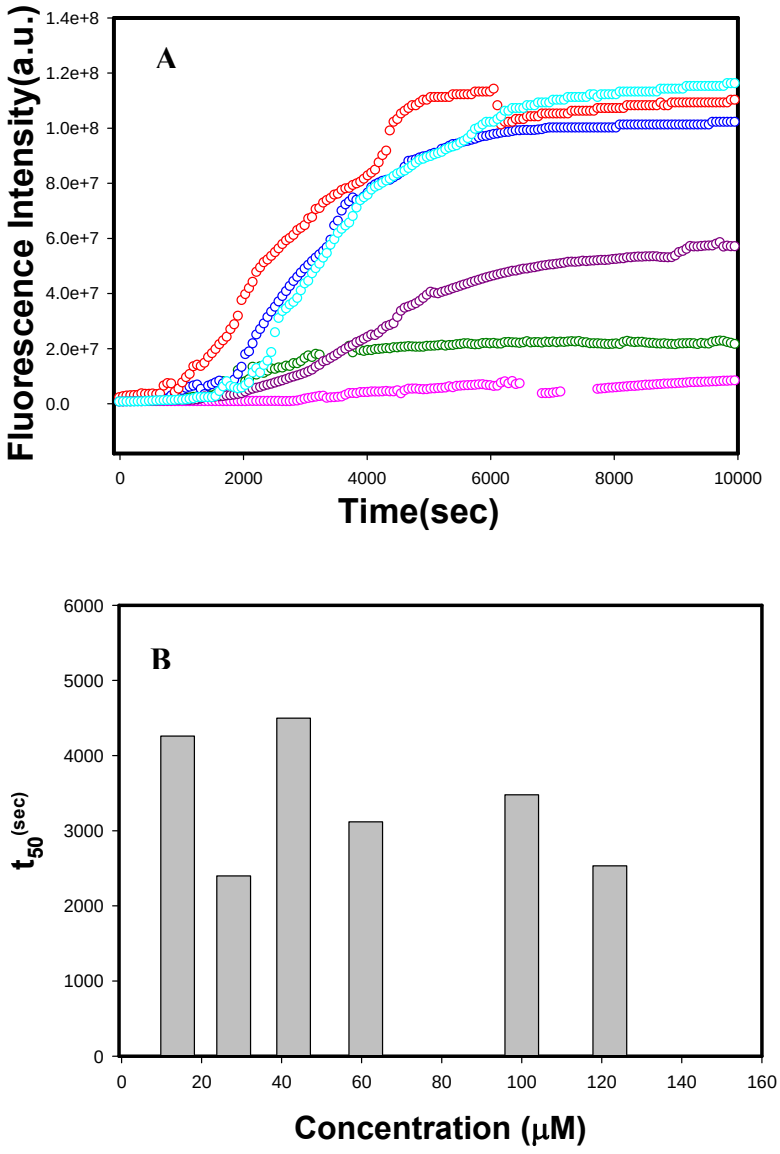

Figure 2. A) Concentration dependent aggregation of Amylin in 2% DMSO and 20mM Tris at pH 7.4 and 25°C. The different concentrations studied are 14μM (pink), 28μM (green), 43μM (purple), 61μM (cyan), 100μM (blue) and 122μM (red). B) Plot of t_{50} values at various concentrations show no systematic increase or decrease as the concentration of Amylin is increased. t_{50} represents the time needed for 50% of the total fluorescence change.

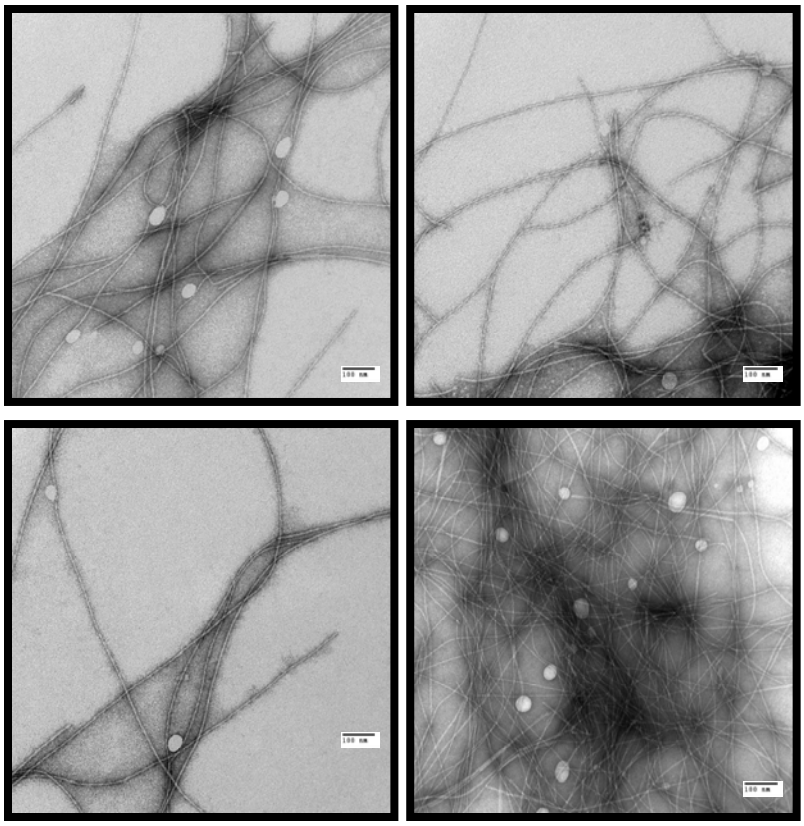

Figure 3. TEM images of 14μM Amylin fibrils formed in 2% DMSO co-solvent and 20mM Tris at pH 7.4 and 25^{o}C. The scale bar in the images is 100nm.

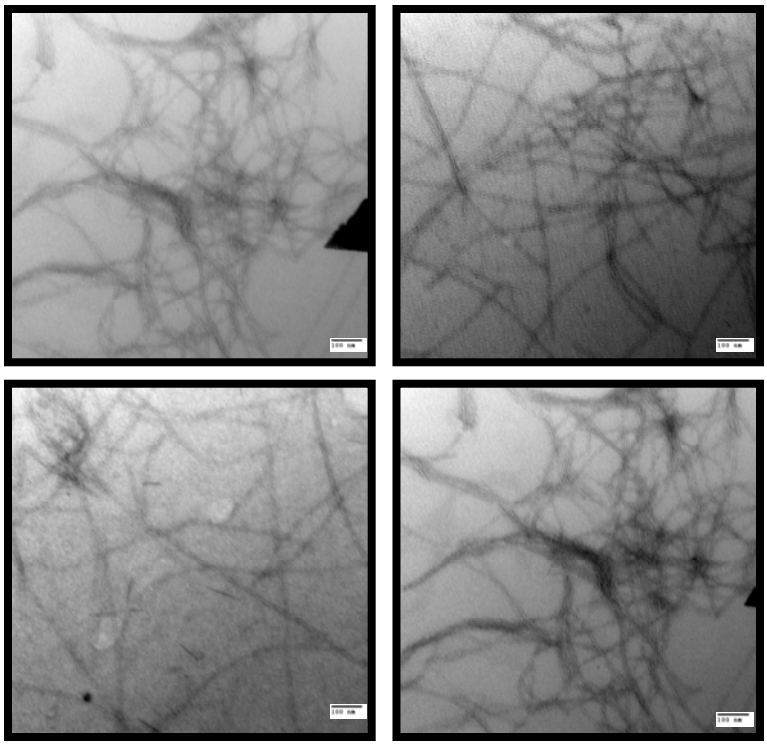

Figure 4. TEM images of 32μM Amylin fibrils formed in 2% DMSO co-solvent and 20mM Tris at pH 7.4 and 25^{o}C. The scale bar in the images is 100nm.

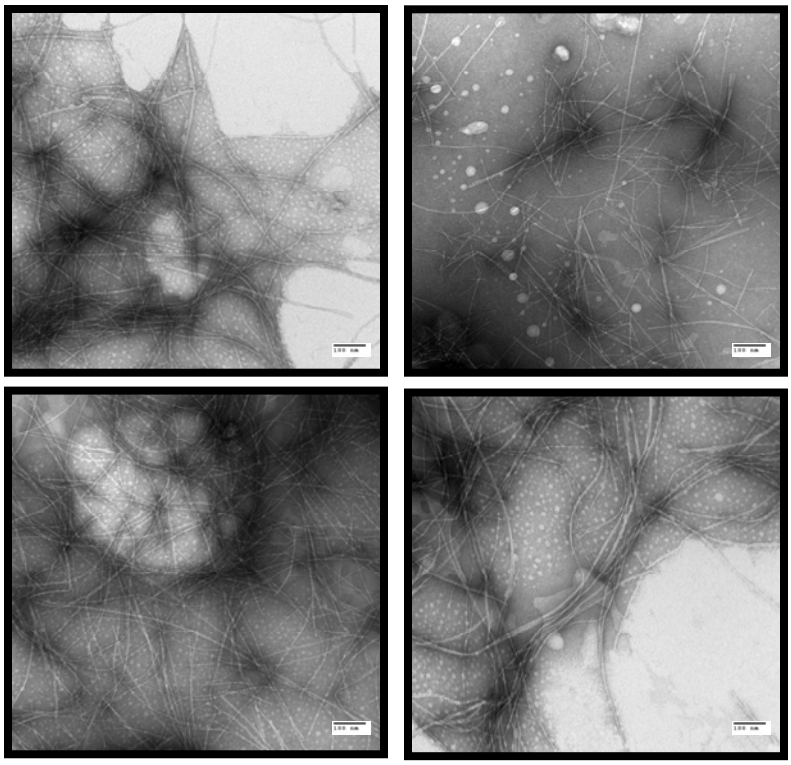

Figure 5. TEM images of 122μM Amylin fibrils formed in 2% DMSO co-solvent and 20mM Tris at pH 7.4 and 25^{o}C. The scale bar in the images is 100nm.

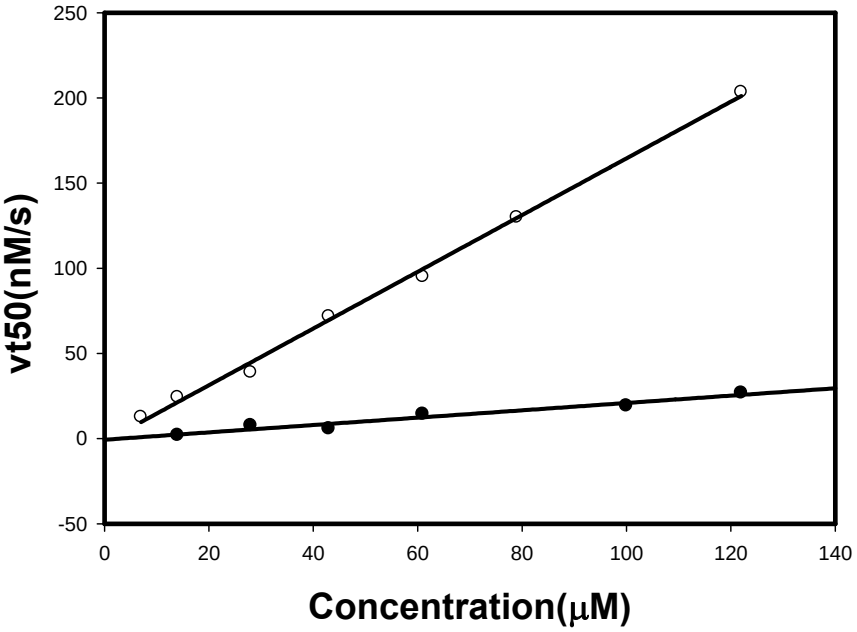

Figure 6. Plot of vt50 with concentration shows a linear dependence of the kinetics of fibril formation with t_{50} concentration. The data points represent Amylin aggregation in 20mM Tris at pH 7.4 containing 2% HFIP (empty circles) or in 2% DMSO (filled circles) as the co-solvent at 25^{o}C. vt50 is the reaction velocity in monomer units at t50.

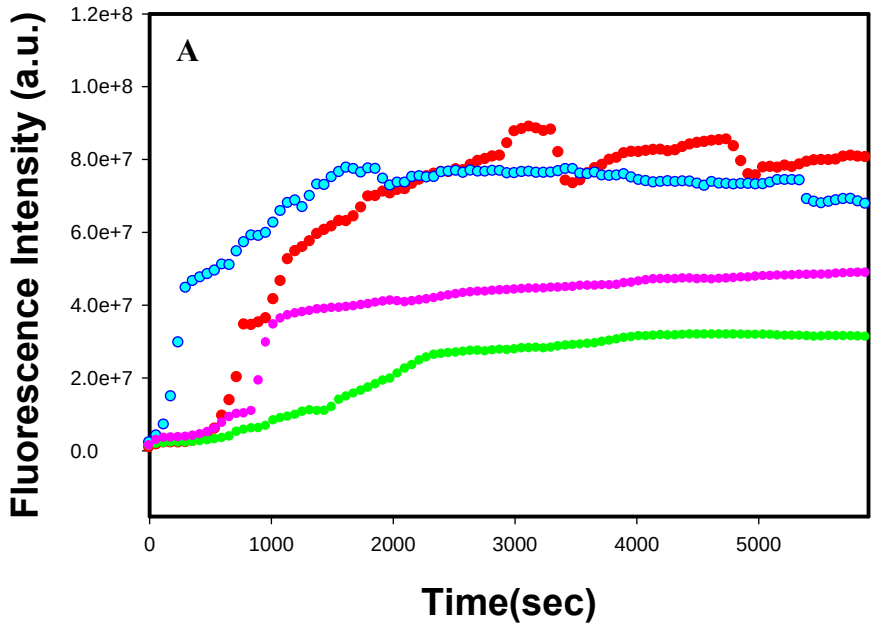
A
Fluorescence Intensity (a.u.)
1.2e+8
1.0e+8
8.0e+7
6.0e+7
4.0e+7
2.0e+7
0.0
0
1000
2000
3000
4000
5000
Time(sec)

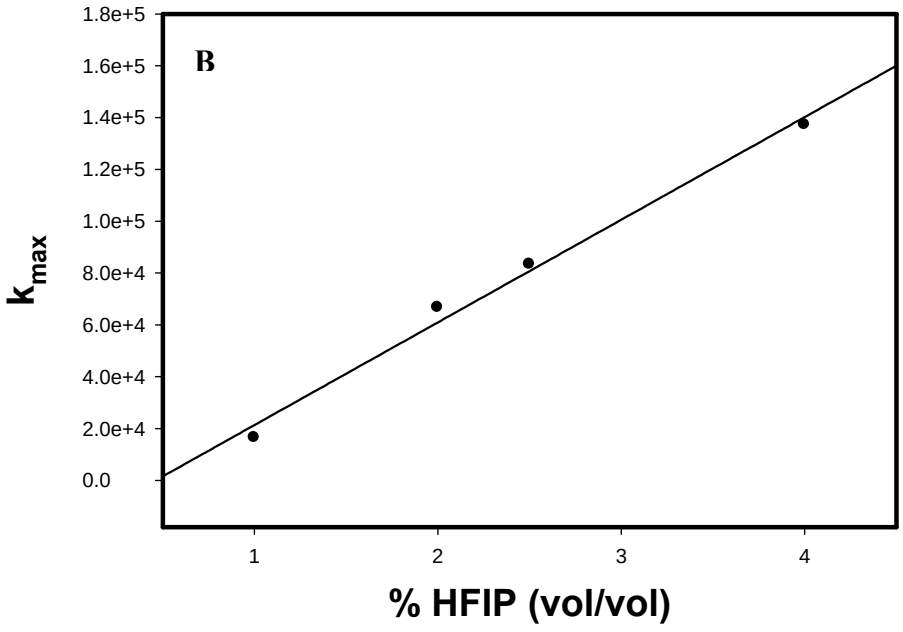
B
k_{max}
1.8e+5
1.6e+5
1.4e+5
1.2e+5
1.0e+5
8.0e+4
6.0e+4
4.0e+4
2.0e+4
0.0
1
2
3
4
% HFIP (vol/vol)

\

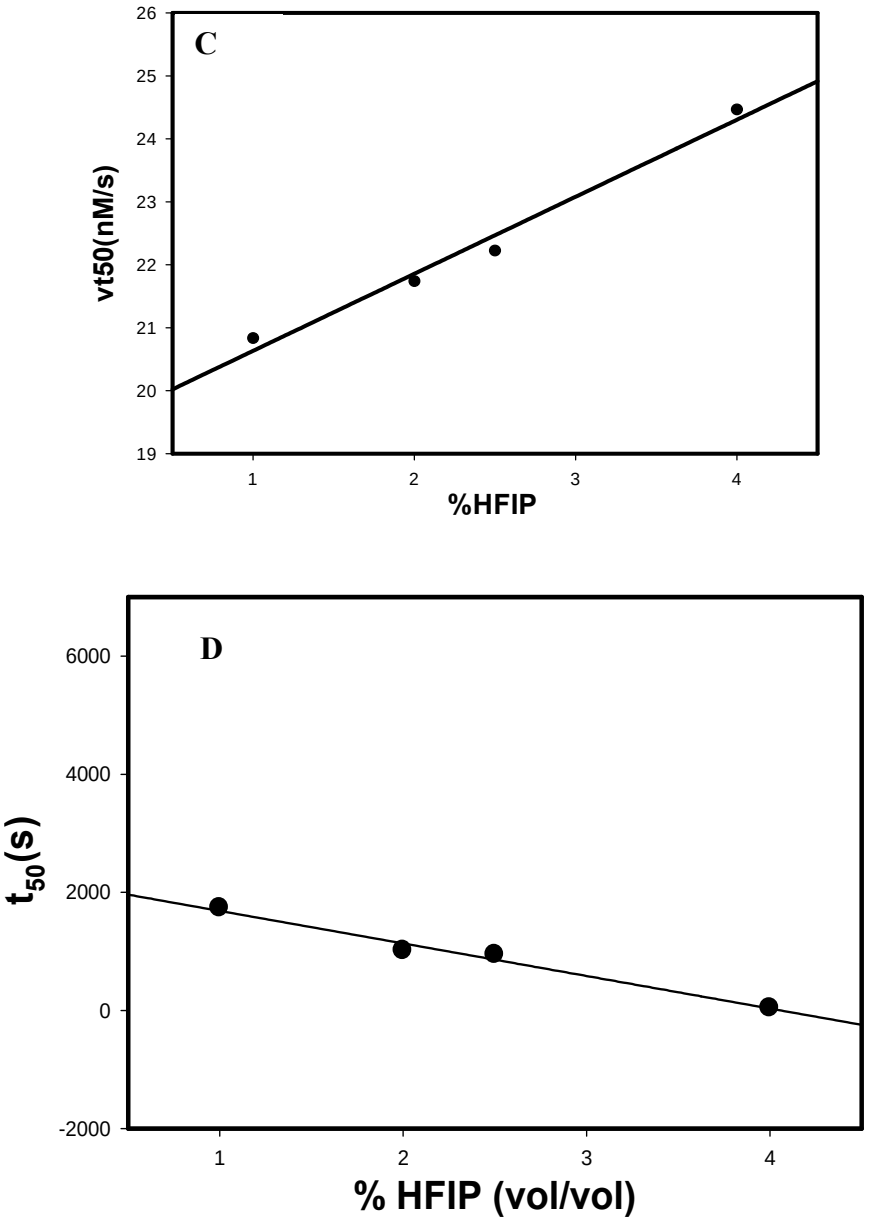

Figure 7. A) Thioflavin-T monitored hIAPP kinetics of 32μM Amylin aggregation in varying concentrations of HFIP: Green is 1% HFIP, pink is 2%HFIP, red is 2.5% and blue is 4% HFIP. B) Rate constant, k_{max}, for growth phase of Amylin fibril formation and C) the velocity at t_{50} show a linear increase as the HFIP concentration is increased in the reaction medium. D) t_{50} values linearly decrease with an increase in HFIP concentration because of the reduction in lag phase and enhancement in growth phase.

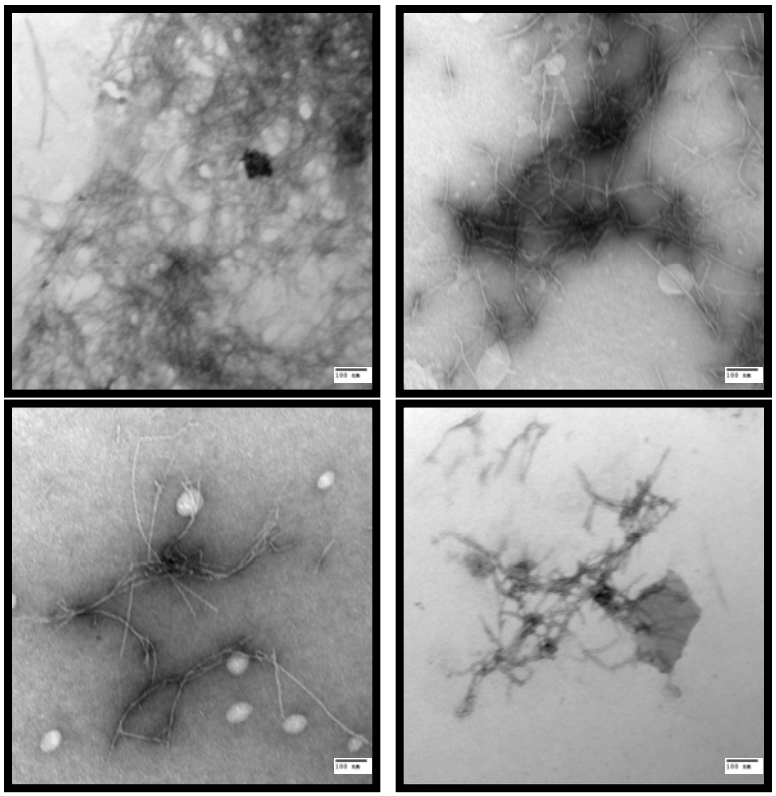

Figure 7e. TEM images of 32μM Amylin fibrils formed in 1% HFIP co-solvent and 20mM Tris at pH 7.4 and 25^{o}C. The scale bar in the images is 100nm.

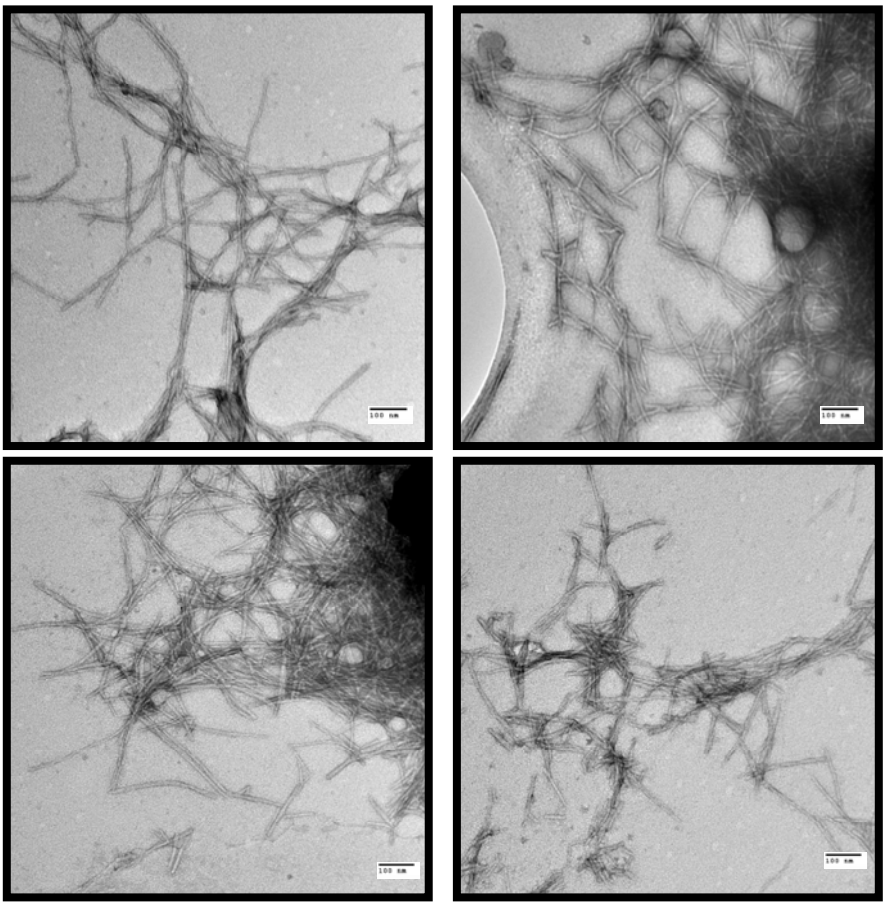

Figure 7f. TEM images of 32μM Amylin fibrils formed in 4% HFIP co-solvent and 20mM Tris at pH 7.4 and 25^{o}C. The scale bar in the images is 100nm.

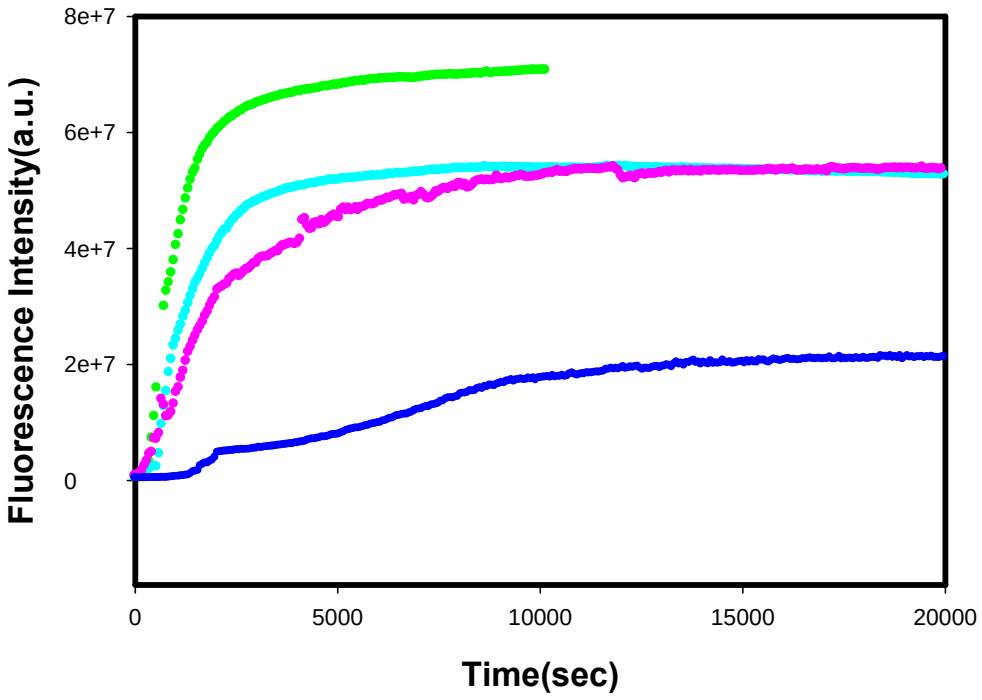

Figure 8. Thioflavin-T monitored hIAPP kinetics of 32μM Amylin aggregation in varying concentrations of DMSO: Green is 3% DMSO, light blue is 4% DMSO, pink is 5% DMSO and blue is 7% DMSO.

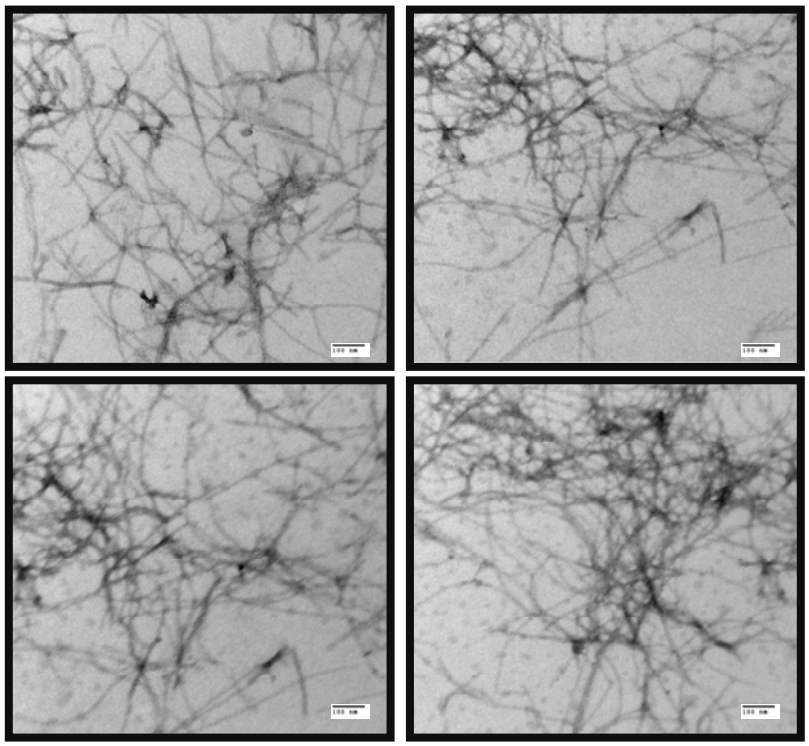

Figure 9. TEM images of 32μM Amylin fibrils formed in 3% DMSO co-solvent and 20mM Tris at pH 7.4 and 25^{o}C. The scale bar in the images is 100nm.

Chapter 4. Expression and biophysical characterization of effector protein YopH and its domains relevant to Bubonic plague

4.1 Introduction

Yersinia is gram-negative coccobacilli with three known human pathogenic strains: *Y.enterocolitica, Y.pseudotuberculosis and Y.pestis*. The strains *Y.enterocolitica* and *Y.pseudotuberculosis* are associated with gastroenteritis whereas *Y.pestis* wears the diadem for the well known bubonic plague. Plague is characterized by large swellings in the groin, blackening of areas around the mouth and extremities along with fever, chills, etc. *Y.pestis* is a lactose non-fermenter, urease and indole negative member of the Enterobacteriaceae with optimal growth temperature of 28^{o}C on blood agar. As a causative agent of plague, the bacterium uses the flea as a vector to facilitate its regurgitation and introduction into the mammalian cells. The flea acquires *Yersinia* through a blood meal from an infected mammal. The bacteria replicate in the gut of the flea by using the nutrients in the ingested blood. This bacterial mass clogs the intestine from receiving any further blood meals making the flea starve and urges it to regurgitate the bacteria into the mammalian blood stream. There these bacteria disseminate and suppresse the inflammatory response to ensure their survival. This dissemination leads to rapid proliferation such that when the next flea bites, the bacterium is available at all sites

of attack. Down the line, the bacterium localizes itself in the lymph nodes causing painful swellings especially in the groin. These "buboes" christened the name "bubonic" plague for this disease. The journey continues through the blood stream until the bacteria reaches the lungs where it takes the form of the pneumonic plague. From here, it claims new victims through aerosol infection shaping this disease into an epidemic (Abigail, 2002).

Y.pestis over the years of evolution from *Y.pseudotuberculosis* has become a very efficacious pathogen (Chain, 2004). Its 9.6 kb plasmid encodes for a protease that can activate plasminogen, a blood protein involved in resolution of blood clots. The anti-phagocytic genes transcribed by 101-kb plasmid allows for early dissemination of bacteria in the blood stream. A 70-kb plasmid (pCD1) encodes the genes for the type-III secretion system, which characterizes all *Yersinia* (Portnoy & Martinez. 1985).

Generally, the mechanism of delivering the toxins into the host is through the excretion of toxins into the extra-cellular medium where they can trace their way to the host cells. However, *Yersinia* ensures delivery by attaching itself to the mammalian cells and injecting the toxins directly through the type-III secretion system.

4.1.1 Type-III secretion system

Type-III secretion systems are utilized by a number of gram negative pathogens. These secretion systems inject virulence factors directly into the cytoplasm of the eukaryotic cells, which then disrupts the signaling pathways of the host (Smith, 2001). The proteins for this assembly are transcribed by the genes on the 70-kbp plasmid carried by *Yersinia* (Portnoy & Martinez, 1985; Cornelis, 1998, Aepfelbache *et al.,* 1999). The expression of these proteins is up regulated at 37^{o}C and a membrane-spanning channel is

formed utilizing these proteins. The full injection apparatus then assembles prior to the contact with the eukaryotic cell. The opening of the gated channel is stimulated by the host cell contact which then triggers the vectorial movement of toxic proteins through a *Yersinia* induced pore and into the cytoplasm of the mammalian cell.

Yersinia type III secretion proteins termed as "Yops" (*Yersinia outer proteins*) are divided into 2 categories, namely the "translocators" and "effectors". Translocators are responsible for the transfer of effectors across the host cell plasma membrane through the formation of a pore (Hueck, 1998). There are six effector Yops: YopE, YopT, YopO/YpkA, YopH, YopJ/P and YopM along with various translocators known to be responsible for virulence of *Y.pestis* (Cornelis *et al.,* 1998). YopK is essential for systemic infection in mice (Holmstrom, 1995). YopB and YopD are believed to be the first ones to be translocated to form a portion of the pore transiting the eukaryotic membrane. "Lcr"V (*Low calcium response*) protein is another important translocator which is thought to induce channel formation. However, its contribution to the virulence of *Yersinia* is still obscure (Nordfelth *et al.*, 2001). YopE and YopH then disassociate the cytoskeletal microfilaments preventing the ingestion of bacterium (Longsdon, 2003). YopE disrupts the actin stress fibers, induces cell rounding and inhibits phagocytosis. YopJ suppresses the production of cytokines and thus attenuates the response of immune cells and phagocytes to launch a defense against bacterium (Espinosa, 2004). YopT also contributes to anti-phagocytosis. It is a cysteine protease which cleaves the N-terminal of prenylated cysteine next to a short length of basic residues (Shao, 2003). This cleavage prevents the GTPase from anchoring to the membrane and disrupts the down-stream signaling of the proteins involved in actin cytoskeletal rearrangement. YopO/YpkA is a

serine-threonine protein kinase which disrupts the actin cytoskeleton, assists in phagocytosis and prevents chemotaxis (Galyov *et al*., 1993; Galyov *et al*., 1994). The role of YopM is not clear. However some evidence suggests that small amounts of extracellular YopM might bind to thrombin and inhibit platelet aggregation (Evdokimov, 2000; Leung *et al.,* 1990). YopM is the only virulence factor known to undergo nuclear localization (Skrzypek *et al.,* 1998).

The focus of the work highlighted here is to understand the biophysical properties of the two domains of YopH. YopH is the most active tyrosine phosphatase known to date (Zhang et al., 1992). This secretory protein is characterized by a single phosphatase domain (Bliska *et al*., 1991) connected to a non-catalytic regulatory domain by a flexible linker (Feng & Pawson, 1994; Zolnierowicz & Bollen, 2000). The crystal structure of both domains of YopH has been solved but the repeated attempts to crystallize the full length YopH have not been successful. It is known that the virulence of *Yersinia pestis* is strongly correlated with the phosphatase activity of YopH. The catalytic activity of YopH disrupts signaling pathways crucial for maintaining cellular immunity and house keeping functions. Thus understanding the role of two domains in facilitating rapid catalysis is crucial for designing effective inhibitors of YopH phosphatase. In order to study this robustly, the two domains were cloned and an expression system was established. Biophysical studies were then carried out with the purified proteins in order to enhance their association state. The N-terminal domain of YopH (YopH-NT) has been studied through various techniques like NMR spectroscopy, crystallization, dynamic light scattering, isoelectric focusing etc. The experimental results show YopH-NT to be monomeric at pH 6.5 by NMR studies and at pH 5.7 by gel filteration and isoelectric

focusing (Smith et al. 2001, Neumayer et al. 2004). However as the pH was raised to 7.2, YopH-NT was reported to form a dimer in crytallization and gel filteration experiments (Bennett et al. 1995, Khandelwal et al. 2002). Thus to facilitate the designing of effective inhibitors against substrate recognition by YopH, it is important to understand the association of the N-terminal domain involved in recognizing proteins targets for de-phosphorylation by the C-terminal phosphatase domain (Black et al. 1998, Ivanov et al. 2005). The de-phosphorylation of important host proteins by YopH is involved in antagonizing bacterial phagocytosis, inhibiting the oxidative burst and disrupting actin stress fibers (Andersson, *et al*., 1996; Fallman, *et al.,* 1995; Rosqvist, *et al*., 1988). The focal adhesions at the sites of cell attachment to the extra-cellular matrix are also found to be disrupted (Black, 1998). This phosphatase activity is basically essential for all *Yersinia* associated anti-host functions recognized to date.

The mechanism of dephosphorylation by YopH involves a highly conserved cysteine. This cysteine functions as a nucleophile to form a thiolphosphate linkage in the phosphoenzyme intermediate. Mutation of the Cys to Ser abolishes the catalytic activity (Bliska, *et al.,* 1993; Guan & Dixon, 1990). However, the mutation does not affect the binding to phospho-tyrosine proteins (Black & Bliska, 1997; Persson *et al*, 1997; Black & Bliska, 2000). The signature motif (I/V)HCXAGXGR(S/T)G forms a strand-loop-helix structure called the P-loop for phosphate-binding loop (Zhang & Dixon, 1994). This loop is responsible for stabilizing the negative charge of the thiol group of the catalytic cysteine through hydrogen bonding. Upon binding of the phosphorus residue in the substrate, an adjacent loop from residues 350-360 moves closer to the active site. The arginine 356 then participates in the acidic hydrolysis of phospho-tyrosine residue and

stabilizes the transition state by accepting an electron. Other catalytic residues include Glu290, which acts as a general base and Arg409 which might interact with the negatively charged phosphate group of the substrate or the aromatic tyrosine residue directly (Stuckey, *et al.,* 1994). The P-loop, the nucleophilic cysteine and the arginine are conserved among all families of known protein tyrosine phosphatases (PTPs) (Zhang & Dixon, 1994).

YopH is a 468 residue protein (51 kDa) with its N-terminal domain (Fig.1) connecting the C-terminal domain (Fig.2) through a 35 residue linker. The structure of full length YopH consists of an eight-stranded β-sheet surrounded by seven α-helices (Fig.3). The N-terminal domain is highly ordered and folds into a single, independent domain (C. Smith & M. Saper). The structured core is made up of residues 1 to 129. It is characterized by four α-helices flanked by a three-stranded β-sheet on one side and a two-stranded β-sheet on the other side (Evdokimov, 2001). The N-terminal domain is involved in the recognition of target proteins (Montagna *et al*., 2001) and localization of focal-adhesions in a phospho-tyrosine dependent manner (Deleuil *et al.,* 2003). YopH exhibits substrate specificity through the recognition of the consensus sequence DADEpYAAP (Zhang & Dixon, 1994). The acidic residues aspartate and glutamate at -1 and -2 positions and proline residue at +3 are critical for high affinity binding and catalysis (Zhang, *et al.,* 1993). The optimal substrate recognition demands that the phospho-tyrosine be placed within the peptide with more than 2 residues at the N-terminus and 3 or more at the C-terminus.

The N-terminal domain contains a proline rich region but shows no structural resemblance to any known SH2 or phospho-tyrosine binding domain. It represents a

novel phospho-tyrosine interaction domain. The C-terminal domain is the catalytic protein tyrosine phosphatase (PTP) domain of YopH (Sun, 2003). The uptake of the pathogen into eukaryotic cells is dependent on binding of the bacterial protein invasin to β-1-integrins present on the surface of host cell. The C-terminal domain dephosphorylates the proteins involved in regulation of the cytoskeleton, thereby inhibiting integrin-mediated uptake. It also hypo-phosphorylates all tyrosine-phosphorylated components in T and B-lymphocytes thereby ensuring the endurance of the pathogen inside the host.

4.2 Materials and methods

4.2.1 Expression of YopH full-length protein

The Tuner (DE3) *E.coli* strain carrying the low copy number plasmid pMMB67 YopH C403S 6xHis was obtained from Prof. J. Bliska's lab. The cells were grown for 3 hours at 37^{o}C to an O.D. of 0.6-0.8 followed by addition of 0.1mM IPTG. Thereafter the cells were spun down and the pellet was resuspended in binding buffer containing 10mM imidazole, 50mM sodium phosphate and 300mM sodium chloride. Protease inhibitor PMSF was also added at a concentration of 0.1mM to avoid proteolytic degradation. The resuspended cells were sonicated over ice and centrifuged at 9000 rpm for 45 min. The supernatant was then loaded onto a Ni-NTA column that has high affinity for the 6xHis tag.

4.2.2 Purification of His-tag YopH protein

20mL of binding buffer (pH=8.0) containing 10mM imidazole, 50mM sodium phosphate and 300mM sodium chloride was run through the Ni-NTA resin. The column

was cleaned using 50 mL of cleaning buffer (pH=8.0) made of 500 mM imidazole and 100 mM Tris-base. After cleaning, the column was equilibrated with 10 times the volume of binding buffer. The supernatant from lysed cells was loaded onto the column followed by washing with 10X volume of wash buffer containing 50 mM sodium phosphate, 300 mM sodium chloride and 20 mM imidazole at pH 8.0. The protein eluted using 30 mL of elution buffer (pH=8.0) consisting of 50 mM sodium phosphate, 300 mM sodium chloride and 250 mM imidazole. After elution, the column was washed thoroughly with cleaning buffer thoroughly.

The Ni-NTA-column purified protein was ran on a SDS-PAGE gel to check for the purity and expression level of the desired protein. The next purification step was carried out using a C18 semiprep HPLC column. The protein was eluted at 50% buffer B when ran through a gradient of 0-90% buffer B (90% Acetonitrile + 10% H_2O + 0.1% TFA) in 90min. The purified protein was concentrated and dialyzed against three liters of buffer containing 10 mM sodium phosphate, 100 mM sodium chloride and 10 mM dithiothreitol and stored at -80^{o}C. Electron spray mass spectrometry was used to confirm the correct molecular mass of 50996.4Da.

4.2.3 Purification of the N-terminal domain of YopH

The vector, p67, containing N-terminal domain of YopH was received from Prof. James Bliska's lab in the Center for Molecular Medicine at Stony Brook. The His-tag protein was expressed using different conditions as summarized in table 1. No protease inhibitor was added during cell lysis. The protein was purified using a Ni NTA column and HPLC. The N-terminal domain of YopH eluted at around 53% acetonitrile from C4

semiprep column using a gradient of 0-90% H_2O/Acetonitrile with 0.1% trifluoroacetic acid in 90min. The identity of the desired protein was confirmed by ESI mass spectrometry. The best yield was 130 mg/L.

4.2.4 Circular Dichroism spectroscopy

The chiral character of amino acids imparts optical properties to the proteins, which can then be harnessed to derive information about protein secondary and tertiary structure (Nolting, 1999). All experiments for deciphering the secondary structure of the protein were performed using Aviv Model 62A DS and 202SF circular dichroism spectrophotometers fitted with Peltier temperature control unit. The buffer used was 100 mM Na_2HPO_4, 100 mM NaCl and 1 mM EDTA at pH=8.0. The set of experiments carried out were as follows:

4.2.4.1 Wavelength scans: The secondary structure of the protein was monitored using circular dichroism spectrometer. The far-UV wavelength scans were performed with 3 repeats and an averaging time of 1.0 second per data point from 190 nm to 260 nm with a protein concentration of 10 μM.

4.2.4.2 Urea denaturation: The chemical denaturation of protein was carried out by gradually increasing the concentration of urea. The protein concentration used was 10 μM. The titration was performed with an equilibration time of 2 minutes and the data was averaged for 30 seconds at each point. The CD signal was recorded at 222 nm at 25^{o}C. The curves were fit using equation (1) to obtain the equilibrium parameters (Pace, 1986):

$$f(urea) = \frac{\alpha_N + \beta_N + (\alpha_D + \beta_D)e^{\frac{-\Delta G^o_{urea}}{RT}}}{1 + e^{\frac{-\Delta G^o_{urea}}{RT}}} \quad (1)$$

where ΔG^o is defined as:

$$\Delta G^o_{urea} = \Delta G^o_{H_2O} - m * [urea] \quad (2)$$

f(urea) is the observed signal as a function of urea, T is the temperature, R is the gas constant, α_N defines the intercept and β_N is the slope of the post-transition region of the curve, α_D defines the intercept and β_D is the slope of the pre-transition region of the curve, ΔG^o is the free energy change for the unfolding reaction, m is proportional to the amount of surface area exposed to the solvent upon unfolding of the protein (Tanford, 1970).

The thermodynamic stability of the protein in the absence of the denaturant can be computed using the above expressions.

4.2.4.3 Thermal unfolding: The unfolding of the protein with temperature was monitored using CD spectrophotometer at a wavelength of 222nm, which is characteristic of an α-helix. The data points were averaged over 30 seconds for every unit increment in temperature. A plot of CD signal versus temperature was fit to equation (3):

$$f(T) = \frac{\alpha_N + \beta_N * T + (\alpha_D + \beta_D * T) * e^{\frac{-\Delta G^o_{-K}(T)}{RT}}}{1 + e^{\frac{-\Delta G^o_{-K}(T)}{RT}}} \quad (3)$$

where,

$$\Delta G^{o}_{D-N}(T) = \Delta H^{o}_{D-N}(T_m) * \left(1 - \frac{T}{T_m}\right) - \Delta C^{o}_{p} * \{(T_m - T) + T * \ln\left(\frac{T}{T_m}\right) \quad (4)$$

f(T) is the signal as a function of temperature, T is the temperature, R is the gas constant, α_N defines the intercept and β_N is the slope of the post-transition region of the curve, α_D defines the intercept and β_D is the slope of the pre-transition region of the curve, T_m is the mid-point of unfolding deined by $\Delta G^{o}_{D-N}(T_m)$. ΔG^{o} is the free energy change for the unfolding reaction, ΔH^{o} is the change in enthalpy at T_m and $\Delta C_p{}^{o}$ is the change in heat capacity. Using the above expressions T_m, the mid-point transition temperature was estimated, along with the change in enthalpy ΔH^{o}_{D-N}, for the unfolding reaction at that T_m.

4.2.5 Analytical Ultracentrifugation

Analytical ultracentrifugation is a versatile technique used to study solution state association behavior of macromolecules (Cole, 1999). The instrument Optima XL1 uses both a UV/VIS spectrophotometer and a Rayleigh interferometer detector. The spectrophotometer is selective and sensitive for the solute and measures its concentration by absorption at any wavelength between 190-800 nm. Analytical ultracentrifugation can be used for sedimentation velocity and sedimentation equilibrium studies. The former measures the rate of movement of a macromolecule under radial acceleration in the ultracentrifuge. It takes into account the mass and the shape of the molecule. Sedimentation equilibrium enables the determination of the molecular weight and the study of stoichiometry of heterogeneous binding reactions. It depends on the distribution of solute concentration under equilibrium conditions (Condino, 1998).

Sedimentation equilibrium studies were carried out at different pHs and at different concentrations. The samples were run for sufficiently long periods of time to allow for the equilibrium to reach. The speeds were decided based on the molecular weight of the protein. Under no net transport conditions, the following correlation should be observed between concentration and the radial distance (Van Holde, 1985):

$$C_r = C_{r_0} * e^{\frac{\sigma\omega^2}{2}(r^2 - r_0^2)} \quad (5)$$

where,

$$\sigma = M(1 - \upsilon\rho)\frac{\omega^2}{RT} \quad (6)$$

where, C_r is the concentration of macrosolute at any radial distance r, C_{r0} is the concentration of the macrosolute at the reference radial distance r_0, υ is the partial specific volume, ω is the angular velocity, ρ is the density, R is the gas constant , T is the absolute temperature and M is the molecular mass. The data was analyzed using Optima^{TM} XL-A/XL-I Data Analysis Software (Beckman, 2001).

4.3 Results

The biophysical studies of the purified full length YopH showed helical structural features in Far-UV wavelength CD. A comparison of the Far-UV CD wavelength scans of the dialyzed versus the lyophilized samples shows that lyophilization of full length YopH leads to a protein which does not refold (Fig.4-5). The lyophilized sample lacks the characteristic structural elements of a folded YopH. However, the scans of dialysed protein showed well defined secondary features with minima around 206 nm and 222 nm

corresponding to β-strands and α-helix respectively. The association state of YopH was determined using Analytical Ultra Centrifugation experiments. At concentration of 50μM protein in buffer containing 100 mM Na_2HPO_4, 100 mM NaCl, 1 mM EDTA at pH 6.8, the molecular mass calculated from the centrifugation data corresponded to monomer of YopH (Fig.6). The results were confirmed by repeating the experiment at two different speeds at the same concentration.

The N-terminal domain of YopH (YopH-NT) was also expressed as a His-tagged protein. Previous attempts at purifying YopH-NT from the p67 vector gave only 2-3mg of purified protein per liter. Several expression conditions with varying amounts of IPTG and induction times as listed in table 1 were done and the protein yield was improved to 130 mg/ml. The Far-UV CD data of both dialyzed and lyophilized samples of YopH-NT at 35 μM concentration showed characteristic secondary structural features of an α-helical protein (Fig.7-8). The protein was well folded and stable at room temperature. The thermal unfolding experiments done on YopH-NT at a concentration of 25 μM gave a T_m of 49.1^oC with a ΔH^o of 65.7 kcal mol^{-1} at pH 7.0 using eq. (3) (Fig. 9). The N-terminal domain of YopH was observed to fold irreversibly through thermal unfolding experiments.

The chemical denaturation of YopH-NT was also monitored at 222 nm at pH 5.0 and pH 7.0 (Fig. 10-11). The buffer used was 10 mM sodium phosphate. The data was analyzed using equation 2 as described in the materials and method section. The stability was found to be strongly pH dependent. These denaturation curves show that the stability of N-terminal domain of YopH increases from acidic to neutral pH. The transition mid-

point changed from 1.35 M to 2.93 M urea concentration as the pH underwent a two unit increment.

To further test if the stability was affected by association of the protein molecules, analytical ultracentrifugation studies were performed at different pH values. The buffer used was 10 mM sodium phosphate and the pH was adjusted accordingly. The expected molecular weight for monomer of YopH-NT is 14.1kDa. AUC data was collected for pH 5.0, 5.7, 7.0 and 8.0 (Fig 12-26). YopH-NT and the results show that YopH-NT exists as a dimer under all these conditions. The molecular mass computed from AUC data at pH 5.0 was 29.9kDa for 100 μM concentration (Fig. 12) and around 29.7 kDa at 162 μM concentration of protein (Fig 13). The physical parameters used for YopH-NT were as follows:

ρ = 1.00416 g/ml V-bar = 0.7278 ml/g

As the pH was increased from 5.0 to 8.0, the analysis of the AUC data gave a molecular mass corresponding to the molecular mass of the dimeric species. The results were confirmed by repeating the experiments at different speeds for each pH value. At pH 8.0, molecular mass calculated for 200 μM concentration of YopH-NT varied from 23.4 kDa at speed 30000 rpm (Fig. 14) to 21.8 kDa at 40000 rpm (Fig. 15). Any non-specific association was ruled out by collecting data at several different concentrations. YopH-NT, at pH 8.0 and speed 40000 rpm, existed as a dimer at 50 μM concentration (with computed molecular mass of 26.7 kDa) (Fig. 16) as well as at 200 μM concentration (with computed molecular mass of 21.8 kDa). The results from AUC experiments at different pH values have been tabulated in table 2 and 3. The results highlight the tendency of YopH-NT to associate and form dimeric species over a pH

range of 5.0 to 8.0. Thus the phenomenon of dimerisation by YopH-NT cannot explain the observed increase in stability with increase in pH.

After having established the basic biophysical properties of the full length YopH and its N-terminal domain, the next step was to determine the orientation of C-terminal and N-terminal domains in the full length YopH. To accomplish this task, an intein strategy was employed. The idea was to make a suitable N-terminal construct with an intein at the C-terminus and a C-terminal construct whose N-terminal residue is cysteine. The two domains, when brought together, can undergo the intein mediated splicing reaction to give the full length protein. Each domain can then be selectively labeled and then combined together through intein chemistry to yield the full length YopH. NMR studies on the selectively labeled constructs can give useful insight into the dynamics of interactions of the two domains in the full length protein. Ultimately, we were unable to prepare the required constructs. A description of our results is provided to aid any future researchers who may tackle this project.

The gene for the full length YopH, obtained from Prof. Bliska's lab in Center for Infectious Diseases at Stony Brook, was cloned into the pMMB67HE vector between BamHI and EcoRI restriction sites. The first task was to decide what region should be chosen to constitute the N-terminal domain. The solution structure available for N-terminal domain corresponds to YopH-(1-129)-Ser-His_6 (Khandelwal, 2002). Therefore, the aim was to design the new construct around this length. To use the intein strategy, a Cys at the N-terminus of C-terminal domain was needed. Since there was no cysteine in the vicinity of residue 130, the alternative was to introduce a point mutation. The most conservative mutations are Ser → Cys or Ala → Cys. Since the closest are S132 and

S133, the latter was chosen to be at a safe distance from the N-terminal domain to be able to use the available assignments.

Having decided the incision site, primers were designed to obtain the desired N-terminal domain construct from full length YopH using PCR.

forward primer 5'-3'

AAAAAA-CATATG-AAC-TTA-TCA-TTA-AGC-GAT-CTT-CAT-CGT-CAG-GTA-TC

NdeI

reverse primer 5'-3'

AAAAAA-GCTCTTC-A-GCA-TGA-TAC-ATG-CCC-CCT-CGC-TCC-C

SapI

Use of SapI allowed the peptide to be made with no additional residues between N-terminal domain and intein. The PCR product was cloned into a pET Blue2 vector through Blunt end ligation. The vector was then digested using NdeI and SapI enzymes for two hours and the insert was gel purified. Simultaneously, intein containing pTXB1 vector was also digested with Nde1 and Sap1 enzymes. The insert was ligated into the digested vector and transformed into XL1 blue cells. The plasmid was tested through DNA sequencing for the presence of the right insert. The YopH-NT-intein construct was transformed in BL21(DE3) cells and the overnight culture was used for protein expression. E.coli was grown to an OD of 1.5 followed by a three hour induction with 1mM IPTG. The culture was spun down and the cell pellet was resuspended in column buffer containing 20 mM Tris-HCl and 500 mM NaCl at pH 8.0. The cells were sonicated on ice and centrifuged at 20000g for 30min. The chitin beads were washed with 5 column volumes of column buffer. The supernatant from the spin was loaded on 10-20 ml of bed

volume of chitin beads in the column at a rate of 1-5 ml/min. The column was washed with sample buffer (100 mM Na_2HPO_4 + 100 mM NaCl) at pH 8.0. The wash was checked with Bradford assay for elution of the desired protein. Once the binding of protein was confirmed to the chitin beads, the column was quickly washed with 3-4 volumes of sample buffer with 50 mM MESNA. The beads were incubated overnight with sample buffer and MESNA. After 12-15 hours, the beads were then washed with sample buffer without MESNA and the eluted protein was detected through a Bradford assay. The yield for YopH-NT-intein was 2 mg/L.

For the C-terminal domain, the primers were designed with Factor Xa sequence whose cleavage at a later stage will give a Cys at the N-terminus. The DNA construct carrying the S133-Cys mutation was obtained from the full-length *yopH* through quick change mutagenesis. The gene was then cloned into pET23b between the restriction sites NdeI and EcoRI.

forward primer 5'-3'

NdeI *factor Xa*

AAAAAA-CATATG-*ATTGAAGGTCGT*-TGC-CAT-TCA-CAT-TCA-GCC-CTT-CAC-GCA-CCG-GG

reverse primer 5'-3'

EcoRI

AAAAAA-GAATTC-TTA-GTG-ATG-GTG-ATG-GTG-ATG-GCT-ATT-TAA-TAA-TGG-TCG-CCC

The YopH-CT construct was confirmed by DNA sequencing. The pET23b vector with the construct was transformed into BL21(DE3) cells and the protein expression was

induced with 0.5 mM IPTG at OD of 1.0. The protein expression was confirmed by SDS-PAGE gel. The supernatant from the sonicated cells was loaded on a Ni-NTA column for protein purification. However, the protein did not bind to the Ni column probably because the His-tag was embedded in the C-terminal domain. This was confirmed by doing a western with the His-tag antibody which failed to detect any his-tag on the expressed YopH-CT protein. To overcome this problem, YopH-CT was digested out of pET23b vector with restriction enzymes NdeI and EcoRI. The insert was then cloned into the pGEX2T vector and confirmed by DNA sequencing. The pGEX2T vector with the right CT construct was transformed into BL21(DE3) cells. The cells were allowed to reach an OD of 0.6 after which the protein expression was induced with 0.5mM IPTG at 37^{o}C for 3hrs. The expression of YopH-CT was confirmed through SDS-PAGE. The expressed protein was purified through a GST-Sepharose affinity column using FPLC. The yield of the purified protein was 6mg/L.

4.4 Discussion

YopH is an important tool for the pathogenicity of *Yersinia*. Hence designing inhibitors against this phosphatase activity of YopH is a promising approach in preventing and treating the bubonic plague. However, this approach requires an understanding of the structural and biophysical properties of YopH and its domains. The constructs for both N-terminal and C-terminal YopH were designed and cloned into the specific vectors. The expression and purification system for both domains of YopH was established. The biophysical studies of YopH showed that it existed as a monomer when tested under varying concentrations. The N-terminal domain of YopH, however,

preferred the dimeric state when tested under different conditions of pH and concentrations. The N-terminal domain is important in order to recognize the protein targets for dephosphorylation by the C-terminal domain. To facilitate the understanding of biophysical properties of the N-terminal domain, attempts were made to optimize the expression of the domain from *E.coli*. The yields were maximized to 130 mg/l. The stability of this domain was found to be pH sensitive as evinced by urea denaturation experiments. Thermal unfolding experiments showed that folding of YopH-NT was irreversible. Thus strategies aimed at decreasing the stability of N-terminal domain might compromise the substrate recognition by YopH while inhibitors of phosphatase domain will make *Yersinia* less potent. The current drugs administered for treating the plague like vibramycin, ciprofloxacin, chloramphenicol or vancomycin are general antibiotics (Galimand *et al*., 1997). They either disrupt the protein synthesis in the bacterial cell or interfere with the cell wall synthesis. Understanding of the two domains can help in designing the inhibitors specifically against Yersinia targetting the recognition and/or the catalytic domain. Inhibitors for YopH will be specifically useful as *Yersinia* with non-functional YopH are shown to be avirulent.

4.5 Figures

Figure 1. N-terminal domain of YopH (PDB Code: 1huf).

Figure 2. C-terminal domain of YopH (PDB Code: 1xxp).

```
  1  MNLSLSDLHR QVSRLVQQES GDCTGKLRGN VAANKETTFQ GLTIASGARE
 51  SEKVFAQTVL SHVANIVLTQ EDTAKLLQST VKHNLNNYEL RSVGNGNSVL
101 VSLRSDQMTL QDAKVLLEAA LRQESGARGH VSSHSHSVLH APGTPVREGL
151 RSHLDPRTPP LPPRERPHTS GHHGAGEARA TAPSTVSPYG PEARAELSSR
201 LTTLRNTLTP ATNDPRYLQA CGGEKLNRFR DIQCCRQTAV RADLNANYIQ
251 VGNTRTIACQ YPLQSQLESH FRMLAENRTP VLAVLASSSE IANQRFGMPD
301 YFRQSGTYGS ITVESKMTQQ VGLGDGIMAD MYTLTIREAG QKTISVPVVH
351 VGNWPDQTAV SSEVTKALAS LVDQTAETKR NMYESKGSSA VADDSKLRPV
401 IHCRAGVGRT AQLIGAMCMN DNRNSQLSVE DMVSQMRVQR NGIMVQKDEQ
451 LDVLIKLAEG QGRPLLNS
```

Figure 3. The sequence of full length YopH. The N-terminal domain is shown in pink, linker region is shown in green and C-terminal domain is shown in blue. Ser133 (light green) was mutated to Cys to use intein chemistry.

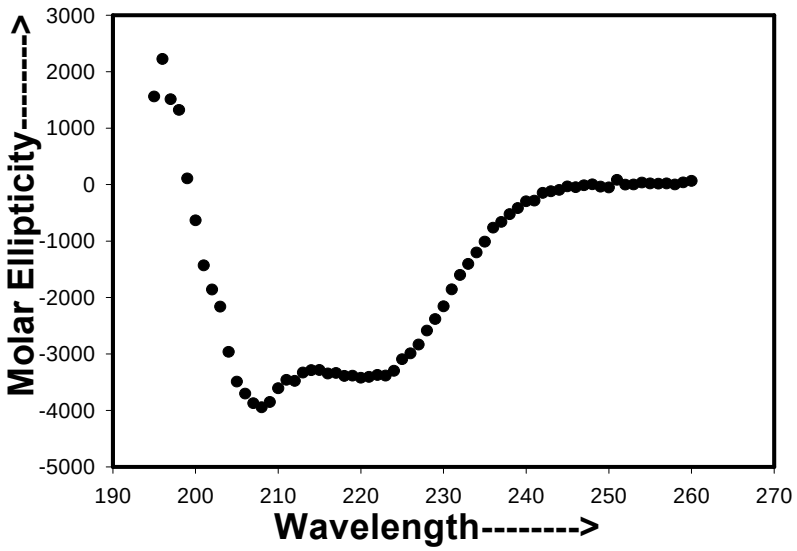

Figure 4. Circular Dichroism data of 5μM YopH dialyzed against buffer containing 10mM sodium phosphate, 100mM sodium chloride and 10mM dithiothreitol.

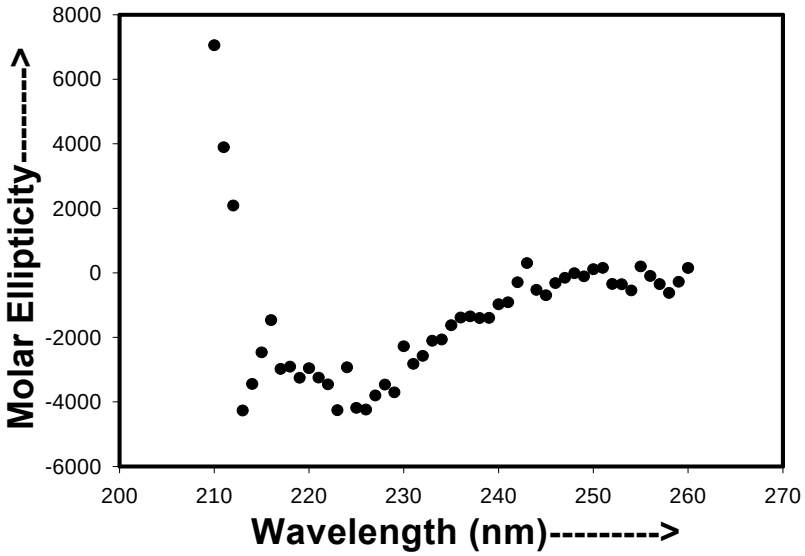

Figure 5. Circular Dichroism data for a 1μM sample of YopH lyophilized after HPLC purification.

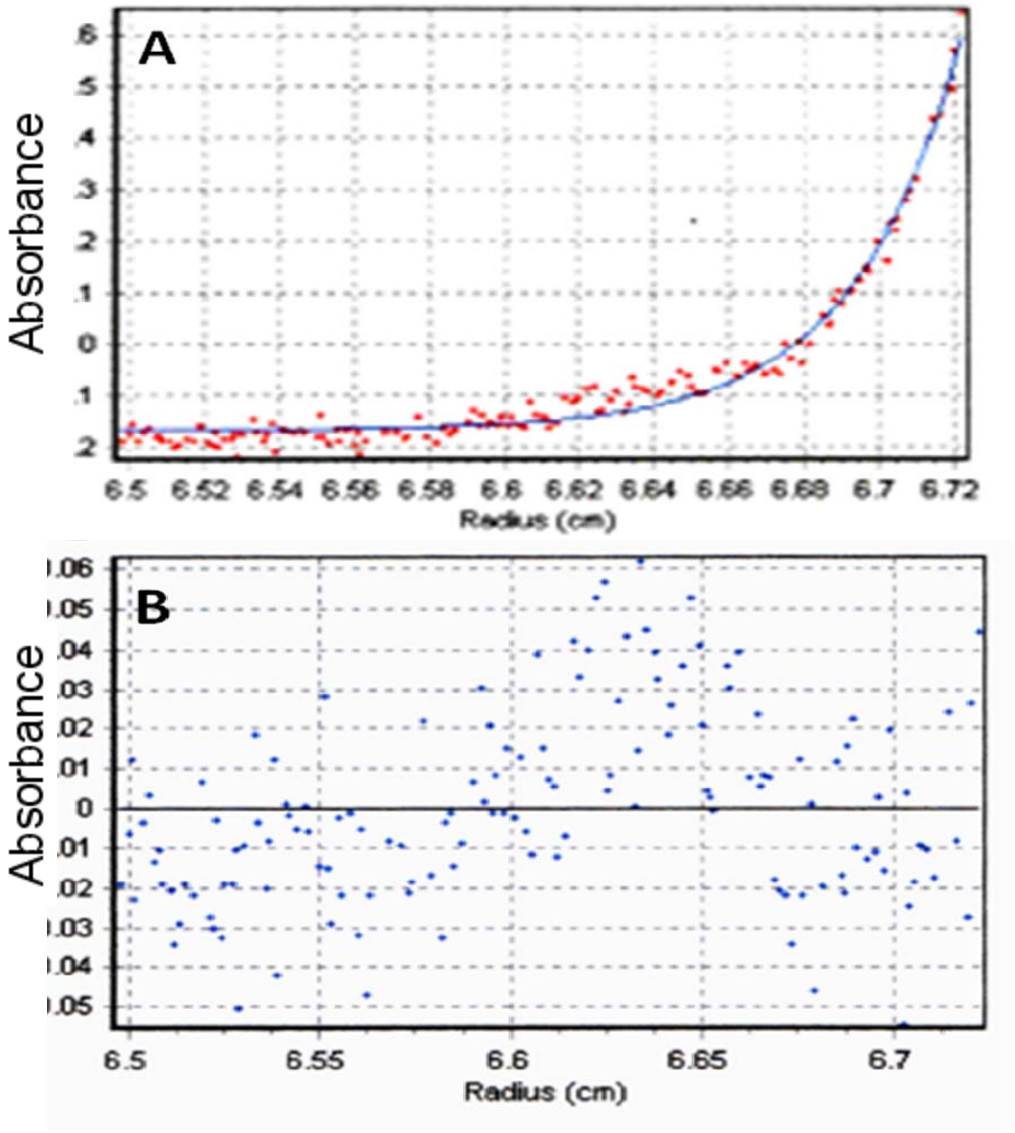
A
Absorbance
.6
.5
.4
.3
.2
.1
0
.1
.2
6.5
6.52
6.54
6.56
6.58
6.6
6.62
6.64
6.66
6.68
6.7
6.72
Radius (cm)
B
Absorbance
.06
.05
.04
.03
.02
.01
0
.01
.02
.03
.04
.05
6.5
6.55
6.6
6.65
6.7
Radius (cm)

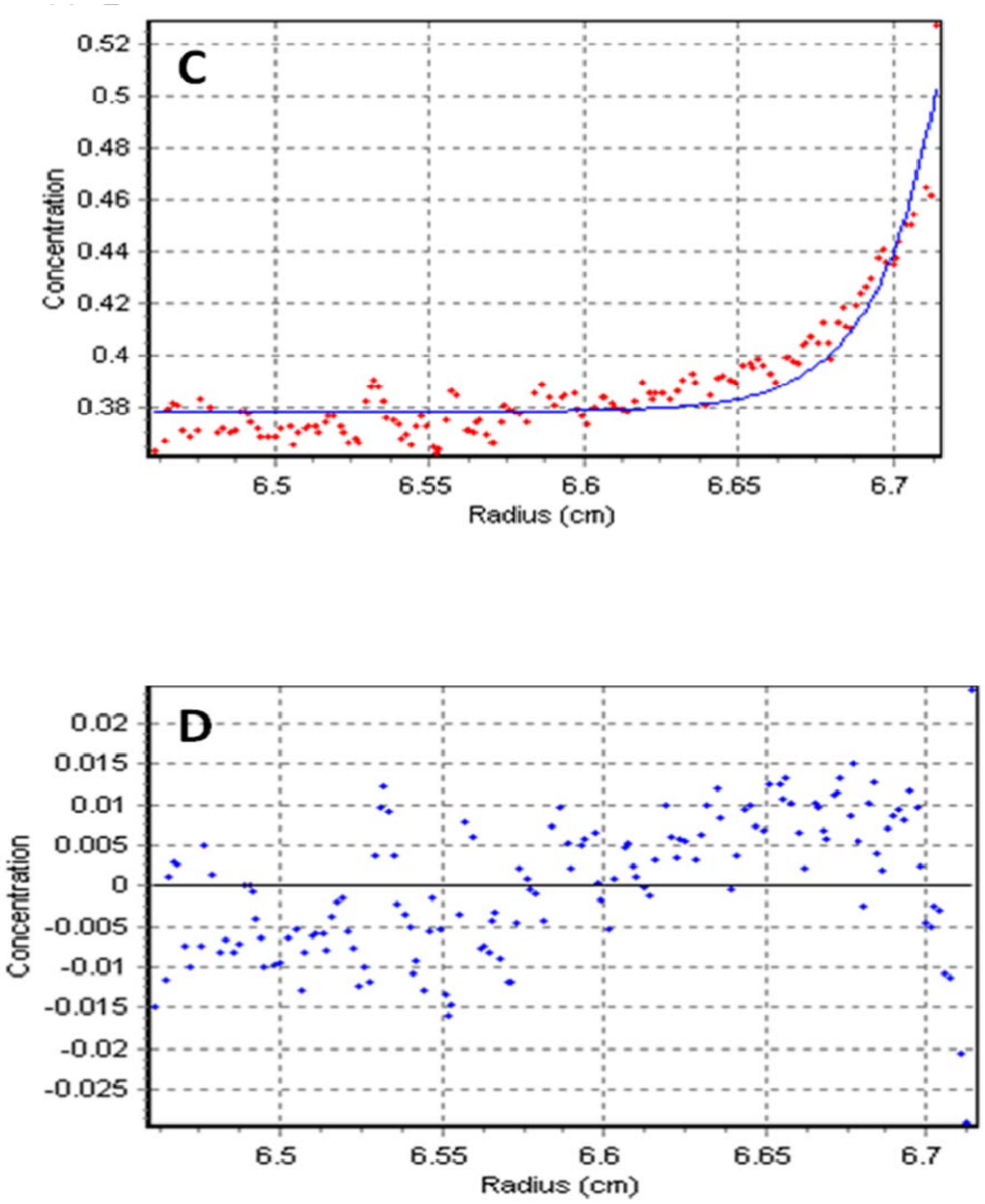

Figure 6. Analytical Ultra Centrifugation data analysis for 58μM YopH gave a molecular mass of 51.8kDa at centrifugation speed of 30000 rpm (A and B) and 40000 rpm (C and D). The molecular mass corresponds to the monomeric YopH. A and C are the fits to the data plots. B and D are plots of the residuals.

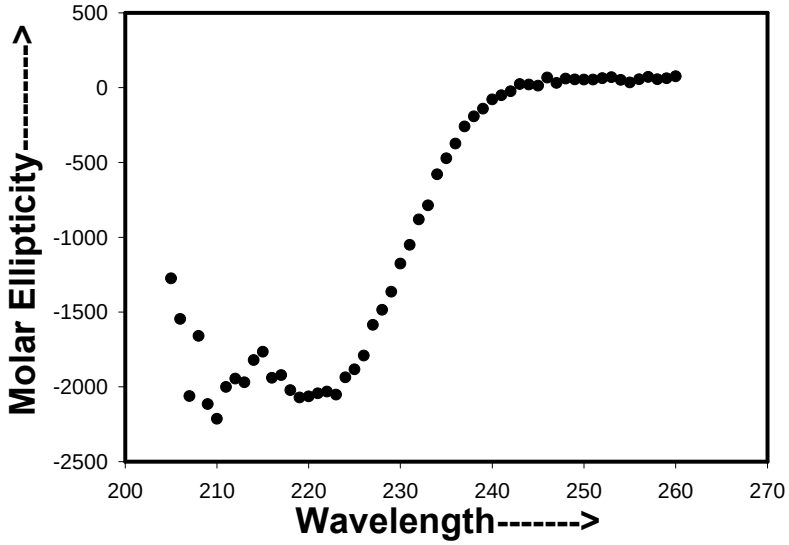
Molar Ellipticity-------->
500
0
-500
-1000
-1500
-2000
-2500
200
210
220
230
240
250
260
270
Wavelength------->
Figure 7. Circular Dichroism data of 35μM YopH-NT dialyzed against a buffer of 25mM Hepes and 50mM NaCl at pH = 7.0.

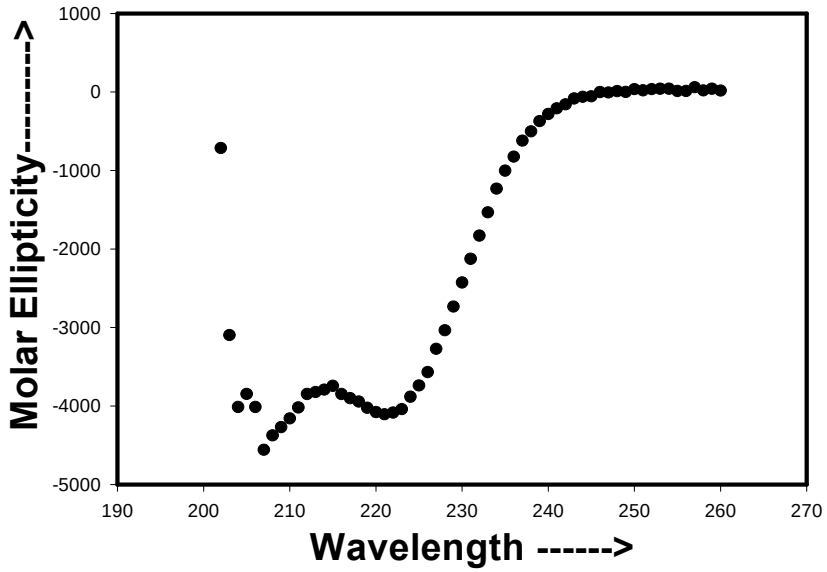

Figure 8. Circular Dichroism data of 35μM YopH-NT subjected to lyophilization after HPLC purification.

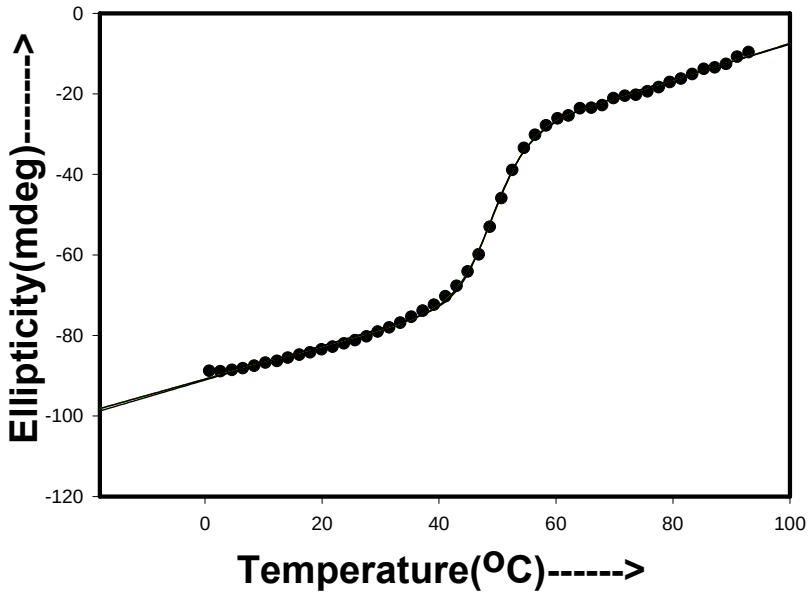

Figure 9. Thermal unfolding curve of YopH-NT fit to eq 3. Thermodynamic parameters obtained from fit are $\Delta H^o = 65.7$ kcal mol^{-1} and $T_m = 49.15$ ^oC.

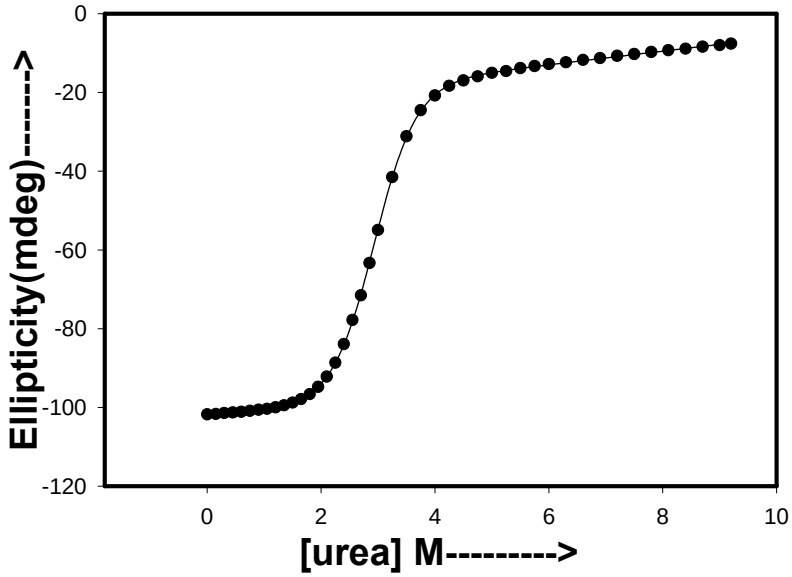

Figure 10. Urea denaturation curve of YopH-NT (20μM) at pH 7.0. The parameters obtained are m = 1.33 kcal mol^{-1} M^{-1} and ΔG = 1.8 kcal/mol.

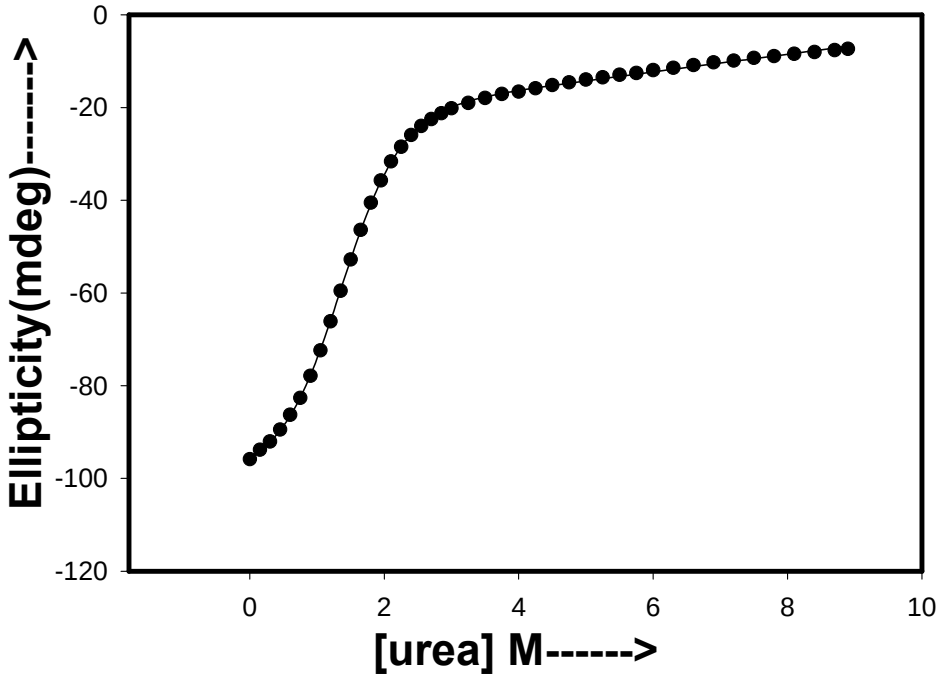

Figure 11. Urea denaturation curve of YopH-NT (19μM) at pH 5.0. The parameters obtained are m = 1.61 kcal mol^{-1} M^{-1} and ΔG = 4.7 kcal/mol.

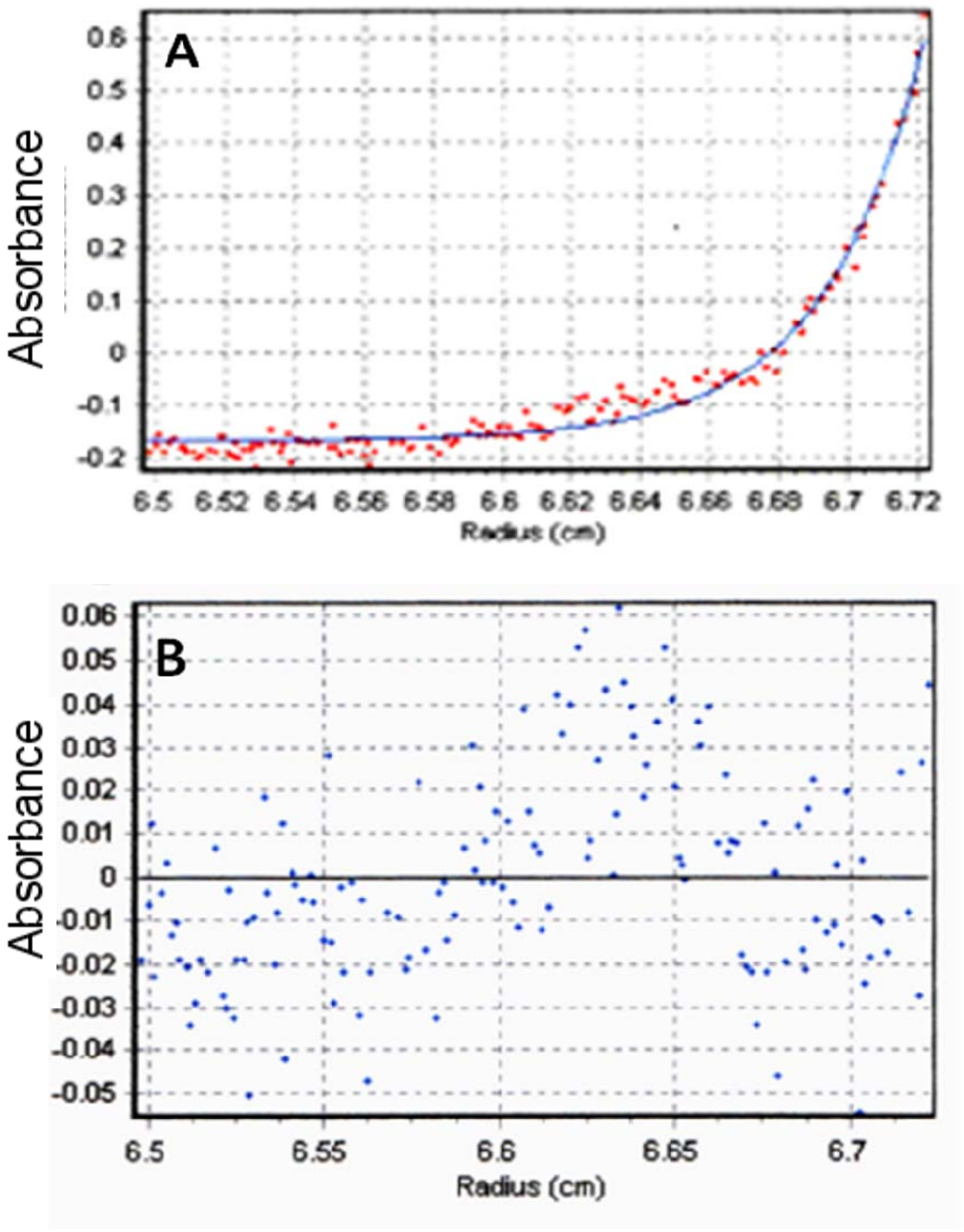

Figure 12. Analytical Ultra Centrifugation data analysis for 100μM YopH-NT gave a molecular mass of 29.9kDa at centrifugation speed of 40000 rpm and pH 5.0. The molecular mass corresponds to the dimeric state of YopH-NT. A is the fit to the data plot. B is a plot of the residual.

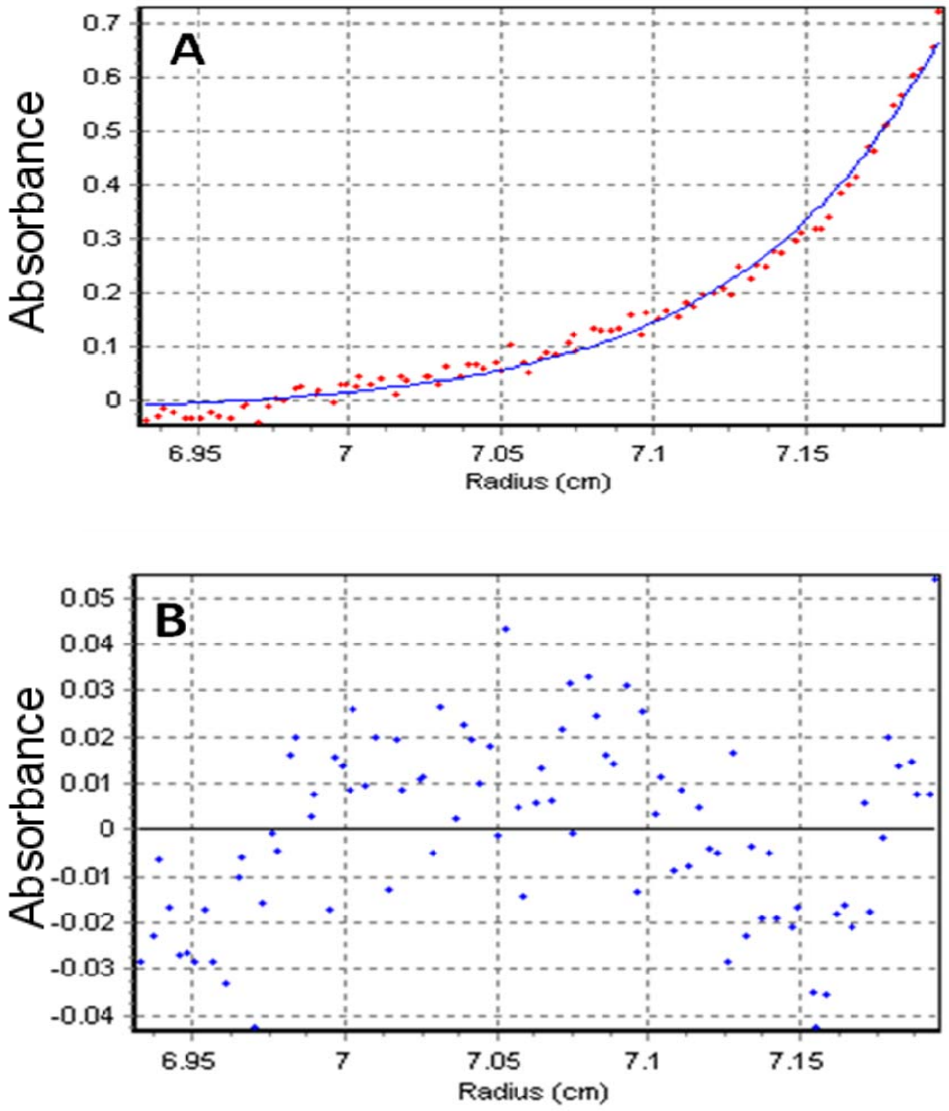

Figure 13. Analytical Ultra Centrifugation data analysis for 162μM YopH-NT gave a molecular mass of 29.7kDa at centrifugation speed of 30000 rpm and pH 5.0. The molecular mass shows the tendency of YopH-NT to dimerize. A is the fit to the data plot. B is a plot of the residual.

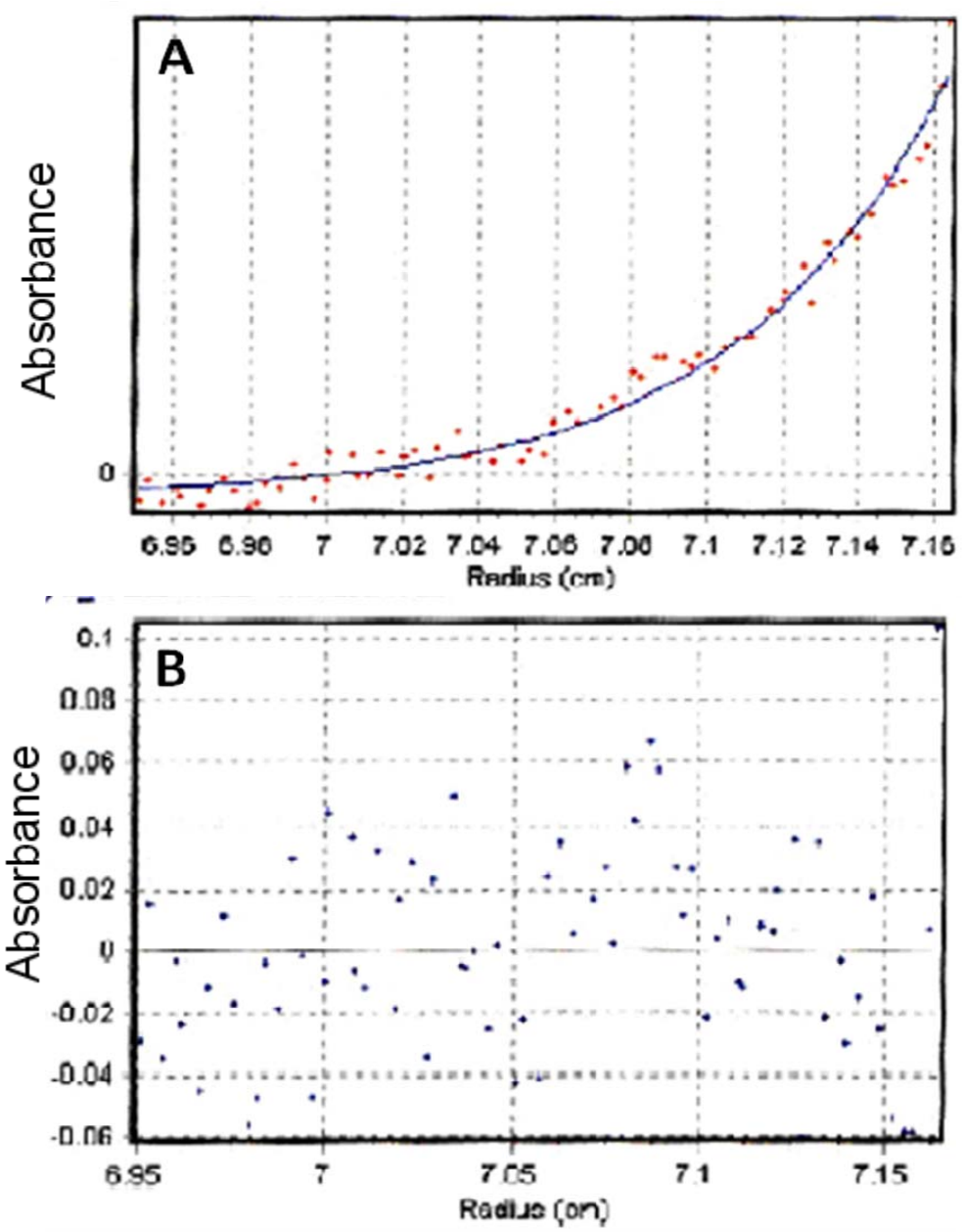

Figure 14. Analytical Ultra Centrifugation data analysis for 200μM YopH-NT gave a molecular mass of 23.4kDa at centrifugation speed of 30000 rpm and pH 8.0. The molecular mass shows that YopH-NT exists as a dimer. A is the fit to the data plot. B is a plot of the residual.

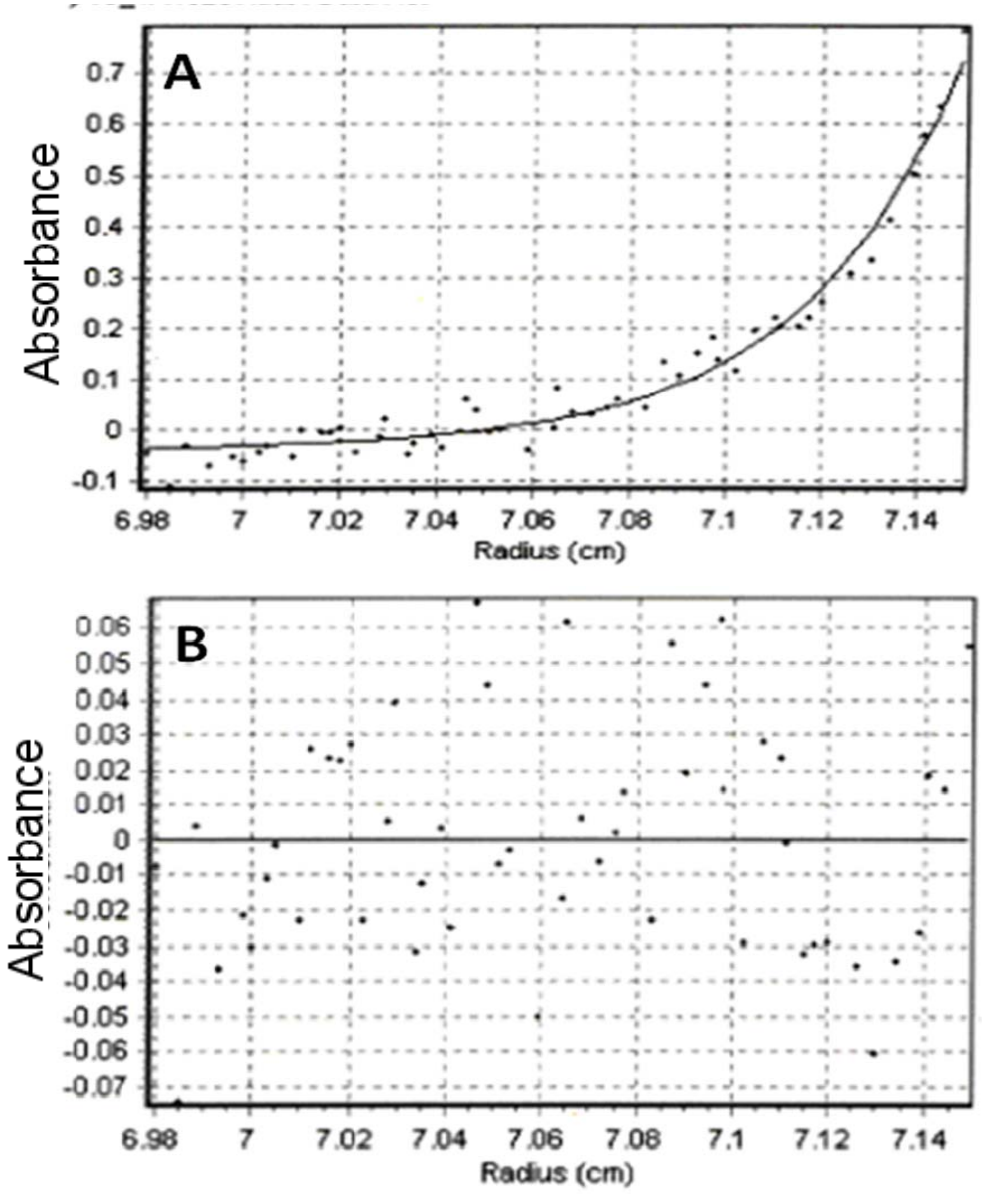

Figure 15. Analytical Ultra Centrifugation data analysis for 200μM YopH-NT gave a molecular mass of 21.8kDa at centrifugation speed of 40000 rpm and pH 8.0. The molecular mass shows that YopH-NT has a tendency to dimerize. A is the fit to the data plot. B is a plot of the residual.

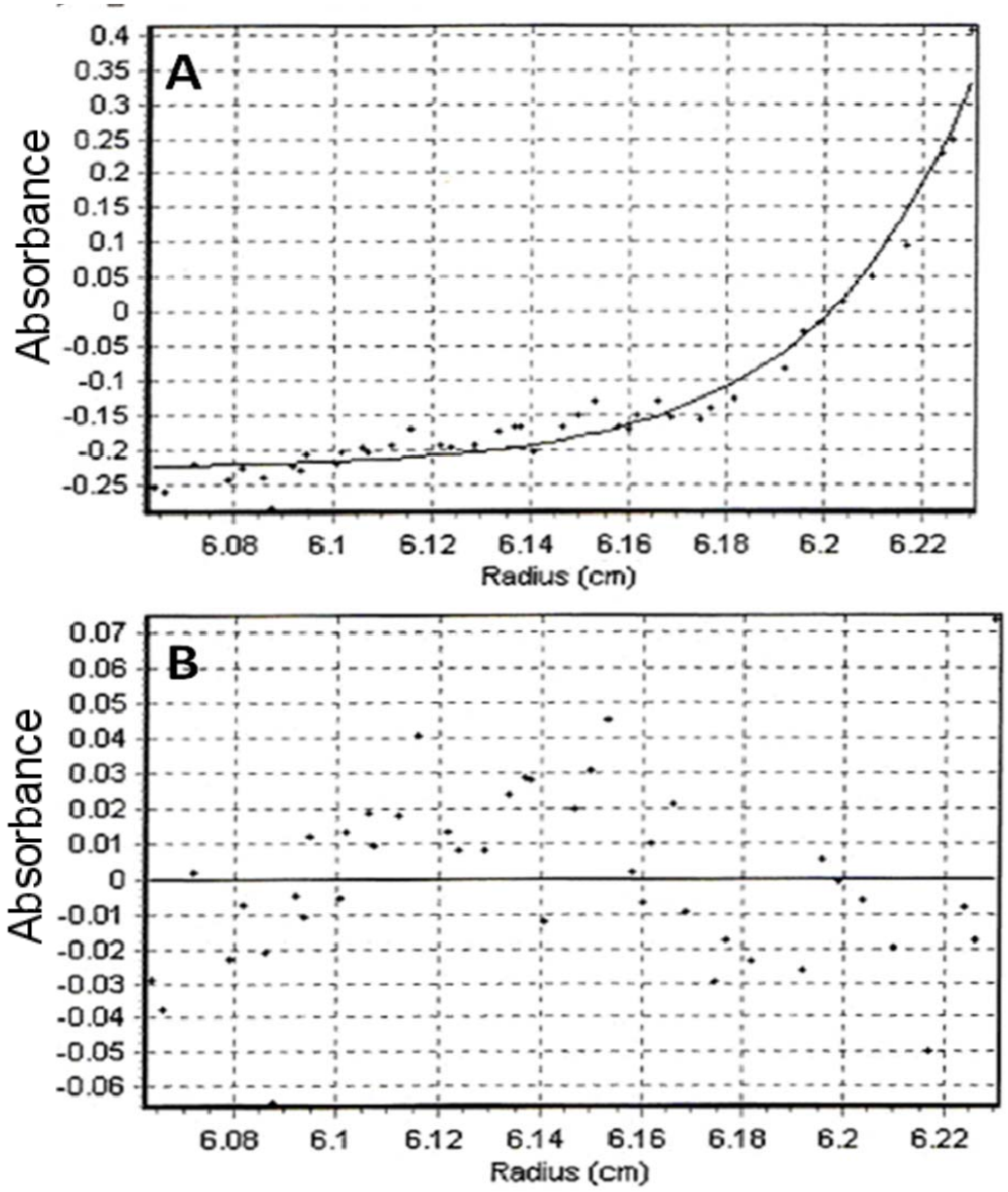

Figure 16. Analytical Ultra Centrifugation data analysis for 50μM YopH-NT gave a molecular mass of 26.7kDa at centrifugation speed of 40000 rpm and pH 8.0. The molecular mass shows that YopH-NT exists as a dimer. A is the fit to the data plot. B is a plot of the residual.

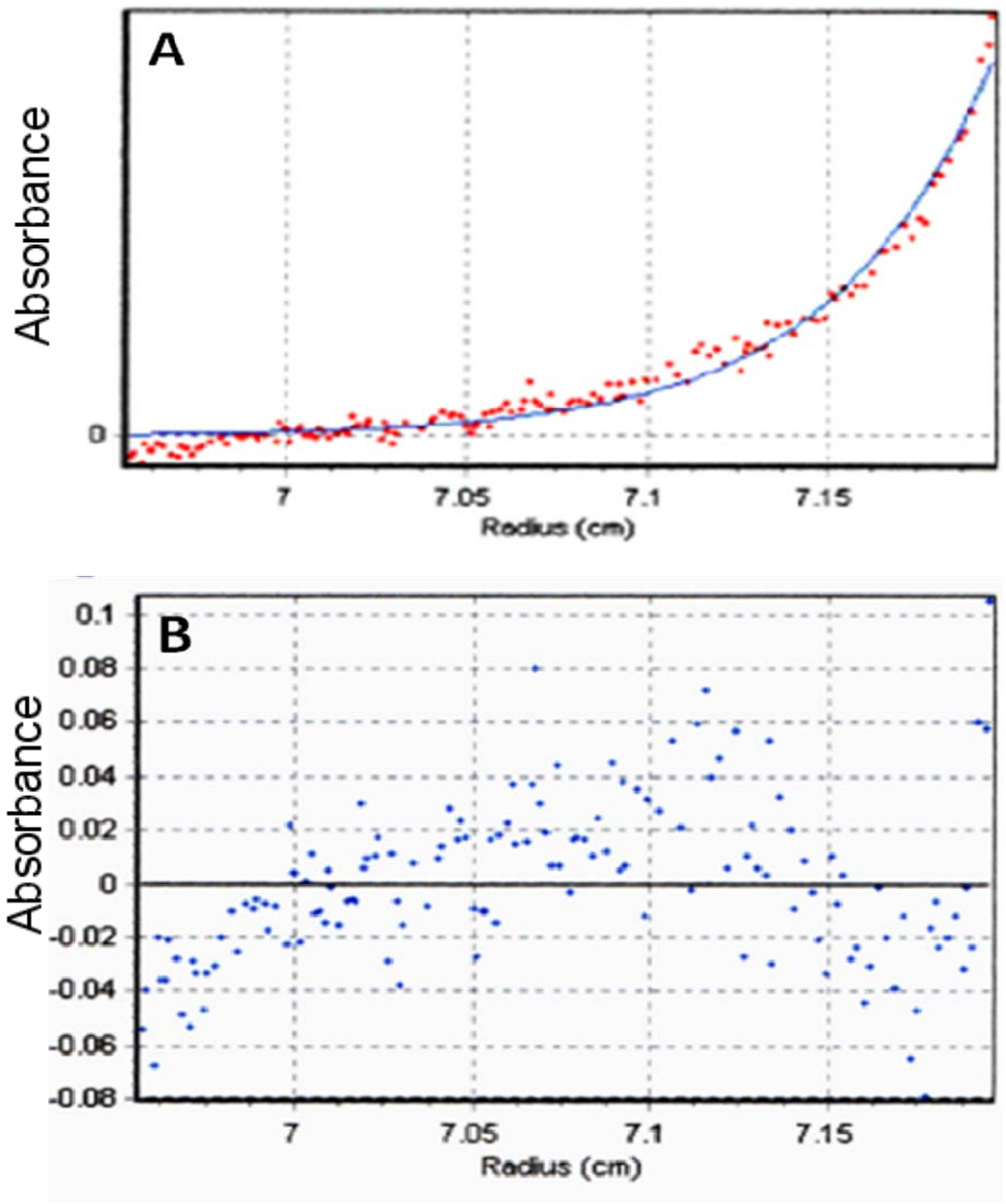

Figure 17. Analytical Ultra Centrifugation data analysis for 100μM YopH-NT gave a molecular mass of 24.2kDa at centrifugation speed of 35000 rpm and pH 5.0. The molecular mass corresponds to the dimeric state of YopH-NT. A is the fit to the data plot. B is a plot of the residual.

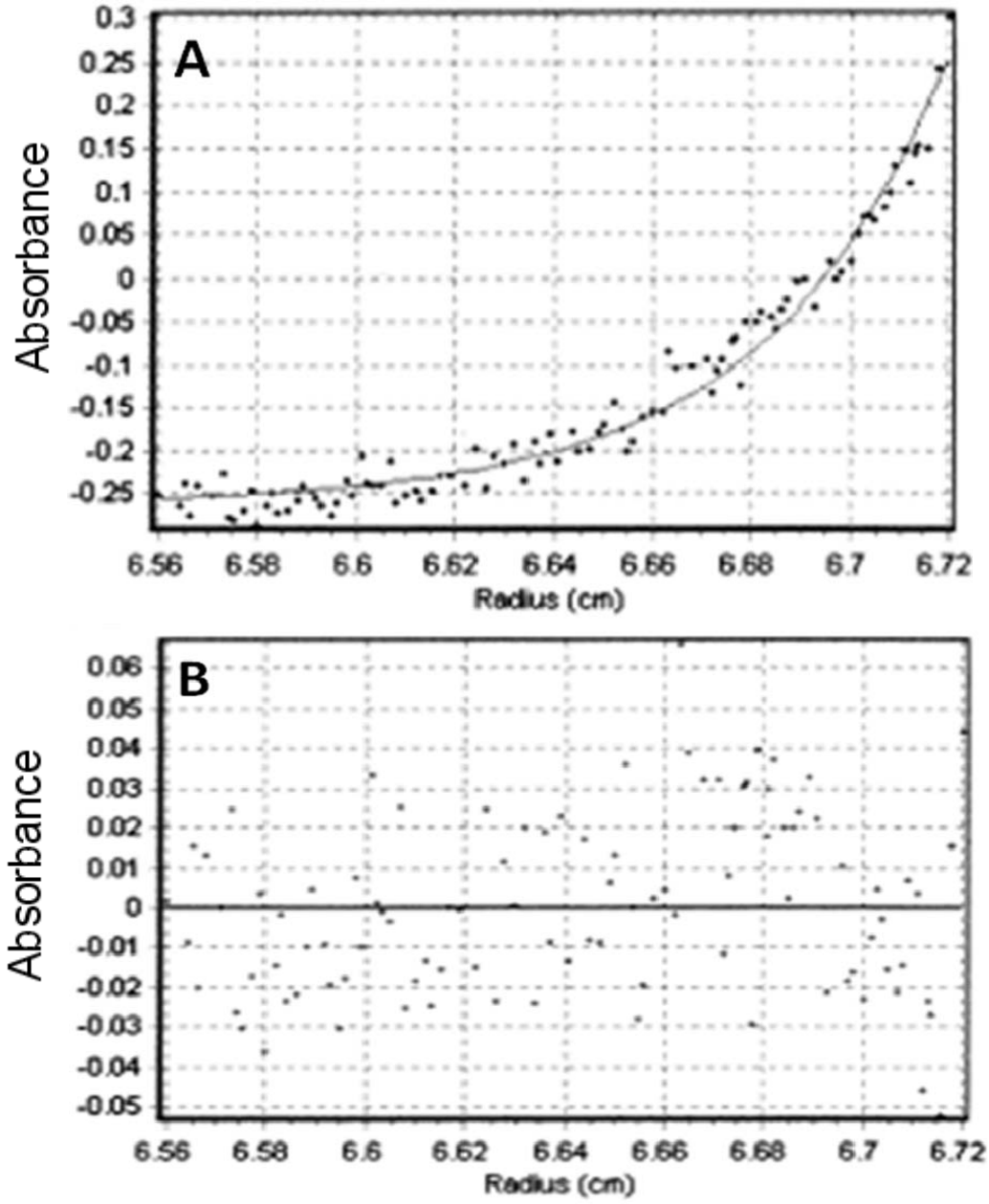

Figure 18. Analytical Ultra Centrifugation data analysis for 100μM YopH-NT gave a molecular mass of 26.1kDa at centrifugation speed of 35000 rpm and pH 5.7. The molecular mass corresponds to a YopH-NT dimer. A is the fit to the data plot. B is a plot of the residual.

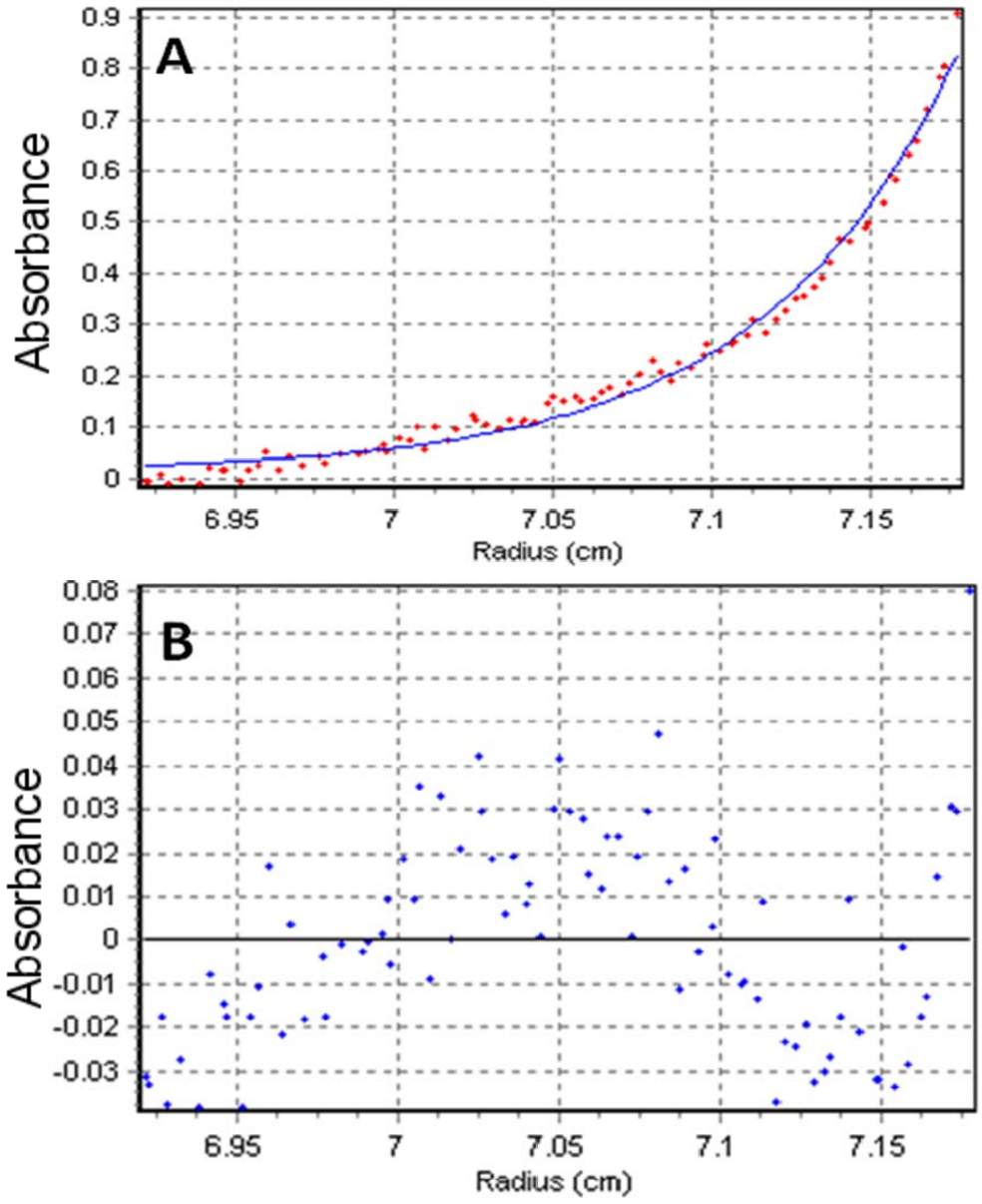

Figure 19. Analytical Ultra Centrifugation data analysis for 177μM YopH-NT gave a molecular mass of 22.2kDa at centrifugation speed of 30000 rpm and pH 5.7. The molecular mass shows the tendency of YopH-NT to dimerize. A is the fit to the data plot. B is a plot of the residual.

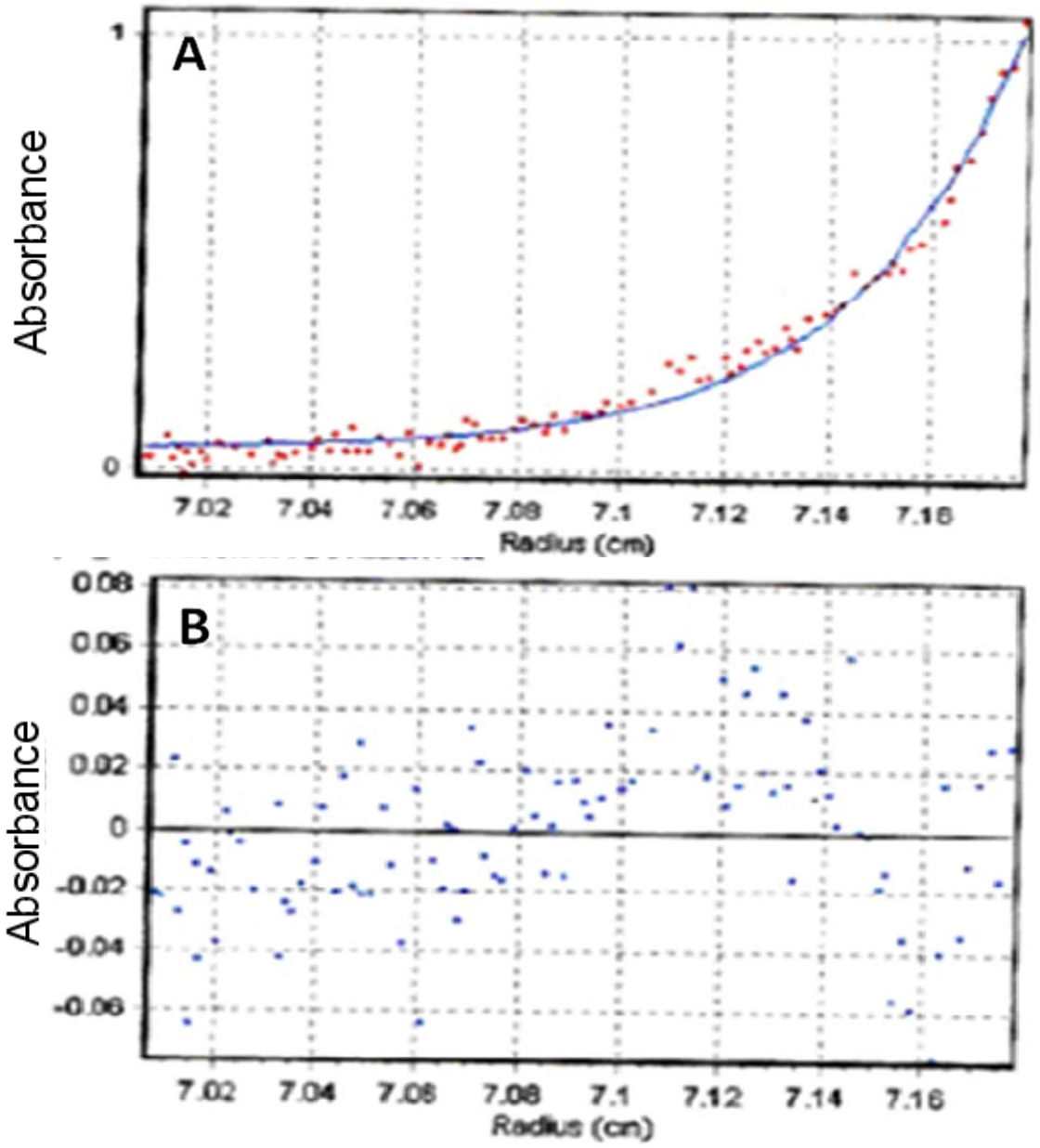

Figure 20. Analytical Ultra Centrifugation data analysis for 177μM YopH-NT gave a molecular mass of 32.9kDa at centrifugation speed of 35000 rpm and pH 5.7. The molecular mass shows that YopH-NT exists as a dimer. A is the fit to the data plot. B is a plot of the residual.

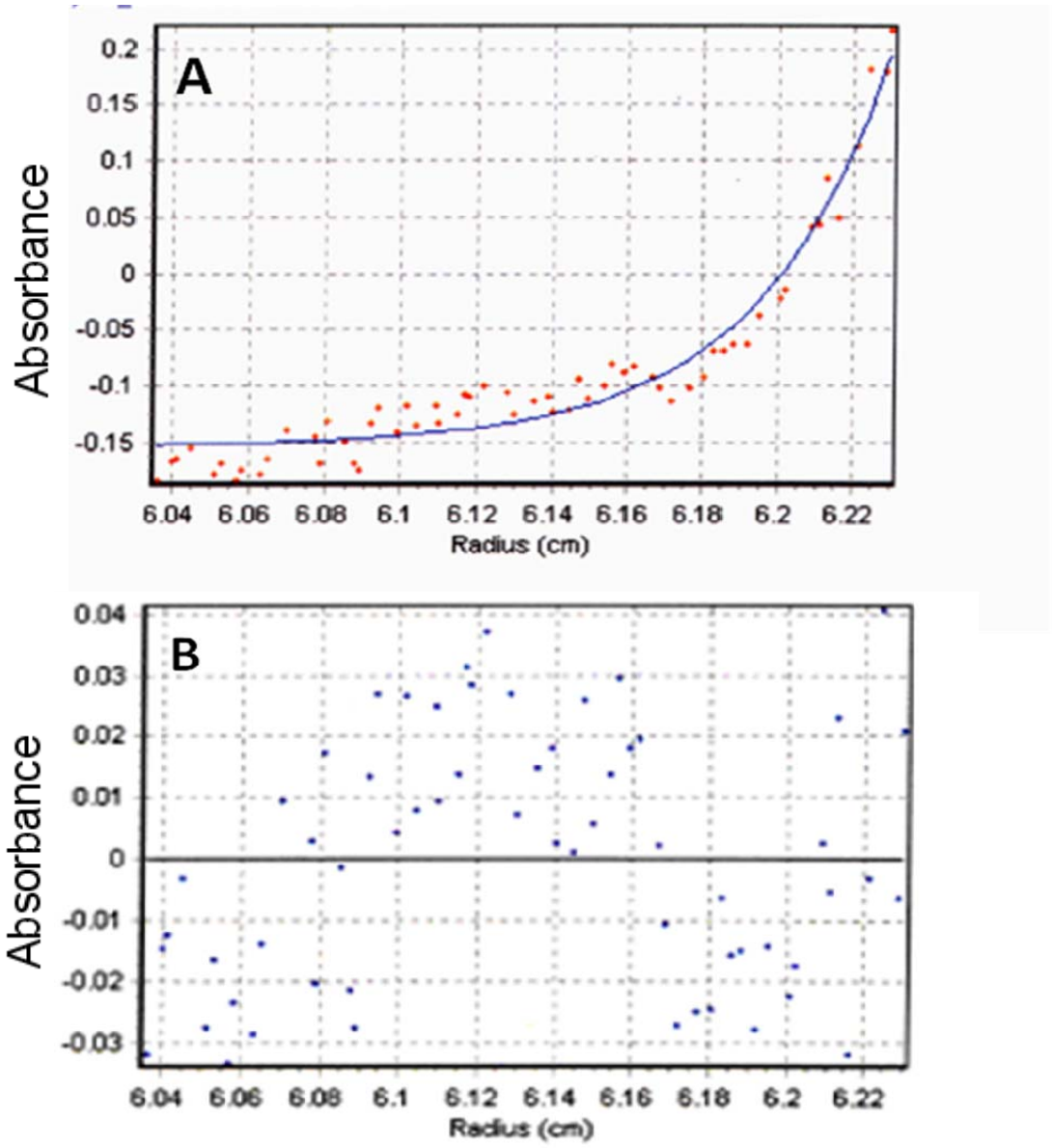

Figure 21. Analytical Ultra Centrifugation data analysis for 50μM YopH-NT gave a molecular mass of 27.1kDa at centrifugation speed of 40000 rpm and pH 5.7. The molecular mass shows that YopH-NT exists as a dimer. A is the fit to the data plot. B is a plot of the residual.

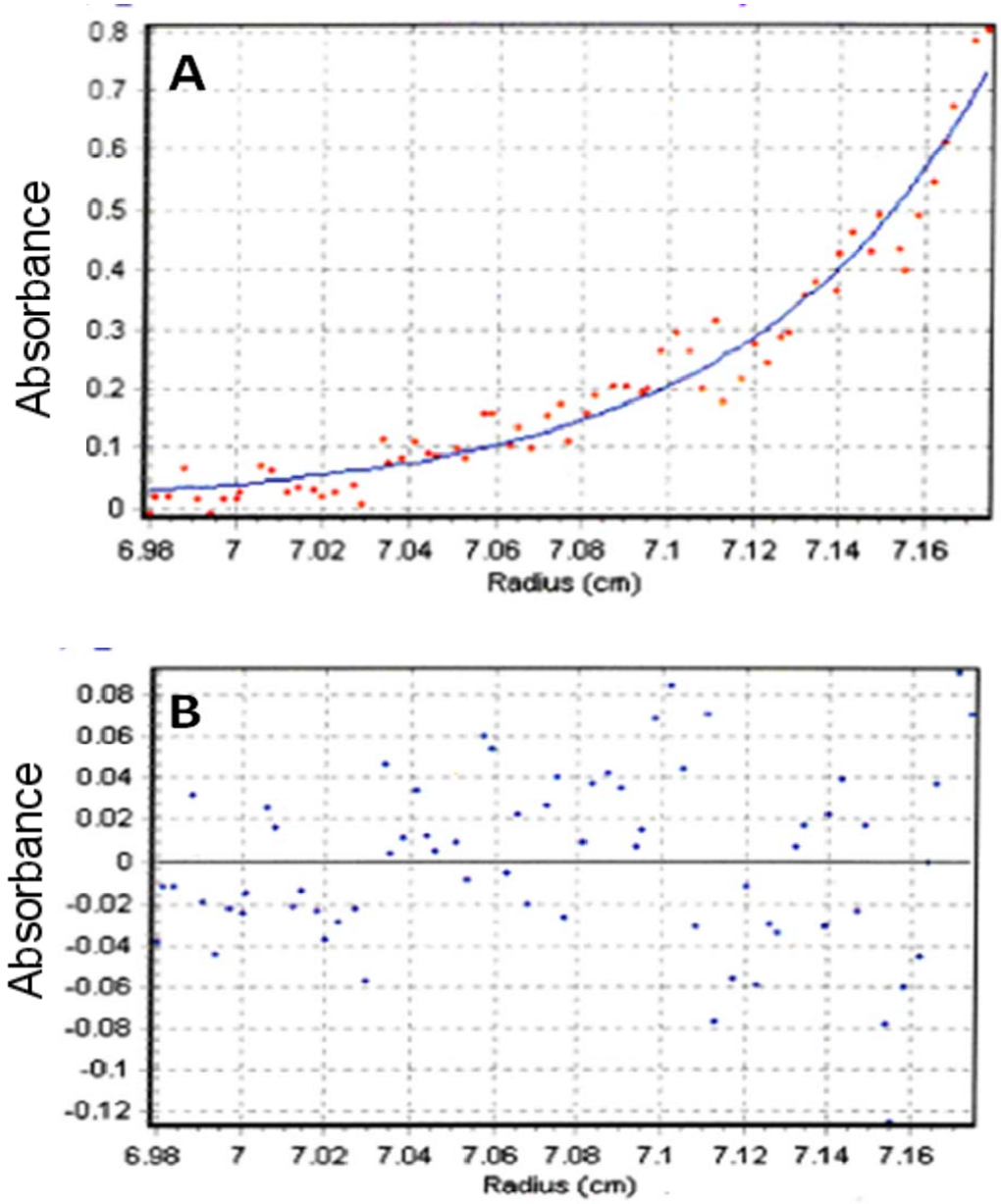

Figure 22. Analytical Ultra Centrifugation data analysis for 200μM YopH-NT gave a molecular mass of 24.1kDa at centrifugation speed of 30000 rpm and pH 7.0. The molecular mass shows that YopH-NT exists as a dimer. A is the fit to the data plot. B is a plot of the residual.

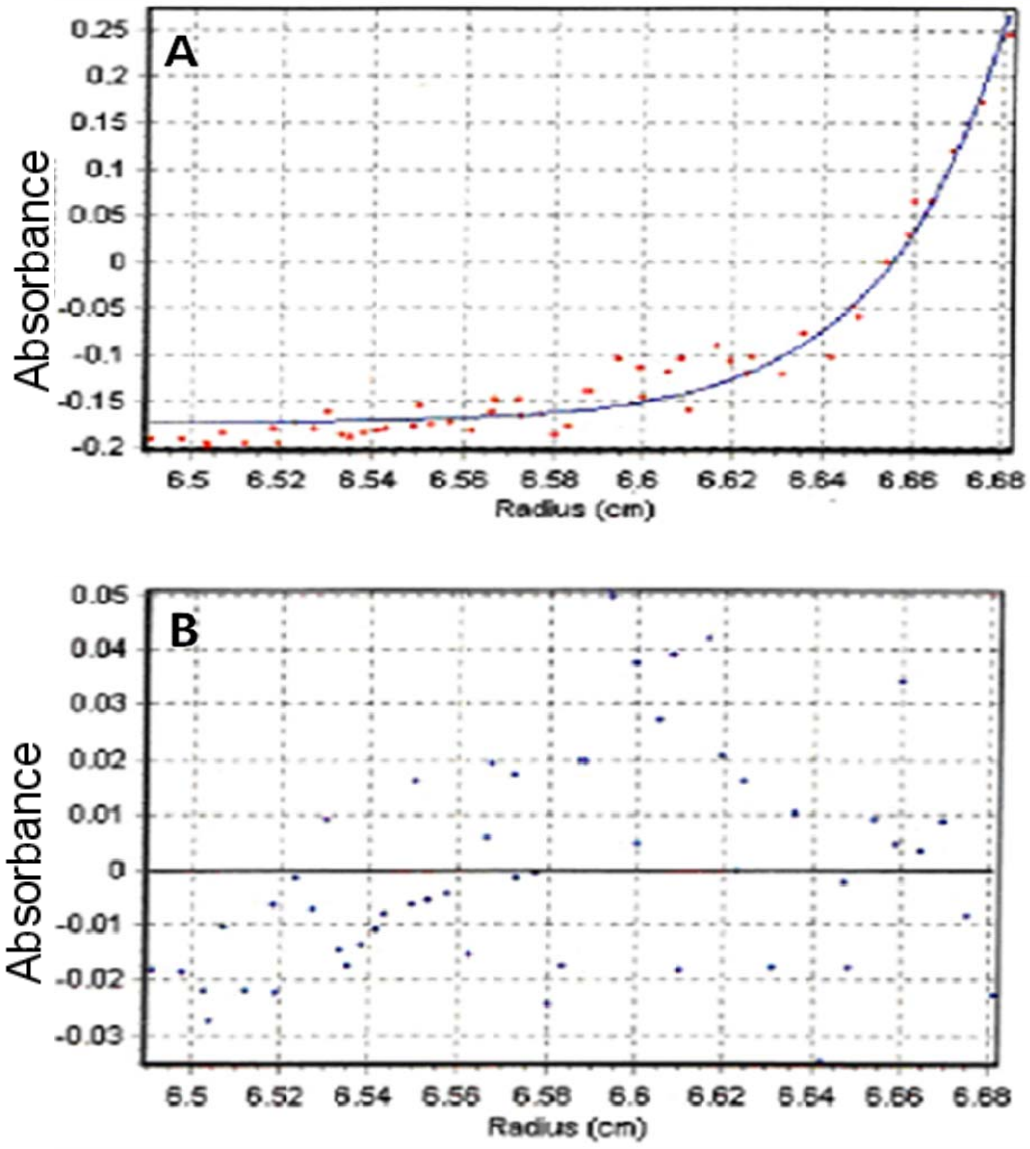

Figure 23. Analytical Ultra Centrifugation data analysis for 100μM YopH-NT gave a molecular mass of 28.8kDa at centrifugation speed of 40000 rpm and pH 8.0. The molecular mass shows that YopH-NT exists as a dimer. A is the fit to the data plot. B is a plot of the residual.

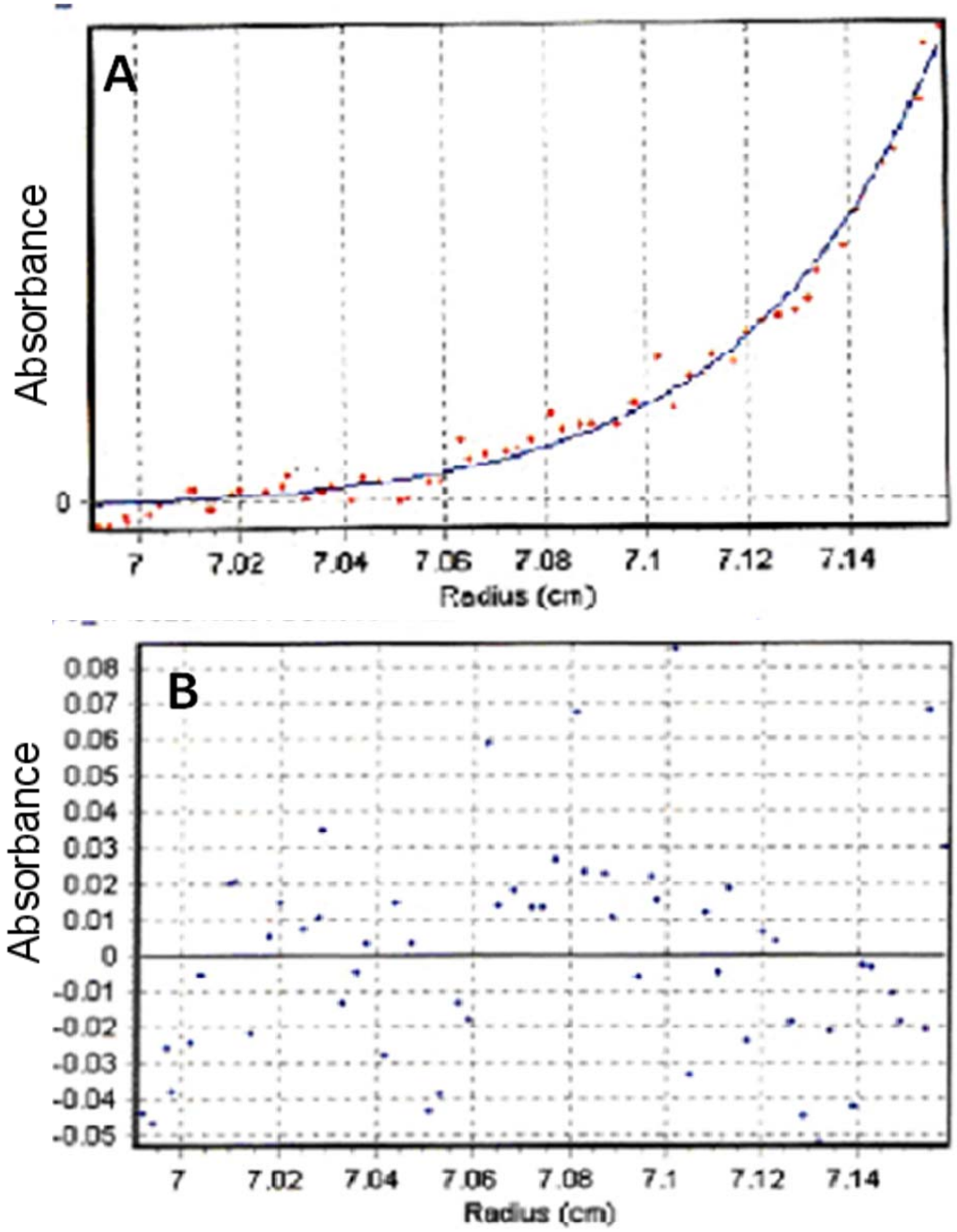

Figure 24. Analytical Ultra Centrifugation data analysis for 200μM YopH-NT gave a molecular mass of 25.3kDa at centrifugation speed of 35000 rpm and pH 8.0. The molecular mass shows that YopH-NT exists as a dimer. A is the fit to the data plot. B is a plot of the residual.

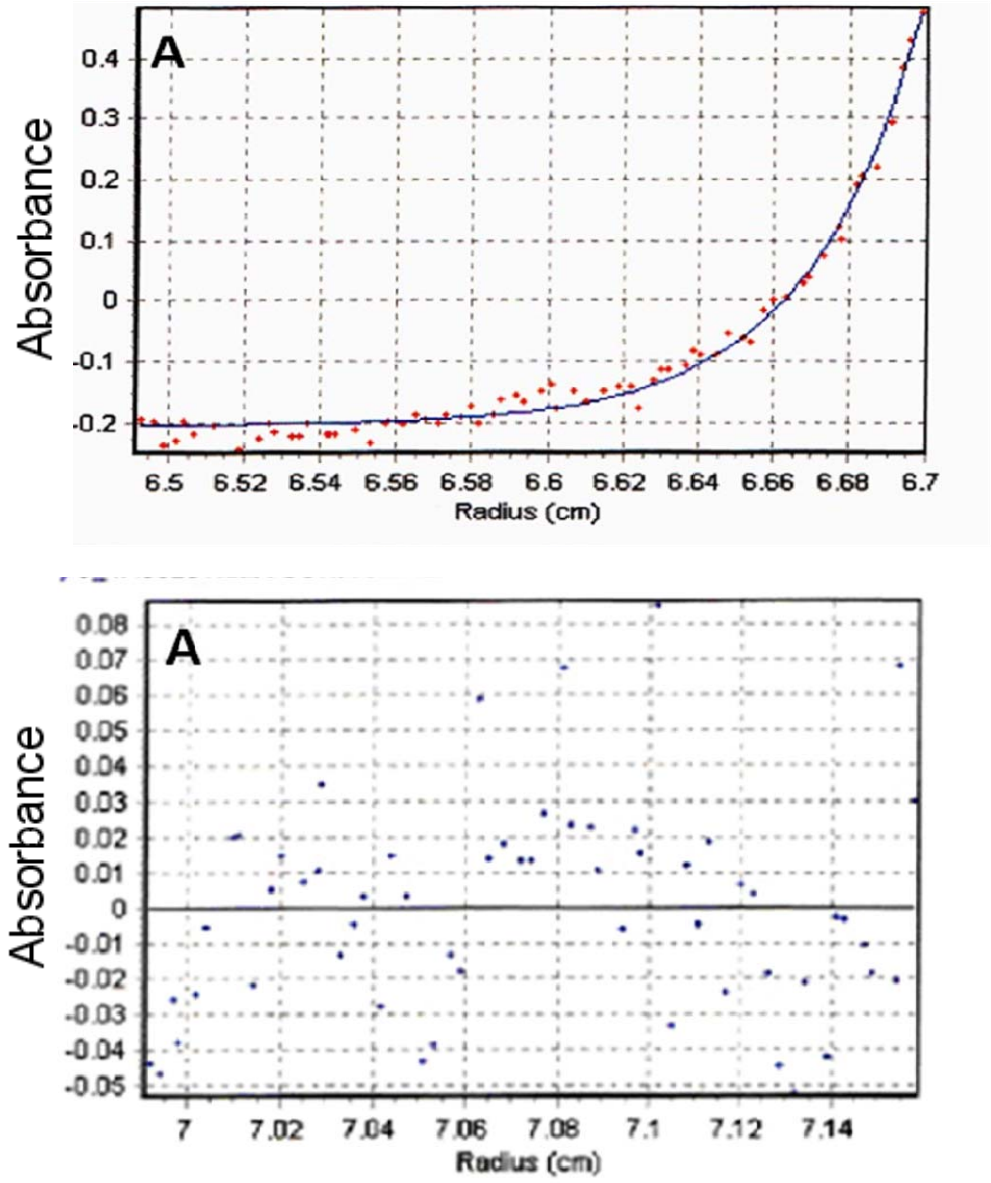

Figure 25. Analytical Ultra Centrifugation data analysis for 100μM YopH-NT gave a molecular mass of 33.9kDa at centrifugation speed of 35000 rpm and pH 8.0. The molecular mass shows that YopH-NT exists as a dimer. A is the fit to the data plot. B is a plot of the residual.

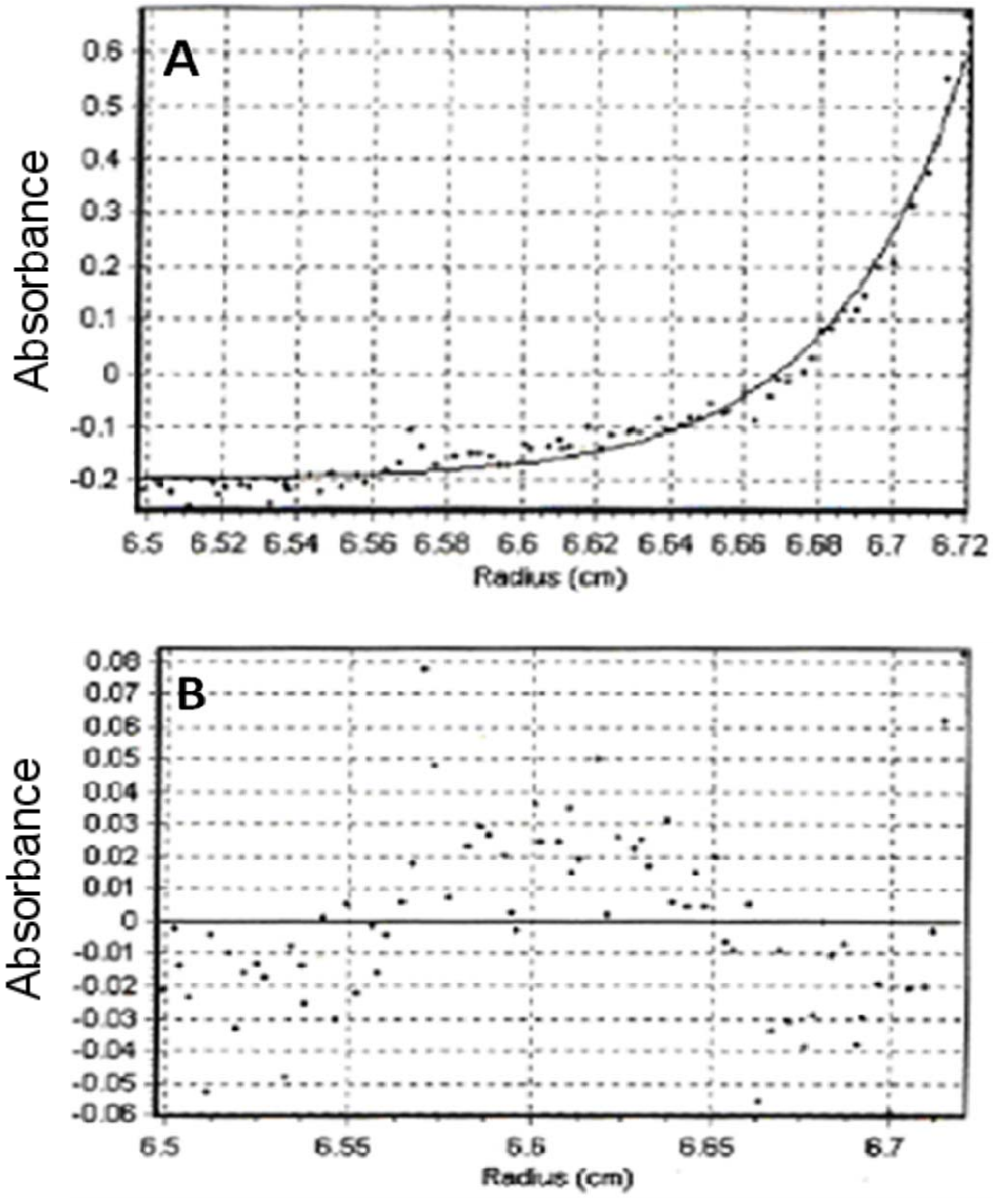

Figure 26. Analytical Ultra Centrifugation data analysis for 100μM YopH-NT gave a molecular mass of 38.5kDa at centrifugation speed of 30000 rpm and pH 8.0. The molecular mass shows that YopH-NT exists as a dimer. A is the fit to the data plot. B is a plot of the residual.

4.6 Tables

Table 1. Expression conditions of N-terminal domain of YopH.

Serial #	Growth			Induction			Yield
	Temperature	***Time***	***OD reached***	***Temperature***	***Time***	***Reagents***	***mg/L***
A	37^{o}C	3.5hrs	1.2	37^{o}C	3hrs	3% EtOH + 0.5mM PTG	55
B	37^{o}C	3.5hrs	1.2	37^{o}C	3hrs	1mM IPTG	130
C	37^{o}C	3.5hrs	1.1	25^{o}C	O/N	3%EtOH + 0.5mM IPTG	100
D	37^{o}C	3.5hrs	1	25^{o}C	O/N	0.1mM IPTG	70

Table 2. Analytical Ultracentrifugation Data for the N-terminal domain of YopH at pH 7.0 using different rotor speeds and protein concentrations (σ is defined by eq. 6). Molecular weight was obtained from the best fit to a single species model.

pH	Speed(rpm)	Conc. (μM)	Mol.wt.(kDa)	σ (cm^{-2})
7	30000	100	28.7	3.081
		200	25.8	2.762
	35000	50	21.2	2.759
		100	39.2	5.099
		200	42.1	5.476
	40000	50	27.1	4.599
		100	37.9	6.313
		200	25.2	4.273

Table 3. Analytical Ultracentrifugation Data collected on the N-terminal domain of YopH at pH 8.0 using different rotor speeds and protein concentrations (σ is defined by eq. 6). Molecular weight was obtained from the best fit to a single species model.

pH	Speed(rpm)	Conc. (μM)	Mol.wt.(kDa)	σ (cm^{-2})
8	30000	100	38.5	4.128
		200	23.4	2.511
	35000	100	33.9	4.943
		200	25.3	3.689
	40000	50	26.7	5.095
		100	28.8	5.491
		200	21.9	4.168

Chapter 5. Residue-specific structural information on the folding of Amylin using 2D IR spectroscopy

5.1. Introduction

Aggregation of proteins and peptides into amyloid fibrils is involved in more than thirty different diseases. The prefibrillar and fibrillar species formed in this process have been shown to cause the disruption of different cellular pathways (Harrison et al. 2007). The final fibrillar structure formed is so stable that once amyloidogenesis is triggered, the pathway for the formation of these amyloid fibrils takes the preferred direction. These amyloid fibrils, irrespective of the protein or peptide involved, have β-strands arranged in parallel or anti-parallel direction to form β-sheets. The techniques that are available to get any structural information about these aggregates are, primarily, CD and NMR. Time dependent CD shows that unfolded monomers of Amylin, during the process of aggregation, form a α-helical intermediate, which over the course of time adopts a β-sheet morphology characteristic of the fibrils (Williamson and Miranker 2007, Abedini and Raleigh unpublished). Repeated attempts to crystallize fibrils have not been fruitful to date. Thus, solid state NMR spectroscopy was employed to decipher the structure of the final aggregated state of Amylin and Aβ (Luca et al. 2007). However, NMR

spectroscopy does not have the appropriate time resolution to obtain any structural details about the intermediate species. Hence, two-dimensional infrared spectroscopy was applied to get residue specific information on the folding of Amylin to β-sheet fibrils from unstructured monomers. 2D IR spectroscopy has an intrinsic time resolution of a few picoseconds but the conventional methods of collecting 2D IR spectrum may take from minutes to hours. These methods make 2D IR unsuitable for application to the study of amyloidogenesis. Recently, Prof. Martin Zanni's lab, at University of Wisconsin, developed a rapid scan method for collecting 2D IR spectra using a pulse sharper that automates data collection (Shim et al. 2007). This advancement can reduce the time needed for collecting a 2D IR spectrum to less than one minute. This allowed the application of advanced 2D IR for studying the folding of Amylin into amyloid fibrils. We established a collaboration with Prof. Zanni to study amyloid formation by Amylin using ^{13}C ^{18}O labeled Amylin. The incorporation of ^{13}C ^{18}O labels allows residue specific resolution. I have prepared a set of labeled Amylin peptides in this chapter. I describe their synthesis and purification. ^{13}C ^{18}O labeled amino acids were incorporated at specific sites in Amylin and residue specific information during folding was obtained by collecting continuous 2D IR spectra (Fig. 1).

5.2 Methods and Materials

5.2.1 Protein Synthesis and Purification

Wild type human IAPP (hIAPP) (Fig. 2) and all its site-specific labeled variants were synthesized on a 0.25mmol scale using 9-fluornylmethoxycarbonyl (Fmoc) chemistry on an Applied Biosystems 433A Peptide Synthesizer. 5-(4'-Fmoc-

aminomethyl-3',5-dimethoxyphenol) valeric acid (PAL-PEG) resin was used to generate an amidated C-terminus. Pseudoproline dipeptide derivatives were employed as described (Abedini and Raleigh 2005). Fmoc-protected pseudoproline (oxazolidine) dipeptide derivatives were purchased from Novabiochem. Fmoc protected $^{13}C^{18}O$ labeled amino acids were prepared in house by Jim Marecek All other reagents were purchased from Advanced Chemtech, Fischer Scientific, PE Biosystems and Sigma Aldrich. All solvents used were of A.C.S. grade. Standard Fmoc reaction cycles were used. The first residue added to the resin, pseudoproline dipeptide derivatives, all β-branched residues and all residues following the β-branched residue were double coupled. The peptide was cleaved from the resin using standard trifluoroacetic acid (TFA) methods. The crude peptide was treated with 20% (v/v) acetic acid and lyophilized. The disulfide bond was formed via DMSO induced oxidation of the crude peptide. The oxidized peptide was purified via reverse-phase HPLC using a Vydac C-18 preparative column. A two-buffer system utilizing HCl as an ion-pairing agent was used for the purification. Buffer A consisted of 0.045% (v/v) HCl in distilled de-ionized (DDI) water. Buffer B consisted of 80% (v/v) acetonitrile, 20% (v/v) DDI water and 0.045% (v/v) HCl. The purity of the peptides was checked by HPLC and was 97-99%.

The purified peptides were analyzed by matrix-assisted laser desorption/ionization time-of-flight (MALDI-TOF) mass spectroscopy.

5.3 Results

Thioflavin-T monitored kinetics of Amylin aggregation is associated with a lag phase needed for nucleation followed by a rapid growth phase involving the rapid growth

of fibrils (Goldsbury et al. 2000). Amyloid formation by Amylin is believed to involve a helical intermediate probably initiated by the loop present between residues C2 and C7. Thus the first position of choice for labeling was Ala13, which is reasonably away from the loop region. The HPLC traces for purification of Ala13 and MALDI-TOF and analytical HPLC trace of the purified peptide are shown in Fig. 3. 2D IR data collected in Prof. Zanni's lab shows that Ala13 folds slightly slower than the β-sheet (Fig. 4). The next labeled position was Ala8 (Fig. 5), which follows the disulfide bond formed at position 7. 2D IR data showed comparable rates of folding for Ala8 as observed for Ala13 (Fig. 6). $^{13}C^{18}O$ labeled Ala was also incorporated at position 5 (Fig. 7) which is at the center of the loop formed by C2, C7 disulfide bond.

Recently published, solid-state NMR structure of Amylin fibrils showed that residues 18-27 form a β-turn in the final amyloid structure (Luca et al. 2007). However, earlier studies had postulated that residues 22-29 adopt β-sheet structure in the fibrils. Isotope labeled Ala was thus incorporated at position 25 (Fig. 8) to understand this discrepancy. Ala25 kinetics monitored by 2D IR by our collaborators show that Ala25 folds faster than the other β-sheet region (Fig. 6). Ala25 shows a broad random coil feature at 1648cm^{-1} and a narrow feature at 1660cm^{-1}. This later feature however decayed with time and showed no existence in the amyloid fibrils (Fig. 9). Thus it is probable that Ala25 might be involved in β-sheet initiation but exists in β-turn in the final fibrillar structure. Similar kinetics of folding was observed when the labeled amino acid was incorporated at Leu27 (Fig. 10). 2D IR experiments on Val17 (Fig. 11) labeled hIAPP showed the fastest rate of β-sheet formation amongst all labeled positions. The ^{13}C ^{18}O labeled amino acid incorporated at position 32 (Fig. 12) showed the slowest folding

kinetics (Fig. 6). Data sets of 2D IR spectroscopy when put together suggest a new model of folding of Amylin monomers into β-sheet fibrils (Fig. 13). The results suggest that initial nucleation event might involve Val17-Ala25 fragment for initiation of β-sheet structure. The fibrillization then proceeds through a zipper mechanism to incorporate the fragment including Ala13 into the β-sheet domain. The β-sheet then extends further to include Ala8. Both C-terminal and N-terminal domain remain flexible in the intial intermediates of fibrillization. Fragment involving Val 32 finally gets incooporated into the β-sheet structure as the fibrils undergo maturation.

5.4 Discussion

The incorporation of $^{13}C^{18}O$ labeled amino acid in the peptide chain is the least perturbing modification. Selectively changing the vibrational frequency of the bonds in one amino acid can give residue specific structural information in 2D IR spectroscopy. Improvement in the time resolution by new methods developed at University of Wisconsin allowed for the use of 2D IR spectroscopy in studying amyloidogenesis of Amylin. In the studies outlined here, labeled hIAPP peptides with $^{13}C^{18}O$ amino acids incorporated at specific positions were synthesized, purified and characterized. Each of the labeled peptides was then subjected to 2D IR studies in Prof. Zanni's lab. The IR frequency of labeled amino acid was shifted away from the unlabelled features. Appearance of cross peaks with random-coil or β-sheet structure gave time dependent information of the labeled position during the course of fibrillization reaction. Site-specific structural details presented a zipper mechanism for conversion of Amylin monomers into amyloid fibrils. Residues 17-27 initiated the β-sheet formation, which

then extended towards the N-terminus to include the fragment containing Ala13 and Ala8. The kinetics shows that the fragment containing Val32 gets incorporated into β-sheet at a rate slower than observed for other fragments. The results outlined here give detailed mechanistic insight into the process of aggregation of Amylin. These results highlight the crucial fragments involved in the initiation of fibrillization process. This fragment can be a critical target for designing of effective inhibitors against amyloidogenesis. The site-specific information for progression of monomers into protofibrillar species can give insight into structural features of the intermediate species. These can be used as epitopes for vaccine development or for developing inhibitors that will help in preventing further fibrillization.

5.5 Figures

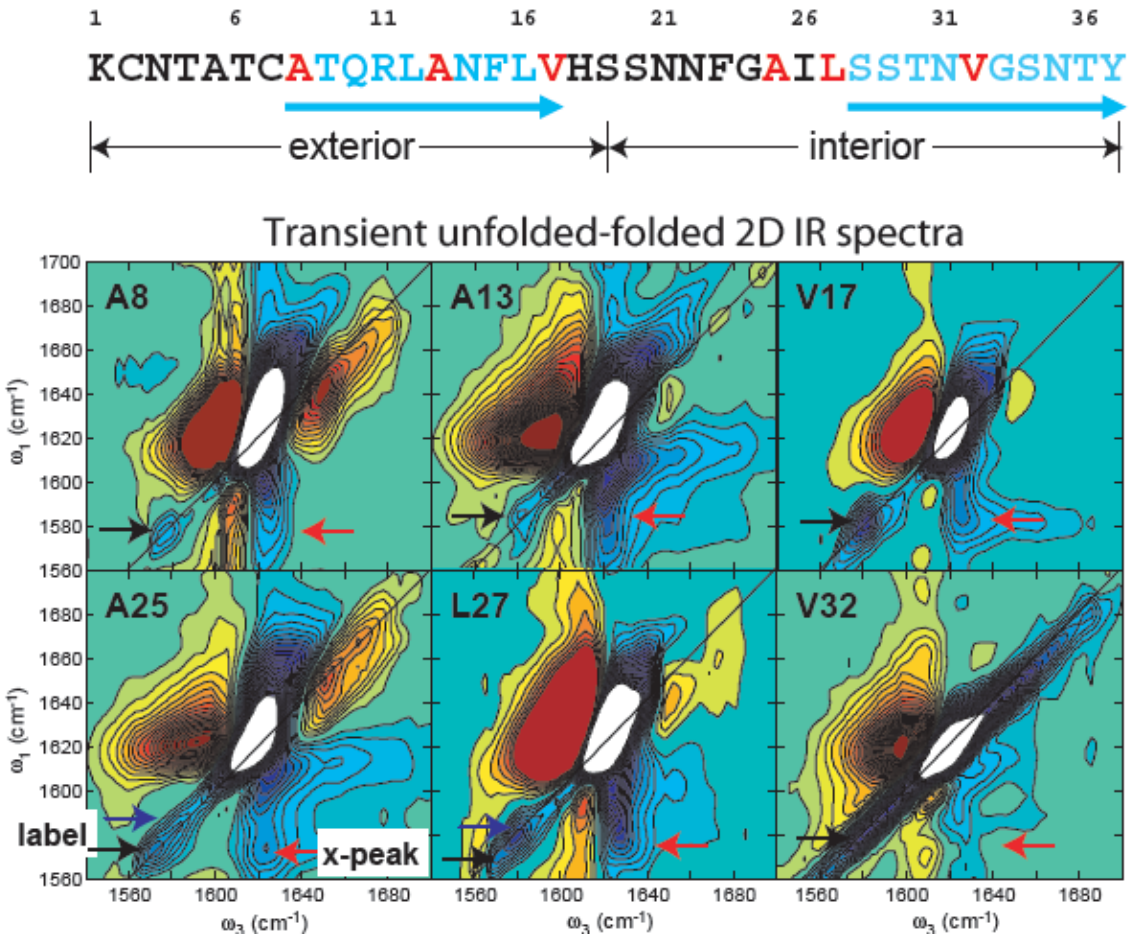

Figure 1. 2D IR spectra of mature fibrils of Amylin incorporated with $^{13}C^{18}O$ labeled amino acid at six different positions.

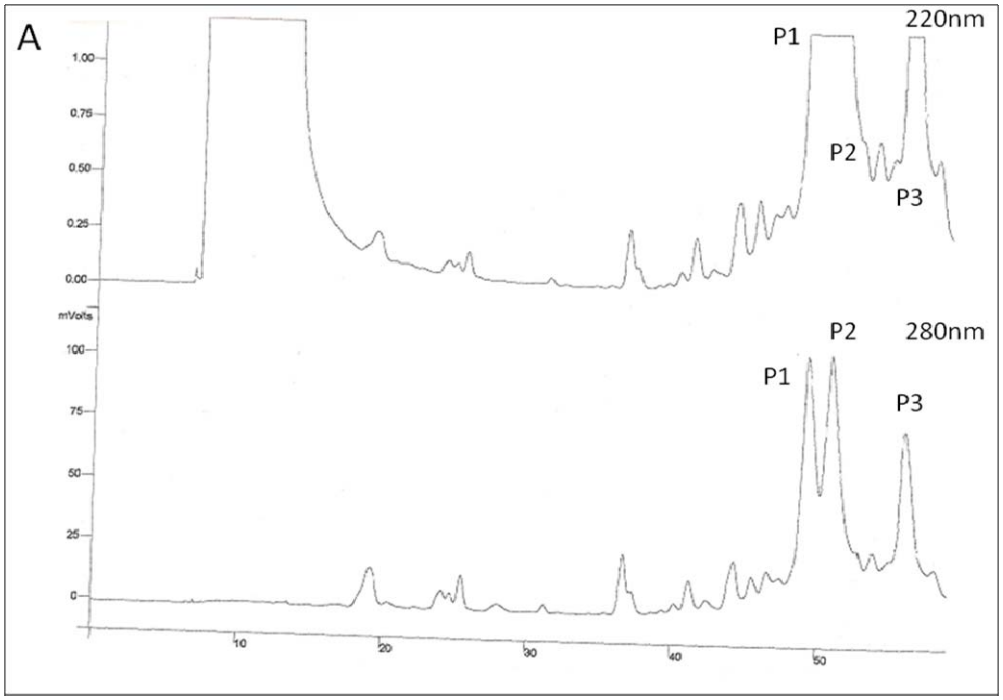
A
220nm
P1
P2
P3
mVolts
280nm
P2
P1
P3

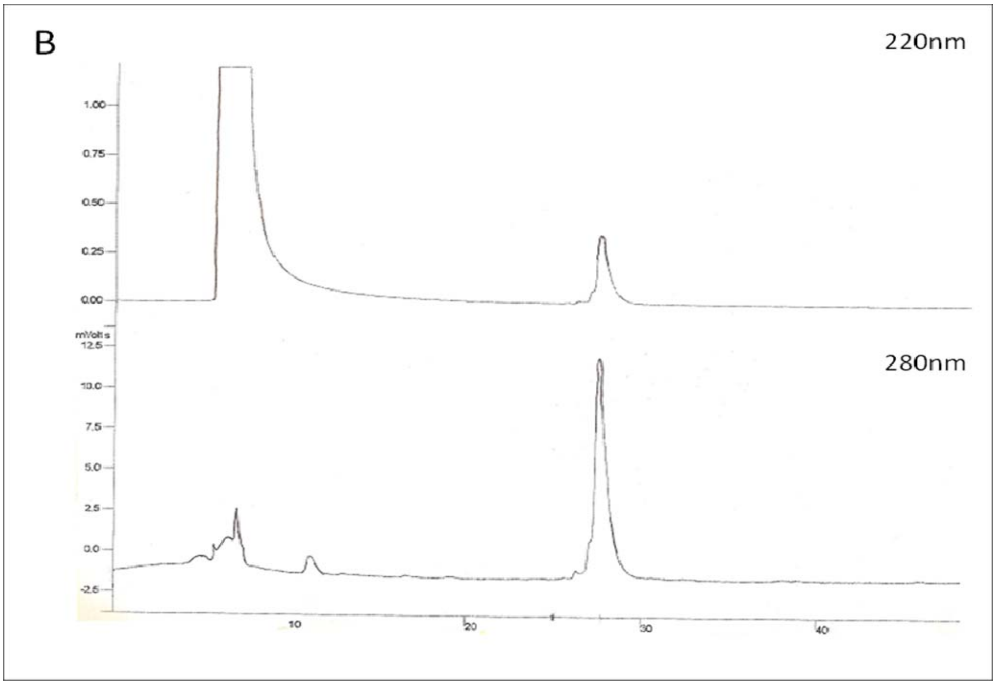
B
220nm
mVolts
280nm

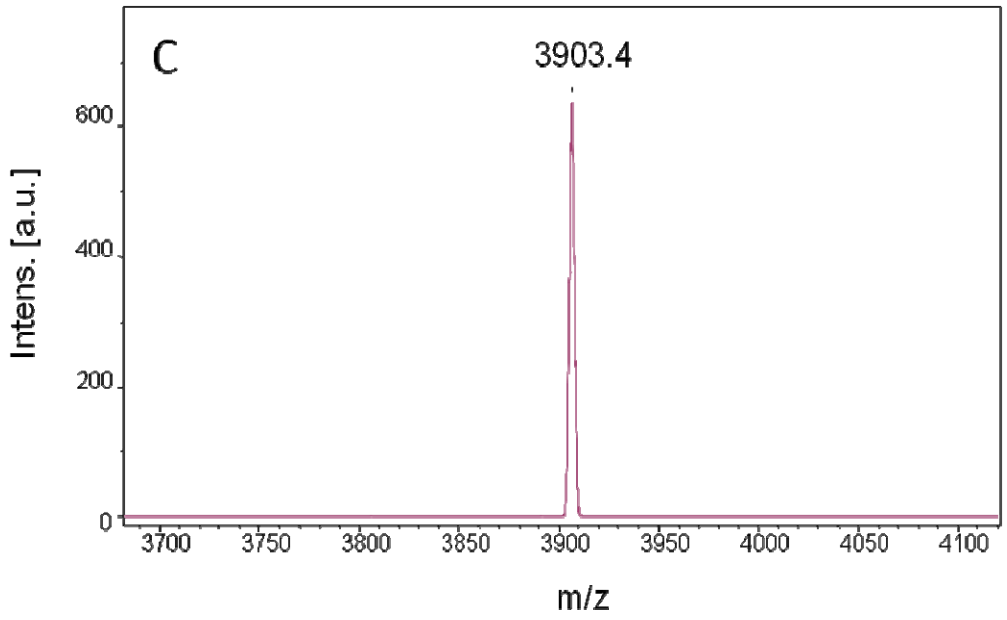

Figure 2. hIAPP A) HPLC purification of the crude peptide product from the synthesis of unlabeled Amylin. The gradient used was 0-90% buffer B in 90 minutes. B) Analytical HPLC trace of the purified peak P2 at a gradient of 25-90% buffer B in 55 minutes. C) MALDI-TOF of the purified peptide showing the expected molecular weight, which is, 3903.4Da.

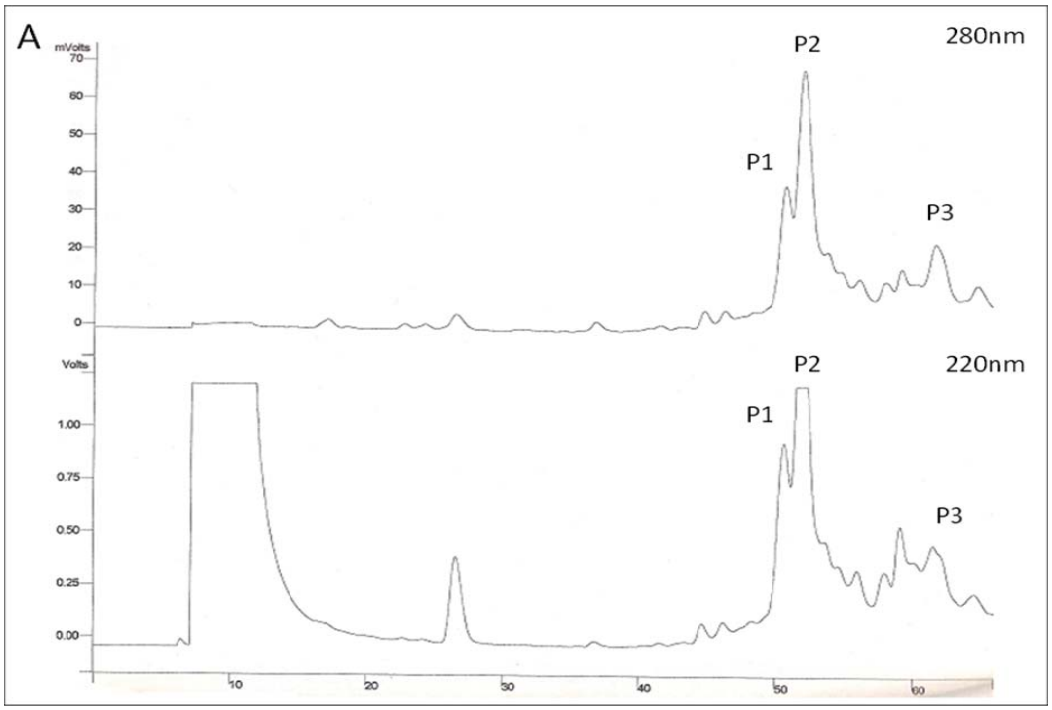
A
mVolts
70
60
50
40
30
20
10
0
P2
280nm
P1
P3
Volts
1.00
0.75
0.50
0.25
0.00
P2
220nm
P1
P3
10
20
30
40
50
60

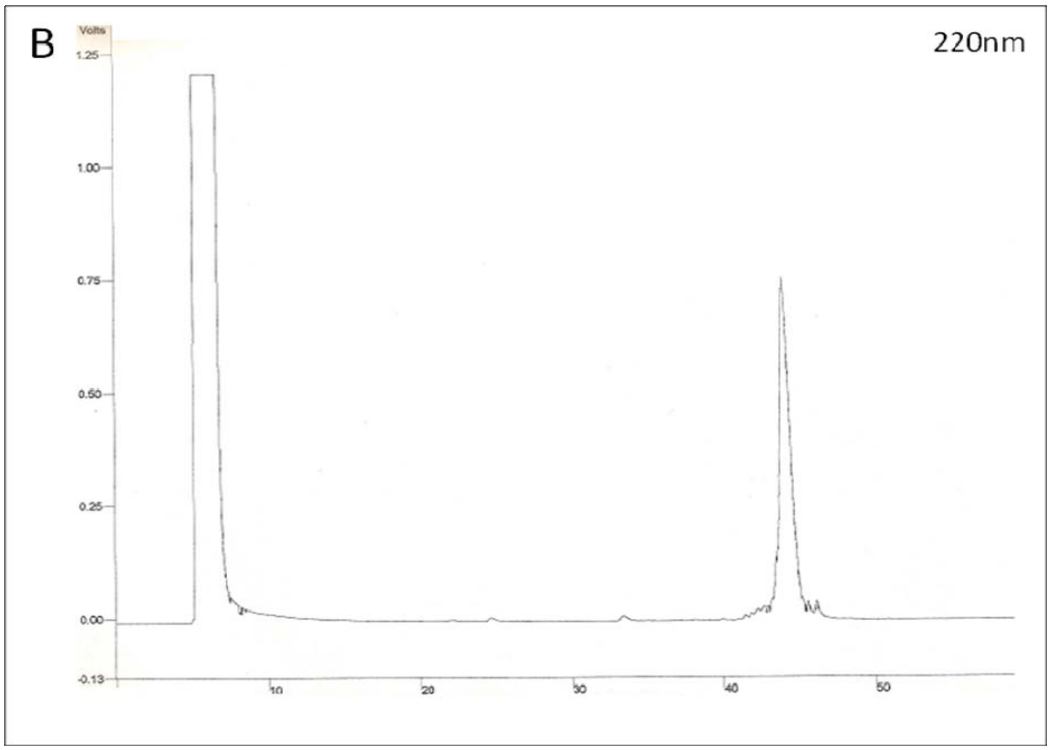
B
Volts
1.25
1.00
0.75
0.50
0.25
0.00
-0.13
220nm
10
20
30
40
50

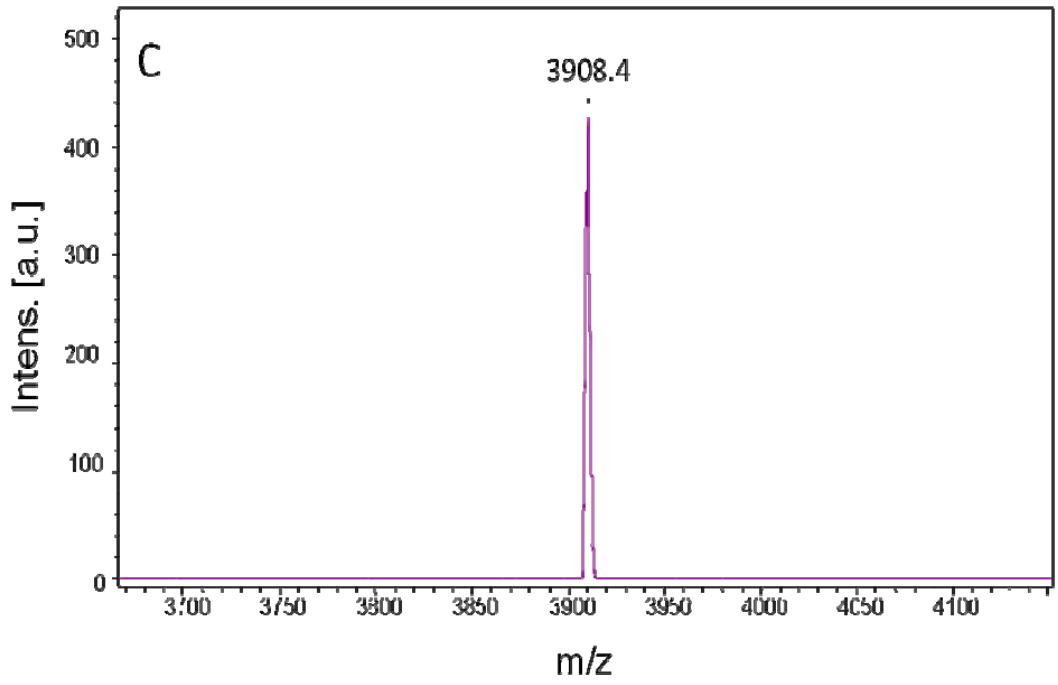

Figure 3. hIAPP $^{13}C^{18}O$ labeled at Ala13 A) HPLC purification of the crude peptide. The gradient used was 0-90% buffer B in 90 minutes. B) Analytical HPLC trace of the purified peak P2 at a gradient of 0-90% buffer B in 90 minutes. C) MALDI-TOF of the purified peptide showing the expected molecular weight, which is, 3908.8Da.

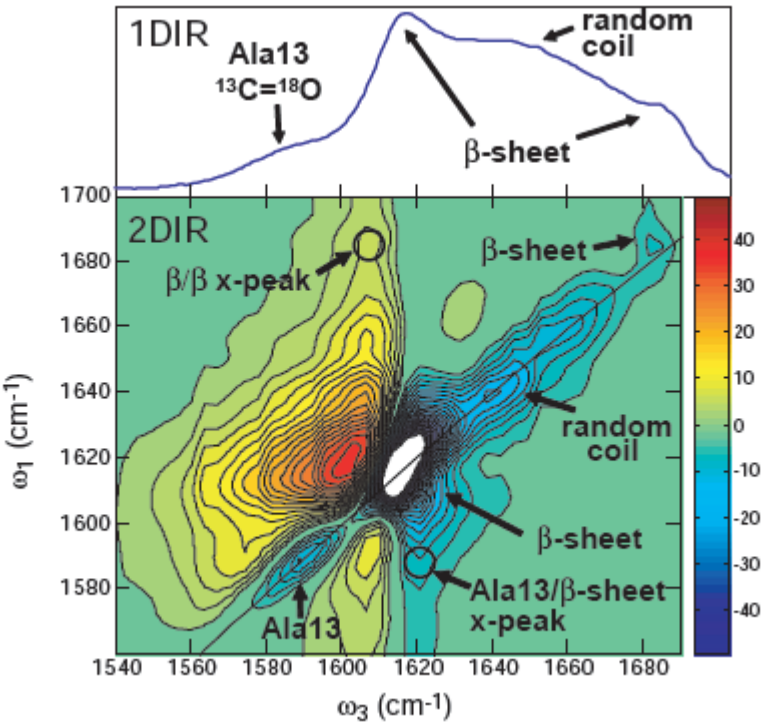

Figure 4. 1D IR and 2D IR spectra of Amylin with $^{13}C^{18}O$ labeled Ala13.

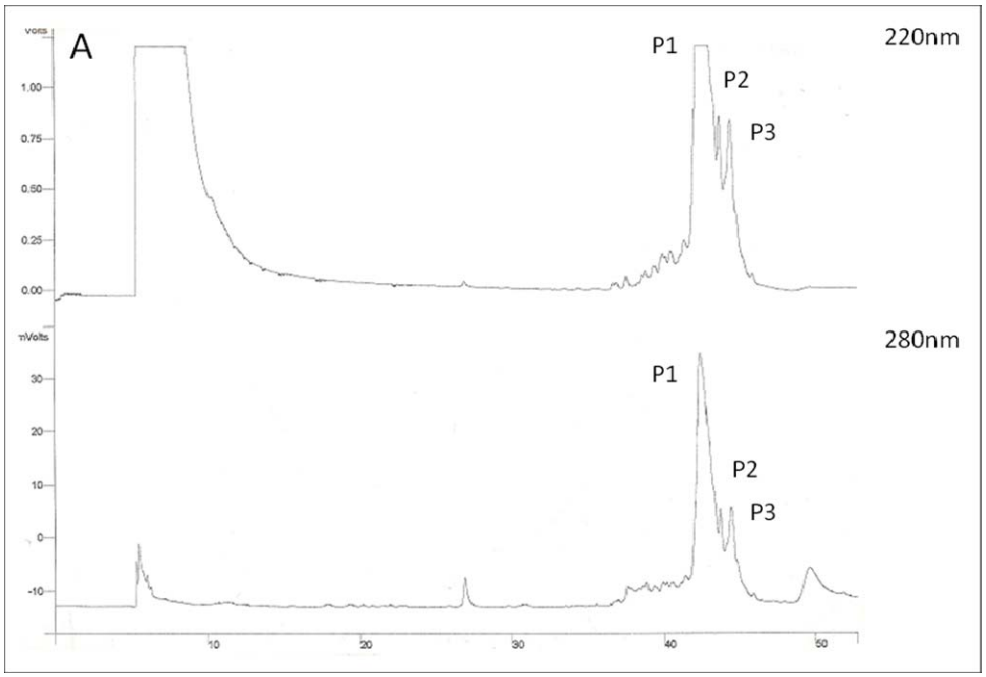
A
220nm
P1
P2
P3
280nm
P1
P2
P3

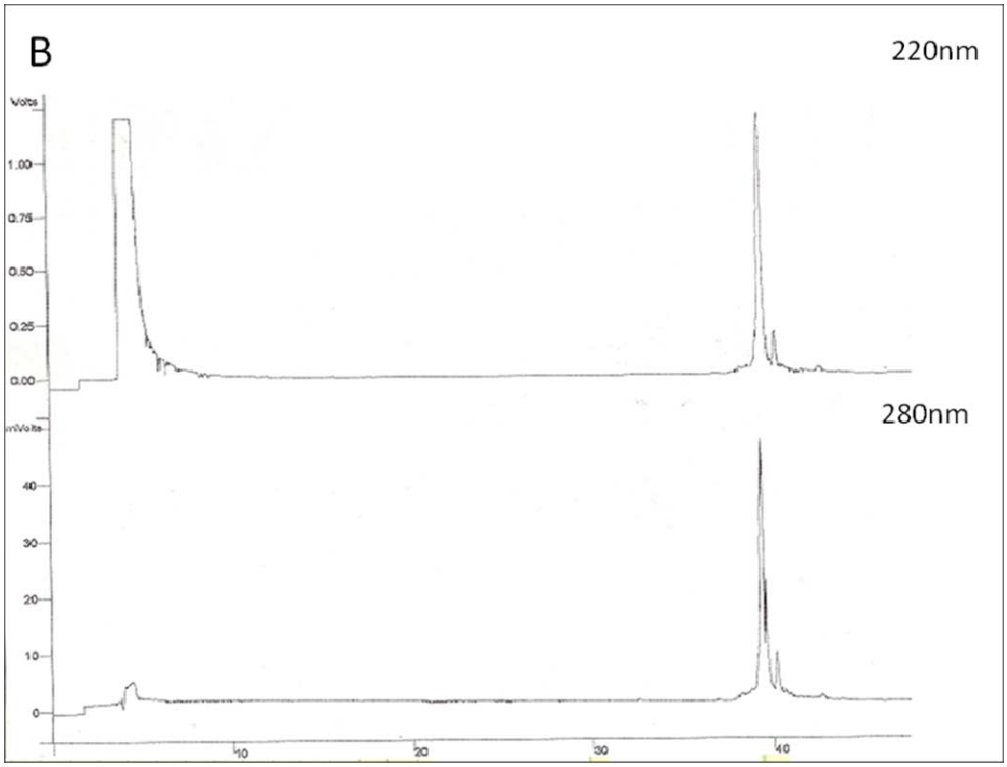
B
220nm
280nm

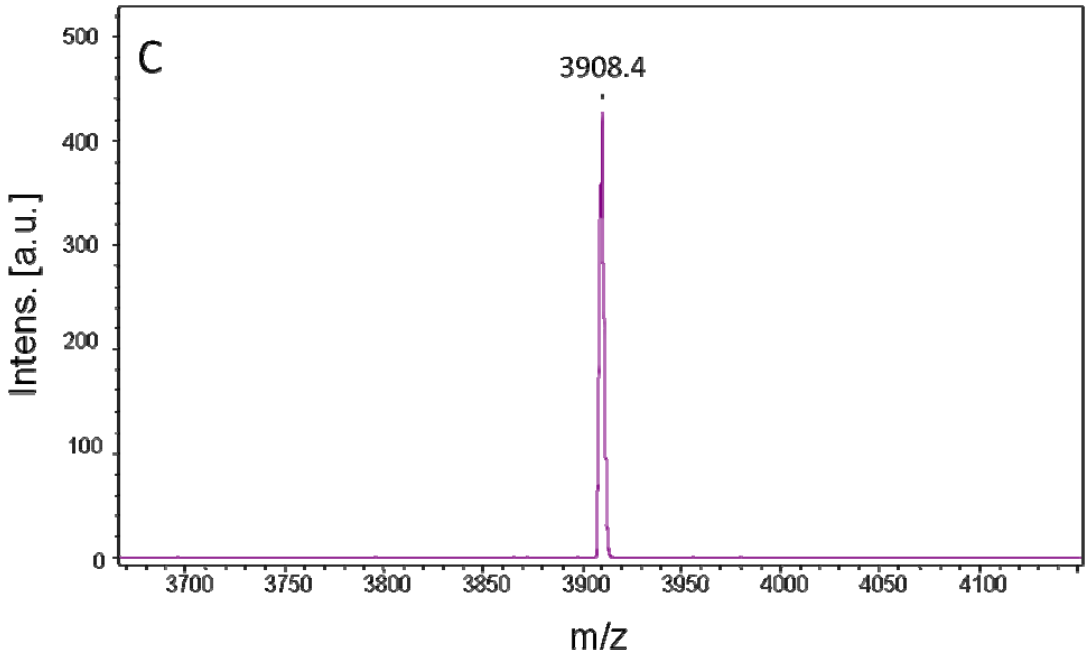

Figure 5. hIAPP $^{13}C^{18}O$ labeled at Ala8 A) HPLC purification of the crude peptide. The gradient used was 0-90% buffer B in 90 minutes. B) Analytical HPLC trace of the purified peak P1 at a gradient of 0-90% buffer B in 90 minutes. C) MALDI-TOF of the purified peptide showing the expected molecular weight, which is, 3908.8Da.

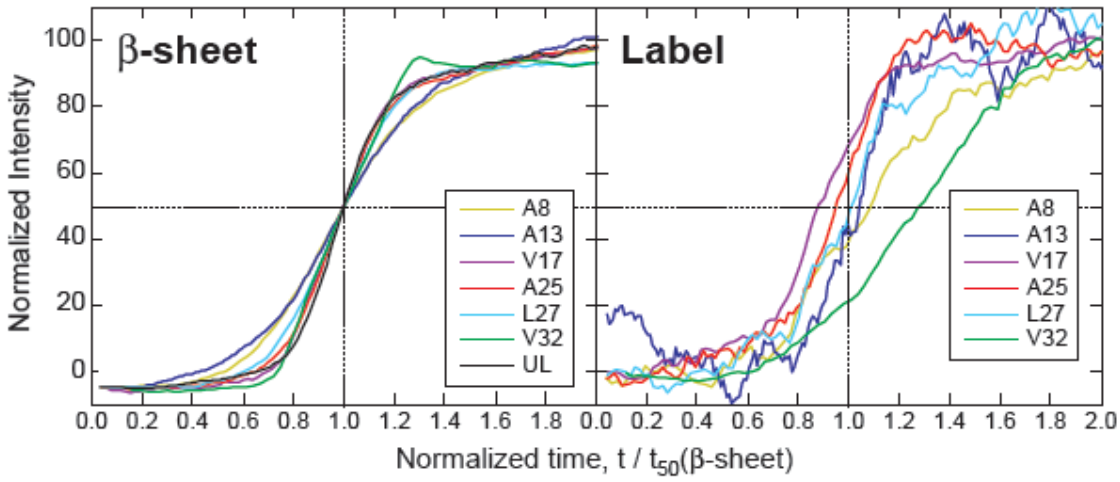

Figure 6. Kinetic curves of $^{13}C^{18}O$ labeled Amylin peptides with labeled amino acid incorporated at six different positions.

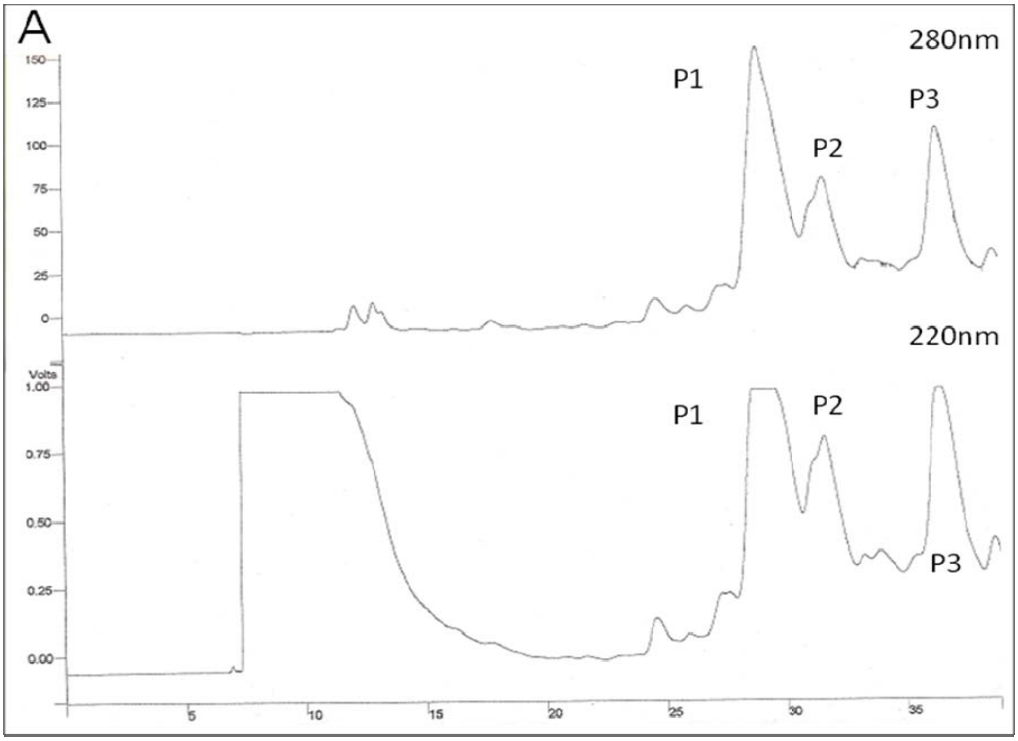
A
280nm
P1
P3
P2
220nm
Volts
P1
P2
P3

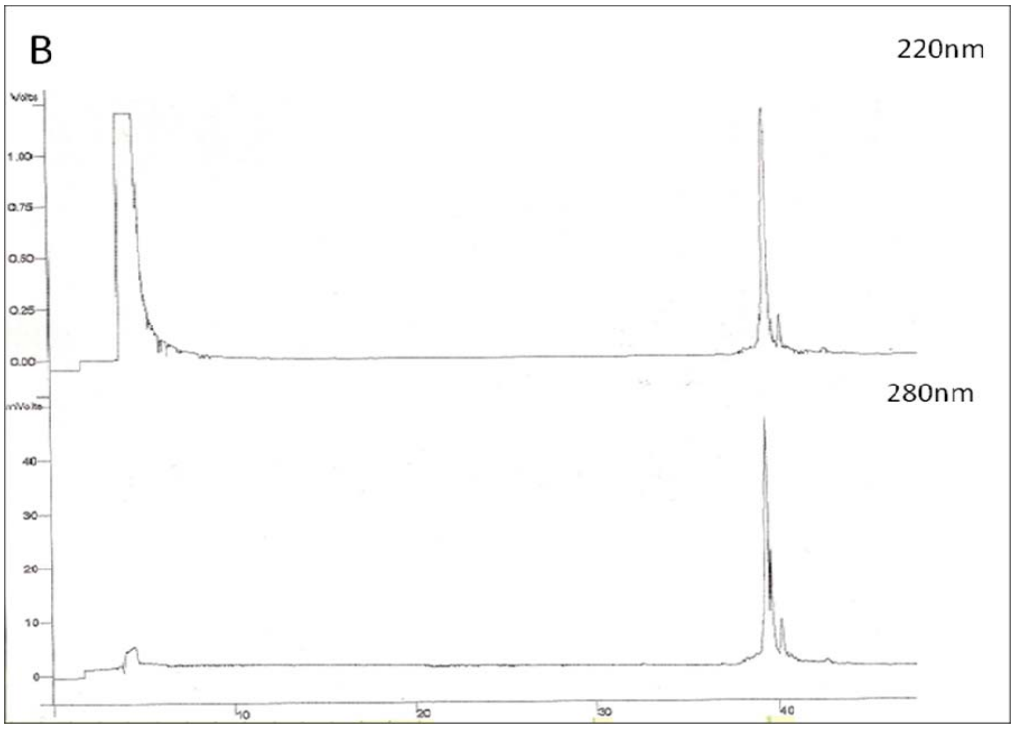
B
220nm
Volts
280nm
mVolts

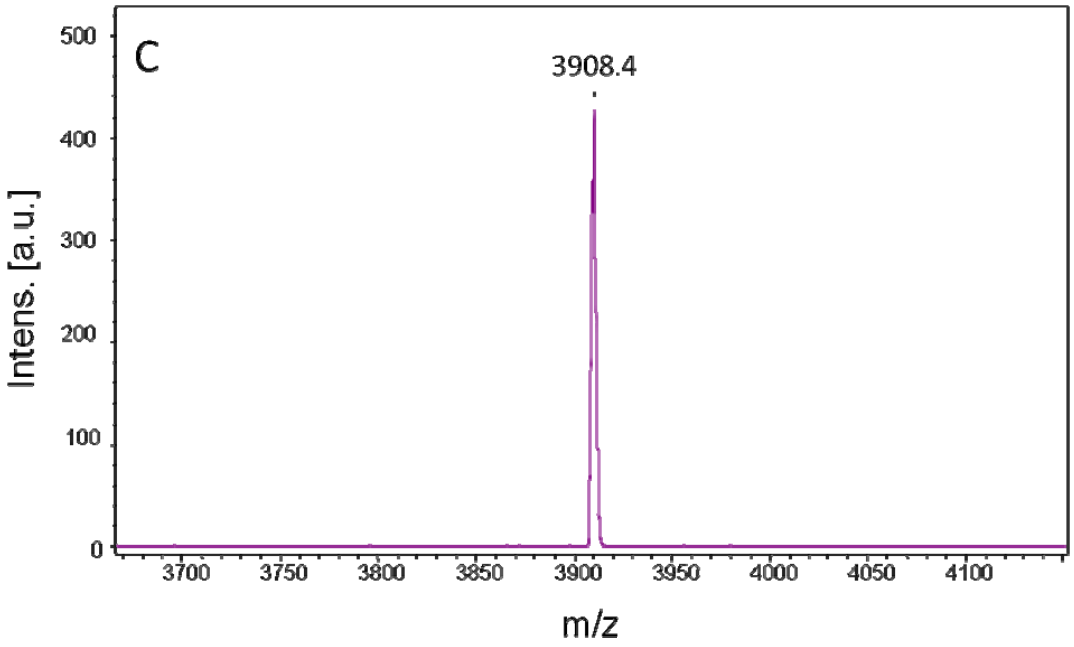

Figure 7. hIAPP $^{13}C^{18}O$ labeled at Ala5 A) HPLC purification of the crude peptide. The gradient used was 15-90% buffer B in 75 minutes. B) Analytical HPLC trace of the purified peak P1 at a gradient of 15-90% buffer B in 75 minutes. C) MALDI-TOF of the purified peptide showing the expected molecular weight, which is, 3908.8Da.

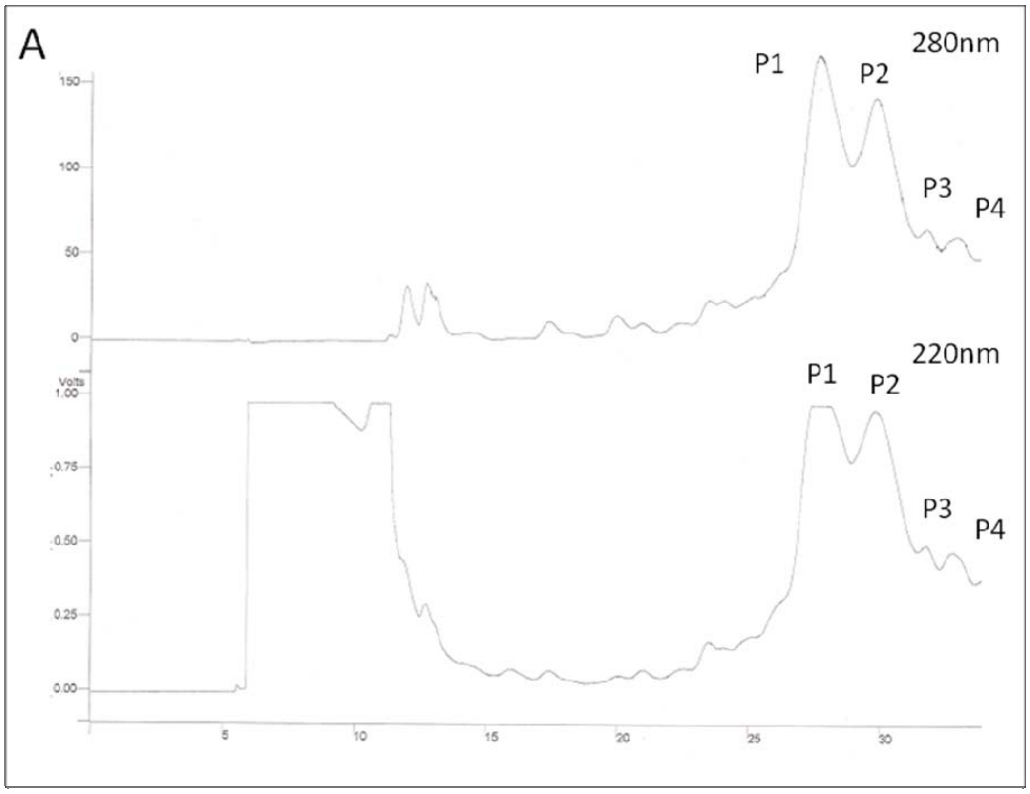
A
280nm
P1
P2
P3
P4
220nm
P1
P2
P3
P4

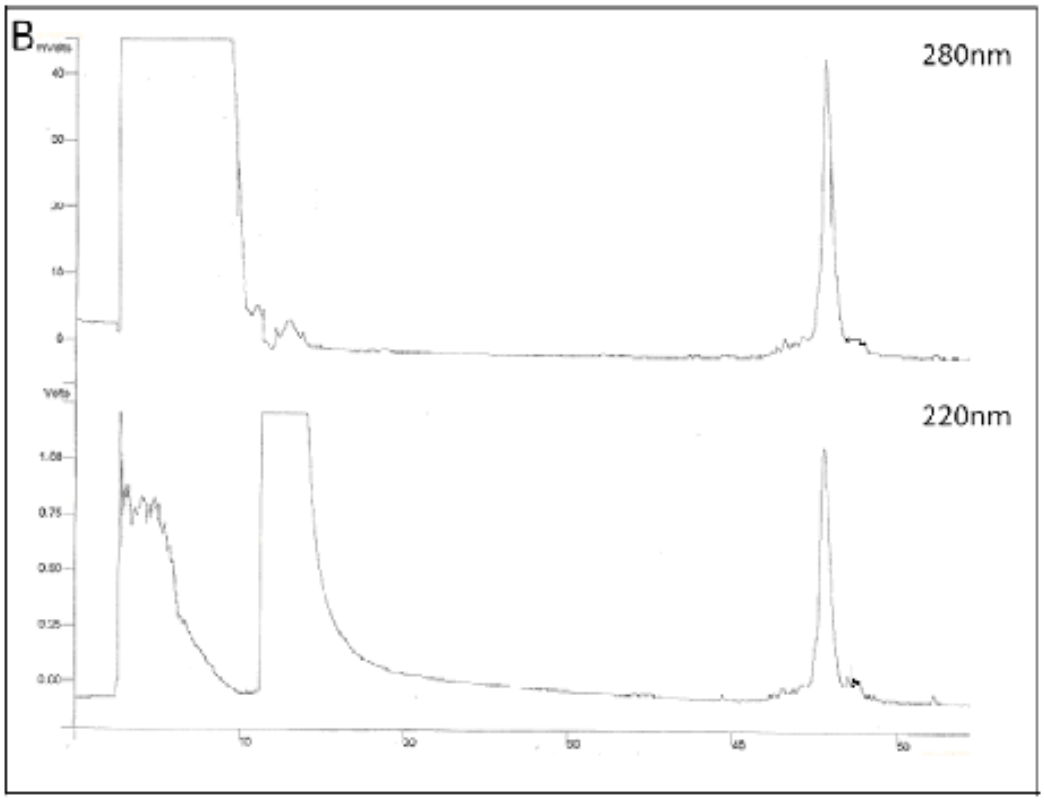
B
280nm
220nm

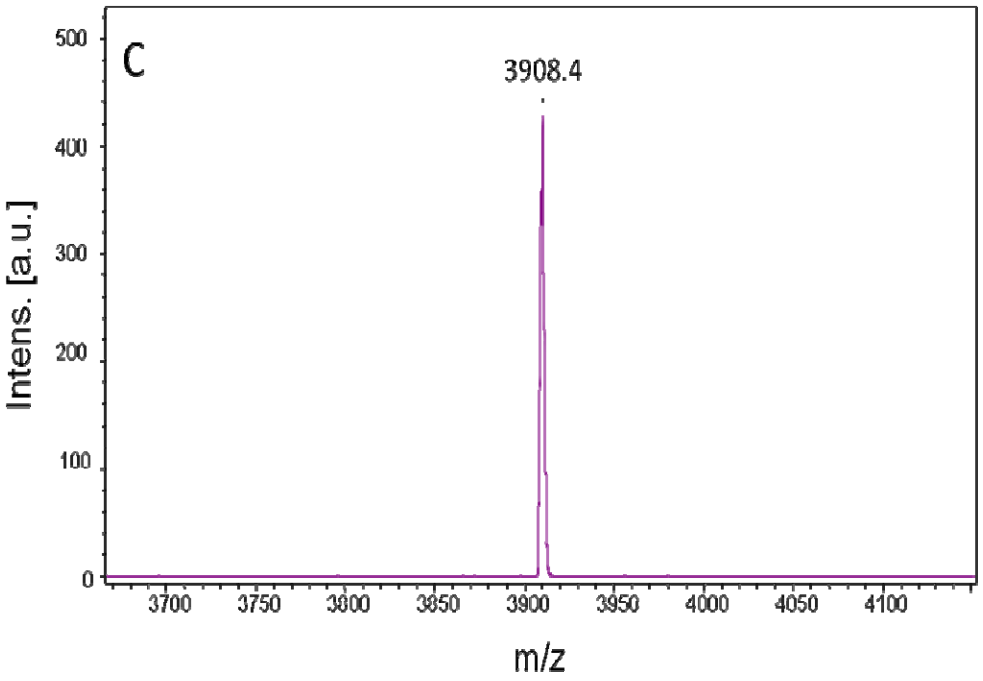

Figure 8. hIAPP $^{13}C^{18}O$ labeled at Ala25 A) HPLC purification of the crude peptide. The gradient used was 15-90% buffer B in 75 minutes. B) Analytical HPLC trace of the purified peak P1 at a gradient of 0-90% buffer B in 90minutes. C) MALDI-TOF of the purified peptide showing the expected molecular weight, which is, 3908.8Da.

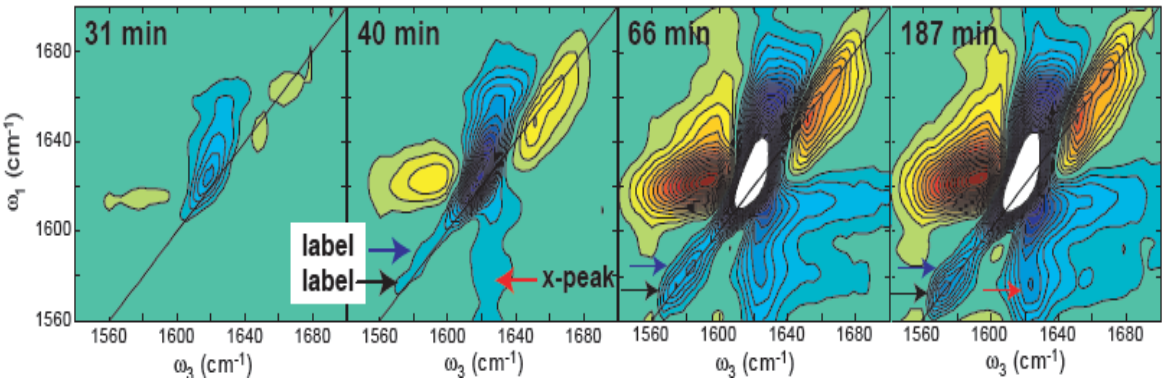

Figure 9. Tracking aggregation of $^{13}C^{18}O$ labeled Amylin at Ala25 with rapid scan 2D IR.

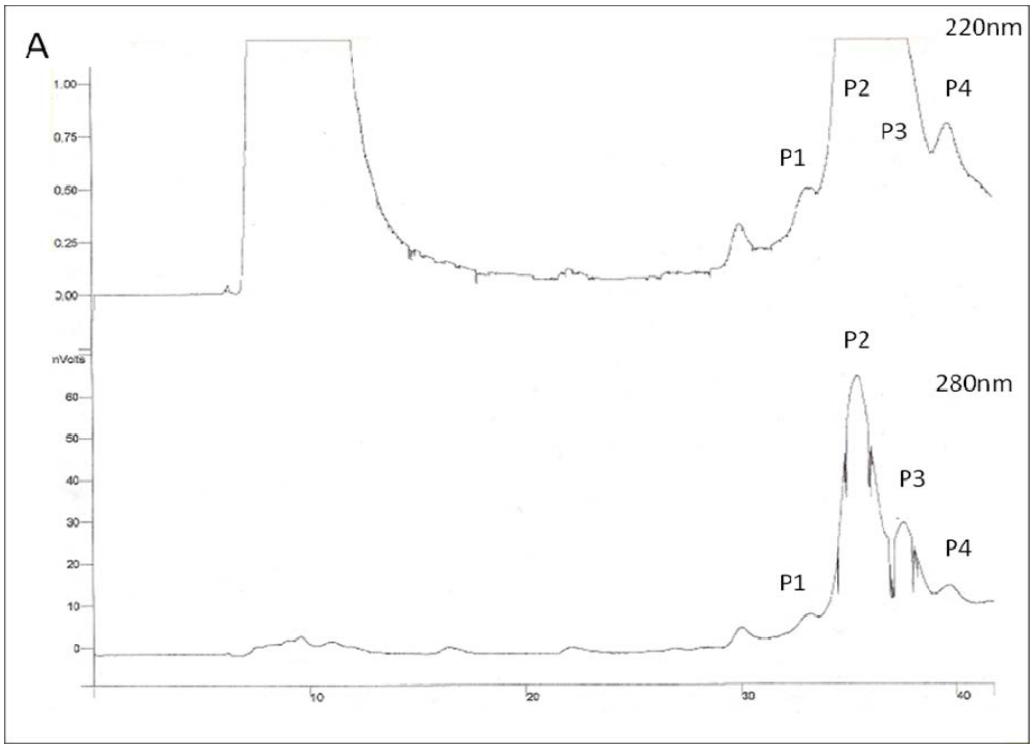
A
220nm
P1
P2
P3
P4
mVolts
280nm
P1
P2
P3
P4

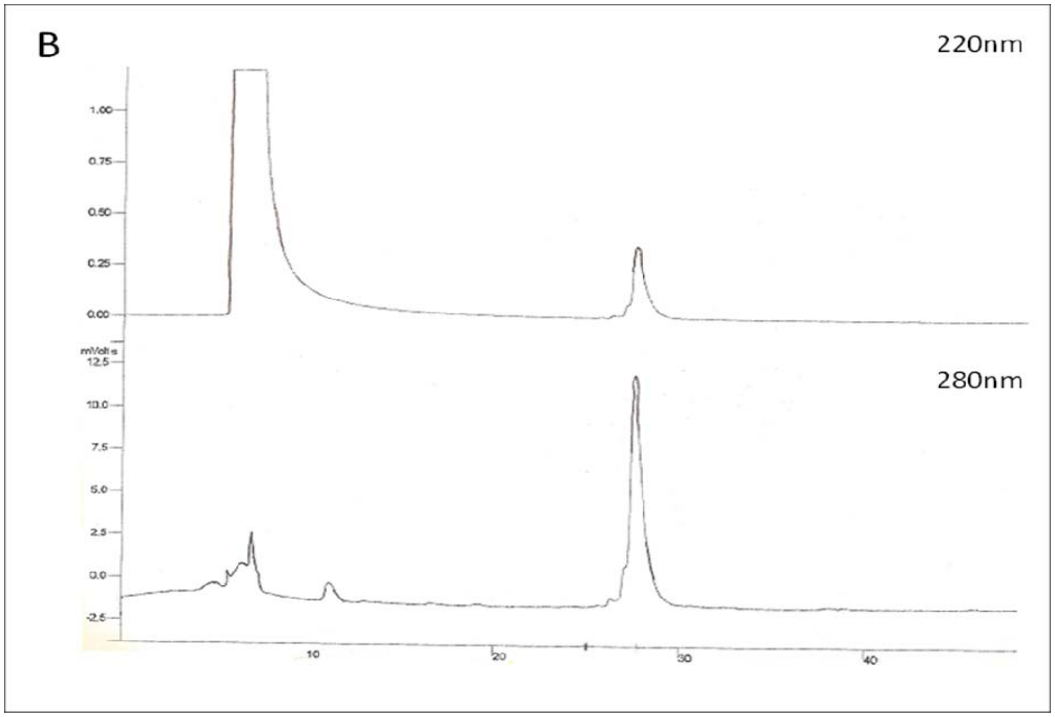
B
220nm
280nm

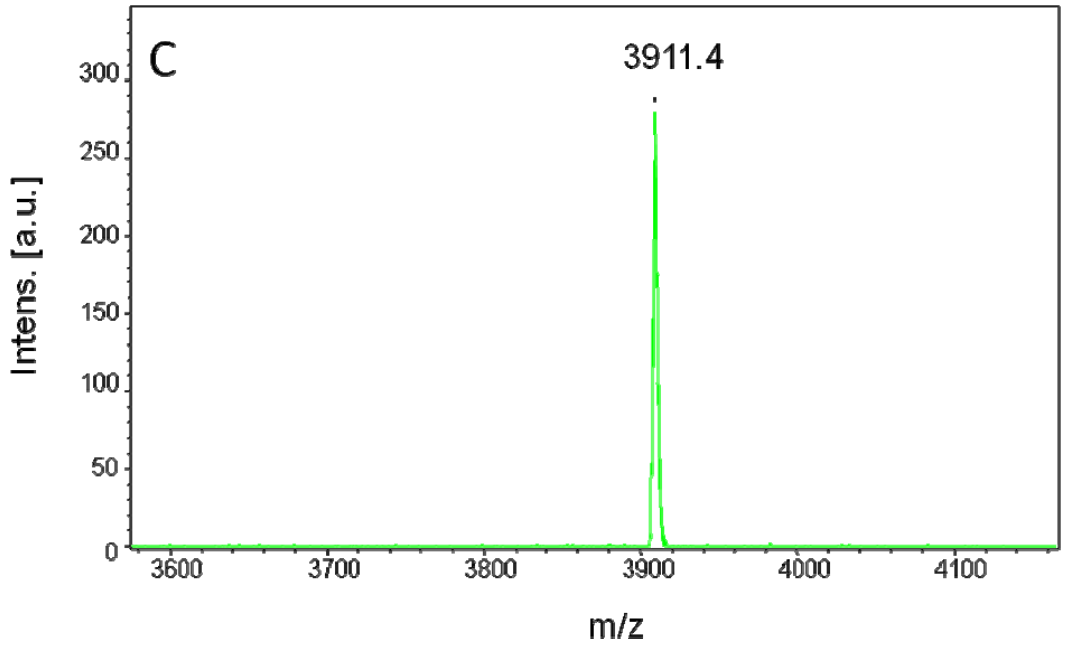

Figure 10. hIAPP $^{13}C^{18}O$ labeled at Leu27 A) HPLC purification of the crude peptide. The gradient used was 15-90% buffer B in 75 minutes. B) Analytical HPLC trace of the purified peak P2 at a gradient of 15-90% buffer B in 75 minutes. C) MALDI-TOF of the purified peptide showing the expected molecular weight, which is, 3911.4Da.

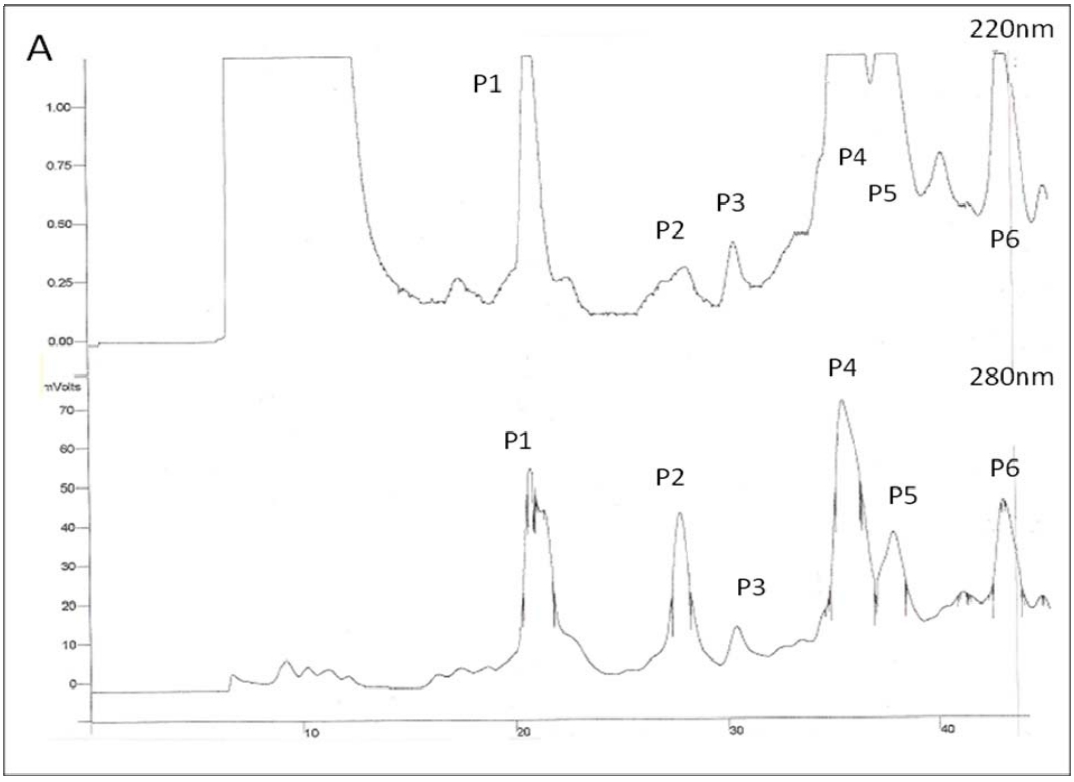
A
220nm
P1
P2
P3
P4
P5
P6
1.00
0.75
0.50
0.25
0.00
mVolts
280nm
P1
P2
P3
P4
P5
P6
70
60
50
40
30
20
10
0
10
20
30
40

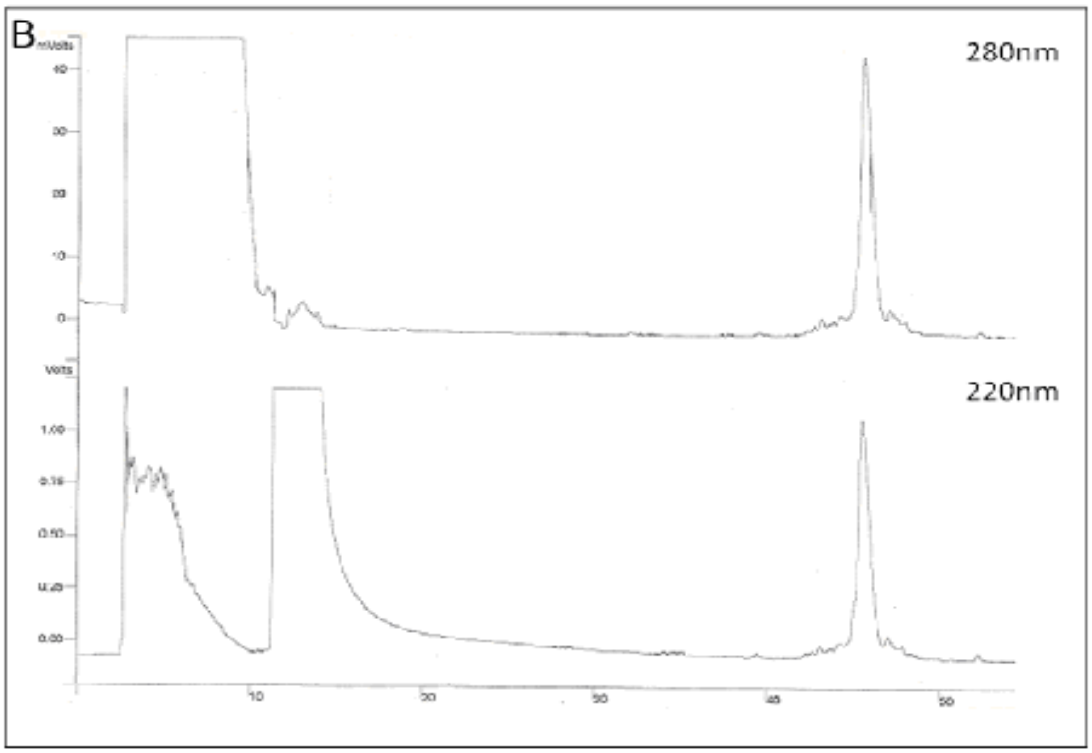
B
mVolts
280nm
Volts
220nm
10
30
50
45
50

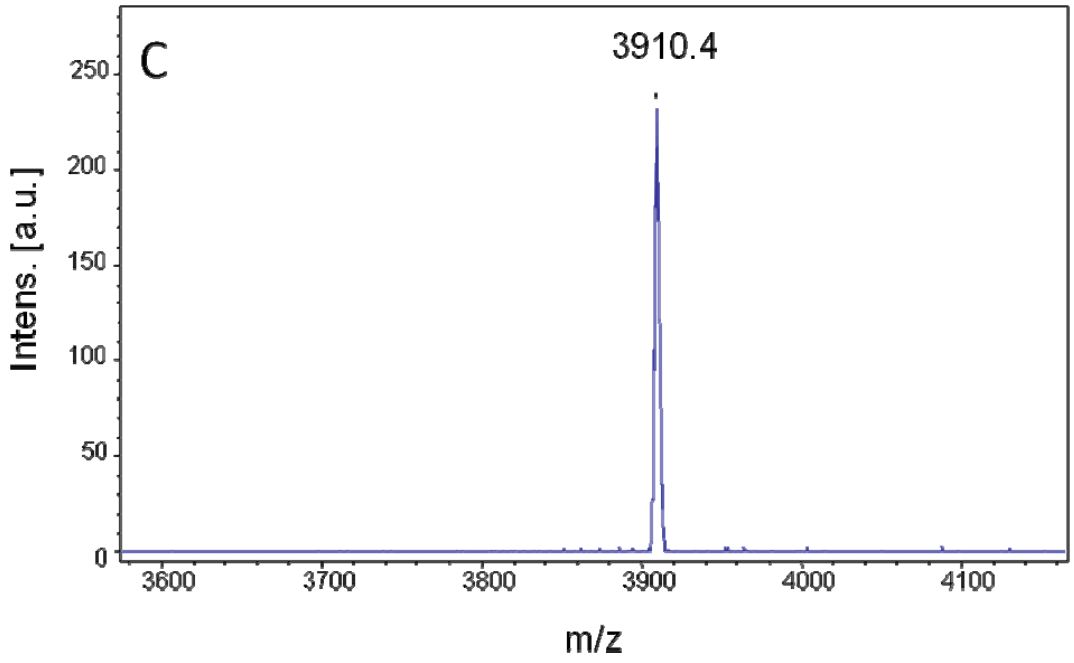

Figure 11. hIAPP $^{13}C^{18}O$ labeled at Val17 A) HPLC purification of the crude peptide. The gradient used was 15-90% buffer B in 75 minutes. B) Analytical HPLC trace of the purified peak P5 at a gradient of 0-90% buffer B in 90 minutes. C) MALDI-TOF of the purified peptide showing the expected molecular weight, which is, 3910.4Da.

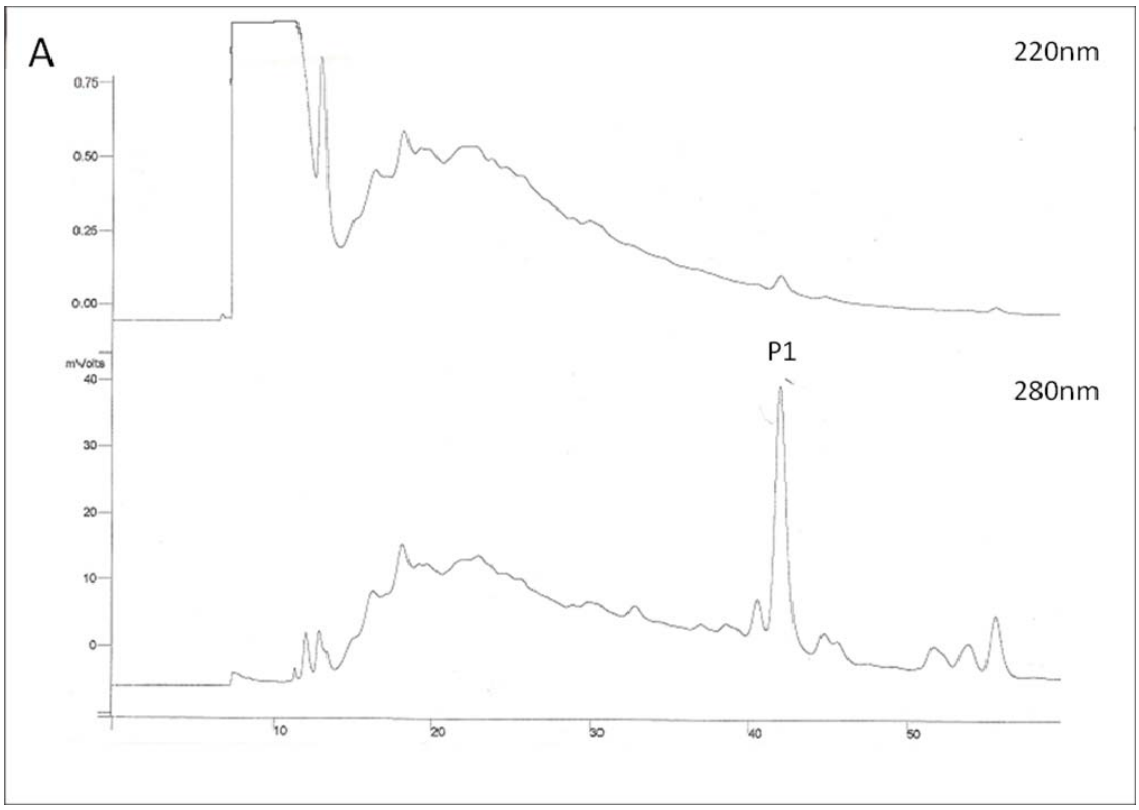
A
220nm
0.75
0.50
0.25
0.00
mVolts
40
30
20
10
0
P1
280nm
10
20
30
40
50

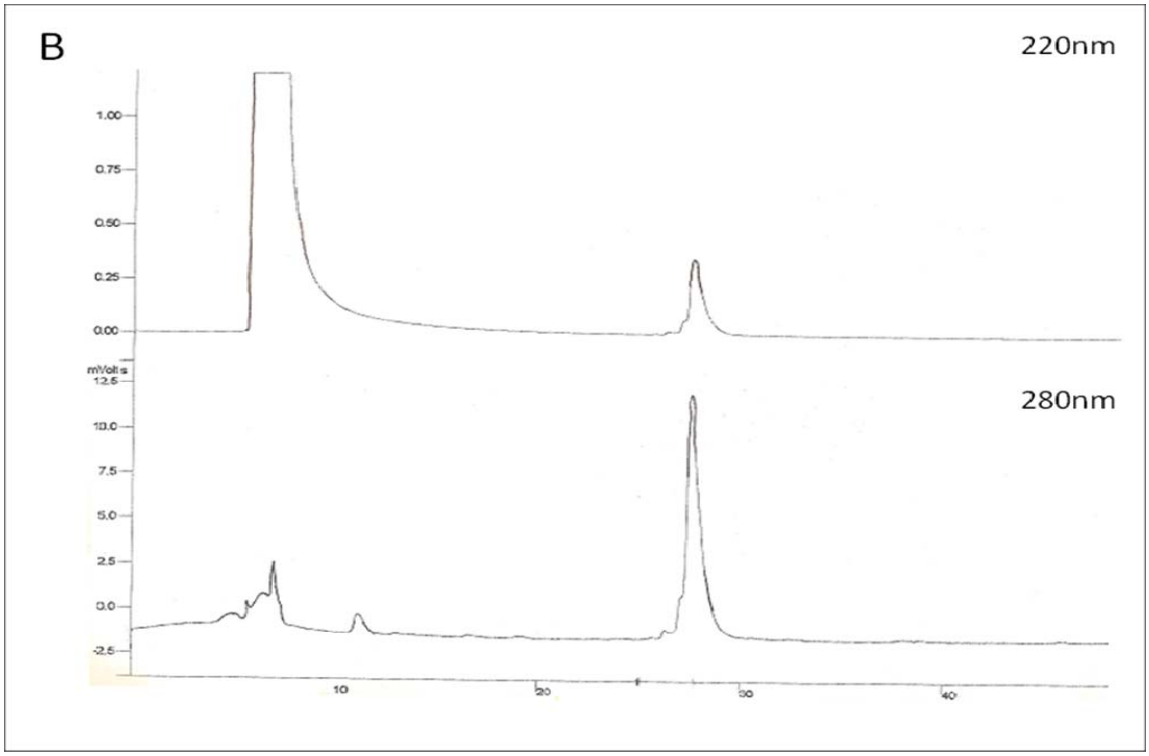
B
220nm
1.00
0.75
0.50
0.25
0.00
mVolts
12.5
10.0
7.5
5.0
2.5
0.0
-2.5
280nm
10
20
30
40

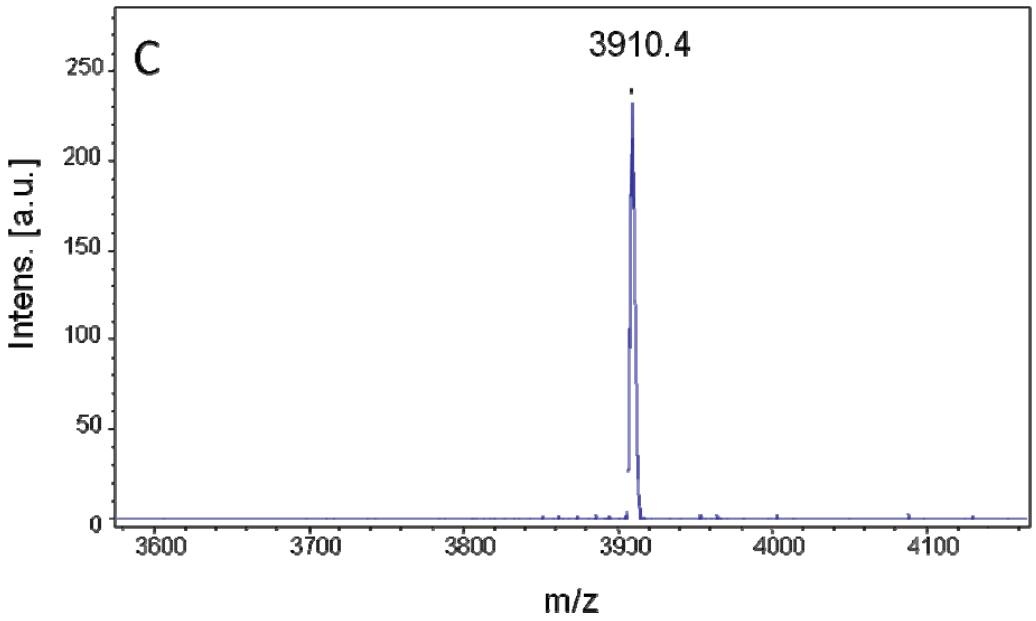

Figure 12. hIAPP $^{13}C^{18}O$ labeled at Val32 A) HPLC purification of the crude peptide. The gradient used was 0-90% buffer B in 90 minutes. B) Analytical HPLC trace of the purified peak P2 at a gradient of 15-90% buffer B in 75 minutes. C) MALDI-TOF of the purified peptide showing the expected molecular weight, which is, 3910.4Da.

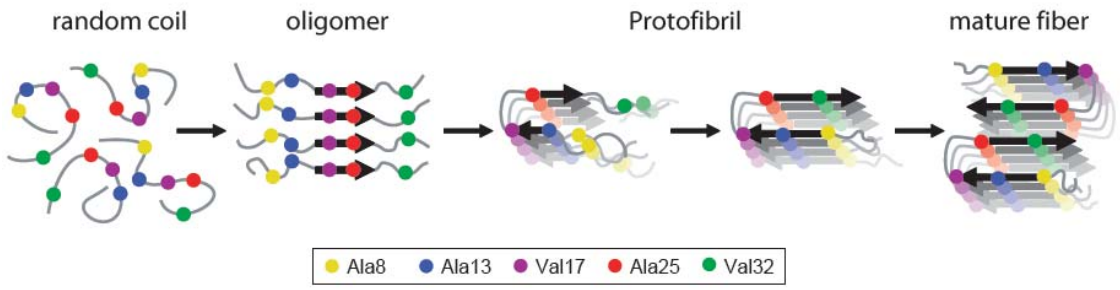

Figure 13. Model of Amylin aggregation as deduced from 2D IR studies of site-specific isotope labeled hIAPP peptides. Val17-Ala25 fragment initiates β-sheet formation, which further extends through Ala13 to Ala8. The C-terminus then participates in β-sheet formation as protofibrils mature into fibrils.

Table 5-1: List of $^{13}C^{18}O$ labeled Amylin peptides synthesized

Peptide	Final yield of purified peptide (mg)
$^{13}C^{18}O$-Ala5	18
$^{13}C^{18}O$-Ala8	50
$^{13}C^{18}O$-Ala13	35
$^{13}C^{18}O$-Val17	40
$^{13}C^{18}O$-Ala25	42
$^{13}C^{18}O$-Leu27	23
$^{13}C^{18}O$-Val32	2.4

Chapter 6. Protocol for Aβ42 and Aβ40 fibril formation

6.1 Introduction

Aβ aggregation plays a central role in the pathogenesis of Alzheimer's disease. The extensive Aβ cerebral deposits are a characteristic feature observed in the brains of demented patients. Aβ is produced by γ-secretase cleavage of β-secretase fragment of Amyloid Precursor Protien, APP (Selkoe 1998). The amount of Aβ normally produced is very small, however, increased activity of mutated γ-secretase in Alzheimer's disease brains causes an increase in Aβ production. These hydrophobic peptides then oligomerize and form amyloid fibrils with a characteristic β-sheet morphology (Sunde et al. 1997). Aβ generated by γ-secretase has two isoforms Aβ40 and Aβ42 (Glenner and Wong 1984) (Fig. 1). Both isoforms can undergo amyloidogenesis to form fibrils but the observed rate of aggregation is faster for Aβ42 than Aβ40. A number of different protocols for preparing samples for fibrillization studies have been reported. However, the slow rate of aggregation of Aβ peptide makes in vitro biophysical studies of fibrillisation time consuming. In addition many methods lead to mixtures of fibrils and less ordered material, which in turn causes problems in structural studies. In this chapter, I describe a simple method for reproducibly generating very homogenous preparations of Aβ fibrils.

The protocol also offers the advantage that the observed rate of amyloid formation is notably faster; a day rather than a week. The existing methods include dissolving the peptide in organic medium of HFIP (Osada et al. 2005). The HFIP stock is lyophilized and the dry powder is weighted and added to the buffer a desired concentration. The reaction is then set for aggregation and the process is monitored by Thioflavin-T assay, TEM, CD, etc. Teplow and others have popularized the use of NaOH for preparation of initial stock solutions wherein the peptide is initially dissolved in NaOH and lyophilized. NaOH treated peptide is then dissolved in the buffer followed by filtration through a cutoff filter. The filtrate is then used immediately for aggregation reaction (Teplow 2006). However, all these protocols accomplish fibrillization in 5-8 days depending on the protocol used (Fig. 2-4). This time length makes it difficult to test proteins of interest for their inhibition properties because these proteins may not be stable for long periods of time at room temperature. Thus a new protocol was designed and tested to allow for fibrillization in a shorter period of time.

6.2 Methods

6.2.1 Protein Synthesis and Purification

Aβ40 was synthesized on a 0.25mmol scale using 9-fluornylmethoxycarbonyl (Fmoc) chemistry on an Applied Biosystems 433A. Valine coupled Wang resin was used to generate a free C-terminus. Pseudoproline dipeptide derivatives were employed as described (Johnson et al. 1993, Wohr et al. 1996). Fmoc-protected pseudoproline (oxazolidine) dipeptide derivatives were purchased from Novabiochem. All other reagents were purchased from Advanced Chemtech, Fischer Scientific, PE Biosystems

and Sigma Aldrich. All solvents used were of A.C.S. grade. Standard Fmoc reaction cycles were used. The first residue added to the resin, pseudoproline dipeptide derivatives, all β-branched residues and all residues following the β-branched residue were double coupled. The peptide was cleaved from the resin using standard trifluoroacetic acid (TFA) methods. The crude peptide was treated with 20% (v/v) acetic acid and lyophilized. The dry peptide was then dissolved in DMSO and purified via reverse-phase HPLC using a Vydac C-18 preparative column. A two-buffer system utilizing HCl as an ion-pairing agent was used for the purification. Buffer A consisted of 0.045% (v/v) HCl in distilled de-ionized (DDI) water. Buffer B consisted of 80% (v/v) acetonitrile, 20% (v/v) DDI water and 0.045% (v/v) HCl. HCl was used as the ion pairing agent in anticipation of IR studies. The purity of the peptide was checked by HPLC and was 99% (Fig 5a-b). The purified peptide was analyzed by matrix-assisted laser desorption/ionization time-of-flight (MALDI-TOF) mass spectroscopy. The expected molecular mass of Aβ40 is 4329.8Da (Fig. 5c). The observed mass was 4.3kDa. Purified Aβ42 was purchased from Keck facility at Yale University.

6.2.2 Protocol for Fibril Formation

The dry peptide was weighed and 0.4-0.5mg was added to 200μL of DDI water. The sample was vortexed briefly for 20s followed by the addition of 200μL of 200mM Tris buffer at pH 7.4. The solution was vortexed again for 20s and then centrifuged at 17,200g for 3.5min. The supernatant was immediately withdrawn and its concentration was calculated using UV-Vis at 280nm. This Aβ solution was then used for a fibrillization reaction at the needed concentration in 100mM Tris buffer at pH 7.4.

6.2.3 Circular Dichroism Spectroscopy

All CD experiments were performed using an Aviv 62A DS CD spectrophotometer. Far-UV CD spectra were recorded at the end of each kinetic run. Spectra were recorded over the wavelength range of 190-250nm at 1nm intervals with an averaging time of 3 seconds using a 0.1cm path length cell. Background spectrum was subtracted from each of the collected data sets. Each spectrum shown is an average of 3 scans.

6.2.4 Thioflavin-T monitored kinetics

The protocol described above was used to set up Aβ fibrillization reactions at a high concentration of 130-150uM. Aliquots were withdrawn at different time points and diluted into 100μM Thio-T in 100mM Tris buffer at pH 7.4 to give a final Aβ concentration of 15μM. The emission scan of each aliquot was recorded from 462nm to 600nm. The intensity of Thio-T fliuorescence at 485nm was then plotted with time to obtain the kinetic curve. The curve was fit using a 5 parameter sigmoidal equation (Eq.1),

$$y(t) = y(t_0) + \frac{a}{\left[1 + e^{\left\{\frac{t_0 - t}{b}\right\}}\right]^c} \qquad (1)$$

where, y(t) is the observed fluorescence at time t, b is the slope of the growth phase, a is the final fluorescence intensity and c is the lag phase.

6.2.5 Transmission electron microscopy (TEM)

TEM of Aβ40 and Aβ42 samples was performed at the Bioimaging Center at Rockefeller University. Samples were prepared by placing 5μl of solution onto formvar coated 300 mesh copper grids and stained with 2% aqueous uranyl acetate. Samples were viewed with a FEI Tecnai12 BioTwinG^2 transmission electron microscope at 80 kV. Digital images were acquired with an AMT XR-60 CCD Digital Camera System and compiled using Adobe Photoshop CS2.

6.3 Results

Aβ is a hydrophobic peptide with a high tendency to self-aggregate. The aggregation can either result in well-ordered β-sheet amyloid fibrils or can also lead to formation of amorphous aggregates. Carefully designed protocols have been developed to allow Aβ aggregation to selectively result in amyloid fibrils. These homogenous fibrils are a necessity for structural studies. The protocol outlined here was initially used for formation of Aβ42 fibrils starting at monomer concentration of 64μM. The progress of the reaction was monitored through TEM images (Fig. 6). In 5 hours small protofilaments were seen all over the grid (Fig. 7). In 12 hours the images showed the presence of long fibrils as well as protofibrils (Fig. 8). However, only well resolved fibrils were present in the 24 hour images (Fig. 9). Aliquots at time points after 24 hours did not show any further change in the formation of fibrils. The protocol was further tested on lower concentration of Aβ42. TEM confirmed that even at 32μM concentration, highly resolved fibrils were formed within 24 hours (Fig. 10).

The protocol was also applied on Aβ40 to check for fibril formation. TEM images showed extensive fibrils being formed in 24 hours (Fig 11). The kinetics of Aβ40 fibrillization was measured using thioflavin-T binding assay (Fig. 12). The kinetic curve reaches the plateau indicating completion of aggregation within 24 hours of initiation. This was much faster as compared to 12-18 days reported for Aβ40 fibrillization (2001, 2007). The protocol was found to be applicable to both Aβ40 and Aβ42 fibrillization. The thioflavin-T kinetic curve for Aβ42 shows the fibrillization was complete within 16 hours (Fig. 13). All TEM images collected showed only fibrillar or pre-fibrillar species. There were no amorphous aggregates to disrupt the homogeneity of the formed fibrils.

We examined the effect of omitting steps in the protocol. Aβ42 fibrillization was performed according to the aforementioned protocol but the centrifugation step was omitted. Aliquots were withdrawn at different time intervals and analyzed through TEM. The fibrils were formed within 24 hours but the images showed presence of both amorphous and fibrillar aggregates (Fig. 14-16). As the fibrillization was allowed to proceed further, amorphous aggregates and fibrillar aggregates continued to co-exist. Hence, the centrifugation step precipitated the amorphous aggregates allowing the soluble Aβ to form amyloid fibrils. The initial agitation of the solution through vortexing accelerated the nucleation process there by shortening the lag phase. The oligomers formed were small enough to escape precipitation during the centrifugation step. These oligomers then proceeded through a shorter lag phase followed by a rapid growth phase of amyloidogenesis.

6.4 Discussion

Aβ is the most extensively studied amyloidogenic peptide because of its discovery in Alzheimer's disease (Loo et al. 1993). In vitro aggregation of Aβ seems to be a slow process but may not necessarily proceed at the same rate in vivo. The method applied here shows that rate of amyloid formation by Aβ is decreased by competing with formation of amorphous material. The new protocol will be useful for a number of biophysical applications. For example, in the search for effective inhibitors of Aβ amyloid formation because the more rapid rate of amyloid formation increases the rate at which compounds can be screened. In addition, the significant decrease in time makes it easier to conduct in vitro screens of marginally stable proteins that might inhibit Aβ but lose activity during the time course of the normal assay. Recently, a number of heat shock and small heat shock proteins have been reported to inhibit Aβ progression to amyloid fibrils (Wilhelmus et al. 2006A, Wilhelmus et al. 2006B). Thus the protocol outlined here can be of great use for the testing of such proteins for any of their inhibitory properties. Most of these proteins stay well folded when stored at low temperatures but can degenerate if kept at room temperature for long periods of time. An enhancement in the rate of aggregation shortens the time of fibrillization. This can allow for testing proteins of relatively less stability as well. This protocol can serve as an effective way of rapid screening of both small molecule and protein based inhibitors.

6.5 Figures

DAEFRHDSGYEVHHQKLVFFAEDVGSNKGAIIGLNVGGVV

DAEFRHDSGYEVHHQKLVFFAEDVGSNKGAIIGLNVGGVVIA

Figure 1. Amino acid sequence of Aβ40 (blue) and Aβ42 (green) generated from the cleavage of amyloid precursor protein.

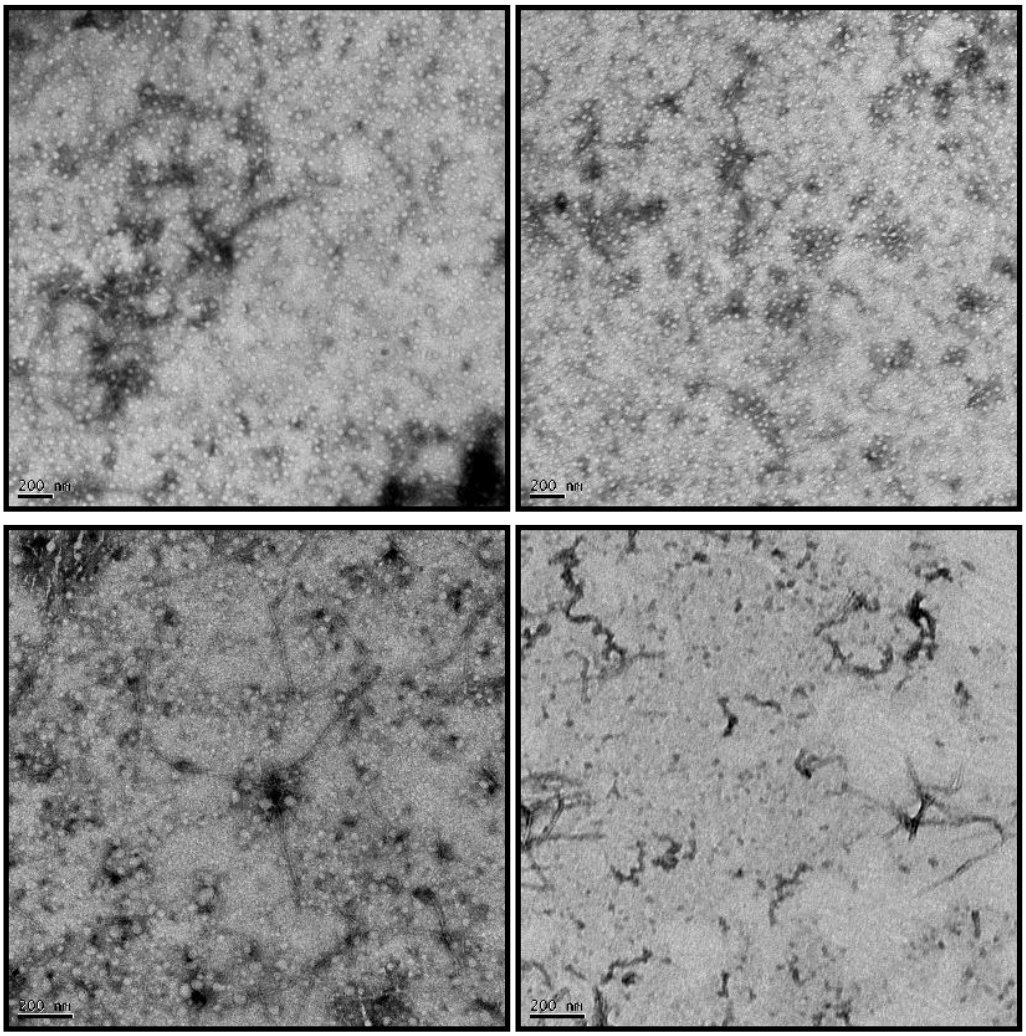

Figure 2. Transmission Electron Micrograph (TEM) images of a 64μM sample of Aβ42 in 20mM NaH_2PO_4 at pH 7.4 using Teplow's protocol after 46 hours. The scale bar corresponds to 200nm.

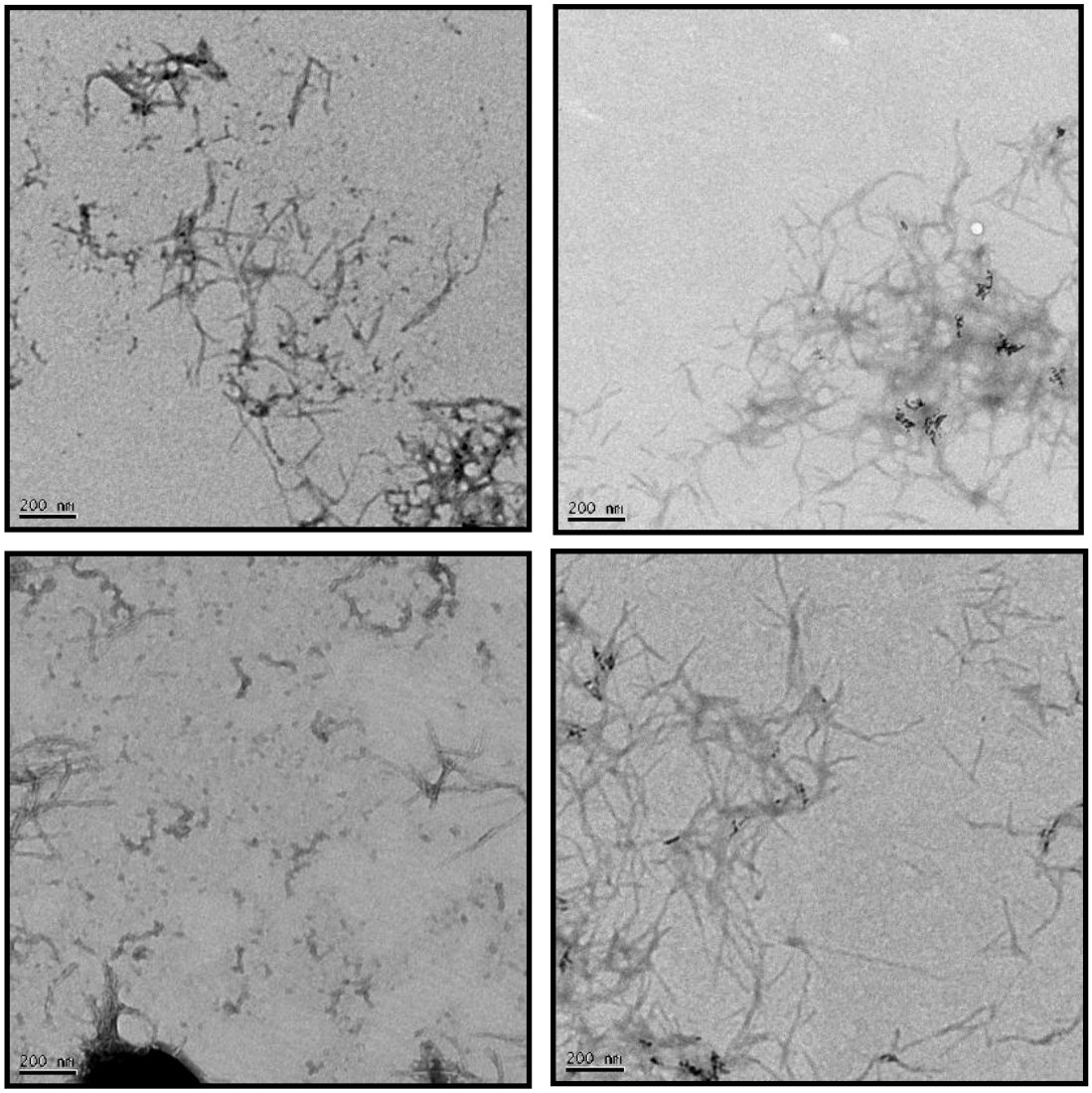

Figure 3. Transmission Electron Micrograph (TEM) images of a 64μM sample of Aβ42 in 20mM NaH_2PO_4 at pH 7.4 using Teplow's protocol after 5 days. The scale bar corresponds to 200nm.

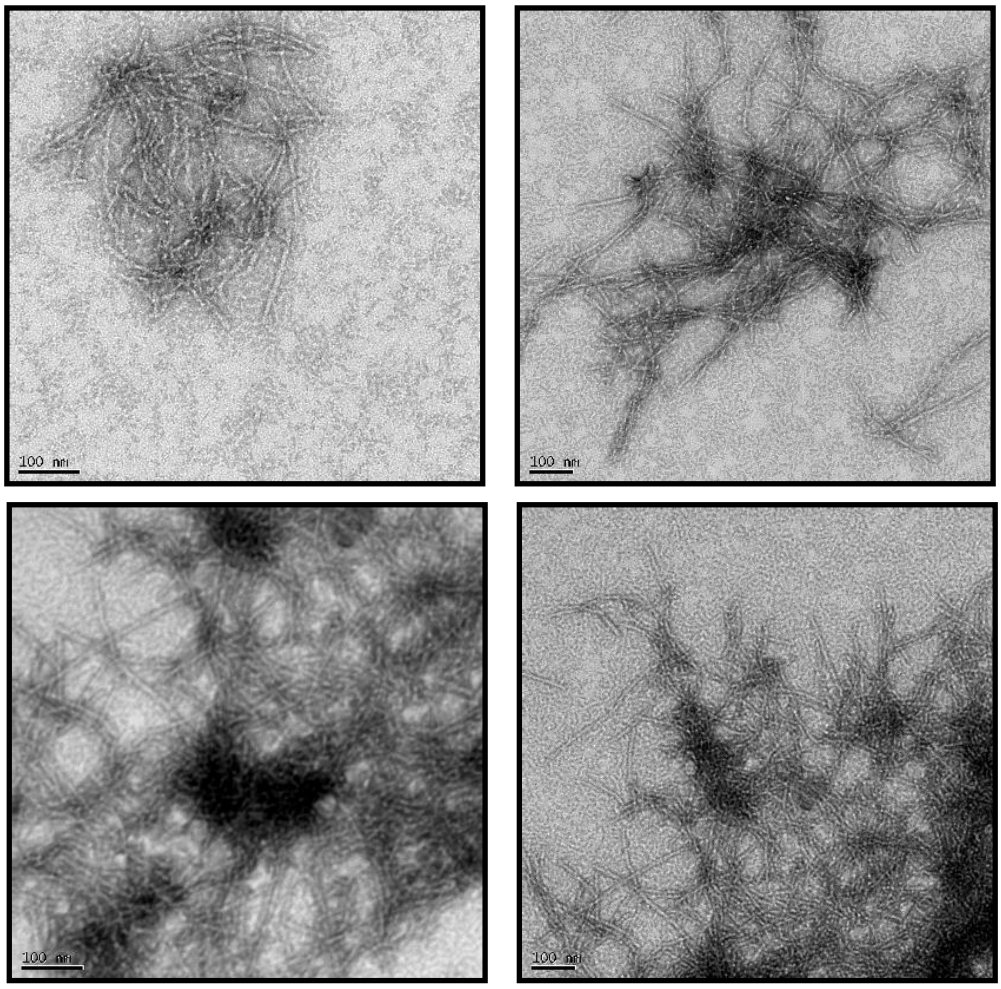

Figure 4. Transmission Electron Micrograph (TEM) images of a 64μM sample of Aβ42 in 20mM NaH_2PO_4 at pH 7.4 using Teplow's protocol after 9 days. The scale bar corresponds to 100nm.

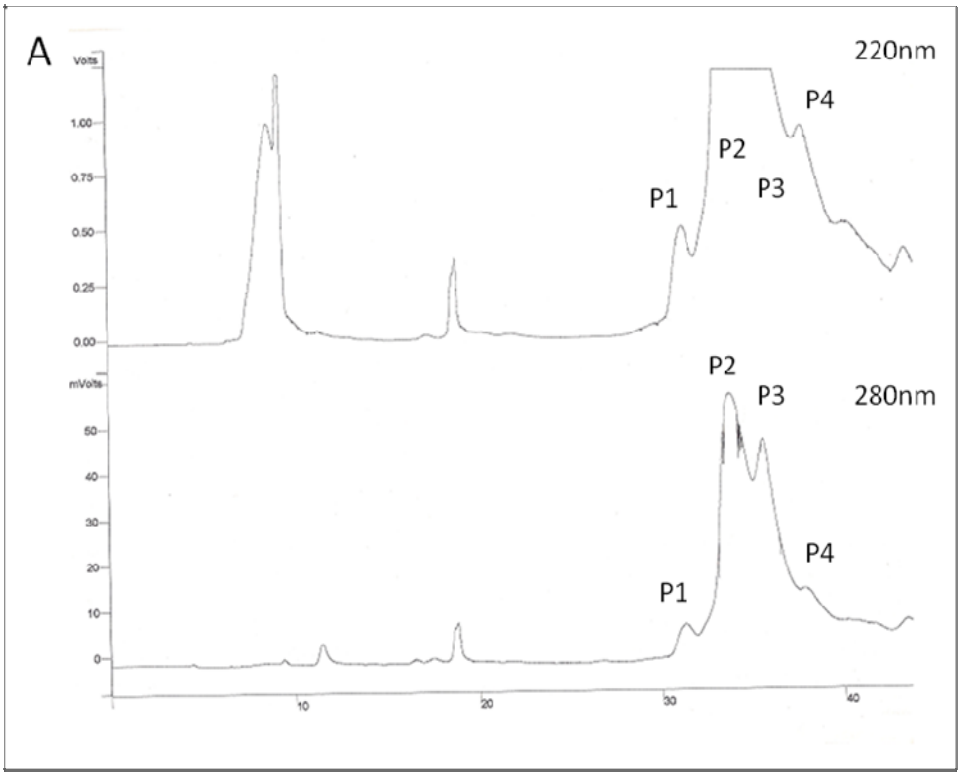
A
220nm
Volts
1.00
0.75
0.50
0.25
0.00
P1
P2
P3
P4
mVolts
50
40
30
20
10
0
280nm
P1
P2
P3
P4
10
20
30
40

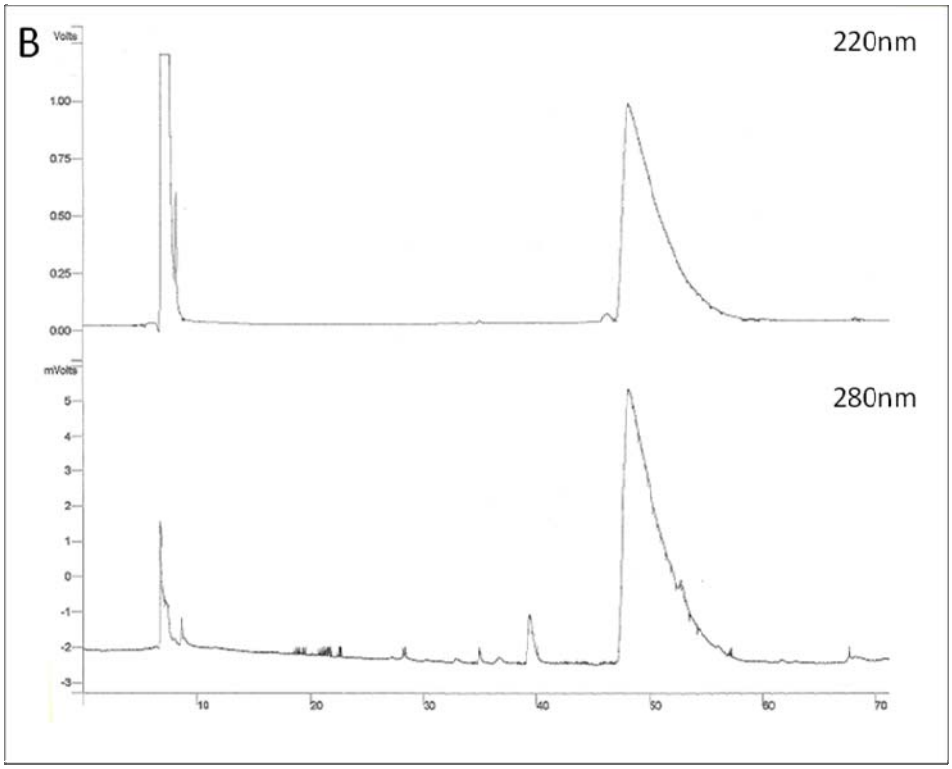
B
Volts
1.00
0.75
0.50
0.25
0.00
220nm
mVolts
5
4
3
2
1
0
-1
-2
-3
280nm
10
20
30
40
50
60
70

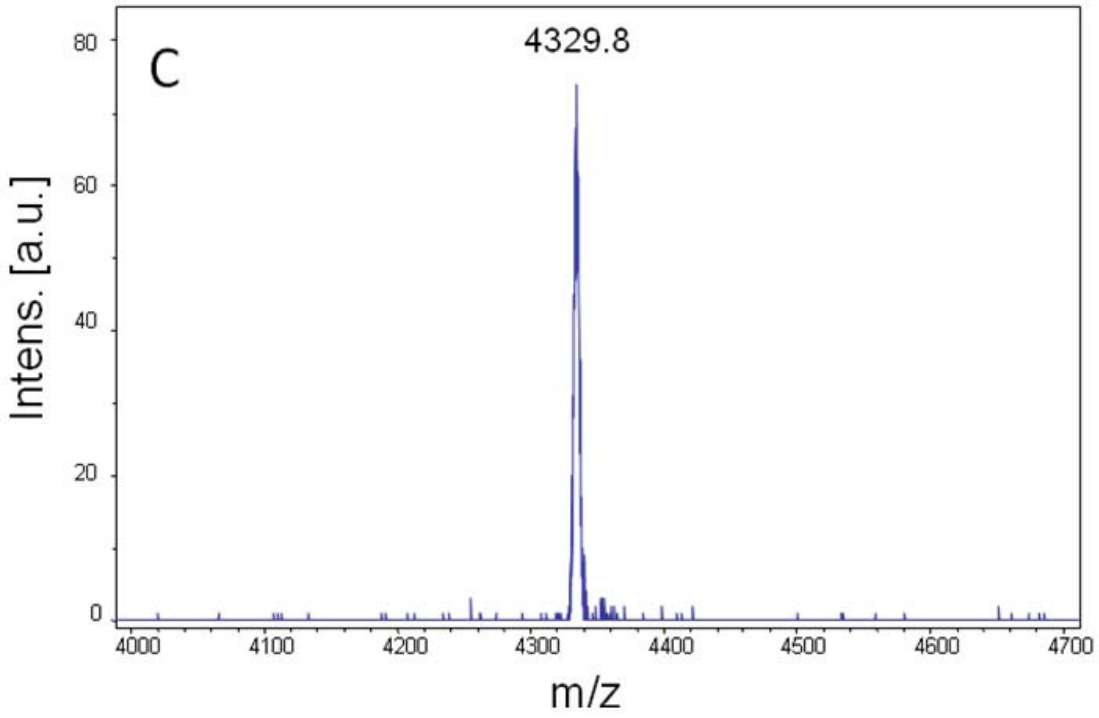

Figure 5. Aβ40 A) HPLC purification of the crude peptide. The gradient used was 15-90% buffer B in 75 minutes. B) Analytical HPLC trace of the purified peak P2 at a gradient of 0-90% buffer B in 90 minutes. C) MALDI-TOF of the purified peptide (from peak P2) showing the expected molecular weight, which is, 4329.8Da.

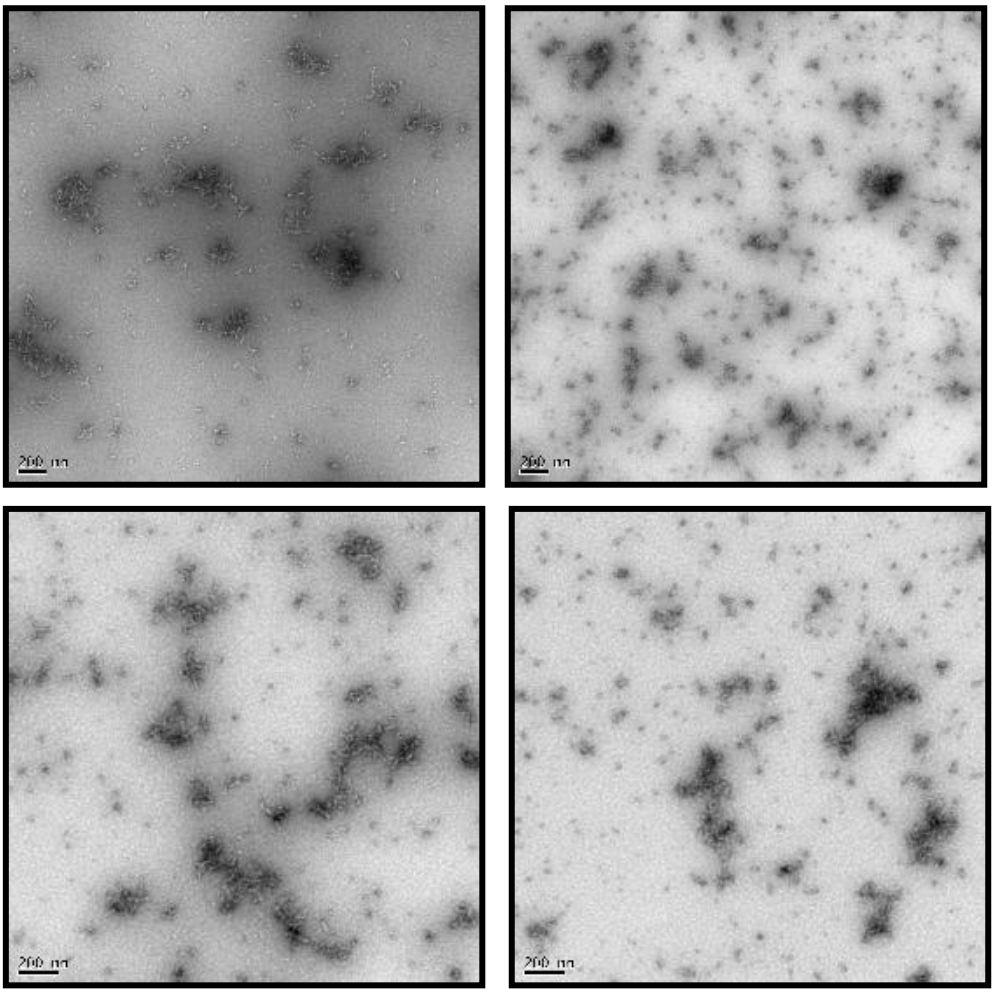

Figure 6. TEM images of aliquots withdrawn at 0 hr from Aβ42 fibril formation reaction. The concentration of the peptide was 64μM in 100mM Tris at pH 7.4. The scale bar corresponds to 200nm.

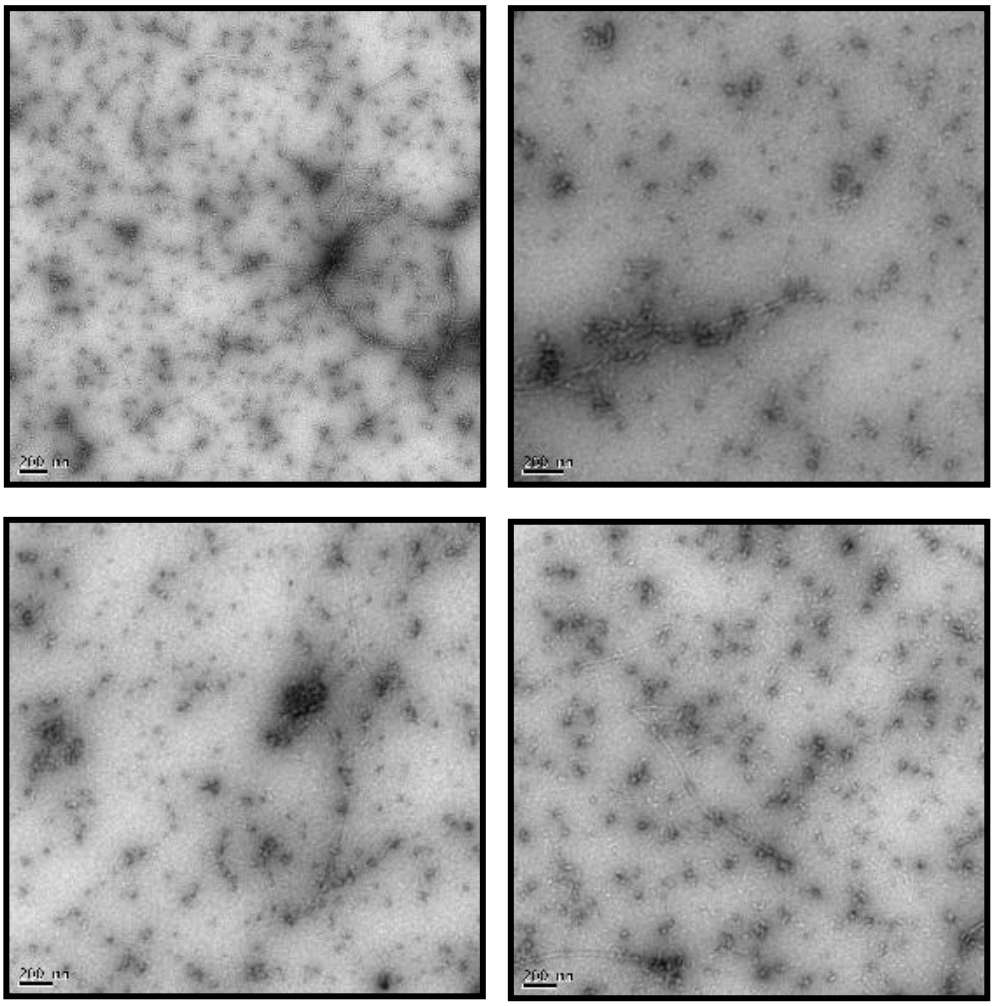

Figure 7. TEM images of aliquots withdrawn at 5 hrs from Aβ42 fibril formation reaction. The concentration of the peptide was 64μM in 100mM Tris at pH 7.4. The scale bar corresponds to 200nm.

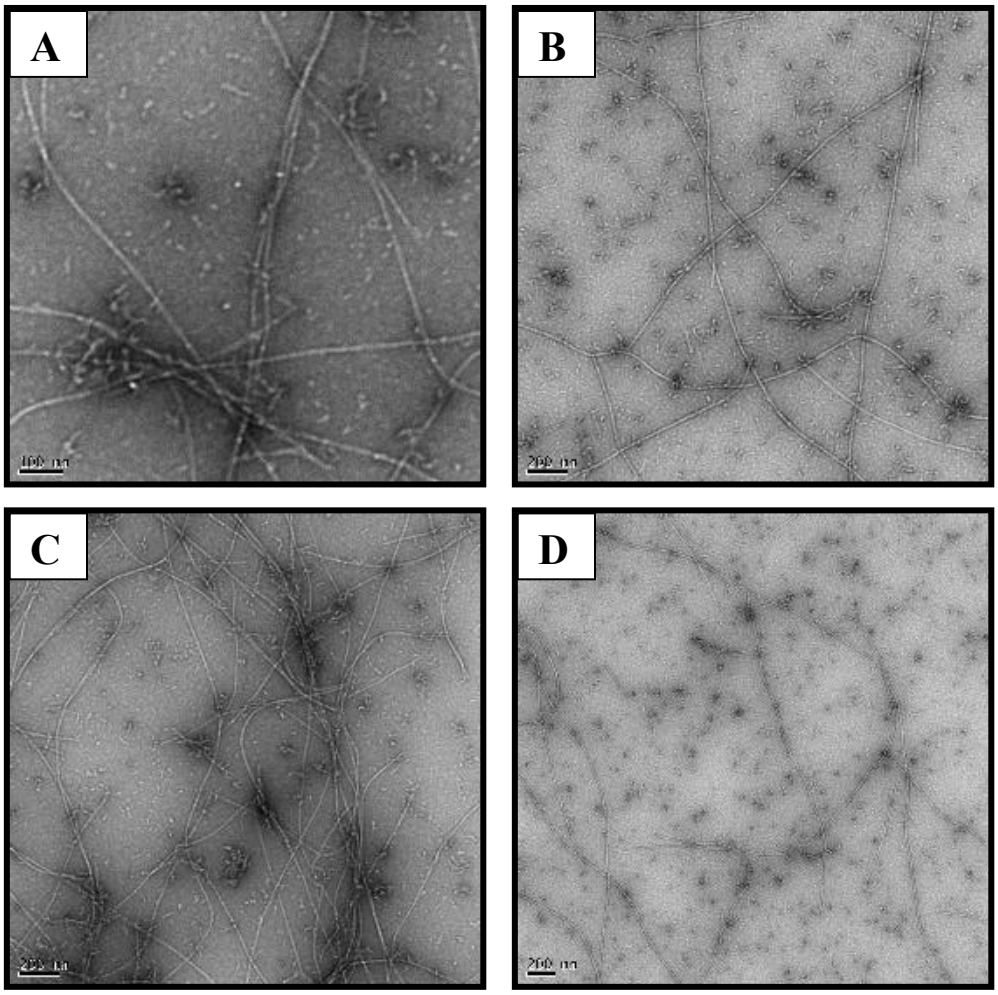

Figure 8. TEM images of aliquots withdrawn at 12 hrs from Aβ42 fibril formation reaction. The concentration of the peptide was 64μM in 100mM Tris at pH 7.4. The scale bar for A corresponds to 100nm and B-D corresponds to 200nm.

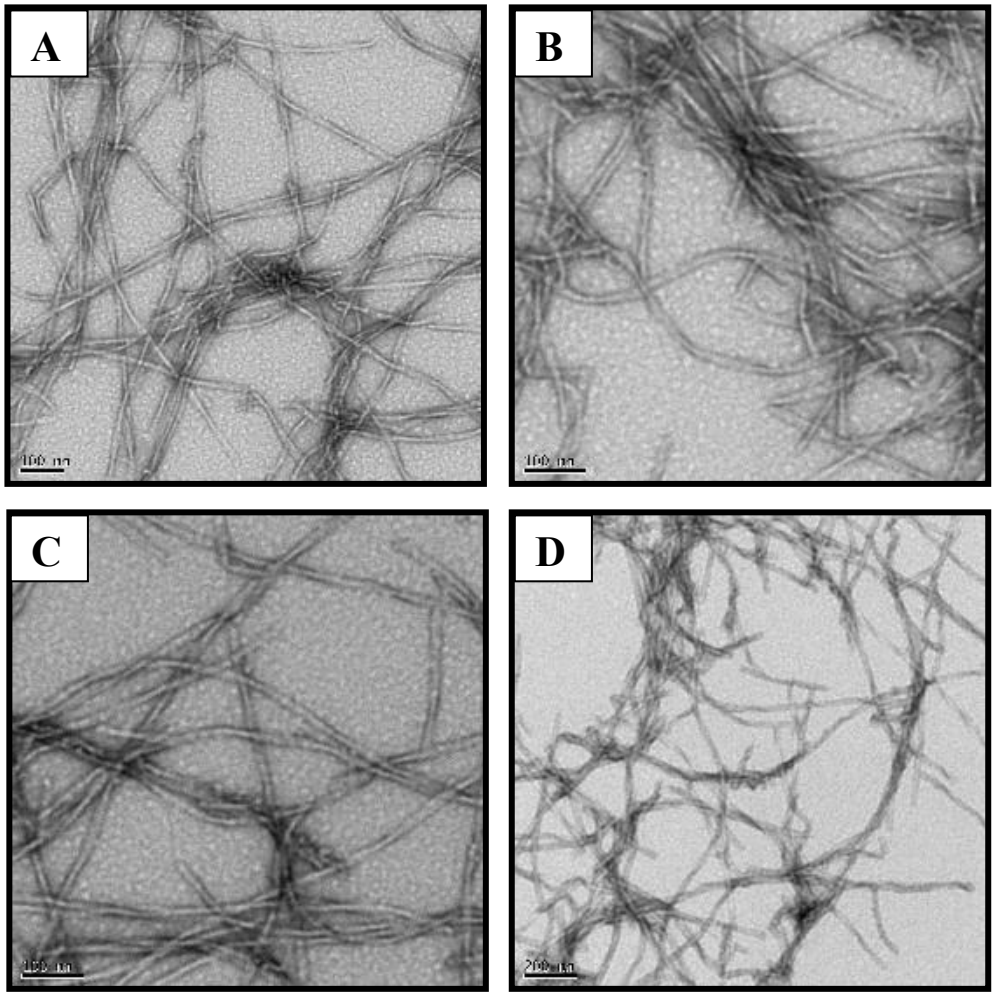

Figure 9. TEM images of aliquots withdrawn at 24 hrs from Aβ42 fibril formation reaction. The concentration of the peptide was 64μM in 100mM Tris at pH 7.4. The scale bar for A-C corresponds to 100nm and D corresponds to 200nm.

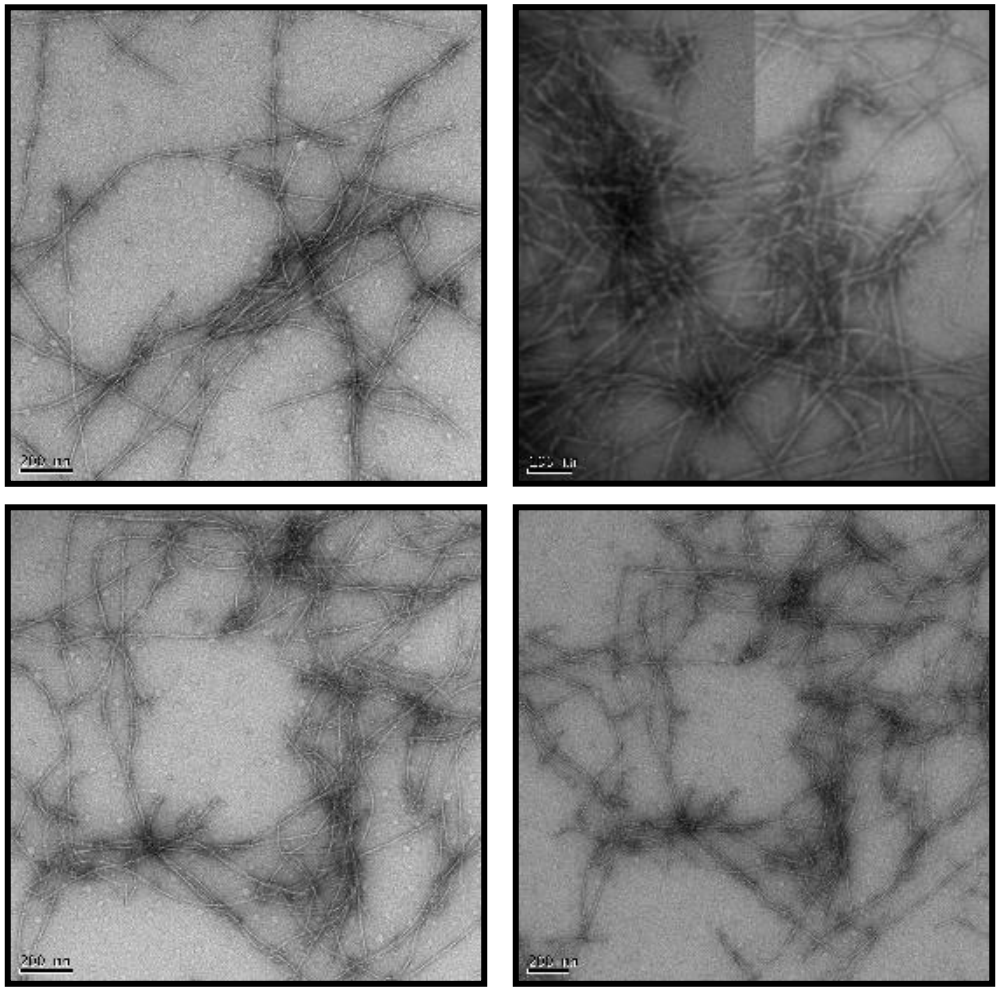

Figure 10. TEM images of aliquots withdrawn at 24 hrs from Aβ42 fibril formation reaction. The concentration of the peptide was 32μM in 100mM Tris at pH 7.4. The scale bar corresponds to 200nm.

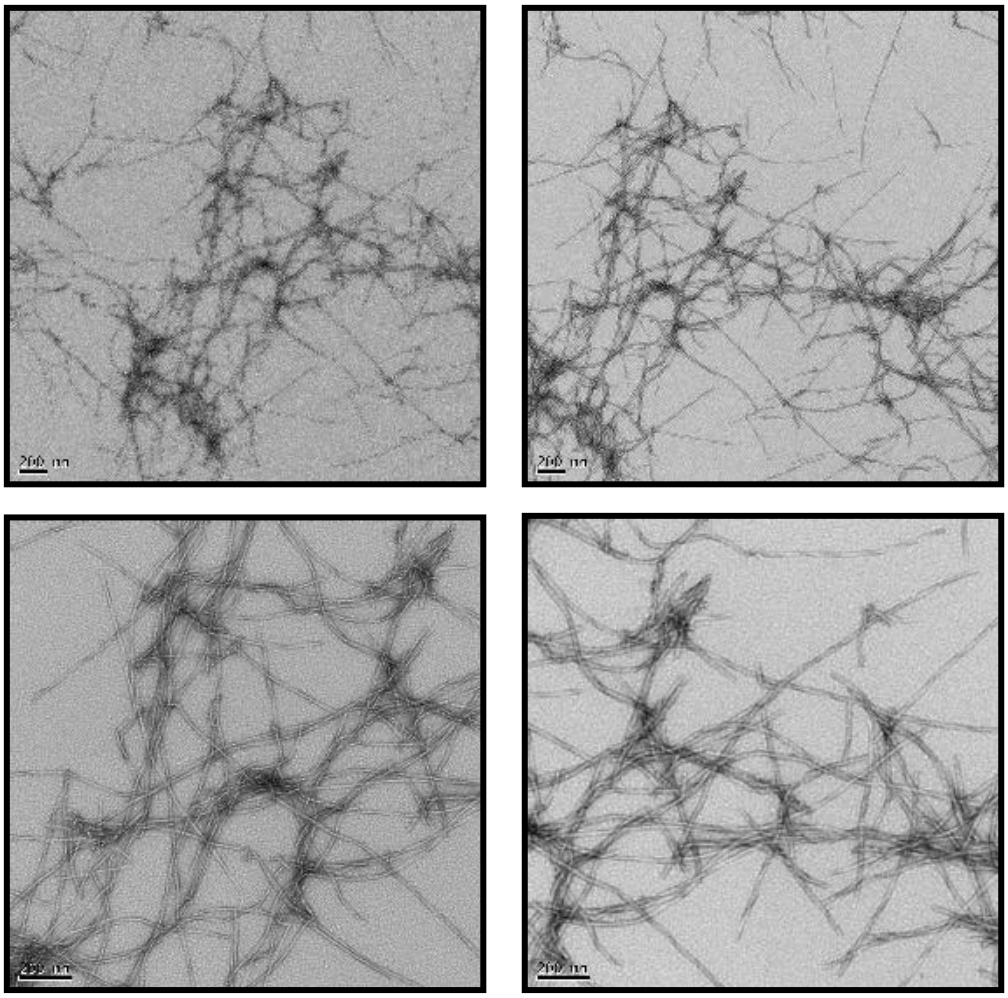

Figure 11. TEM images of aliquots withdrawn at 24 hrs from Aβ40 fibril formation reaction. The concentration of the peptide was 248μM in 100mM Tris at pH 7.4. The scale bar corresponds to 200nm.

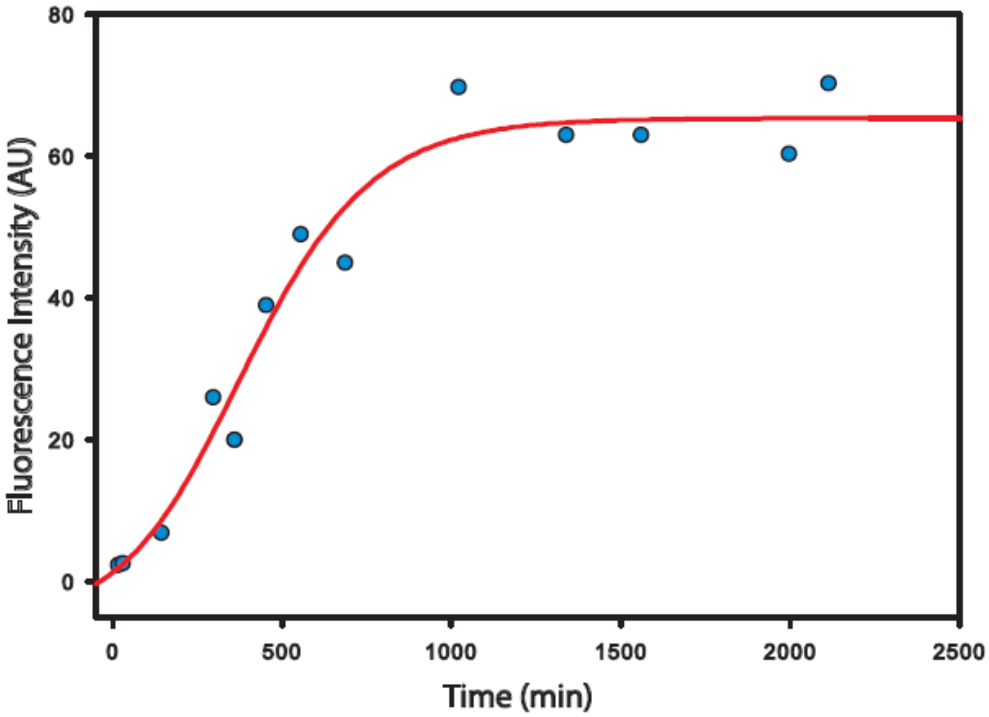

Figure 12. Thioflavin-T monitored kinetic curve for Aβ40 fibrillization reaction.

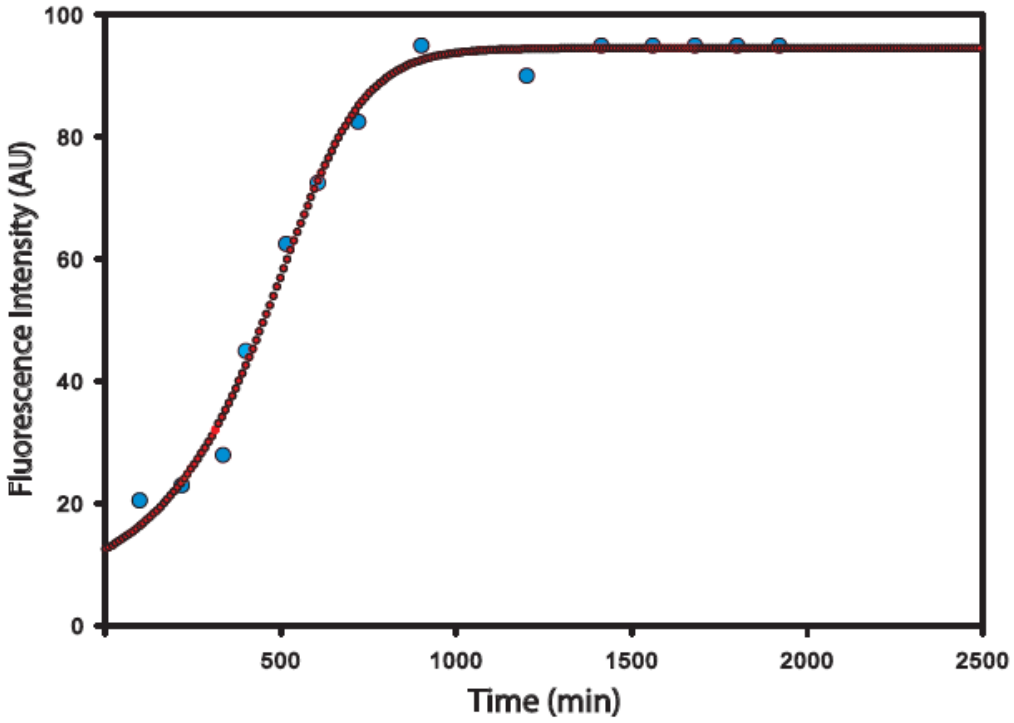

Figure 13. Thioflavin-T monitored kinetic curve for Aβ42 fibrillization reaction.

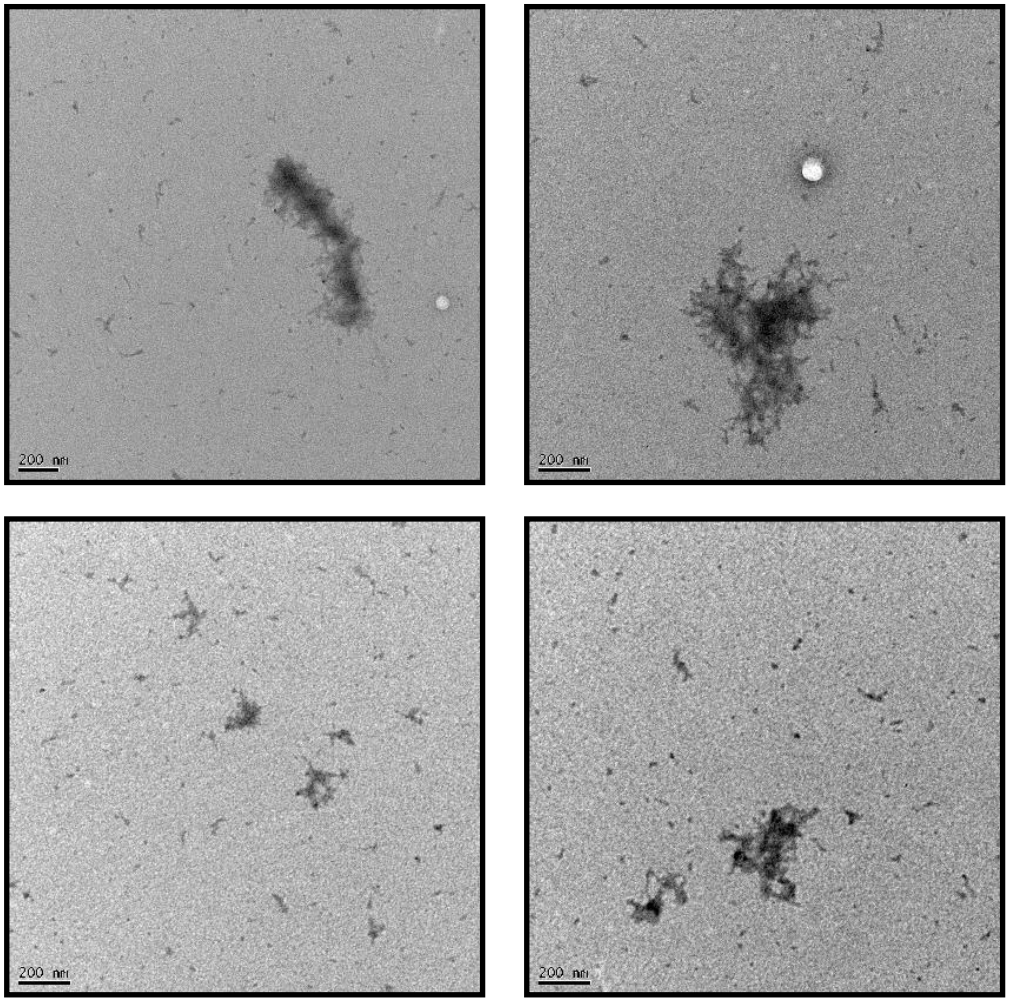

Figure 14. TEM images of aliquots withdrawn at 5 hrs from Aβ42 fibril formation reaction, without centrifugation. The concentration of the peptide was 64μM in 100mM Tris at pH 7.4. The scale bar corresponds to 200nm.

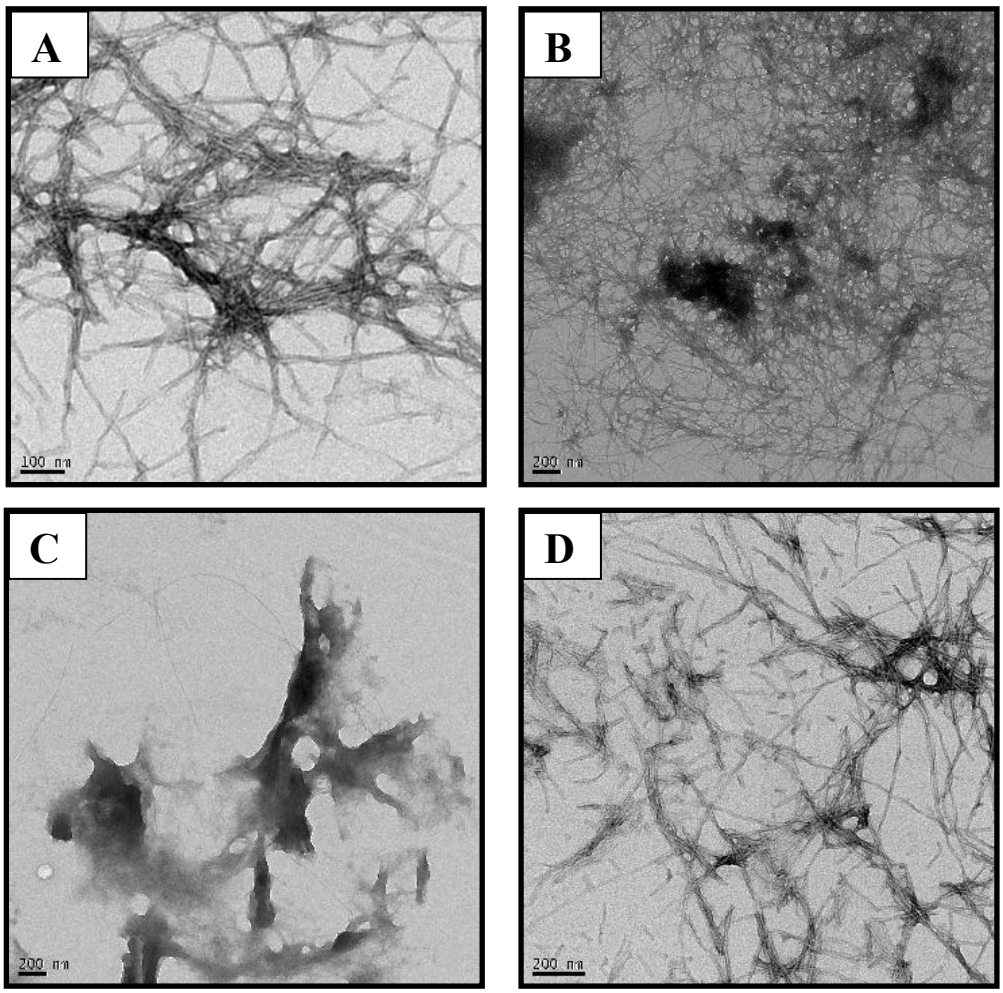

Figure 15. TEM images of aliquots withdrawn at 19 hrs from Aβ42 fibril formation reaction, without centrifugation. The concentration of the peptide was 64μM in 100mM Tris at pH 7.4. The scale bar for A corresponds to 100nm and B-D corresponds to 200nm.

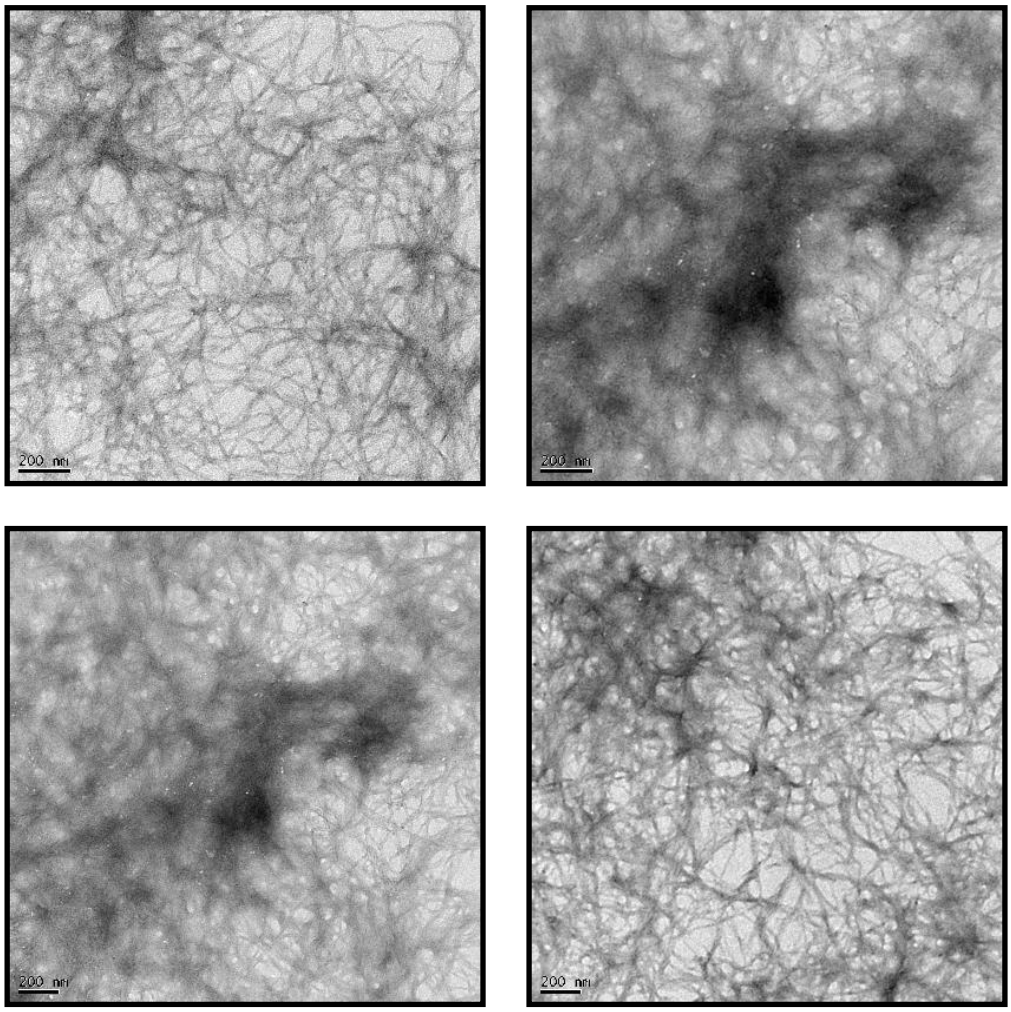

Figure 16. TEM images of aliquots withdrawn at 24 hrs from Aβ42 fibril formation reaction, without centrifugation. The concentration of the peptide was 64μM in 100mM Tris at pH 7.4. The scale bar for corresponds to 200nm.

Chapter 7. Inhibition of amyloidogenesis by a novel human protein Calnuc

7.1 Introduction

The work described in this chapter was conducted as part of collaboration between Professor Thomas Sakmar's laboratory at Rockefeller University and Professor Raleigh's laboratory at Stony Brook University. The Sakmar laboratory has a long standing interest in Calnuc. The experiments outlined below were performed with Mr. Neeraj Kapoor at the Sakmar lab and additional assistance was provided by Dr. Santosh Menon for selected studies.

Calnuc or Nucleobindin1 (NUCB1) is a 55kDa protein, which was first reported to be a growth and differentiation factor associated with lupus syndrome (Kanai et al, 1992). Calnuc acquires its name from its DNA-binding and calcium binding ability. Its domain structure comprises of a signal sequence at its N-terminus followed by a DNA binding domain of basic residues, 2 EF hands and a leucine zipper (Miura et al. 1992). Both the DNA binding domain and leucine zipper are crucial for binding of Calnuc to DNA. This chapter describes the role of Calnuc in the inhibition of amyloidogenesis.

Calnuc has been postulated to be involved in several important cellular functions. However, the pathways associated with the functionality of Calnuc, which require its

conservation across the animal kingdom, still remain to be deciphered. Since its discovery, Calnuc has been reported to be widely expressed in cells and tissues and is conserved from flies to humans (Kawano et al. 2000). This suggests that Calnuc is an essential calcium binding protein present in the eukaryotic genome. Calnuc is primarily a golgi resident protein found in both cytosolic and membrane fractions (Lin et al. 1998). $^{45}Ca^{2+}$-binding assays with golgi fractions revealed Calnuc to be the major calcium binding protein in golgi. In fact, Calnuc shows high homology with the ER resident protein Calreticulin and displays similar properties suggesting it has a role in both calcium storage and homeostasis in golgi. Osteocytes and osteoblasts have also been reported to produce Calnuc where it is thought to function as a modulator of matrix maturation during mineralization process in the bone (Petersson et al. 2004). The calcium binding ability of Calnuc was found to cause accumulation and transport of Ca^{2+} ions to the mineralization front before hydroxyapatite deposition in bones (Somogyi et al. 2004).

As a first step in understanding the ubiquitous nature of Calnuc, the pathway of secretion for this protein was investigated through pulse-chase experiments. It was found that Calnuc is synthesized in the ER and then transported to the Golgi where it resides for more than 12 hours. In the Golgi, Calnuc undergoes O-glycosylation and sulfation and is then secreted into the extracellular medium via the constitutive-like pathway (Lavoie et al. 2002). Interactions with Cox-1 and Cox-2 isozymes have been shown to be involved in the retention of Calnuc in the ER (Ballif et al. 1996). Calnuc has also been shown to interact with the $G\alpha_i$ and $G\alpha_s$ subunits of heterotrimeric G-proteins and has been postulated to participate in regulating downstream signaling (Lavoie et al. 2002). Recent *in vitro* studies have suggested that overexpression of Calnuc down-regulates the mRNA

production of Amyloid precursor protein (APP) and inhibits its biosynthesis (Lin et al. 2007). Aggregation of Aβ isoforms generated from the sequential proteolytic cleavage of APP by β- (Beta Amyloid Cleaving Enzyme-1) and γ-secretase has been well characterized in Alzheimer's disease. In addition, abnormal calcium homeostasis has also been observed in the brains of demented patients. In further support of the hypothesis for a role of Calnuc in Alzheimer's disease pathogenesis, it was suggested based on one study that the level of Calnuc is decreased in the brains of Alzheimer's disease patients by 50% (Lin et al. 2007).

Research conducted on amyloidogenic peptides over the years has been helpful in explaining the process of fibril formation, energetics governing the process and the structural details of the fibrils. However, the understanding of the events that trigger aggregation of these otherwise soluble proteins and of the natural defense mechanisms against fibril formation is still obscure and speculative. Generally the initiation of aggregation of amyloidogenic peptides *in vivo* goes unnoticed and by the time a patient starts showing any disease symptoms, the aggregating species have already begun damaging important cellular components and disrupting signaling pathways. Thus an ideal therapeutic approach would be to disaggregate fibrils which are already formed, prevent the dissociated aggregates from forming toxic species and inhibit any further aggregation of the soluble monomer. This work describes studies of Calnuc and shows it has promising function in both disaggregation and inhibition of the amyloidogenic peptides Amylin and Aβ.

7.2 Methods and Materials

7.2.1 Protein Synthesis and Purification

Wild type human IAPP (Amylin) was synthesized on a 0.25mmol scale using 9-fluornylmethoxycarbonyl (Fmoc) chemistry on an Applied Biosystems 433A Peptide Synthesizer at Stony Brook. 5-(4'-Fmoc-aminomethyl-3',5-dimethoxyphenol) valeric acid (PAL-PEG) resin was used to generate an amidated C-terminus. Pseudoproline dipeptide derivatives were employed as described (Abedini and Raleigh 2005). Fmoc-protected pseudoproline (oxazolidine) dipeptide derivatives were purchased from Novabiochem. All other reagents were purchased from Advanced Chemtech, Fischer Scientific, PE Biosystems and Sigma Aldrich. All solvents used were of A.C.S. grade. Standard Fmoc reaction cycles were used. The first residue added to the resin, pseudoproline dipeptide derivatives, all β-branched residues and all residues following the β-branched residue were double coupled. The peptide was cleaved from the resin using standard trifluoroacetic acid (TFA) methods. The crude peptide was treated with 20% (v/v) acetic acid and lyophilized. The disulfide bond was formed via DMSO induced oxidation of the crude peptide. The oxidized peptide was purified via reverse-phase HPLC using a Vydac C-18 preparative column. A two-buffer system utilizing HCl as an ion-pairing agent was used for the purification. Buffer A consisted of 0.045% (v/v) HCl in distilled de-ionized (DDI) water. Buffer B consisted of 80% (v/v) acetonitrile, 20% (v/v) DDI water and 0.045% (v/v) HCl. The purity of the peptide was checked by HPLC and was 99%.

The purified peptide was analyzed by matrix-assisted laser desorption/ionization time-of-flight (MALDI-TOF) mass spectroscopy. The observed molecular weight was 3903.4Da and the expected molecular weight was 3903.3Da.

7.2.2 Calnuc Expression and Purification

The expression and purification of Calnuc was done in Prof. Sakmar's lab at Rockefeller University by Neeraj Kapoor and Dr. Santosh Menon.

7.2.3 Circular Dichroism Spectroscopy

Wavelength scan: All CD experiments were performed using an Aviv 62A DS CD spectrophotometer at Stony Brook. Spectra were recorded over the wavelength range of 190-250nm at 1nm intervals with an averaging time of 3s using a 0.1cm path length cell. Background spectrum was subtracted from each of the collected data sets. Each spectrum obtained was an average of 3 scans.

Thermal unfolding: The unfolding of the protein with temperature was monitored using CD at a wavelength of 222nm, which is characteristic of an α-helix at Stony Brook. The data points were averaged over 30 seconds for every unit increment in temperature. A plot of CD signal versus temperature was fit to equation (1):

$$f(T) = \frac{\alpha_N + \beta_N * T + (\alpha_D + \beta_D * T) * e^{\frac{-\Delta G^{\circ}_{D\_N}(T)}{RT}}}{1 + e^{\frac{-\Delta G^{\circ}_{D\_N}(T)}{RT}}} \quad (1)$$

where,

$$\Delta G^{\circ}_{D\_N}(T) = \Delta H^{\circ}_{D\_N}(T_m) * \left(1 - \frac{T}{T_m}\right) - \Delta C^{\circ}_{p} * \{(T_m - T) + T * \ln\left(\frac{T}{T_m}\right) \quad (2)$$

f(T) is the signal as a function of temperature, T is the temperature, R is the gas constant, α_N defines the intercept and β_N is the slope of the post-transition region of the curve, α_D defines the intercept and β_D is the slope of the pre-transition region of the curve, ΔG^o is the free energy change for the unfolding reaction, $\Delta H^o_{D\text{-}N}$ is the change in enthalpy for unfolding at the T_m and ΔC_p^o is the change in heat capacity.

Using the above expressions T_m, the mid-point transition temperature was estimated, along with the change in enthalpy $\Delta H^o_{D\text{-}N}$, for the unfolding reaction at that T_m.

7.2.4 Analytical Ultracentrifugation

Sedimentation equilibrium studies were carried out at different pH values and at different protein concentrations at Stony Brook. The samples were run for sufficiently long periods of time to allow for equilibrium to be reached. The speeds 20000, 30000 and 40000 rpm were decided based on the molecular weight of the protein. Under no net transport conditions, the following correlation should be observed between concentration and the radial distance (Van Holde, 1985):

$$C_{r} = C_{r_0} * e^{\frac{\sigma^2}{2}(r^2 - r_0^2)} \quad (3)$$

where,

$$\sigma = M(1 - \nu\rho)\frac{\omega^2}{RT} \quad (4)$$

where, C_r is the concentration of macrosolute at any radial distance r, C_{r0} is the concentration of the macrosolute at the reference radial distance r_0, υ is the partial specific volume, ω is the angular velocity, ρ is the density, R is the gas constant , T is the

absolute temperature and M is the molecular mass. The data was analyzed using Optima^{TM} XL-A/XL-I Data Analysis Software (Beckman, 2001). The value of solvent density and partial molar specific volume for each buffer was calculated using SEDENTERP 1.08.

7.2.5 Transmission Electron Microscopy

TEM was performed at the Bioimaging facility at Rockefeller University. Samples were prepared by placing 15µl of solution onto formvar coated 300 mesh copper grids and counterstained with 2% aqueous uranyl acetate. Samples were viewed with a FEI Tecnai12 BioTwinG^2 transmission electron microscope at 80 kV. Digital images were acquired with an AMT XR-60 CCD Digital Camera System and compiled using Adobe Photoshop CS2.

7.2.6 MTT Assay

7000 to 9000 undifferentiated PC12 cells were plated in each well per 100µl of culture medium. Cells were grown for an additional 12-16 hrs at 37^{o}C in an incubator with 5% CO_2 supply. Samples to be tested for toxicity were added to the cells at a concentration of 10µM/well and the cells were incubated for an additional 4 hrs. After 4 hrs, 10µl of the MTT stock solution was added to the cells, which were incubated for another 4-6 hrs. After this, the media was withdrawn and 200µl of DMSO was added to each well to dissolve the reduced MTT (formazan) crystals. Spectrophotometric measurement of the absorbance at 570nm was done for each well and cell viability was

calculated based on the measured absorbance with respect to the vehicle absorbance at Rockefeller University.

7.2.7 Right Angle Light Scattering Experiment

Amylin aggregation and formation of amyloid fibrils was monitored by right angle light scattering on a Jobin Yvon Horiba fluorescence spectrophotometer using an excitation and emission wavelength of 500 nm with slit widths of 5 nm for both excitation and emission at Rockefeller University. The samples were prepared in 20mM Tris at pH 7.4 and light scattering was monitored as a function of time.

7.3 Results

Amylin in aqueous solution readily aggregates to form extensive β-sheet fibrils. These fibrillar masses show characteristic β-sheet structure by CD and criss-crossed long fibrils, which are spread all over the grid in TEM images (Fig. 1). The fibrils once formed are stable with no trace of disaggregation over several months and show strong resistance to dilution. However, incubation of these fibrillar deposits with Ca^{2+} free Calnuc triggered complete disassociation of fibrils within minutes of Calnuc addition. Aliquots of the reaction mixture analyzed through TEM showed gradual dissolution of the fibrils into species that lacked fibrillar morphology (Fig. 1). No reappearance of fibrillization was observed even after hours of incubation. Amylin aggregation monitored by light scattering generally shows a characteristic sigmoidal growth curve (Fig. 2a). However when Ca^{2+} free Calnuc was added after completion of the fibril formation, the light scattering intensity gradually decreased reaching values corresponding to the species

present at the start of the reaction (Fig. 2b). The disaggregation of fibrils by Calnuc was reversed when 5mM Ca^{2+} was added to the disaggregation reaction (Fig. 3). Binding of Ca^{2+} to Calnuc seemed to mask the ability of Calnuc to interact with Amylin fibrils and initiate their disaggregation. The disaggregation experiments conducted with Ca^{2+} bound Calnuc showed fibrils under TEM imaging (Fig. 4).

In a similar set of experiments, Ca^{2+} free Calnuc when incubated with Amylin in a 1:1 ratio showed a remarkable ability to inhibit aggregation. Reactions were run with 32 μM Amylin and 32 μM Ca^{2+} free Calnuc. TEM images of the samples withdrawn from the reaction mixture at various time points showed no signs of fibrils (Fig. 5). However, a control experiment of Amylin alone in 20mM Tris at pH 7.4 showed extensive fibrillization with time (Fig. 6). Right angle light scattering measurement of the kinetics of Amylin aggregation in the presence of Ca^{2+} free Calnuc showed no enhancement in the particle size over hours of incubation (Fig. 7). The inhibition of Amylin aggregation by Calnuc was also Ca^{2+} sensitive. Addition of 5mM Ca^{2+} to the inhibition reaction triggered fibril formation as assessed by TEM (Fig. 8).

Calnuc is a 461 amino acid protein, which is about 12 times the size of Amylin (Petersson et al. 2004). In order to test the specificity of Calnuc in inhibiting aggregation and disaggregating fibrils, control experiments were done with bovine serum albumin (BSA). Incubation of Amylin with BSA at a ratio of 1:5 did not inhibit the amyloid formation and extensive fibrillar deposits could be seen spread all over the TEM grid (Fig. 9). Hence, the inhibition and disaggregation ability was indeed a functional activity of Ca^{2+} free Calnuc.

The inhibition was found to be dependent on the concentration of Calnuc. Ca^{2+} free Calnuc when present in equimolar amount with Amylin was very effective in keeping Amylin soluble in solution. As the ratio of Calnuc was decreased to one-third with respect to Amylin, the inhibition was still effective. No significant fibrillization was seen until the ratio was reduced to 1:5 Calnuc to Amylin. However, as the concentration of Ca^{2+} free Calnuc was decreased further, fibrils were observed. The extent of fibril formation was thus correlated to the molar ratio of Calnuc and Amylin in the reaction mixture (Fig. 10).

Aggregation of Amylin involves an initial lag phase, which is associated with the formation of a nucleus. This nucleation phase is followed by the growth phase where monomers/oligomers add on to the nucleus converting the protofibrillar species into mature fibrils (Merlini and Bellotti 2003). Most inhibitors of amyloidogenesis, known to date, either prolong the lag phase or slow down the growth phase. To understand the inhibition of amyloid by Calnuc, Ca^{2+} free Calnuc was added at different time points of the Amylin fibril formation reaction in stoichiometric ratio of 1:1. Calnuc when added to Amylin at the start of the reaction (t=0) resulted in complete inhibition of fibril formation (Fig. 1). In the second reaction, Amylin oligomerization was allowed to proceed for 2 min into the reaction after which equimolar amount of Calnuc was added. TEM images showed complete inhibition of fibril formation (Fig. 11). In the third reaction, Calnuc was added after the nucleation phase of Amylin aggregation was complete (t=7min). TEM analysis convincingly showed that Ca^{2+} free Calnuc was able to inhibit fibrillization even after nucleation of Amylin (Fig. 12). In the fourth experiment, the fibrillization reaction was allowed to proceed to the growth phase and Calnuc was added during the elongation

phase (t=15min). The samples were withdrawn 60min after the addition of Calnuc and TEM analysis showed inhibition of fibrillization (Fig. 13). The results of this last experiment are somewhat difficult to interpret because Calnuc is likely performing two functions namely disaggregating any fibrils formed and inhibiting aggregation of the soluble pool of Amylin. These studies support the observation that Ca^{2+} free Calnuc can inhibit the aggregation of Amylin at any stage during the fibrillization reaction. This result is important because physiologically because Amylin could be present in a wide range of forms varying from monomers to oligomers to fibrils. The results show that Calnuc can interact with monomers, oligomers as well as protofibrils and prevent their progression to fibril formation.

The next aim was to test the generality of Calnuc on other amyloidogenic proteins. The pathogenesis in Alzheimer's disease has been shown to be strongly correlated with the aggregation of Aβ peptide (Loo et al. 1993, Howlett et al. 1995). Aβ is produced in two different isoforms in the body, namely Aβ40 and Aβ42. Aβ42 has been shown to aggregate much more aggressively than Aβ40 (Glenner and Wong 1984). Thus Aβ42 was chosen to test the functional ability of Calnuc. The aggregation of Aβ42 generally takes at least 6 days with constant stirring at room temperature (Teplow 2006). The stability of Calnuc over this time period in a test tube at room temperature could affect the interpretation of the observed results. Thus, a new protocol was developed to accomplish Aβ42 aggregation within 24 hours (refer to Chapter 6). Ca^{2+} free Calnuc was added in equimolar ratio at the end of fibrillization reaction. TEM images of the samples withdrawn at different time points after the addition of Calnuc showed complete dissociation of fibrils (Fig. 14). Rigorous analysis of the grid showed no trace of fibrils in

any of the samples. Similarly, when Ca^{2+} free Calnuc was added in stoichiometric ratio at the start of Aβ42 fibrillization reaction, no fibril formation was observed. TEM images of the samples withdrawn from the reaction mixture at various time points showed no progression of fibrillization (Fig. 15). Thus, the ability of Ca^{2+} free Calnuc to disaggregate formed fibrils and to inhibit aggregation appears to be general or at least to be applicable to Amylin and Aβ42.

The formation of extracellular amyloid deposits by Aβ has been shown to be cytotoxic to neuronal cells. Amyloid aggregation progresses through the formation of various low molecular weight oligomers, which associate to form protofibrils whose 3-dimensional organization further leads to amyloid fibril formation (Kayed et al. 2003). Tissue culture based MTT assays provide evidence of the cytotoxicity of both pre-fibrillar and fibrillar species (Lambert et al. 1998, Hartley et al. 1999, Hoshi et al. 2003). The inhibition and disaggregation of Aβ42 fibrils by Ca^{2+} free Calnuc prevented the formation of fibrillar architecture. However, generation of pre-fibrillar species could not be ruled out by TEM analysis. Thus, it is possible that Aβ42 monomers could associate into oligomers in the presence of Calnuc. If oligomeric species are indeed cytotoxic, interaction of Calnuc with Aβ could enhance cytotoxicity towards neuronal cells. To test the potential toxicity of the species that result from the disaggregation of Aβ42 fibrils by Ca^{2+} free Calnuc, MTT assays were conducted with PC12 cells. In the first set of experiments, samples were withdrawn at different time points during the Aβ42 fibril formation reaction at t=0, t=5 hr and t=24 hr. Each sample was analysed using TEM before administeration to the cells. The morphology of the samples corresponded to the TEM images of Aβ42 aggregation (Fig. 16). These aliquots were then administered to

undifferentiated PC12 cells and their cytotoxicity was assayed through reduction of MTT. The cytotoxicity was found to increase with the progression of fibril formation. In the presence of monomers, neuronal cells showed 80% viability. As the monomers assembled into prefibrillar species, the viability decreased to 60%. The formation of fibrils further reduced the cell viability to 40%. In the next set of experiments, these fibrils were incubated with Ca^{2+} free Calnuc for various time periods and the toxicity of the samples was assayed through MTT reduction by PC12 cells. After incubation for a given time, the samples were added to PC12 cells. The cell viability corresponding to Calnuc disaggregated species was found to be 90% after 5minutes of incubation. The samples withdrawn after 15 to 60 min of incubation with Calnuc showed increased cell survival to more than 95% (Fig. 17). Thus, the results of the cell based assays show very promising effects of Calnuc in disaggregation of neurotoxic species. In each of the cell based experiments, the cells were incubated with the samples for an additional 4 hrs before addition of MTT in the 96-well plate. This might cause further aggregation of the samples. However, the rate of aggregation would be slow since the plate was not stirred or agitated. Similarly, Ca^{2+} free Calnuc was also found to inhibit aggregation of Aβ42 and caused no increase in the cytotoxicity as was observed on aggregation of Aβ42 in the absence of Calnuc (Fig. 18).

In all of the above experiments, the role of Calnuc against amyloidogenesis was effective only in the absence of calcium. This suggested that binding of Ca^{2+} to Calnuc might be inducing some conformational changes in Calnuc. The resulting structure was unable to prevent the fibril formation or cause the disaggregation of existing fibrils. The domain architecture of Calnuc shows 2 EF hand regions sandwiched between a DNA

binding domain and the leucine zipper at its C-terminus (Alba and Tjandra 2004) (Fig. 19). EF hand regions are known to be a characteristic feature of calcium binding proteins. The formation of an octahedral co-ordination sphere on binding of calcium causes structural rearrangement in the protein (Cates et al. 1999). Thus, circular dichroism was employed to monitor any secondary structural rearrangement in Calnuc on binding to calcium. The comparison of the spectra obtained in the presence and absence of calcium showed no significant structural change in Calnuc on calcium binding (Fig. 20). However, Ca^{2+} binding is expected to induce structure in the region of the EF hands which is a small portion of the protein. Furthermore, NMR studies have shown that the EF hand domain is partially structured in the absence of Ca^{2+}. Thus any additional helical structure induced by Ca^{2+} binding may be too modest to be detectable by CD. CD data collected at increasing concentrations of Calnuc showed a smooth structural transition from a α-helix at lower concentrations to β-sheet morphology at concentrations higher than 32μM. The concentration dependent structural change was found to proceed both in the absence and presence of calcium (Fig. 21). A plot of mean residue ellipticity at 222 nm showed an increase with increase in concentration of Calnuc (Fig. 22). This data might suggest concentration dependent association.

Thermal unfolding studies of Calnuc showed an increase in T_m of 4^oC on binding of calcium to Calnuc (Fig. 23). The folding of Calnuc was observed to be irreversible both in the absence and presence of calcium in the sense that the CD signal after heating and re-cooling differed from the initial value. The increase in stabilization on binding to calcium suggests some structural ordering on Ca^{2+} binding. However, Ca^{2+} binding the rearrangement was not visible through CD spectra. This may not be surprising given the

size of the protein and the small number of residues, which would become ordered in the EF hand regions.

The C-terminus of Calnuc also has a leucine zipper motif (Fig. 19). These are helices with a leucine at every seventh position. This structural motif is a common dimerization domain where dimerization proceeds through hydrophobic interactions among stacked leucine residues (Landschulz et al. 1988). Analytical Ultra Centrifugation (AUC) studies on Calnuc revealed that Calnuc preferentially exists as a dimer irrespective of the presence of calcium. The data analysis for Calnuc concentrations varying from 50μM to 150μM gave a molecular mass corresponding to a dimer (Fig. 24). Non-specific association was ruled out by repeating the experiment at several different rotor speeds. CD spectra at 50μM Calnuc concentration corresponded to a β-sheet structure. Thus, it might be possible that the structural transition as observed in CD might be related to the dimerization of Calnuc.

AUC experiments were also conducted on a homolog of Calnuc called NUCB2. NUCB2 is 421 amino acid protein which lacks the 40 residues at the C-terminus found in Calnuc. It shares 65% sequence homology with Calnuc and has a similar domain architecture to Calnuc (Oh-I et al. 2006). Molecular weight analysis from AUC data shows that NUCB2 also exists as a dimer both in the presence and absence of calcium ions (Fig. 25). This can be explained by the presence of a characteristic leucine zipper motif at its C-terminus similar to Calnuc. NUCB2 when incubated with Amylin monomers in a 1:1 ratio during the amyloid formation reaction was efficient in inhibiting fibrillization (Fig. 26-28). However, Amylin fibrils when incubated with NUCB2 showed no signs of dissociation (Fig. 29). The inhibition of amyloidogenesis by NUCB2 like

Calnuc was also calcium sensitive. Thus, NUCB2 was effective in inhibiting fibril formation but the lack of 40 residues at its C-terminus disabled NUCB2 from disaggregating fibrils. Thus, NUCB2 serves as a good model system for understanding the mechanism of Calnuc's efficacious functionality against amyloidogenesis.

7.4 Discussion

The factors that inhibit aggregation of naturally occurring amyloidogenic peptides and prevent the toxicity of peptide aggregates are not well known. In the past decade, the focus of developing Alzheimer's disease inhibitors has grown from small molecule inhibitors to discovering proteins that keep these hydrophobic peptides in solution. Indeed, a significant number of heat shock proteins (Hsp's) and small heat shock proteins (sHsp's) have been shown to inhibit aggregation of amyloidogenic peptides (Wilhelmus et al. 2006, Wilhelmus et al. 2006). These proteins function by interacting with the prefibrillar species and preventing their growth into amyloid fibrils. However, this strategy in some cases like Clusterin results in enhanced toxicity by stabilization of the toxic intermediates (Oda et al. 1995, Yerbury et al. 2007).

The only other known protein candidates for disaggregation agents are Neprilysin (NEP) and low-density lipoprotein receptor-related protein (LRP). NEP targets Aβ diffuse deposits and neuritic plaques to cause their catalytic degradation (Marr et al. 2005). LRP, on the other hand, binds to Aβ or to its chaperone complex with LRP ligands such as α2 Microglobulin or apolipoprotein E4 and delivers the complex to lysosomes for degradation (Ito et al. 2007).

The observation that Calnuc can prevent fibril formation by both Amylin and Aβ42 peptides is remarkable and unique. Calnuc is the first protein of its kind to execute both the inhibition of aggregation and the disassociation of fibrillar deposits of amyloidogenic proteins. It is interesting to consider the possibility that calcium sensitivity might serve as a switch to regulate the levels of functional forms of naturally occurring amyloidogenic proteins. The ability of Calnuc to reverse fibrillization at any stage of aggregation has great potential as a drug. An increase in the cell viability with Calnuc disaggregated fibrils shows that the resulting species are non-toxic and well accepted by cells.

The results offered by the Calnuc experiments described in this chapter are encouraging. The next step in this research is to test for inhibition of the formation of amyloid plaques and the ability to disaggregate pre-existing plaques in the brains of relevant mouse models of amyloid disease. Understanding the mechanism employed by Calnuc in executing its function against amyloid formation should provide insight into strategies for keeping amyloidogenic proteins from aggregating in normal individuals. Protein models like NUCB2 and biophysical tools should aid in decoding this mechanism.

7.5 Figures

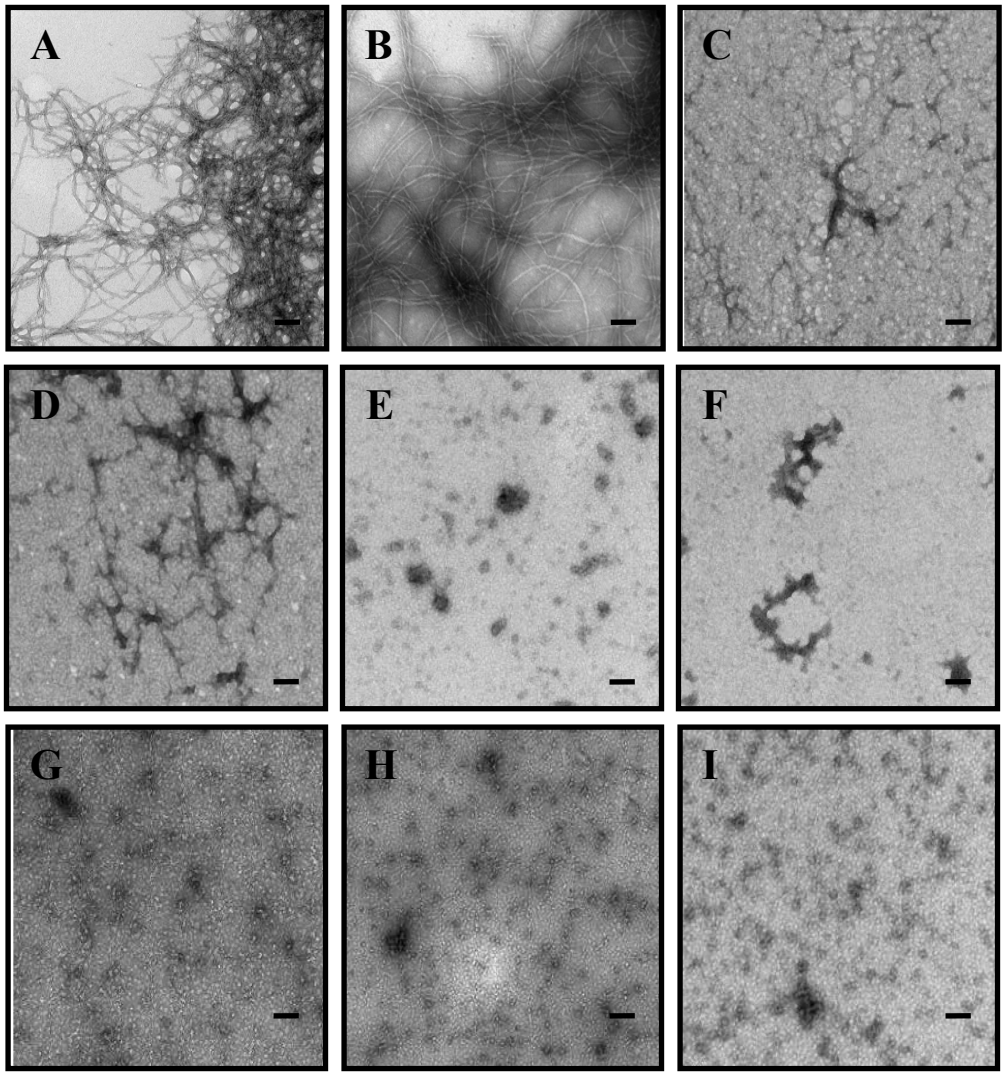

Figure 1. Disaggregation of Amylin fibrils by calcium free Calnuc. The images continue on the next page.

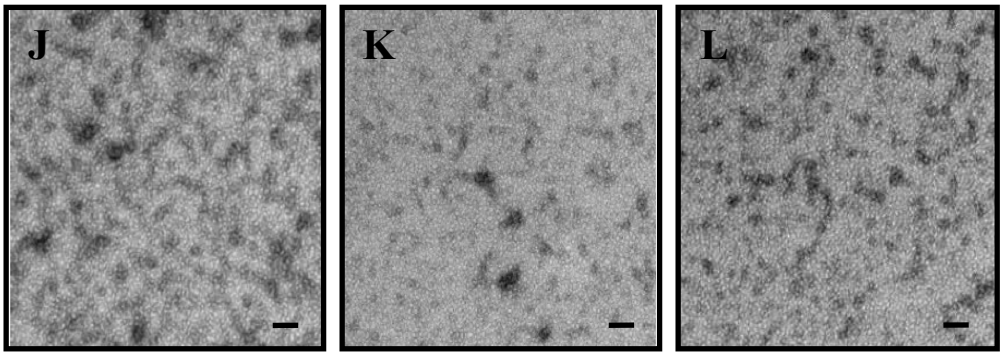

Figure 1. Disaggregation of Amylin fibrils by calcium free Calnuc. Amylin fibrils (panel A-B) were incubated with Ca^{2+} free NUCB1 in a 1:1 stoichiometric ratio at 25^{o}C and 20mM Tris. Samples were withdrawn at different time points to monitor diaggregation. Panel C-D (t = 1min), panel E-F (t = 2min), panel G-H (t = 2min 37sec), panel I-J (t = 8min) and panel K-L (t = 80min). Scale bar in the images represents 200nm. All solutions contain 2% HFIP by volume.

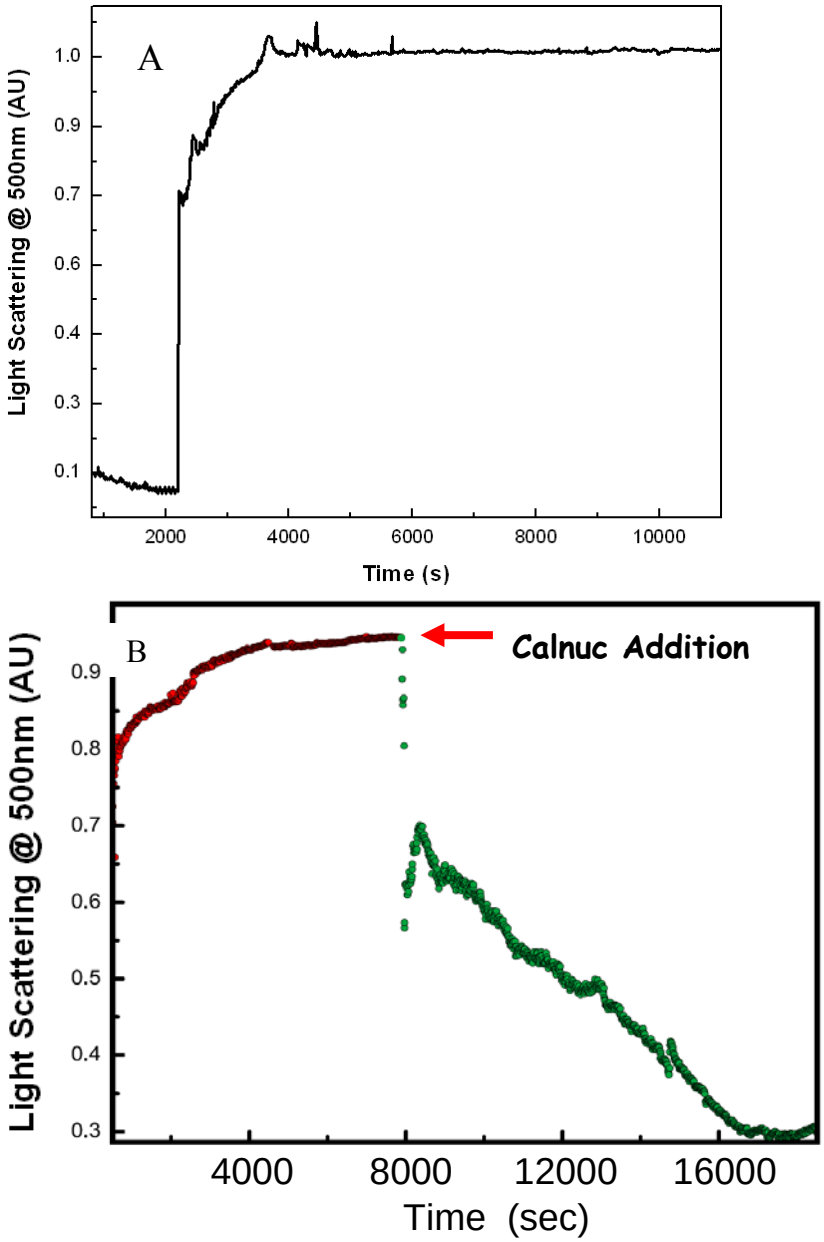

Figure 2. Right Angle Light scattering shows (a) aggregation of the amylin peptide and (b) disaggregation of amylin fibrils once Calnuc is injected into a reaction volume containing amylin fibrils. The vertical scale is individual normalized on each plot. Thus absolute intensities are not comparable in different panels. Each reaction contained 20mM Tris at pH 7.5, 2% HFIP, 32μM Amylin and 32μM Ca^{2+} free Calnuc with stirring speed of 3.

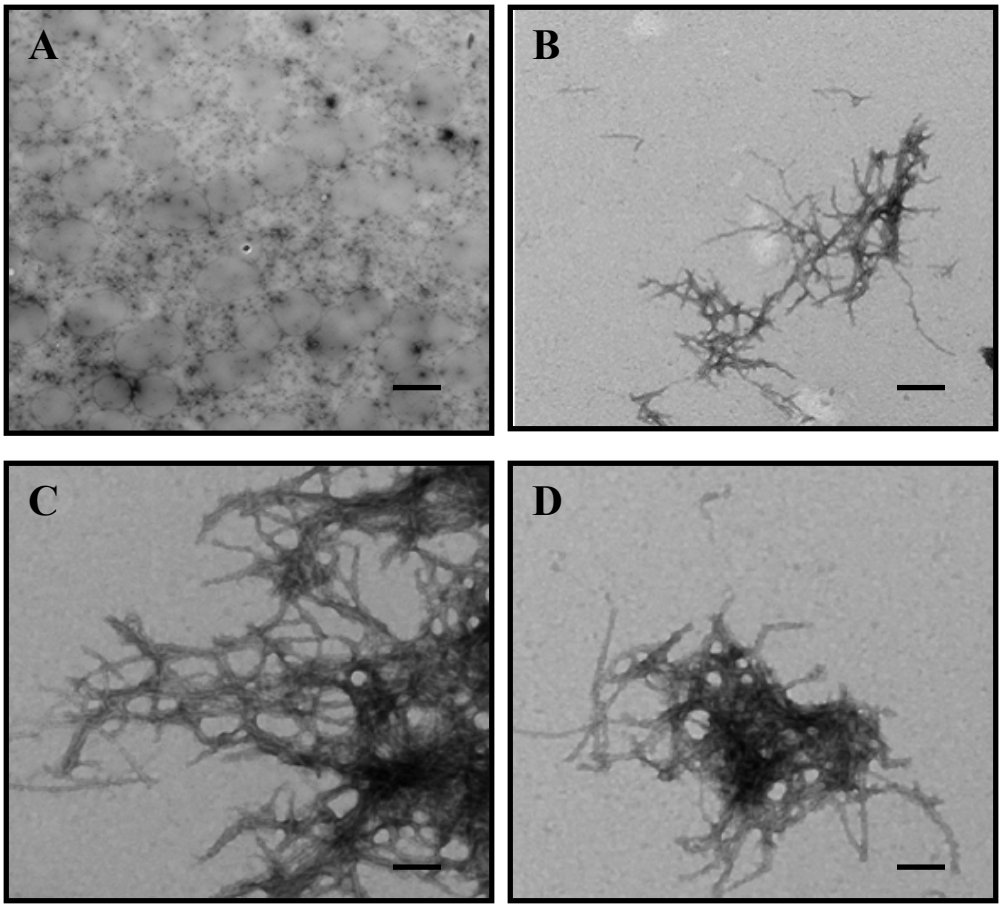

Figure 3. Reappearance of Amylin fibrils upon addition of 5mM Ca^{2+} to the reaction mixture containing Amylin and Calnuc in a 1:1 ratio (32μM concentration of each in 20mM Tris at pH 7.5). TEM analysis of the samples withdrawn after 60mins shows the reappearance of fibrillar species in the reaction mixture. Scale bar in the images represents 200nm. Panel A represents images of samples before addition of Ca^{2+} to the reaction mixture. Panels B, C, D are images of samples 60 min after addition of Ca^{2+} to the reaction. The reaction contained 20mM Tris at pH 7.5, 2% HFIP, 32μM Amylin and 32μM Ca^{2+} free Calnuc with stirring speed of 3.

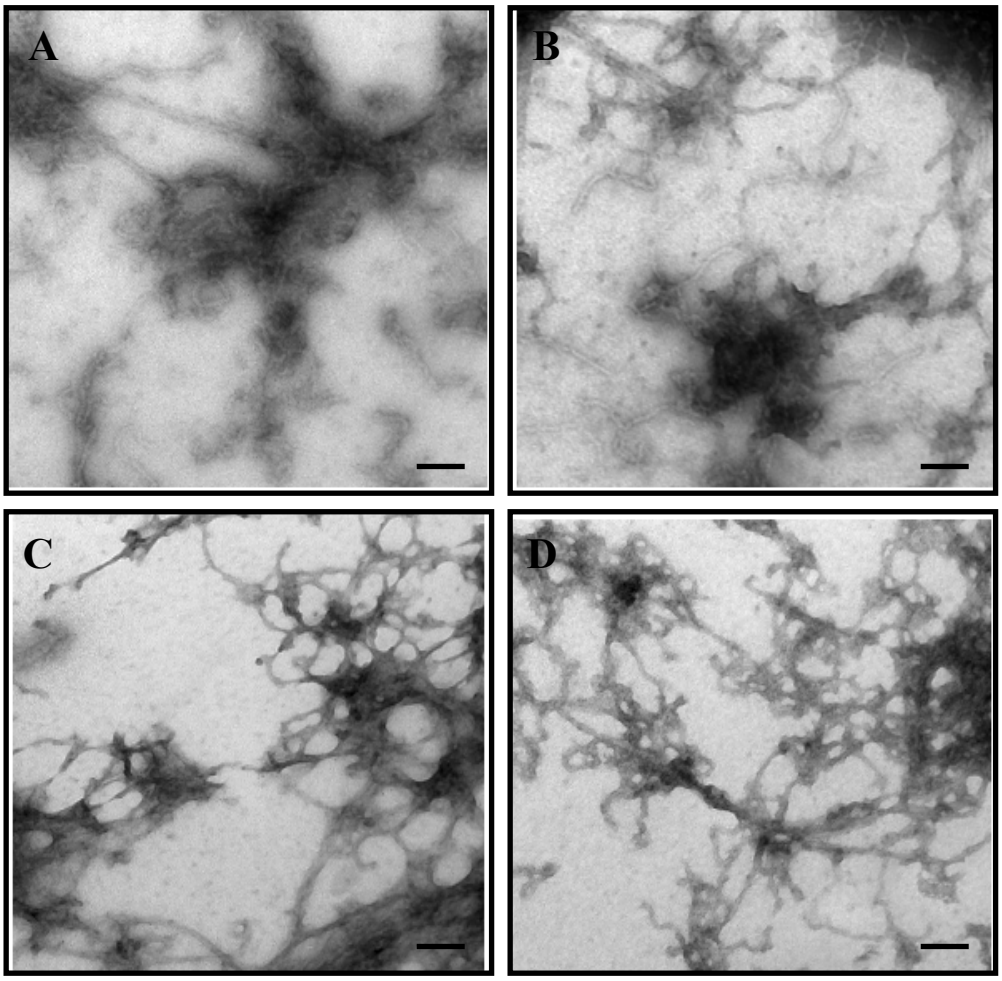

Figure 4. TEM images of samples withdrawn from a 1:1 stoichiometric ratio of 32μM each of calcium bound Calnuc (5mM Ca^{2+}) and Amylin peptide in 20mM Tris at pH 7.5. The samples were withdrawn after 30 minutes of incubation at 25^{o}C. Scale bar in the images represents 200nm. The reaction contained 20mM Tris at pH 7.5, 2% HFIP, 32μM Amylin and 32μM Ca^{2+} bound Calnuc with stirring speed of 3.

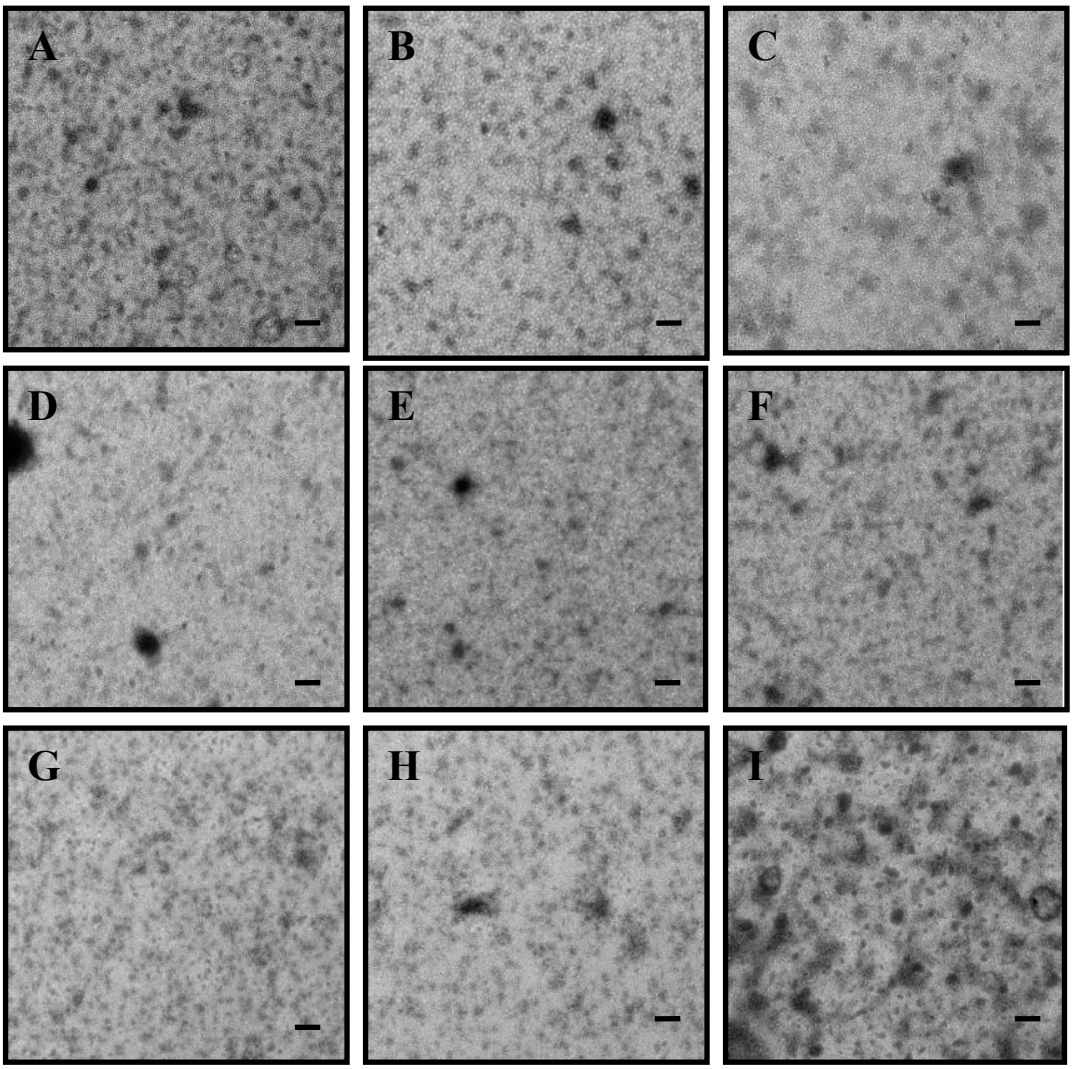

Figure 5. Inhibition of Amylin fibril formation by calcium free Calnuc. The rest of the images are shown on the next page.

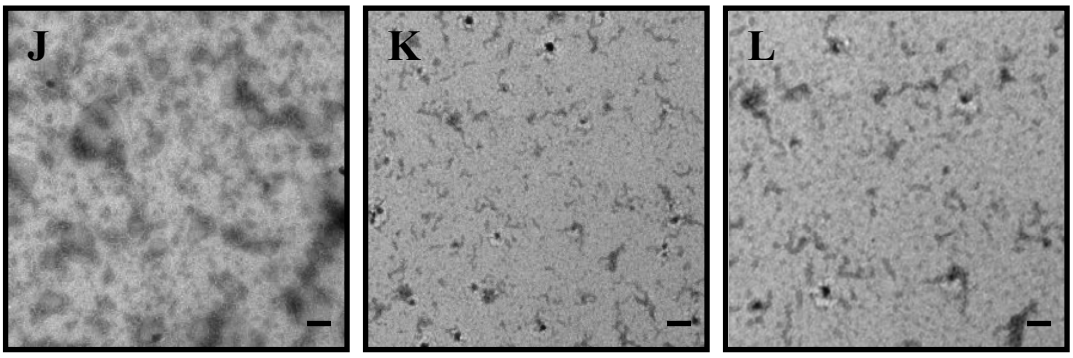

Figure 5. Inhibition of Amylin fibril formation by calcium free Calnuc. Amylin monomers were incubated with Ca^{2+} free Calnuc in a 1:1 stoichiometric ratio at pH 7.5 and 25^{o}C and samples were withdrawn at different time points. Panel A-B (t=2.5min), panel C-D (t = 6.5min), panel E-F (t = 12.5min), panel G-H (t = 25min), panel I-J (t = 47min) and panel K-L (t = 1.5hrs). Scale bar in the images represents 200nm. The reaction contained 20mM Tris at pH 7.5, 2% HFIP, 32μM Amylin and 32μM Ca^{2+} free Calnuc with stirring speed of 3.

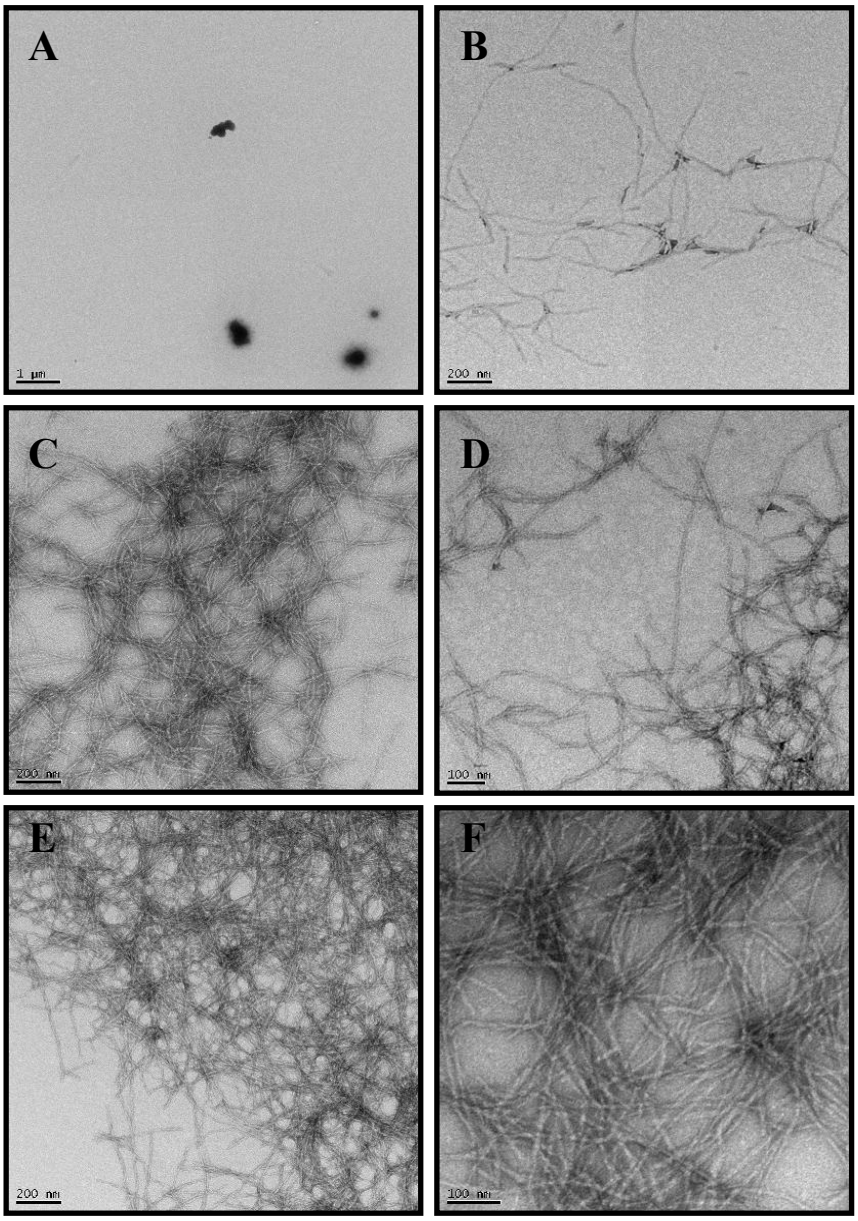

Figure 6. TEM images of Amylin aggregation with time in 2% HFIP and 20mM Tris at pH 7.4 and 25^{o} C. Panel A is Amylin aggregation at 2 min 37 sec after initiating the reaction. Panel B is Amylin aggregation at 7min. Panel C is aggregation in 15 min. Panel D is Amylin aggregation at 30 min. Panel E is Amylin aggregation in 30 min and Panel F is in 90min.

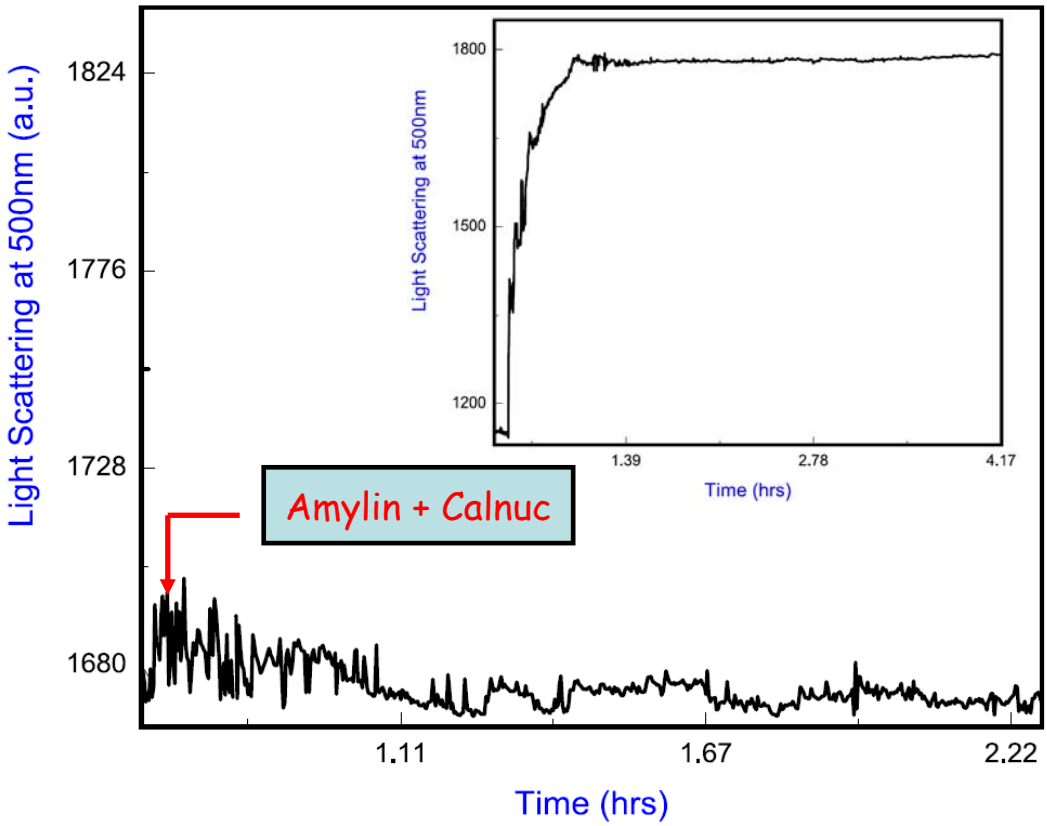

Figure 7. Right Angle Light Scattering experiment done to monitor the inhibition of amylin fibril formation by Ca^{2+} free Calnuc added at time t=0. Inset shows the aggregation of Amylin without Calnuc. Experiments were conducted in 20mM Tris at pH 7.5 and 25^{o}C and 2% HFIP.

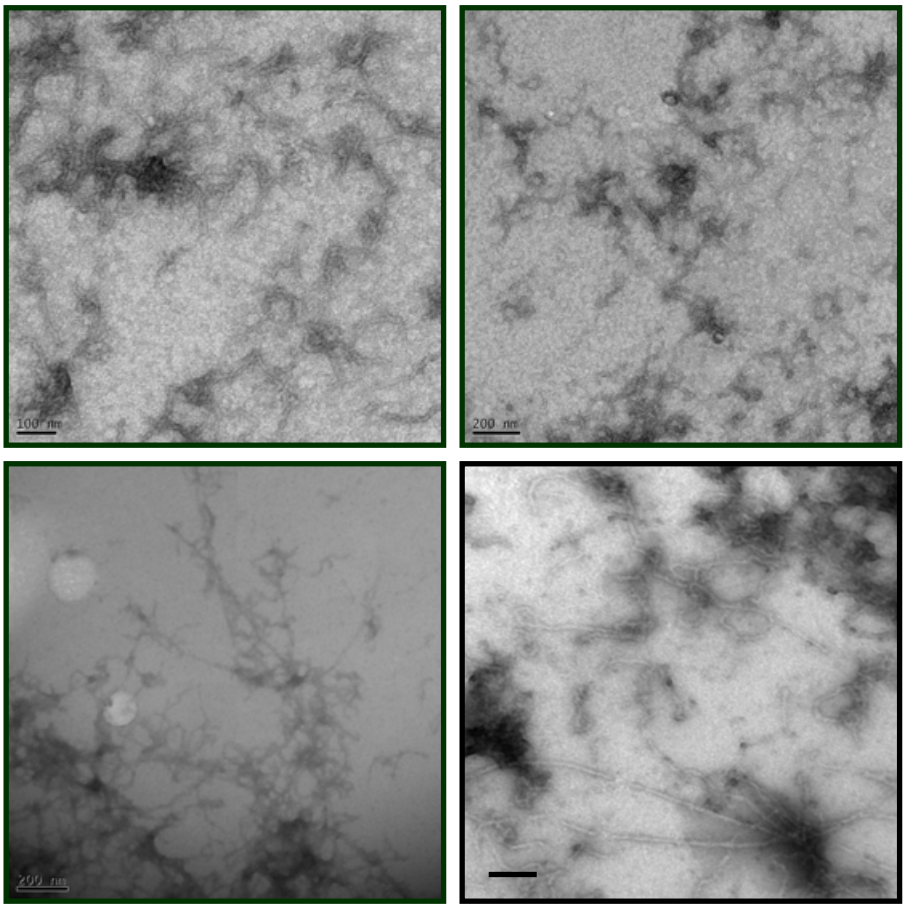

Figure 8. Appearance of fibrils after 60min on addition of 5mM Ca^{2+} to the inhibition reaction containing Ca^{2+} free Calnuc and Amylin in 1:1 ratio. Ca^{2+} free Calnuc and Amylin were incubated for 60min in 20mM Tris at pH 7.5 and 25^{o}C with 2% HFIP before addition of calcium. Scale bar in the images represents 200nm.

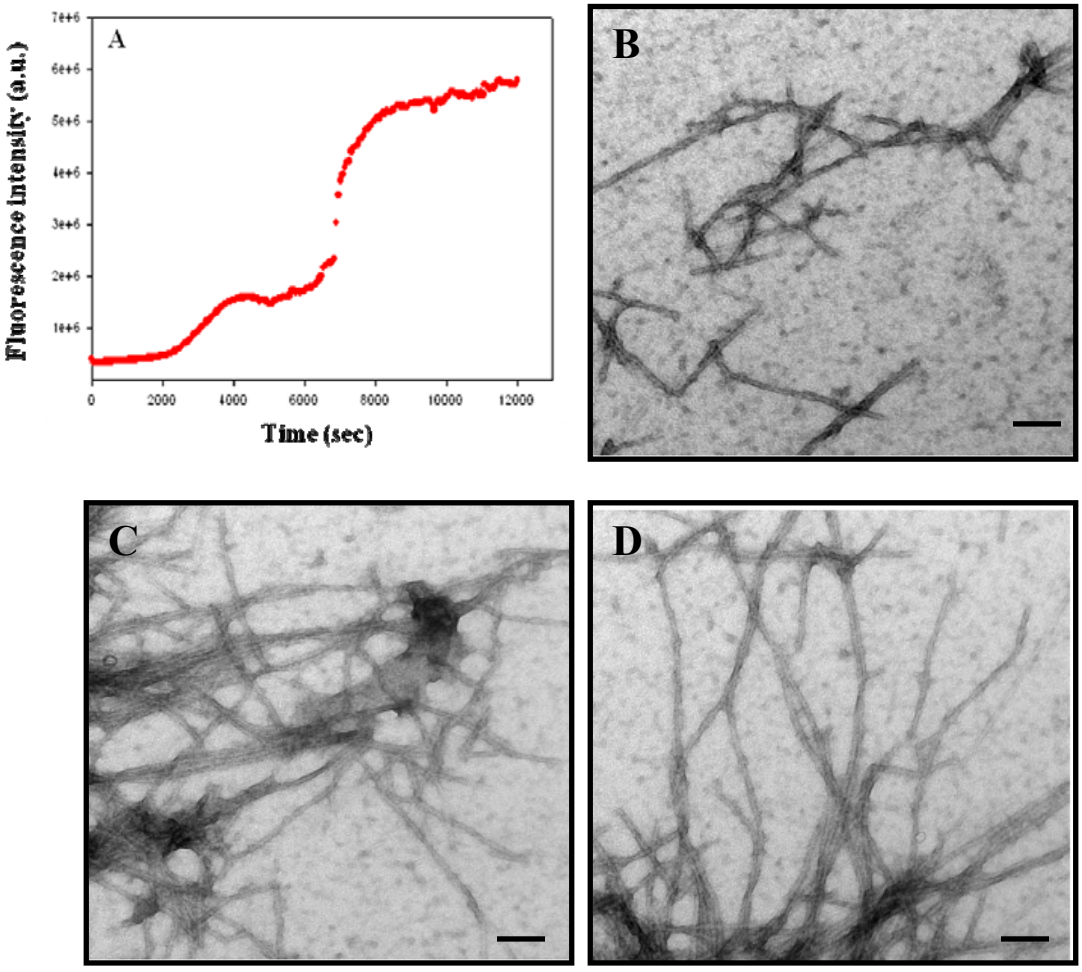

Figure 9. Effect of BSA on Amylin fibril formation. A 1:5 ratio of Amylin to BSA was studied using a thioflavin-T binding assay in 20mM Tris at pH 7.5 and 25^{o}C. Subsequently, TEM analysis of the samples withdrawn at the end of the run showed the presence of fibrillar species in the reaction mixture. Scale bar in the images represents 200nm.

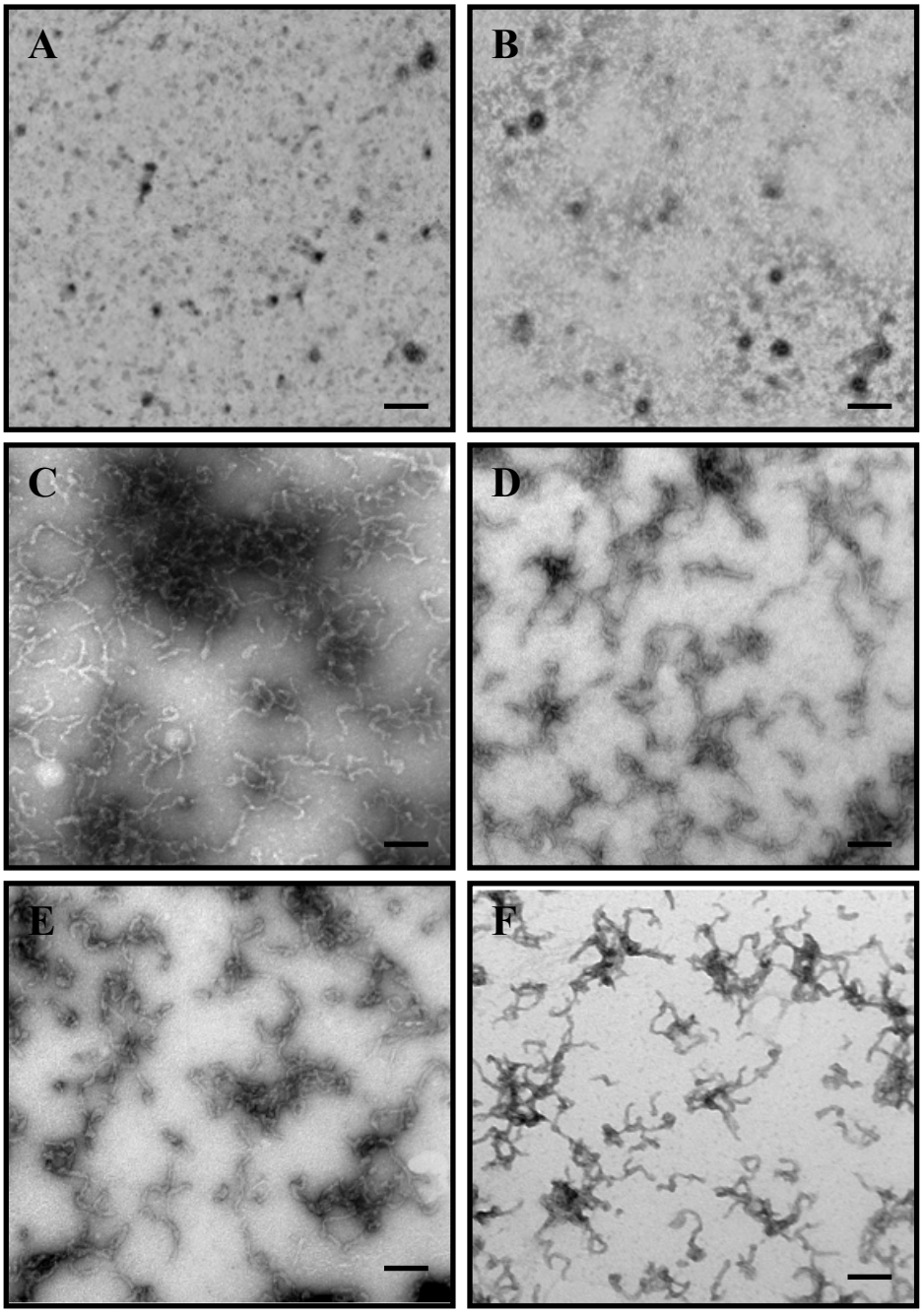

Figure 10. Inhibition of Amylin fibril formation by calcium free Calnuc in a concentration dependent manner. Amylin and Calnuc were in 1:1 (A-B), 1:3 (C-D) and 1:5 (E-F) in 20mM Tris at pH 7.5 and 25^{o}C with 2% HFIP and samples were withdrawn after 60mins. Scale bar in the images represents 200nm.

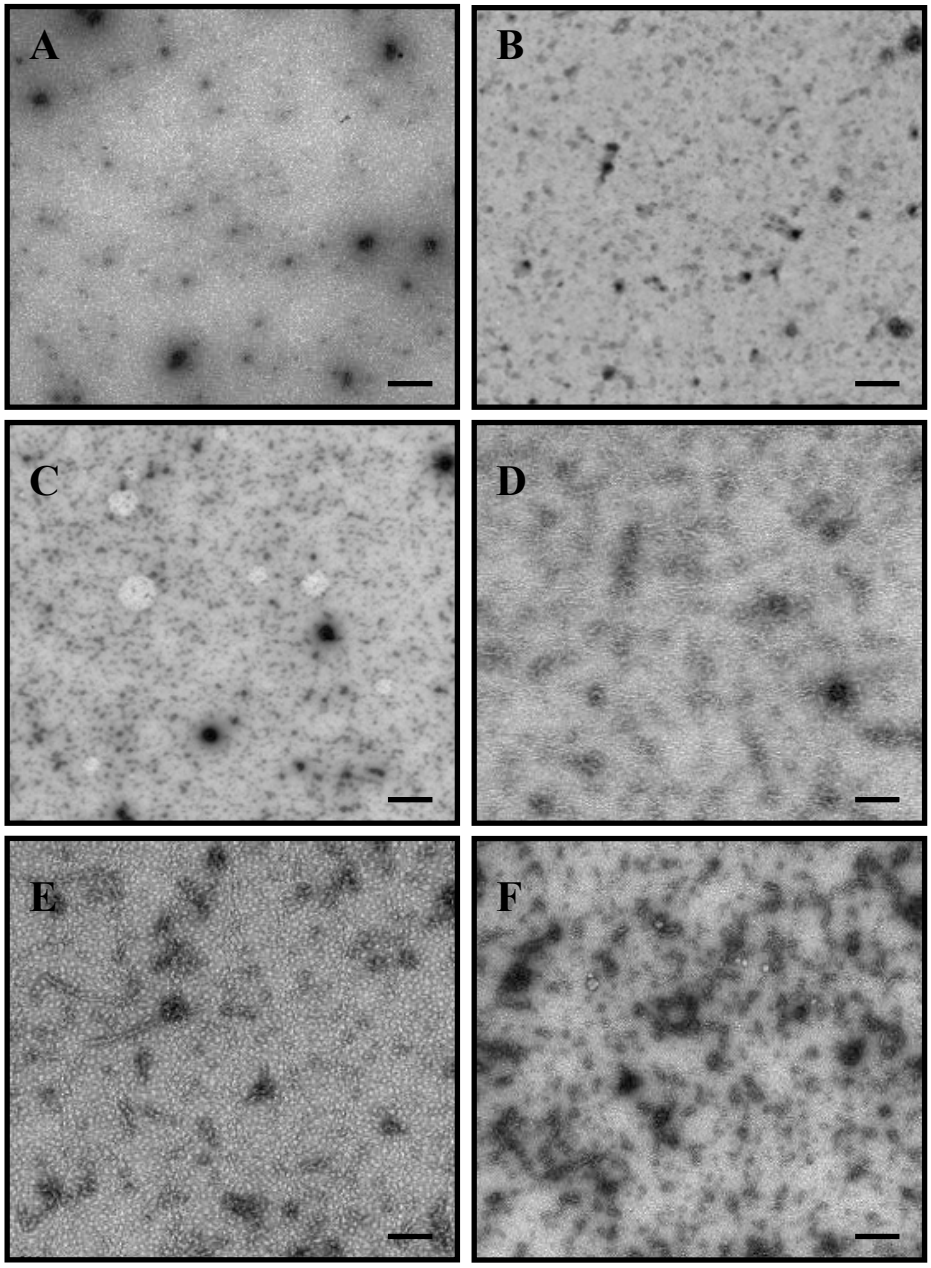

Figure 11. Inhibition of Amylin fibril formation by calcium free Calnuc. Amylin monomer is allowed to aggregate for 2 minutes with stirring and calcium free Calnuc was added in a 1:1 stoichiometric ratio (32μM concentration each) in 20mM Tris at pH 7.5 and 25^{o}C with 2% HFIP and samples were withdrawn at different time points. Panel A is amylin alone at 2min and Panels B-F are after addition of Calnuc at 5min, 15min, 25min, 40min and 63min. Scale bar in the pictures represents 200nm.

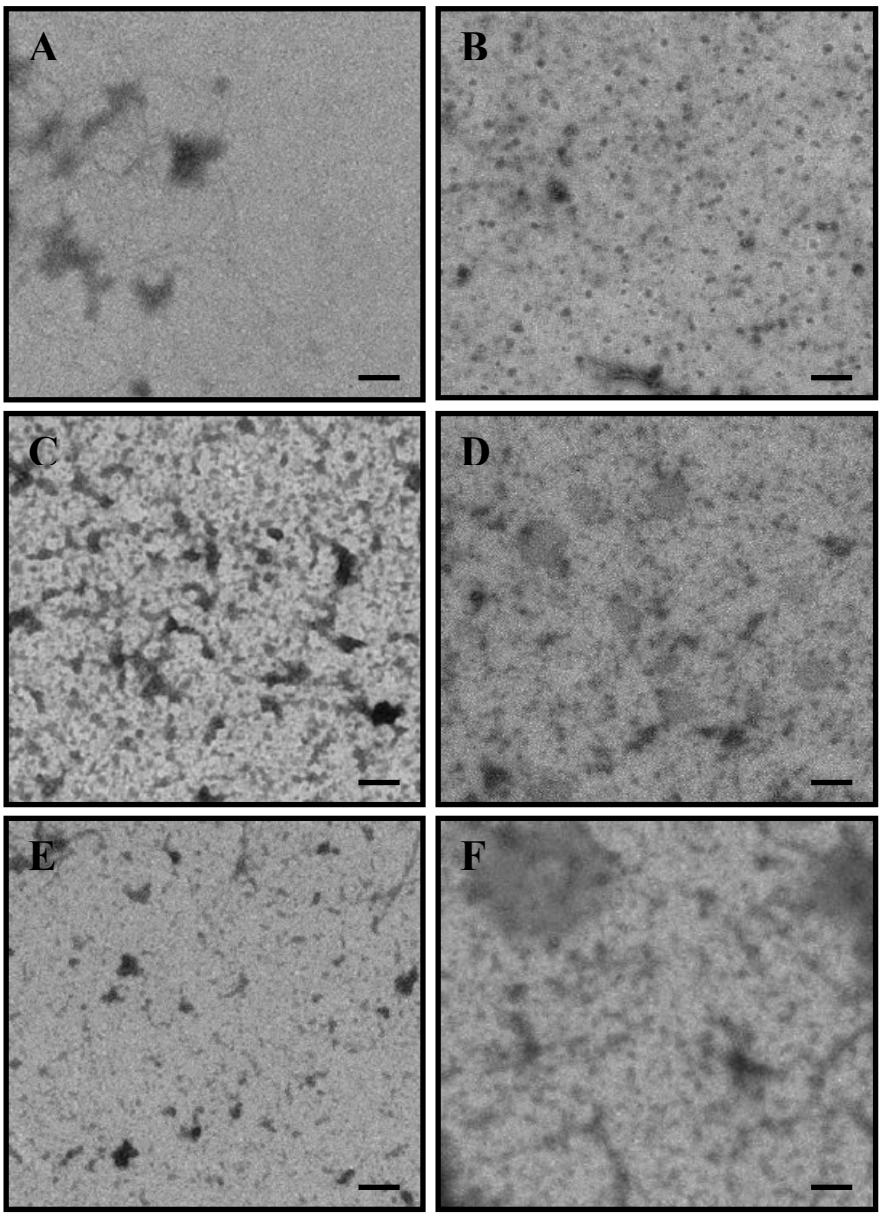

Figure 12. Inhibition of Amylin fibril formation by calcium free Calnuc. wt Amylin monomer is allowed to aggregate for 7 minutes with stirring and calcium free Calnuc was added in a 1:1 stoichiometric ratio (32μM concentration each) in 20mM Tris at pH 7.5 and 25^{o}C with 2% HFIP and samples were withdrawn at different time points. Panel A is amylin alone at 7min and Panels B-F are after addition of Calnuc at 5min, 15min, 25min, 40min and 80min. Scale bar in the images represents 200nm.

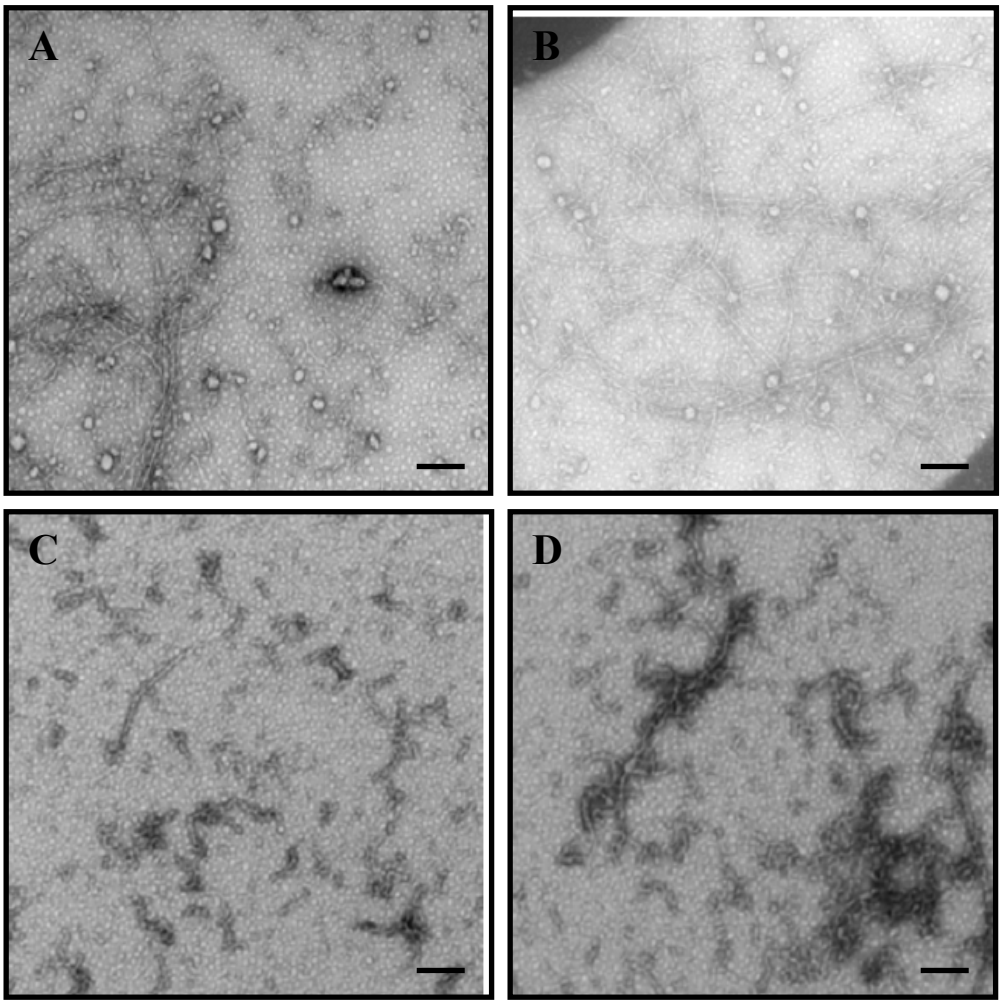

Figure 13. Inhibition of Amylin fibril formation by calcium free Calnuc. wt Amylin monomer is allowed to aggregate for 15 minutes with stirring and calcium free Calnuc was added in a 1:1 stoichiometric ratio (32μM concentration each) in 20mM Tris at pH 7.5 and 25^{o}C with 2% HFIP and samples were withdrawn at different time points. Panel A-B is amylin alone at 15min and Panels C-D are 60 min after addition of Calnuc. Scale bar in the images represents 200nm.

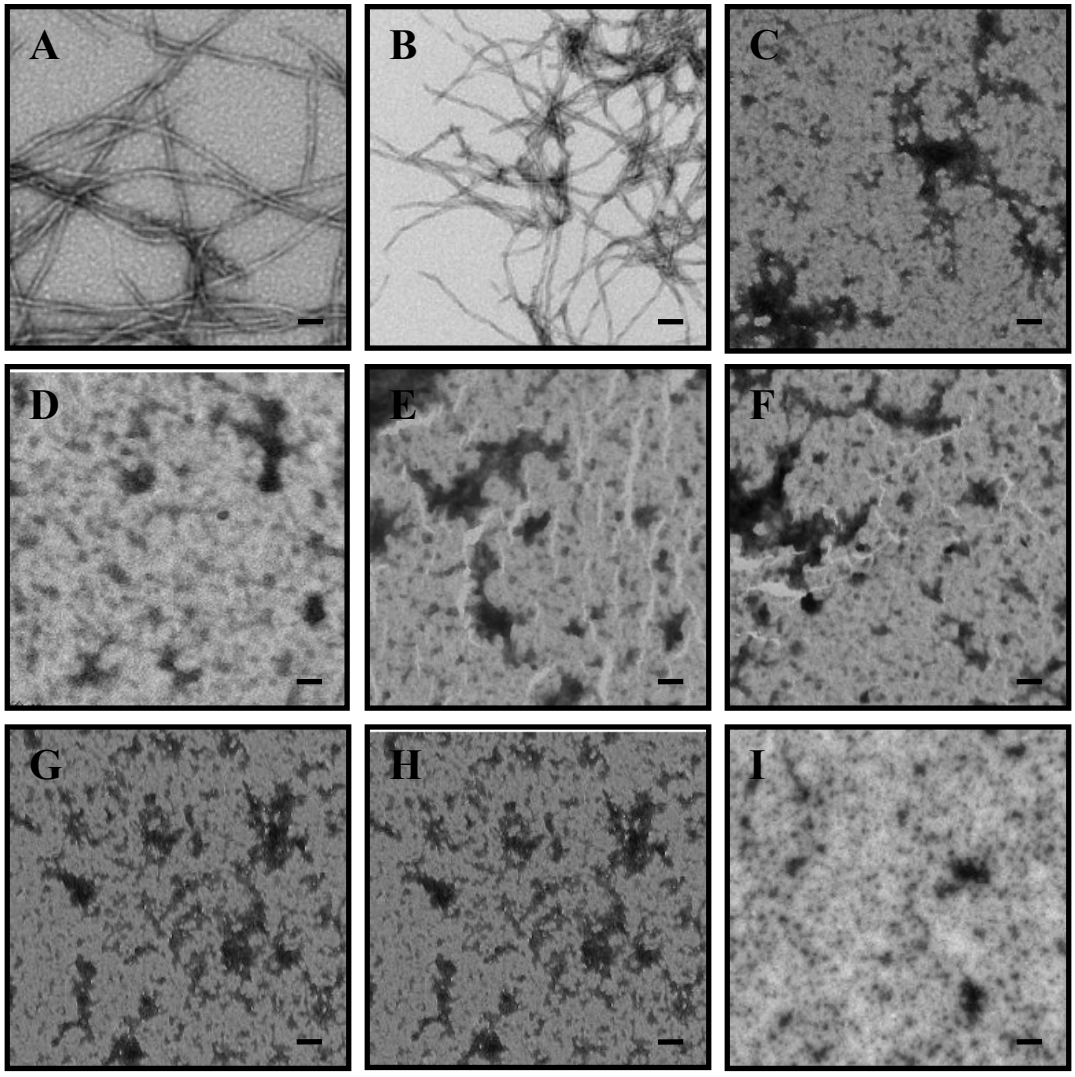

Figure 14. Disaggregation of Aβ42 fibrils by calcium free Calnuc. The rest of the images are continued on the next page.

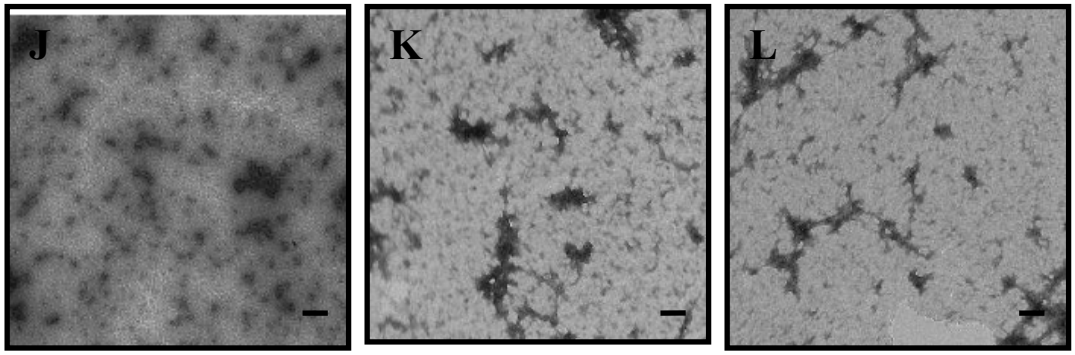

Figure 14. Disaggregation of Aβ42 fibrils by calcium free Calnuc. Aβ42 fibrils (panel A-B) were incubated with Ca^{2+} free NUCB1 in a 1:1 stoichiometric ratio (32μM concentration each) in 100mM Tris at pH 7.5 and 25^{o}C and samples were withdrawn at different time points to monitor diaggregation. Panel C-D (t = 5 min), panel E-F (t = 15 min), panel G-H (t = 30 min), panel I-J (t = 1 hr 30 min) and panel K-L (t = 20 hr). Scale bar in the images represents 200nm except for image A where the scale bar represents 100nm.

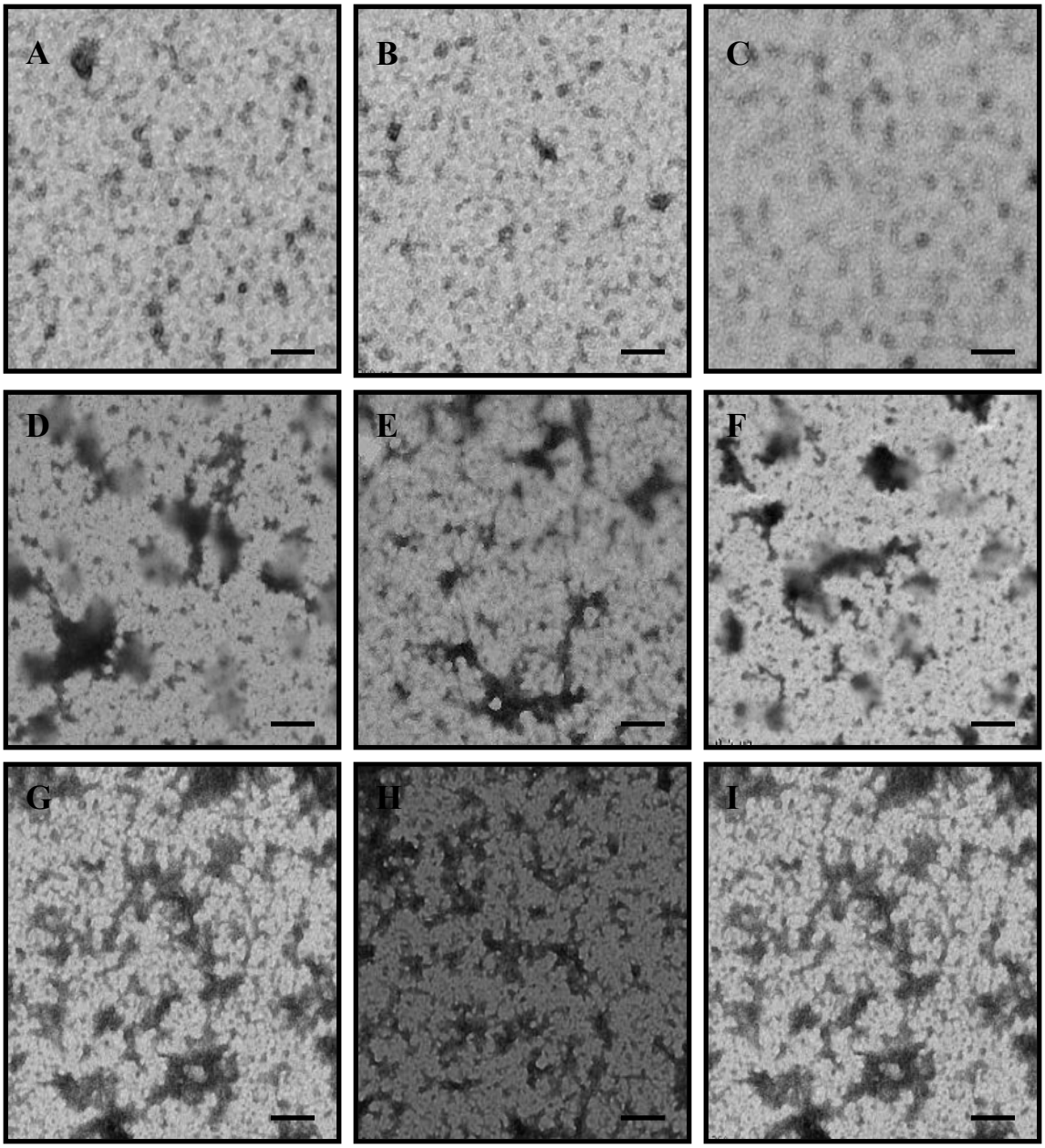

Figure 15. Inhibition of Aβ42 fibril formation by calcium free Calnuc. Aβ42 peptide was incubated with Ca^{2+} free Calnuc in a 1:1 stoichiometric ratio (32μM concentration each) in 20 mM Tris at pH 7.5 and 25^{o} C and samples were withdrawn at different time points. Panel A-C (t = 1 hr), panel D-F (t = 5 hr) and panel G-I (t = 30 hr). Scale bar in the images represents 200 nm.

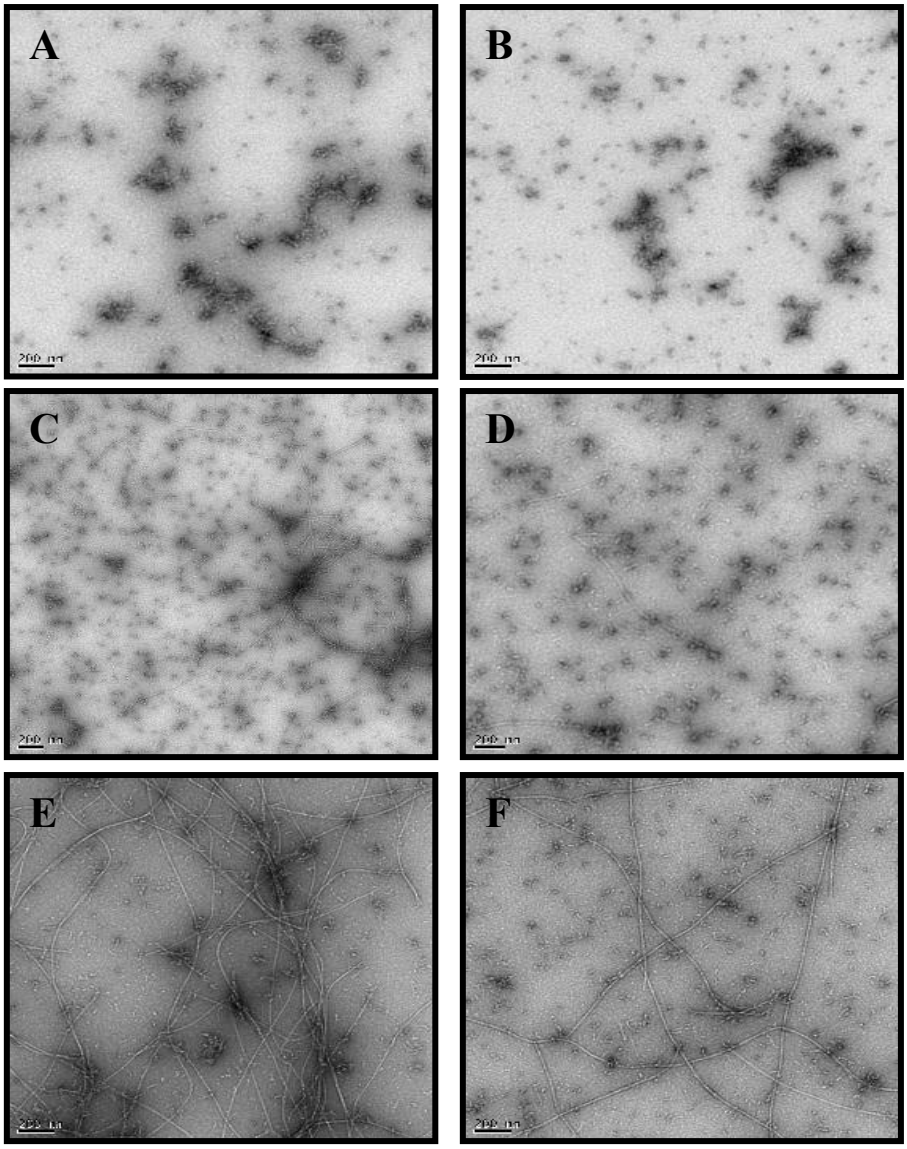

Figure 16. TEM images of Aβ42 fibril formation. The rest of the images are shown on the next page.

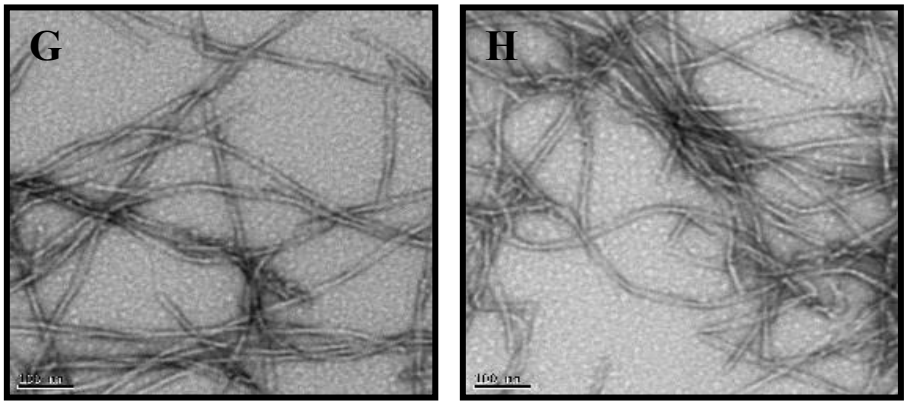

Figure 16. TEM images of aliquots withdrawn at (A-B) 0 hr, (C-D) 5 hr, (E-F) 12 hr and (G-H) 24 hr from Aβ42 fibril formation reaction. The concentration of the peptide was 64μM in 100mM Tris at pH 7.4. The scale bar for A-H corresponds to 200nm.

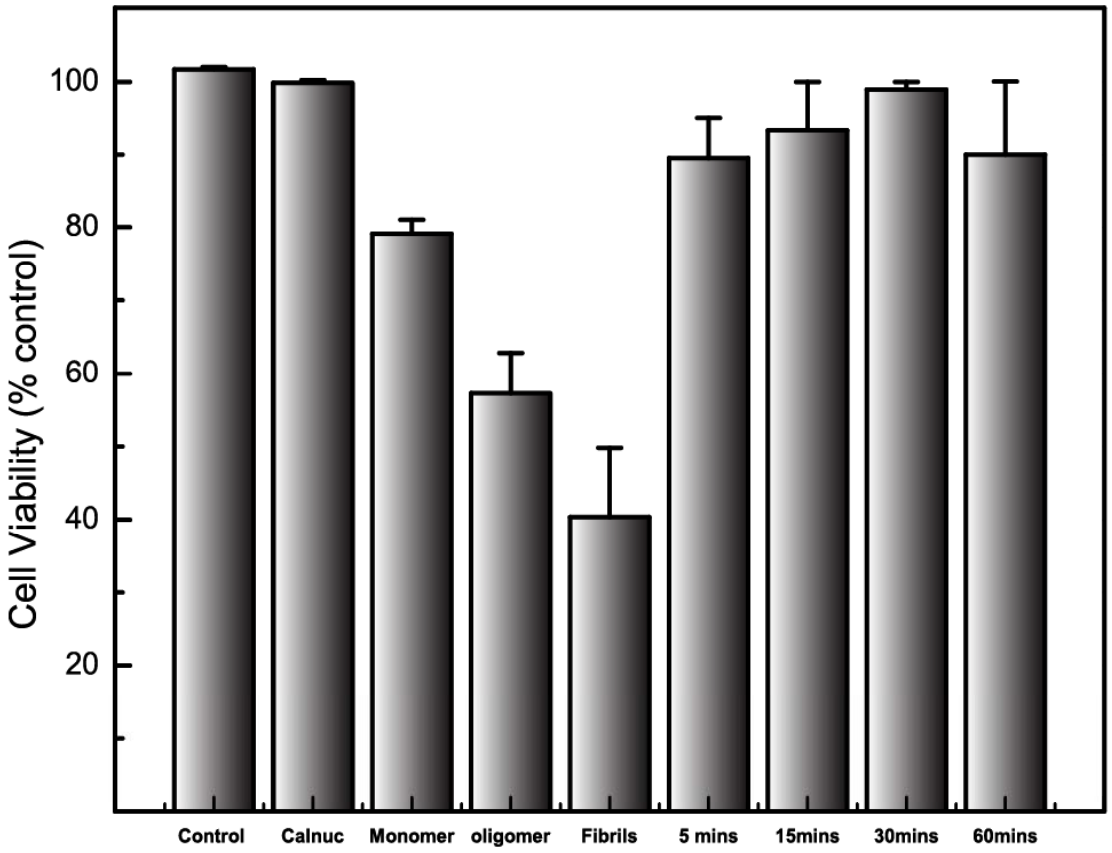

Figure 17. MTT assay results with PC12 cells showing cell viability in the presence of Aβ42 monomers, oligomers and fibrils. The cell viability increased on disaggregation of these fibrils by incubated with Ca^{2+} free Calnuc as compared to the control cells. Monomer samples are Aβ peptide taken from initial aggregation reaction in 10mM Tris at pH 7.5 and 25^{o} C. Oligomer samples were withdrawn at 5 hours and fibrils were withdrawn after 24 hours. All samples were incubated with cells for 4 hours before addition of MTT. The time points on the graph refer to the time for which Amylin and Calnuc were incubated in the cuvette before addition to the cells.

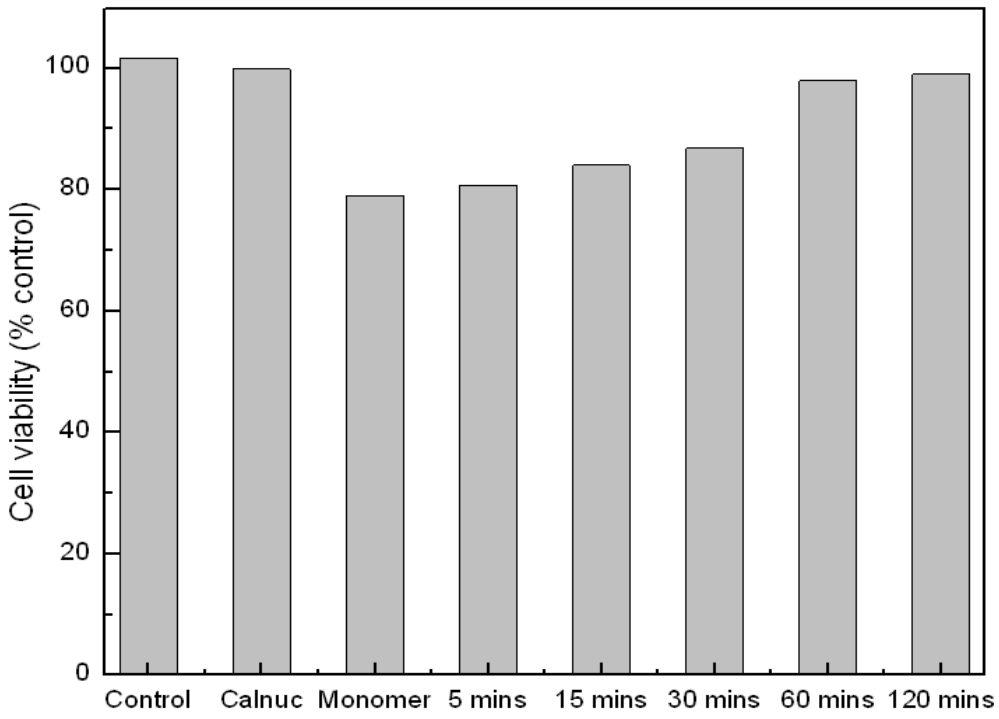

Figure 18. MTT assay results with PC12 cells showing cell viability in the presence of Aβ42 monomers. The cell viability increased by inhibition of aggregation of Aβ42 monomers when incubated with Ca^{2+} free Calnuc as compared to the control cells. Monomer samples are Aβ peptide taken from initial aggregation reaction in 10mM Tris at pH 7.5 and 25^{o} C. All samples were incubated with cells for 4 hours before addition of MTT. The time points on the graph refer to the time for which Amylin and Calnuc were incubated in the cuvette before addition to the cells.

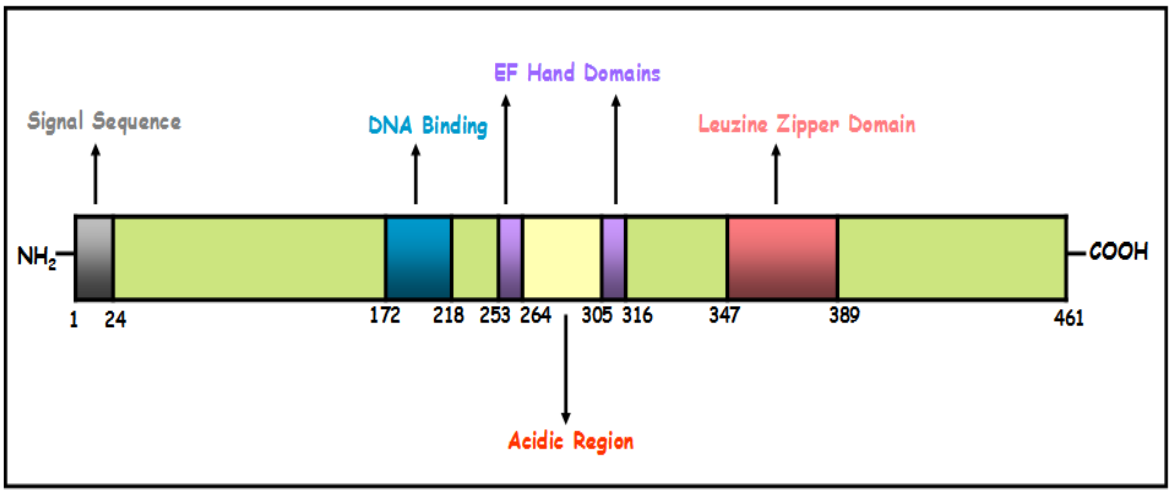

Figure 19. The domain map of Calnuc showing the N-terminal signal sequence, DNA binding region, 2 EF hands and the Leucine zipper domain.

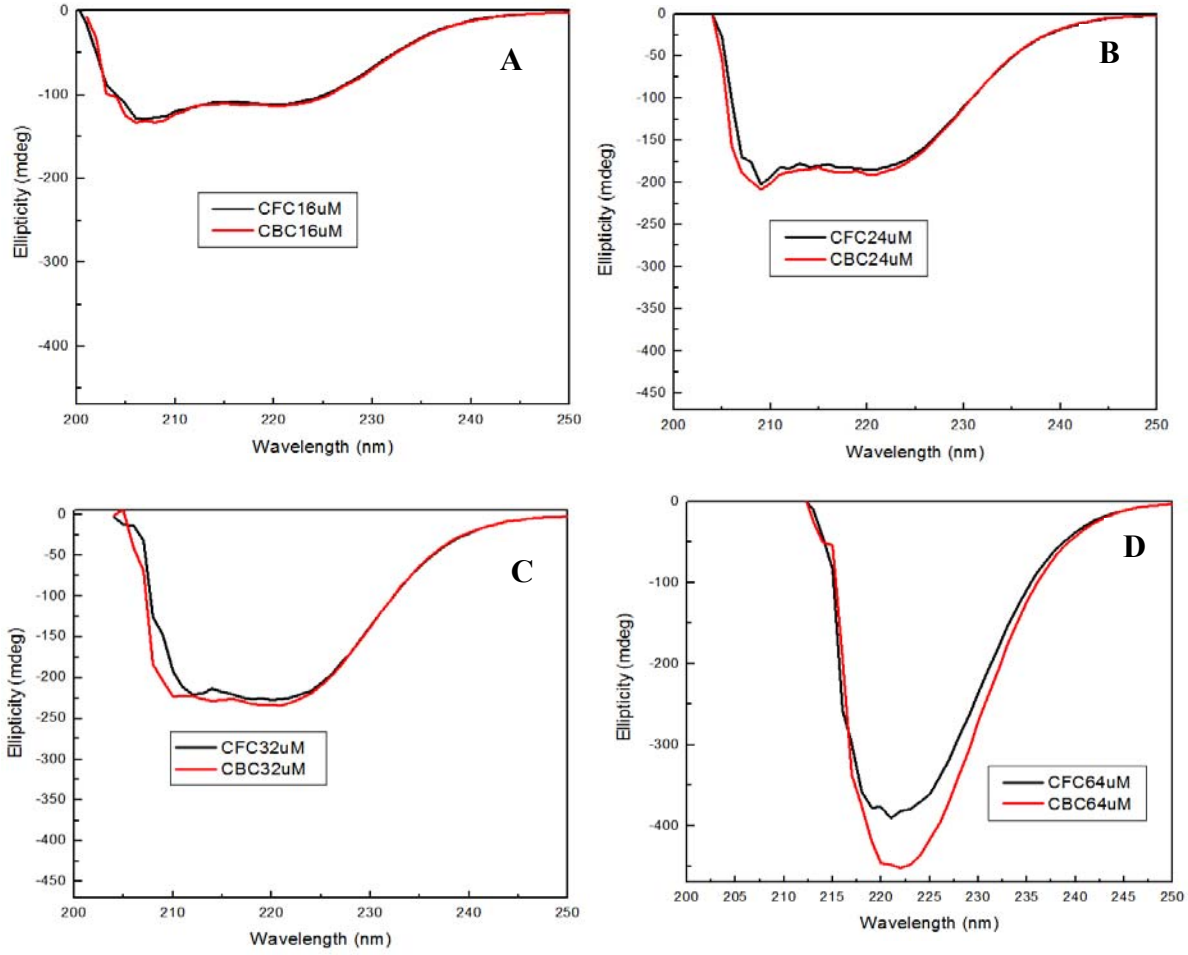

Figure 20. Circular Dichroism spectra of Calnuc shows changes in the secondary structure with increasing proteinconcentration for both Calcium free and Calcium bound Calnuc. Each panel shows the comparison of CD data for Ca^{2+} free Calnuc (CFC in black) and Ca^{2+} bound Calnuc (CBC in red) at concentrations of A) 16μM, B) 24μM, C) 32μM and D) 64μM. The spectra are not normalized for concentration.

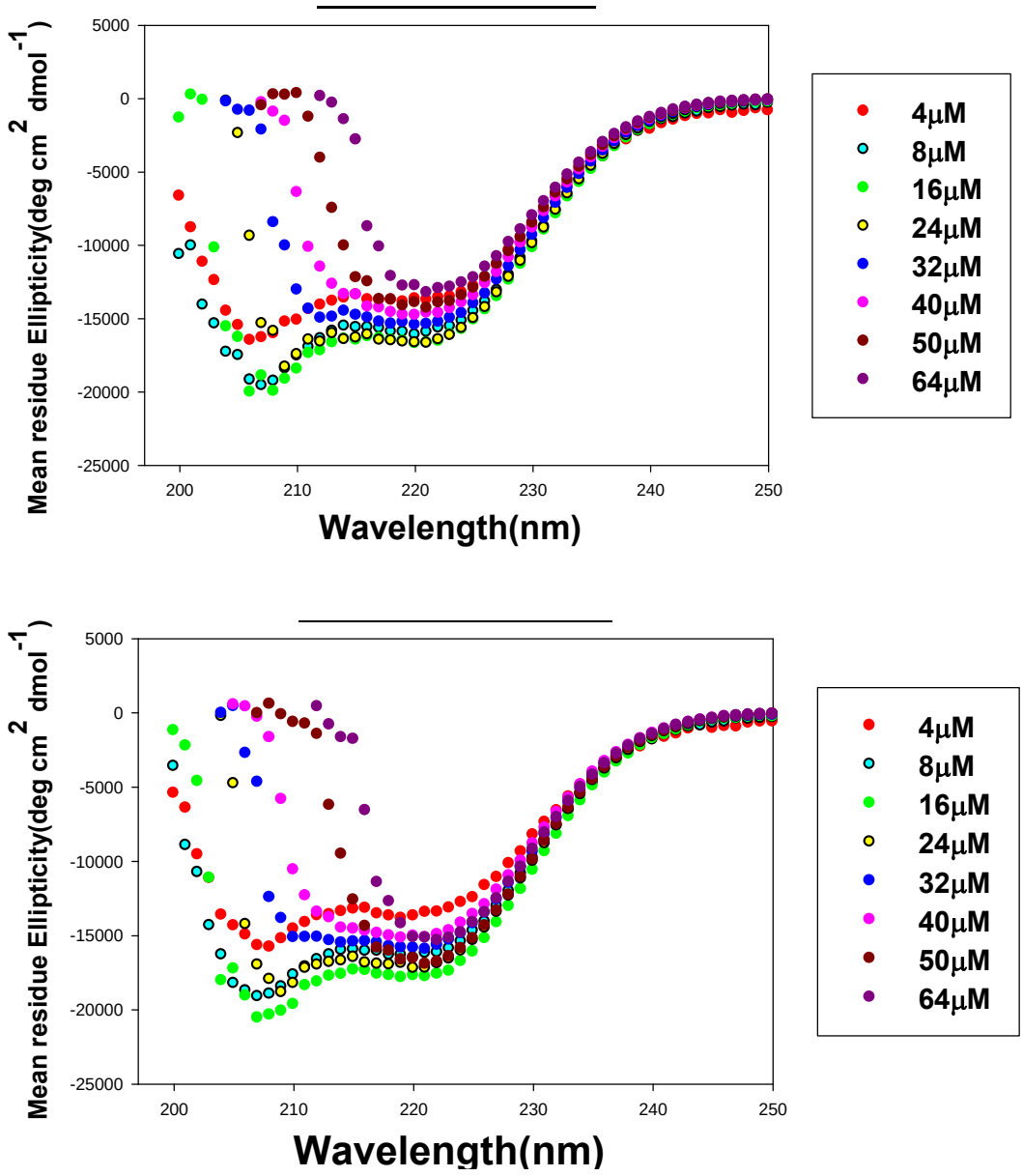

Figure 21. Circular Dichroism spectra of Calnuc shows change in the secondary structure with increasing concentration (a) Calcium free Calnuc (b) Calcium bound Calnuc. The spectra are normalized for concentration.

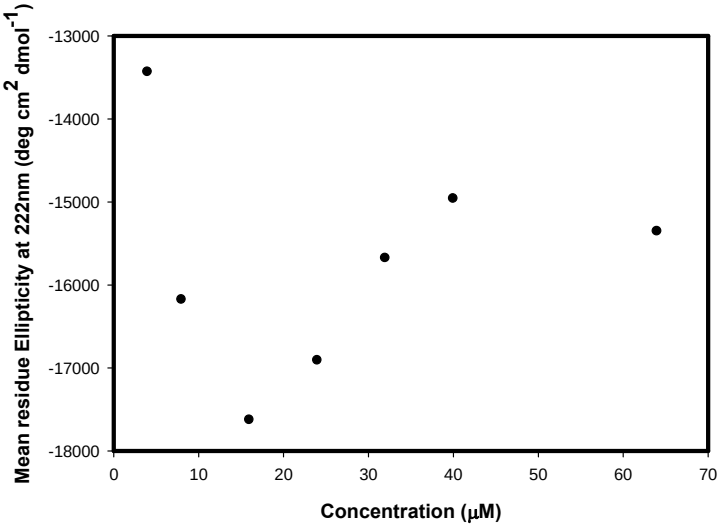

Figure 22. Plot of mean residue ellipticity at 222 nm for Ca^{2+} free Calnuc versus protein concentration in 50 mM Tris and 150 mM NaCl at pH 8.0 and 25^{o}C.

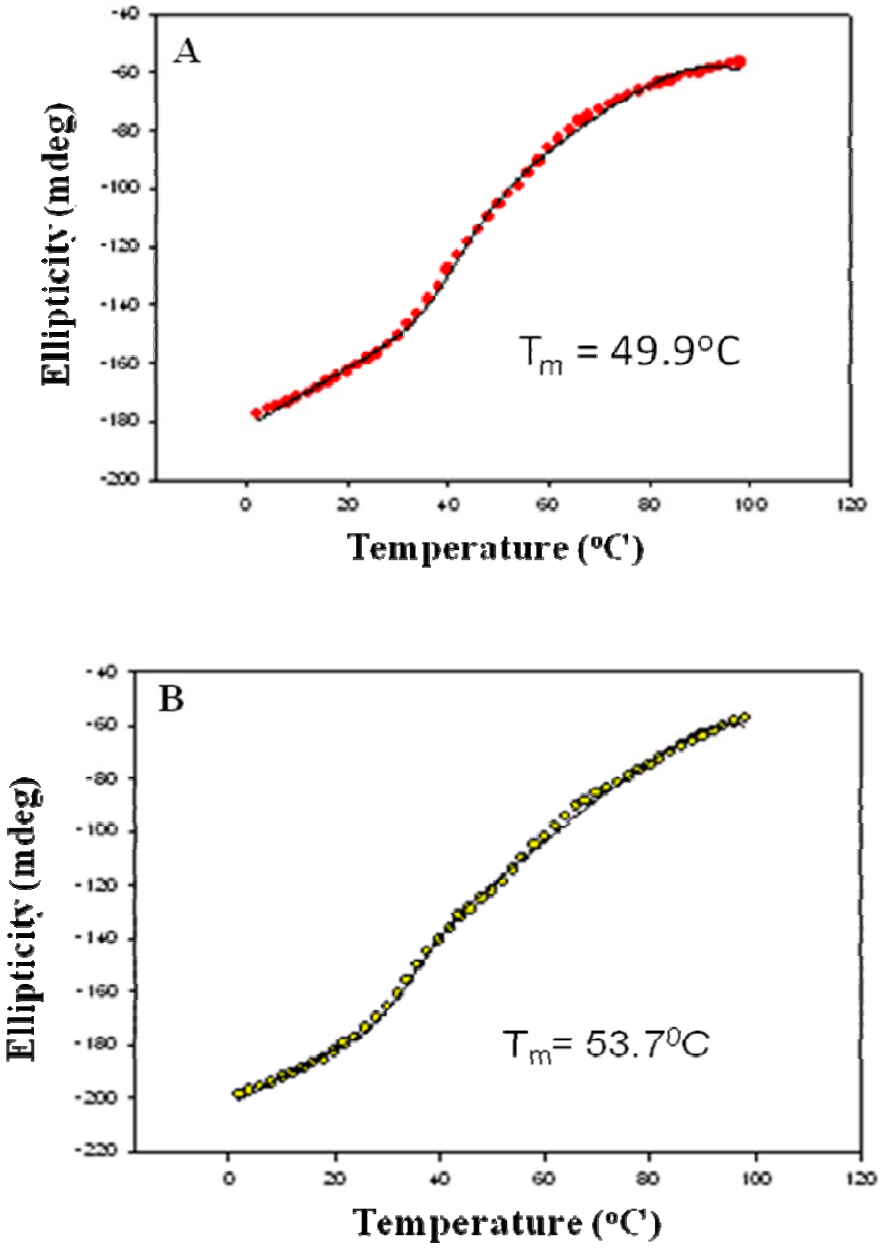

Figure 23. Thermal unfolding experiment performed by monitoring the change in CD signal at 222nm for 8μM concentration of A) Ca^{2+} free Calnuc and B) Ca^{2+} bound Calnuc with increasing temperature.

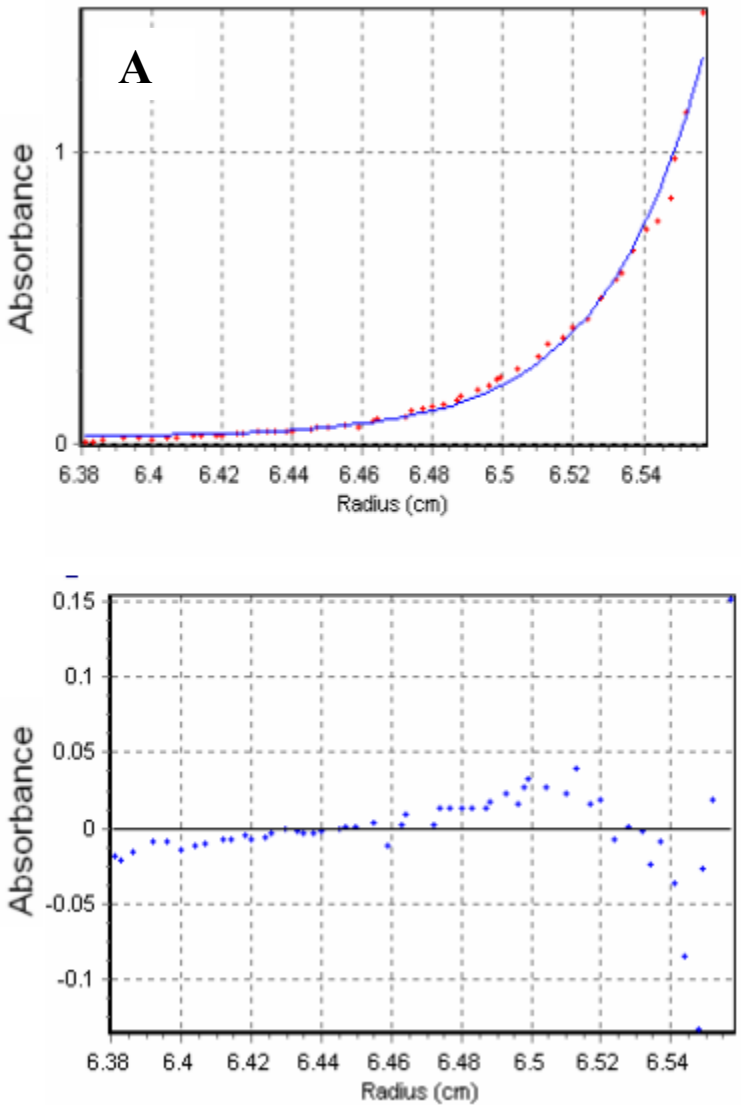
A
Absorbance
1
0
6.38
6.4
6.42
6.44
6.46
6.48
6.5
6.52
6.54
Radius (cm)
Absorbance
0.15
0.1
0.05
0
-0.05
-0.1
6.38
6.4
6.42
6.44
6.46
6.48
6.5
6.52
6.54
Radius (cm)

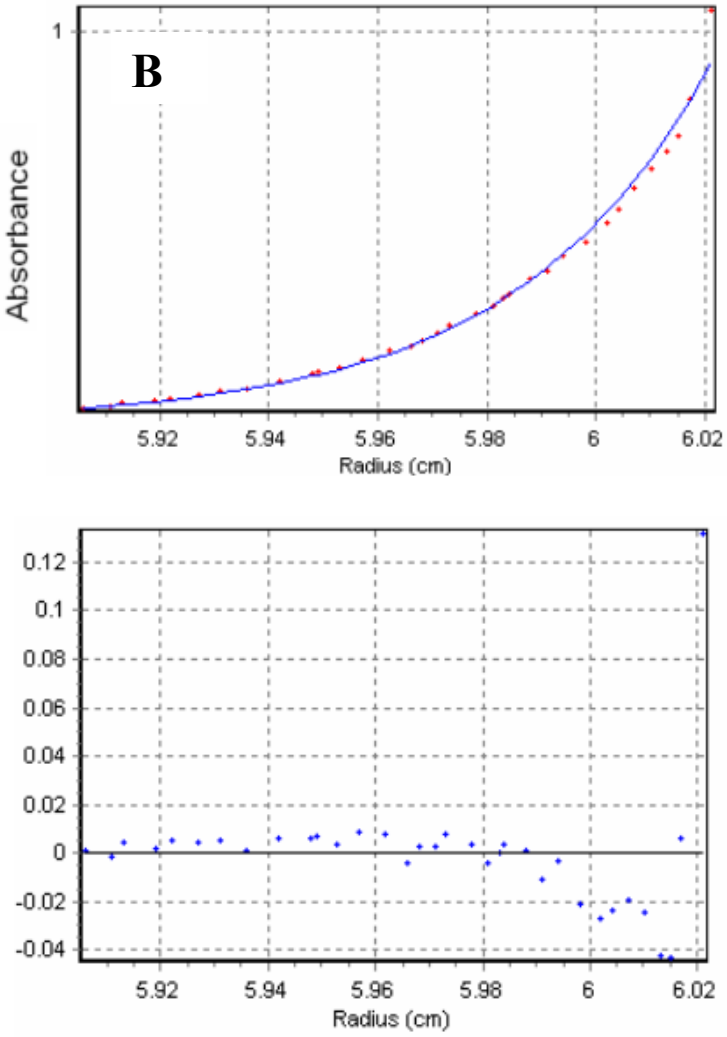
B
1
Absorbance
5.92
5.94
5.96
5.98
6
6.02
Radius (cm)
0.12
0.1
0.08
0.06
0.04
0.02
0
-0.02
-0.04
Absorbance
5.92
5.94
5.96
5.98
6
6.02
Radius (cm)

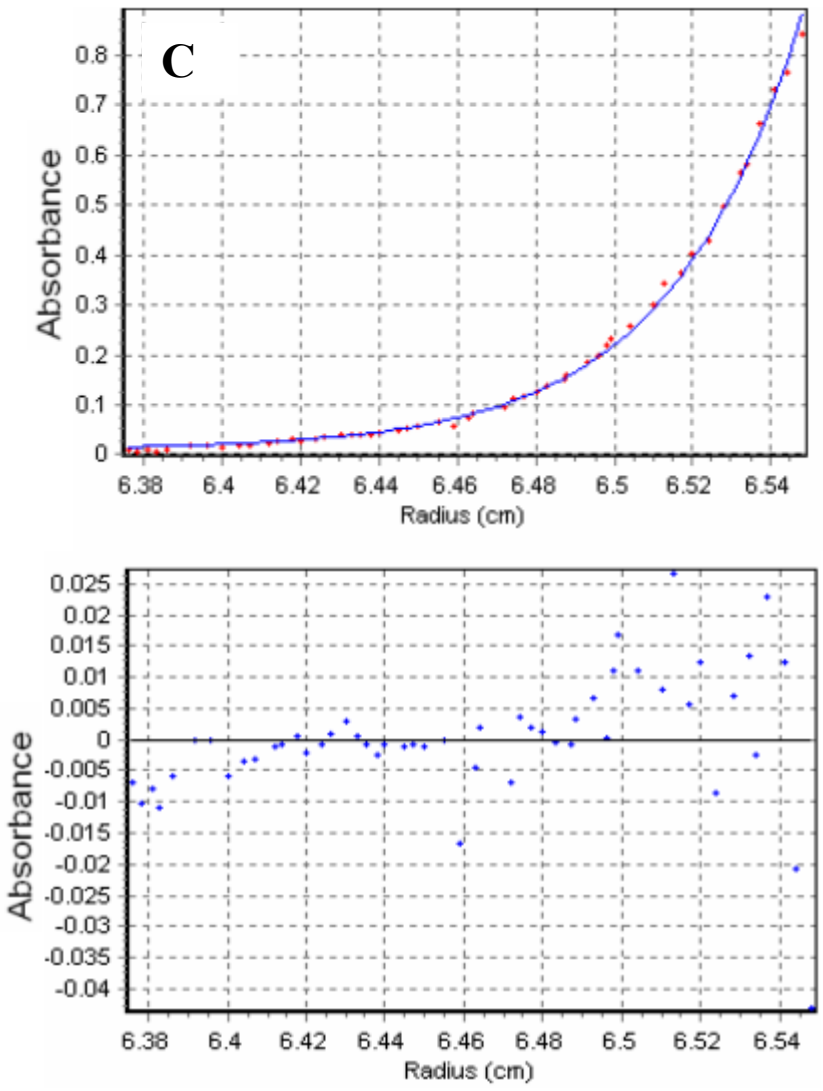

Figure 24a. Analytical Ultracentrifugation analysis for Ca^{2+} bound Calnuc at different concentrations of A) 50μM, B) 100μM and C) 150μM at 20,000rpm. The molecular mass obtained from data analysis was 101.4kDa for 50μM, 116.0kDa for 100μM and 112.5kDa for 150μM which corresponded to a dimeric species of Calnuc. The monomer molecular mass of Calnuc is 55kDa.

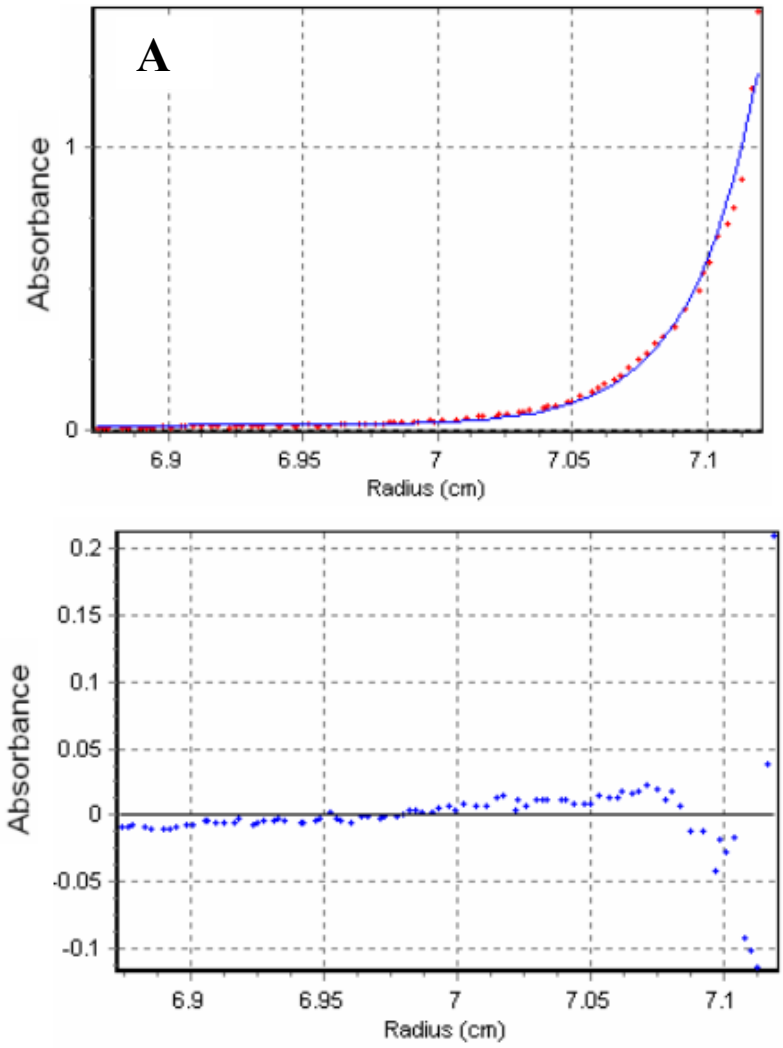
A
Absorbance
1
0
6.9
6.95
7
7.05
7.1
Radius (cm)
Absorbance
0.2
0.15
0.1
0.05
0
-0.05
-0.1
6.9
6.95
7
7.05
7.1
Radius (cm)

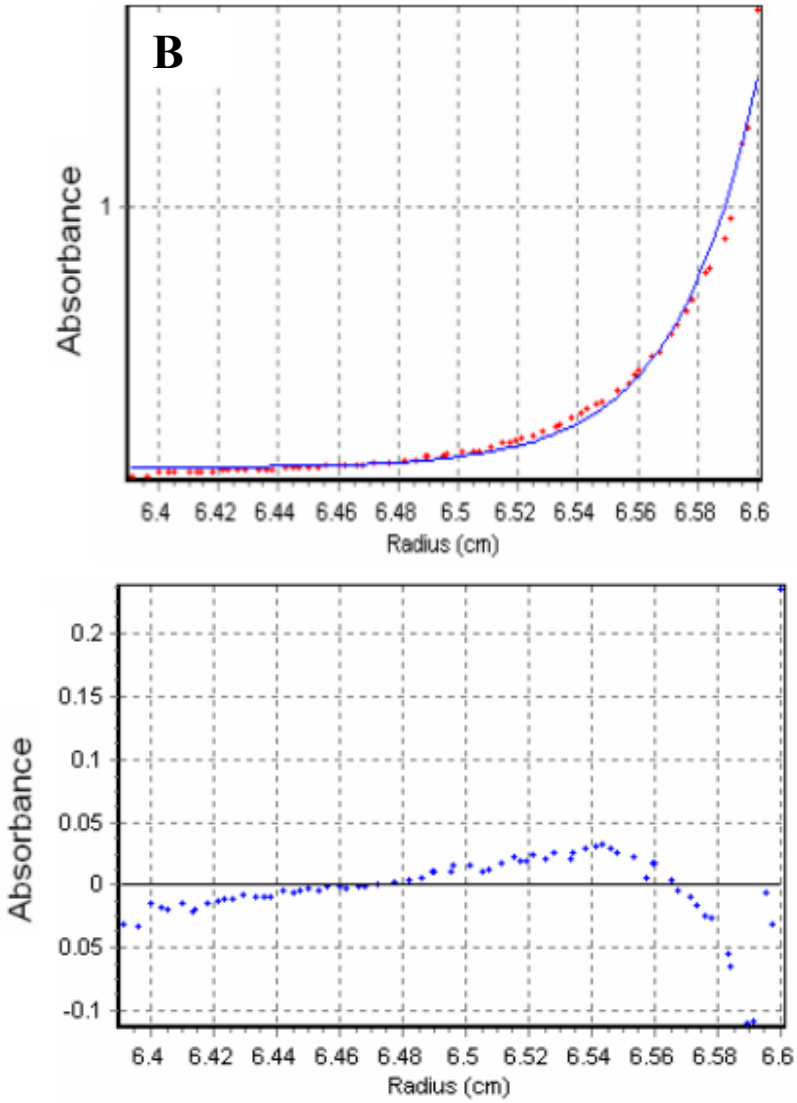

Figure 24b. Analytical Ultracentrifugation analysis for Ca^{2+} free Calnuc at different concentrations of A) 100μM and B) 150μM at 20,000rpm. The molecular mass obtained from data analysis was 119.8kDa for 100μM and 123.5kDa for 150μM which corresponded to a dimeric species of Calnuc. The monomer molecular mass of Calnuc is 55kDa.

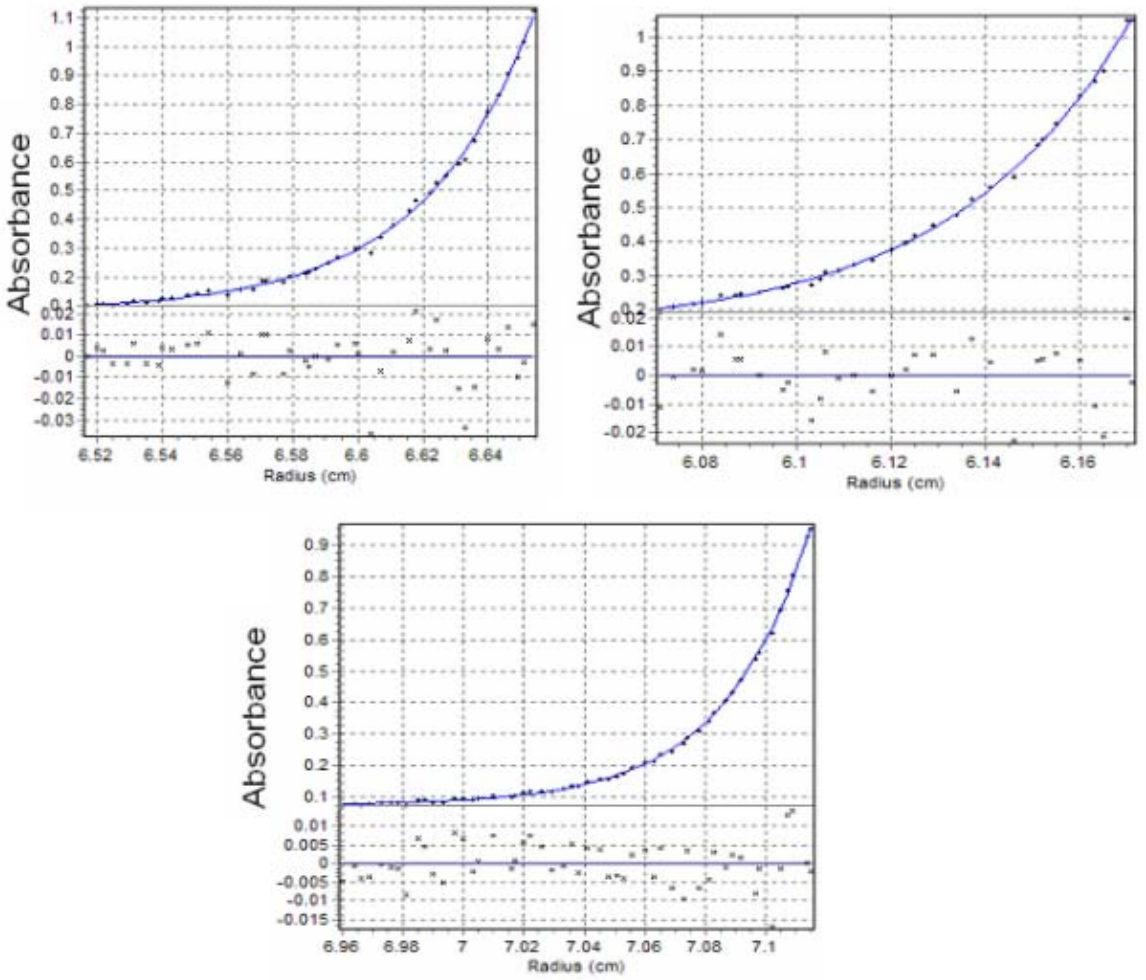

Figure 25. Analytical Ultracentrifugation analysis for Ca^{2+} free NUCB2 at different concentrations of A) 50μM, B) 100μM and C) 150μM at 20,000rpm. The molecular mass obtained from data analysis was 99.8kDa for 50μM, 102.4kDa for 100μM and 100.5kDa for 150μM which corresponded to a dimeric species of Calnuc. The monomer molecular mass of Calnuc is 46.5kDa.

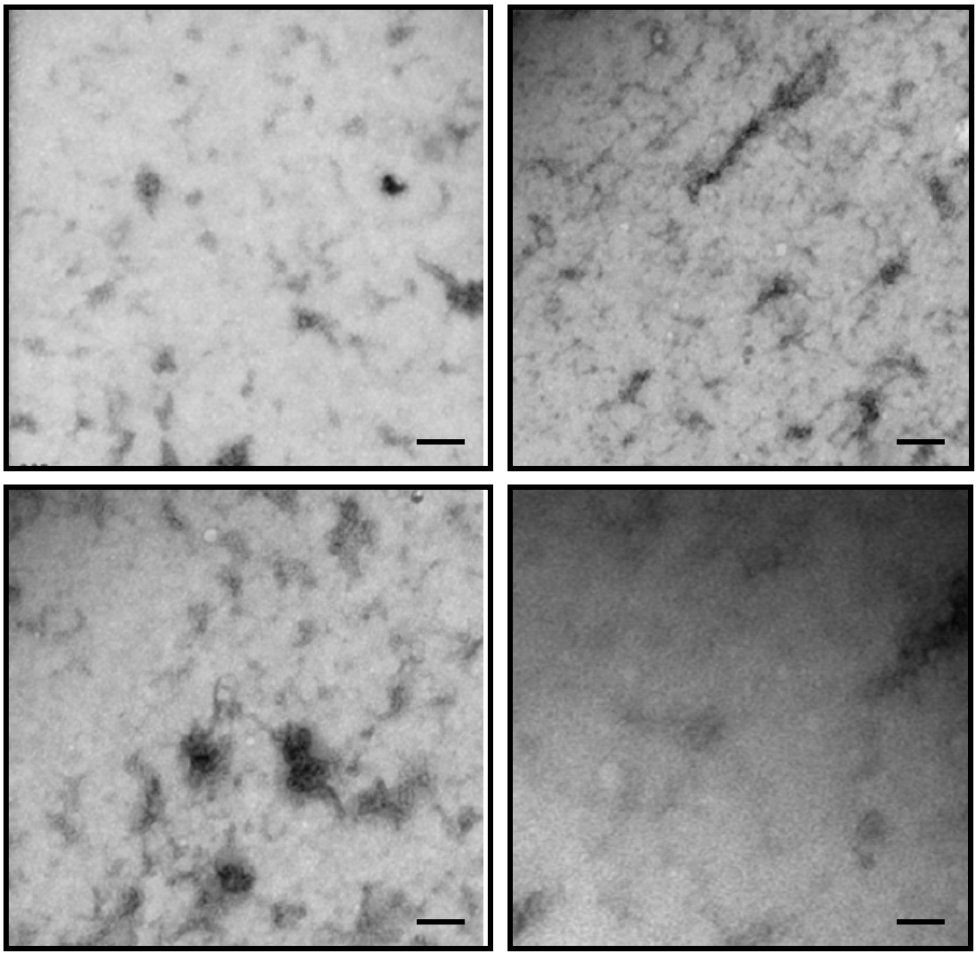

Figure 26. Inhibition of Amylin fibril formation by calcium free Calnuc. wt Amylin monomer is incubated with calcium free NUCB2 in a 1:1 stoichiometric ratio (32μM concentration each) in 20mM Tris at pH 7.5 and 25^{o}C with 2% HFIP and samples were withdrawn after 15 minutes. Scale bar in the images represents 200nm.

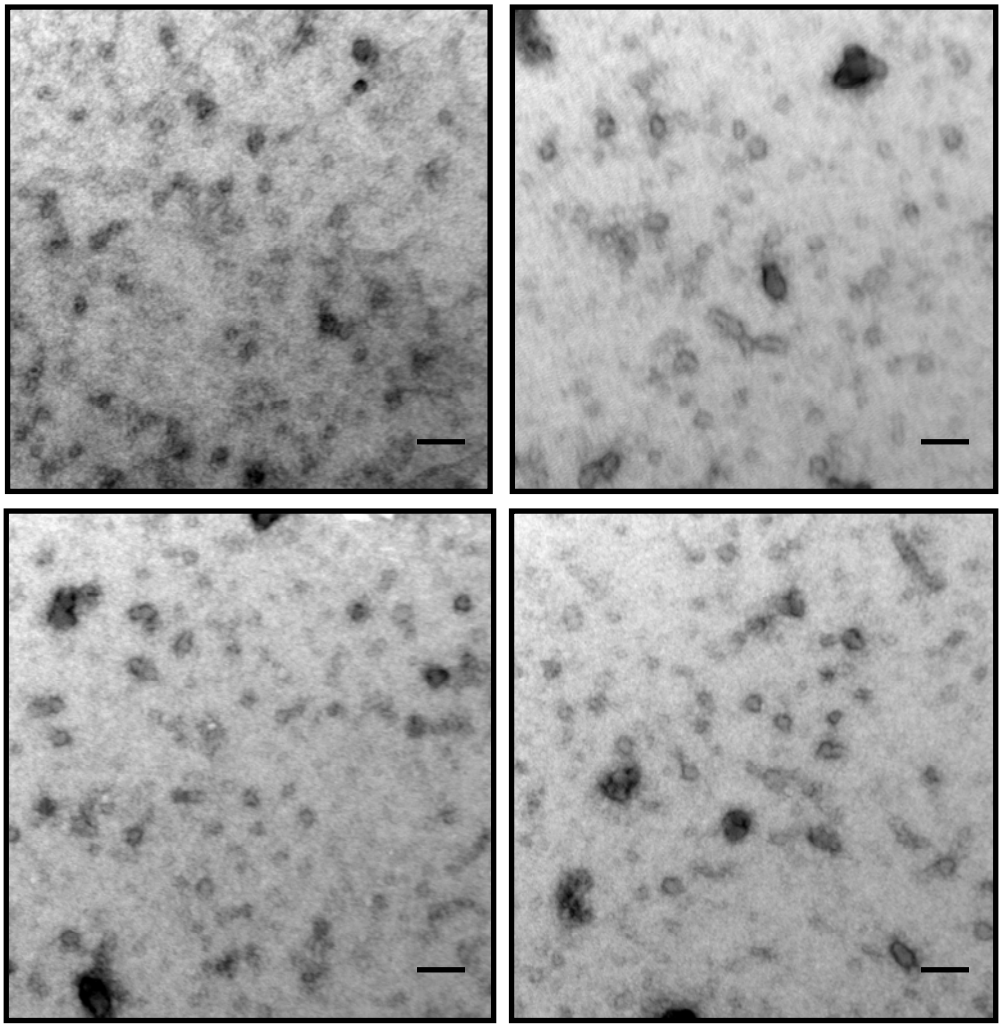

Figure 27. TEM images of samples withdrawn from a 1:1 stoichiometric mixture (32μM concentration each) of calcium free NUCB2 and wt Amylin fibrils. The samples were withdrawn after 30 minutes of incubation in 20mM Tris at pH 7.5 and 25^{o}C with 2% HFIP. Scale bar in the images represents 100nm.

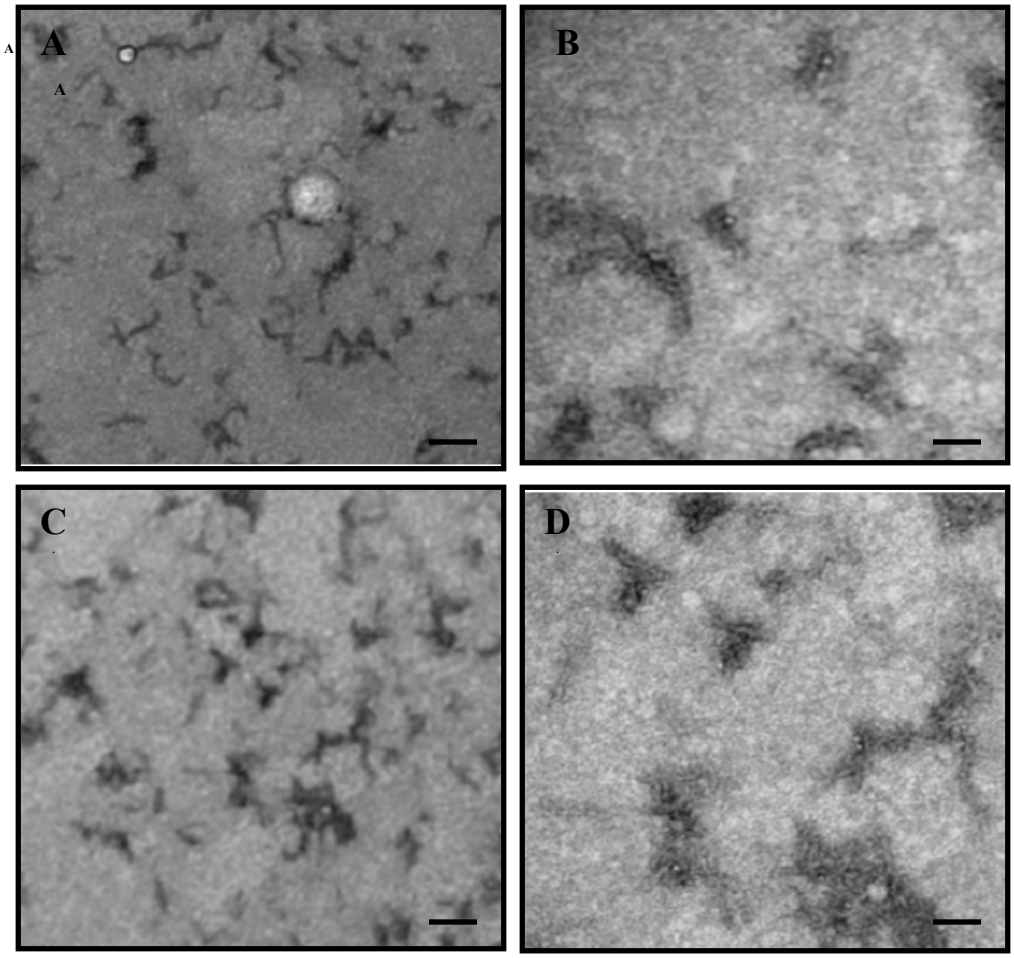

Figure 28. Inhibition of Amylin fibril formation by calcium free NUCB2. wt Amylin monomer is incubated with calcium free NUCB2 in a 1:1 stoichiometric ratio (32μM concentration each) in 20mM Tris at pH 7.5 and 25^{o}C with 2% HFIP and samples were withdrawn after 40 minutes. Scale bar in the images A and C represents 200nm, in image B represents 50nm and in image D represents 100nm.

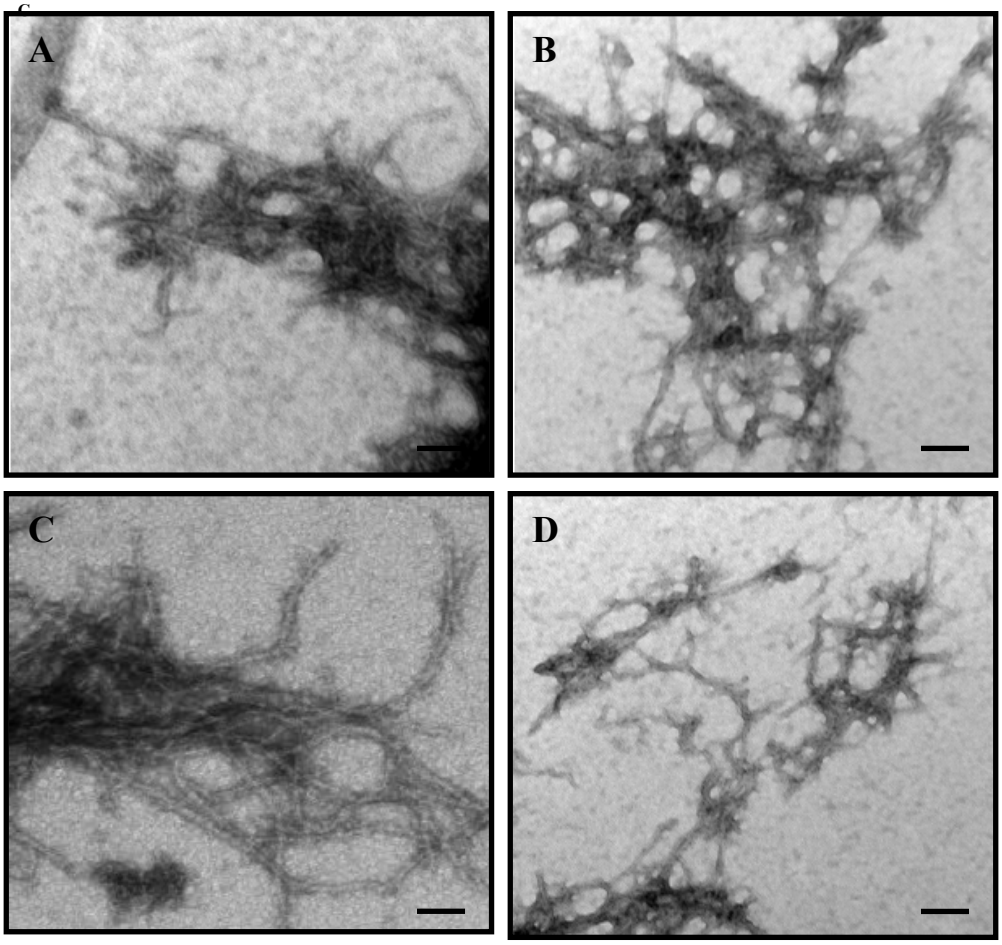

Figure 29. Disaggregation of Amylin fibril by Ca^{2+} free NUCB2 in a 1:1 stoichiometric ratio (32μM concentration each) in 20mM Tris at pH 7.5 and 25^{o}C with 2% HFIP. TEM analysis of the samples withdrawn after 60mins shows the presence of fibrillar species in the reaction mixture. Scale bar in the images represents 200nm.

Bibliography

Abedini, A., and Raleigh, D. P. (2005). Incorporation of pseudoproline derivatives allows the facile synthesis of human IAPP, a highly amyloidogenic and aggregation-prone polypeptide. *Org Lett.* 7, 693-696.

Aepfelbacher, M., Zumbihl, R., Ruckdeschel, K., Jacobi, C. A., Barz, C., and Heesemann, J. (1999). The tranquilizing injection of *Yersinia* proteins: a pathogen's strategy to resist host defense. *Biological Chemistry*, 380, 795-802.

Alexander, G. E., Chen, K., Pietrini, P., Rapoport, S. I., and Reiman, E. M. (2002). Longitudinal PET evaluation of cerebral metabolic decline in dementia: a potential outcome measure in Alzheimer's disease treatment studies. *Am. J. Psychiatry*, 159, 738–745.

Alzheimer, A. (1906). Über einen eigenartigen schweren erkrankungsprozeβ der hirnrinde. *Neurologisches Centralblatt*. 23, 1129–1136.

Andersson, K., Carballeira, N., Magnusson, K. E., Persson, C., Stendahl, O., Wolf-Watz, H., and Fallman, M. (1996). YopH of *Yersinia pseudotuberculosis* interrupts early phosphotyrosine signaling associated with phagocytosis. *Mol. Microbiol.,* 20, 1057-1069.

Arrasate, M., Mitra, S., Schweitzer, E. S., Segal, M. R. and Finkbeiner, S. (2004). Inclusion body formation reduces levels of mutant huntington and the risk of neuronal death. *Nature*, 431, 805-810.

Badman, M. K., Shennan, K. I., Jermany, J. L., Docherty, K., and Clark, A. (1996). Processing of pro-islet amyloid polypeptide (proIAPP) by the prohormone convertase PC2. *FEBS Lett*., 378, 227-231.

Ballif, B. A., Mincek, N. V., Barratt, J. T., Wilson, M. L., and Simmons, D. L. (1996). Interaction of cyclooxygenases with an apoptosis- and autoimmunity-associated protein. *Proc. Natl. Acad. Sci.*, 93, 5544-9.

Bennett, M. J., Schiunegger, M. P., and Eisenberg, D. (1995). 3D domain swapping: a mechanism for oligomer assembly. *Protein Sci.* 4, 2455-2468.

Benson, M. D. (1989). Familial amyloidotic polyneuropathy. *Trends Neurosci.*, 12, 88–92.

Bentahir, M., Nyabi, O., Verhamme, J., Tolia, A., Horré, K., Wiltfang, J., Esselmann, H., and De Strooper, B. (2006). Presenilin clinical mutations can affect gamma-secretase activity by different mechanisms. *J. Neurochem.*, 96 732–742.

Bergstrom, C. P., Sloan, C. P., Wang, H. H., Parker, M. F., Smith, D. W., Zheng, M., Hansel, S. B., Polson, C. T., Barber, L. E., Bursuker, I., Guss, V. L., Corsa, J. A., Barten, D. M., Felsenstein, K. M., and Roberts, S. B. (2008). Nitrogen-appended N-alkylsulfonamides as inhibitors of gamma-secretase. *Bioorg. Med. Chem. Lett.*, 18, 175-178.

Black, D. S., and Bliska, J. B. (1997). Identification of p130Cas as a substrate of *Yersinia* YopH (Yop51), a bacterial protein tyrosine phosphatase that translocates into mammalian cells and targets focal adhesions. *EMBO J.,* 16, 2730-2744.

Black, D. S., Montagna, L. G., Zitsmann, S., and Bliska, J. B. (1998). Identification of an amino-terminal substrate-binding domain in the *Yersinia* tyrosine phosphatase that is required for efficient recognition of focal adhesion targets. *Mol. Microbiol.,* 29, 1263-1274.

Black, D. S., and Bliska, J. B. (2000). The *Yersinia* tyrosine phosphatase YopH targets a novel adhesion-regulated signaling complex in macrophages. *Cellular Microbiology,* 2, 401-414.

Blaschke, U. K., Cotton, J. C., and Muir, T. W. (2000). Synthesis of multi-domain proteins using expressed protein ligation: strategies for segmental isotopic labeling of internal regions. *Tetrahedron,* 56, 9461-9470.

Bliska, J. B., Guan, K. L., Dixon, J. E., and Falkow, S. **(**1991**).** Tyrosine phosphate hydrolysis of host proteins by an essential *Yersinia* virulence determinant. *Proc. Natl. Acad. Sci. USA.,* 88, 1187-91.

Bliska, J. B., Galan, J. E., and Falkow, S. (1993). Signal transduction in the mammalian cell during bacterial attachment and entry. *Cell,* 73, 903-920.

Boado, R. J., Zhang, Y., Xia, C. F., and Pardridge, W. M. (2007). Fusion antibody for Alzheimer's disease with bidirectional transport across the blood-brain barrier and abeta fibril disaggregation. *Bioconjug. Chem.*, 18, 447-455.

Braak, H., Rub, U., Gai, W. P., and Del Tredici, K. (2003). Idiopathic Parkinson's disease: possible routes by which vulnerable neuronal types may be subject to neuroinvasion by an unknown pathogen. *J. Neural. Transm.*, 110, 517–536.

Busciglio, J., Lorenzo, A., Yeh, J., and Yankner, B. A. (1995). Beta-amyloid fibrils induce tau phosphorylation and loss of microtubule binding. *Neuron*, 14, 879–888.

Calabrese, B., Shaked, G. M., Tabarean, I. V., Braga, J., Koo, E. H., and Halpain, S. (2007). Rapid, concurrent alterations in pre- and postsynaptic structure induced by naturally-secreted amyloid-beta protein. *Mol. Cell Neurosci.*, 35, 183–193.

Camberos, M. C. and Cresto, J. C. (2006). Insulin-degrading enzyme hydrolyzes ATP. *Exp. Biol. Med.,* 232, 281-292.

Cardoso, I., Goldsbury, C. S., Muller, S. A., Olivieri, V., Wirtz, S., Damas, A. M., Aebi, U. and Saraiva, M. J. (2002). Transthyretin fibrillogenesis entails the assembly of monomers: a molecular model for in vitro assembled transthyretin amyloid-like fibrils. *J. Mol. Biol.*, 317, 683–695.

Cardoso, I., Merlini, G., and Saraiva, M. J. (2003). 4'-iodo-4'-deoxydoxorubicin and tetracyclines disrupt transthyretin amyloid fibrils in vitro producing noncytotoxic species: screening for TTR fibril disrupters. *FASEB J.*, 17, 803-809.

Cates, M. S., Berry, M. B., Ho, E. L., Li, Q., Potter, J. D. and Phillips, G. N., Jr. (1999). Metal-ion affinity and specificity in EF-hand proteins: coordination geometry and domain plasticity in parvalbumin. *Structure,* 7, 1269-1278.

Chain, P. S. G., Carniel, E., Larimer, F. W., Lamerdin, J., Stoutland, P. O., Regala, W. M., Georgescu, A. M., Vergez, L. M., Land, L. M., Motin, V. L., Brubaker, R. R., Fowler, J., Hinnebusch, J., Marceau, M., Medigue, C., Simonet, M., Chenal-Francisque, V., Souza, B., Dacheux, D., Elliott, J. M., Derbise, A., Hauser, L. J., and Garcia, E. (2004). Insights into the evolution of *Yersinia pestis* through whole-genome comparison with *Yersinia pseudotuberculosis*. *Proc. Natl. Acad. Sci. USA*, 101, 13826-13831.

Chien, P., Weissman, J. S., and DePace, A. H. (2004). Emerging princples of conformation-based prion inheritance. *Annual Review of Biochemistry*, 73, 617-656.

Chiti, F. and Dobson, C. M. (2006). Protein misfolding, functional amyloid, and human disease. *Annu. Rev. Biochem.*, 75, 333-336.

Christensen, M. D., and White, H. K. (2007). Dementia assessment and management. *J. Am. Med. Di.r Assoc.*, 8, e89–98.

Clark, A., Saas, M. F., Nezzer, T., Uren, C., Knowler, W. C., Bennett, P. H., and Turner, R. C. (1990). Islet amyloid polypeptide in diabetic and non-diabetic Pima Indians. *Diabetologia*, 33, 285-289.

Cleary, J. P., Walsh, D. M., Hofmeister, J. J., Shankar, G. M., Kuskowski, M. A., Selkoe, D. J., and Ashe, K. H. (2005). Natural oligomers of the amyloid-beta protein specifically disrupt cognitive function. *Nat. Neurosci.*, 8 79–84.

Colon, W., Lai, Z., McCutchen, S. L., Miroy, G. J., Strang, C. and Kelly, J. W. (1996). FAP mutations destabilize transthyretin facilitating conformational changes required for amyloid formation. *Ciba Found Symp.* 199, 228–238.

Combettes, M., and Kargar, C. (2007). Newly approved and promising antidiabetic agents. *Therapie*., 62, 293-310. Comparison of the effects of chronic central

administration and chronic peripheral administration of islet amyloid polypeptide on food intake and meal pattern in the rat.

Cooper, G. J. S., and Willis, A. C. (1987). Purification and characterization of a peptide from amyloid-rich pancreas of type 2 diabetic patients. *Proc. Natl. Acad. Sci. USA,* 84, 8628-8632.

Cornelis, G. R. (1998). The *Yersinia* deadly kiss. *J. Bacteriol.,* 180, 5495-5504.

Cornelis, G. R., Boland, A., Boyd, A. P., Geuijen, C., Iriarte, M., Neyt, C., Sory, M. P., and Stanier, I. (1998). The virulence plasmid of *Yersinia*, an antihost genome. *Microbiol. Mol. Biol. Rev.,* 62, 1315-1352.

de Alba, E., and Tjandra, N. (2004). Structural studies on the Ca^{2+}-binding domain of human nucleobindin (calnuc). *Biochemistry*, 43, 10039-10049.

De Strooper, B. and Annaert, W. (2000). Proteolytic processing and cell biological functions of the amyloid precursor protein. *J. Cell Sci.,* 113, 1857-1870.

Deleuil, F., Mogemark, L., Francis, M. S., Wolf-Watz, H., and Fallman, M. (2003). Interaction between the *Yersinia* protein tyrosine phosphatase YopH and eukaryotic Cas/Fyb is an important virulence mechanism. *Cell Microbiol.,* 5, 53-64.

Dinamarca, M. C., Cerpa, W., Garrido, J., Hancke, J. L., and Inestrosa, N. C. (2006). Hyperforin prevents beta-amyloid neurotoxicity and spatial memory impairments by disaggregation of Alzheimer's amyloid-beta-deposits. *Mol. Psychiatry*, 11, 1032-1048.

Dolphin, G. T., Chierici, S., Ouberai, M., Dumy, P., and Garcia, J. (2008). A multimeric quinacrine conjugate as a potential inhibitor of Alzheimer's beta-amyloid fibril formation. *Chembiochem.*, EPUB.

Edelman, S. V. (2008). Optimizing diabetes treatment using an Amylin analogue. *Diabetes Educ.*, 34, 4S-10S

El-Agnaf, O. M., Jakes, R., Curran, M. D., Middleton, D., Ingenito, R., Bianchi, E., Pessi, A., Neill, D., and Wallace, A. (1998). Aggregates from mutant and wild-type alpha-synuclein proteins and NAC peptide induce apoptotic cell death in human neuroblastoma cells by formation of beta-sheet and amyloid-like filaments. *FEBS Lett.*, 440, 71–75.

Eriksson, S., Janciauskiene, S., and Merlini, G. (1995). The putative role of alpha-1-antitrypsin in the disaggregation of amyloid lambda fibrils. *J. Intern Med.*, 237, 143-149.

Espinosa, A., and Alfano, J. R. (2004). Disabling surveillance: bacterial type III secretion system effectors that suppress innate immunity. *Cell Microbiol.*, 6, 1027-40.

Evdokimov, A. G., Anderson, D. E., Routzahn, K. M., and Waugh, D. S. (2000). Overproduction, purification, crystallization and preliminary X-ray diffraction analysis of YopM, an essential virulence factor extruded by the plague bacterium *Yersinia pestis.* *Acta Cryst.*, 56, 1676-1679.

Evdokimov, A. G., Tropea, J. E., Routzahn, K. M., Copeland, T. D., and Waugh, D. S. (2001). Structure of the N-terminal domain of *Yersinia pestis* YopH at 2.0 A^{o} resolution. *Acta Crystallogr. D. Biol. Crystallogr.*, 57, 793-799.

Fallman, M., Andersson, K., Hakansson, S., Magnusson, K. E., Stendahl, O., and Wolf-Watz, H. (1995). *Yersinia pseudotuberculosis* inhibits Fc receptor-mediated phagocytosis in J774 cells. *Infect. Immun.,* 63, 3117-3124.

Feany, M. B., and Bender, W. W. (2000). A drosophila model of Parkinson's disease. *Nature*, 404, 394–398.

Fehmann, H. C., Weber, V., Göke, R., Göke, B., and Arnold, R. (1990). Cosecretion of Amylin and insulin from isolated rat pancreas. *FEBS Lett.*, 262, 279-281.

Feng, G., and Pawson, T. (1994). Phosphotyrosine phosphatases with SH2 domains: regulators of signal transduction. *TIG,* 10, 54-58.

Frenkel, D., Dewachter, I., Van Leuven, F., and Solomon, B. (2003). Reduction of beta-amyloid plaques in brain of transgenic mouse model of Alzheimer's disease by EFRH-phage immunization. *Vaccine*, 21, 1060-1065.

Galimand M., Guiyoule A., Gerbaud G., Rasoamanana B., Chanteau S., Carniel E., and Courvalin P. (1997). Multidrug Resistance in *Yersinia pestis* Mediated by a Transferable Plasmid. *The New England Journal of Medicine*, 337, 667-680.

Galyov E. E., Hakansson S., and Wolf-Watz H. (1994) Characterization of the operon encoding the YpkA Ser/Thr protein kinase and the YopJ protein of *Yersinia* pseudotuberculosis. *J. Bacteriol.,* 176, 4543-4548.

Galyov E. E., Hakansson S., Forsberg A., and Wolf-Watz H. (1993) A secreted protein kinase of *Yersinia pseudotuberculosis* is an indispensable virulence determinant. *Nature,* 361, 730-732.

Garcia-Alloza, M., Borrelli, L. A., Rozkalne, A., Hyman, B. T., and Bacskai, B. J. (2007). Curcumin labels amyloid pathology in vivo, disrupts existing plaques, and partially restores distorted neurites in an Alzheimer mouse model. *J. Neurochem.*, 102, 1095-1104.

García-Palomero, E., Muñoz, P., Usan, P., Garcia, P., Delgado, E., De Austria, C., Valenzuela, R., Rubio, L., Medina, M., and Martínez, A. (2008). Potent beta-amyloid modulators. *Neurodegener Dis.*, 5, 153-156.

Georganopoulou, D. G., Chang, L., Nam, J. M., Thaxton, C. S., Mufson, E. J., Klein, W. L., and Mirkin, C. A. (2005). Nanoparticle-based detection in cerebral spinal fluid of a soluble pathogenic biomarker for Alzheimer's disease. *Proc. Natl. Acad. Sci. USA.*, 102, 2273–2276.

Glenner, G. G., and Wong, C. W. (1984). Alzheimer's disease: initial report of the purification and characterization of a novel cerebrovascular amyloid protein. *Biochem. Biophys. Res. Commun.*, 120, 855-890.

Goldsbury, C., Goldie, K., Pellaud, J., Seelig, J., Frey, P., Müller, S. A., Kistler, J., Cooper, G. J., and Aebi, U. (2000). Amyloid fibril formation from full-length and fragments of amylin. *J. Struct. Biol.*, 130, 352-362.

Gotz, J., Chen, F., van Dorpe, J., and Nitsch, R. M. (2001). Formation of neurofibrillary tangles in P301l tau transgenic mice induced by Abeta 42 fibrils. *Science*, 293, 1491–1495.

Greenberg, S. M., Koo, E. H., Selkoe, D. J., Qiu, W. Q., and Kosik, K. S. (1994). Secreted beta-amyloid precursor protein stimulates mitogen-activated protein kinase and enhances tau phosphorylation. *Proc. Natl. Acad. Sci. USA*, 91, 7104–7108.

Groenning, M., Olsen, L., van de Weert, M., Flink, J. M., Frokjaer, S., and Jørgensen, F. S. (2007). Study on the binding of thioflavin T to beta-sheet-rich and non-beta-sheet cavities. *J. Struct. Biol.*, 158, 358-369.

Guan, K., and Dixon, J. E. (1990). Protein tyrosine phosphatase activity of an essential virulence determination in *Yersinia.* Science, 249, 553-556.

Guan, K. L., and Dixon, J. E. (1993). Bacterial and viral protein tyrosine phosphatases. *Semin Cell Biol.,* 4, 389-96.

Hackeng, T. M., Griffin, J. H., and Dawson, P. E. (1999). Protein synthesis by native chemical ligation: Expanded scope by using straightforward methodology. *Proc. Natl. Acad. Sci. USA,* 96, 10068-10073.

Harrison, R. S., Sharpe, P. C., Singh, Y. and D. P. Fairlie (2007). Amyloid peptides and proteins in review. *Reviews of Physiology, Biochemistry and Pharmacology,* 159, 1-77.

Hartley, D. M., Walsh, D. M., Ye, C. P., Diehl, T., Vasquez, S., Vassilev, P. M., Teplow, D. and Selkoe, D. J. (1999). Protofibrillar intermediates of amyloid beta -protein induce

acute electrophysiological changes and progressive Neurotoxicity in Cortical Neurons. *J. Neurosci.,* 19, 8876-8884.

Hartter, E., Svoboda, T., Ludvik, B., Schuller, M., Lell, B., Kuenburg, E., Brunnbauer, M., Woloszczuk, W., and Prager, R. (1991). Basal and stimulated plasma levels of pancreatic Amylin indicate its co-secretion with insulin in humans. *Diabetologia*, 34, 52-54.

Hayden, M. R., Tyagi, S. C. (2001). "A" is for amylin and amyloid in type 2 diabetes mellitus. *JOP. J. Pancreas*, 2, 124-139.

Heuck, C. J. (1998). Type III protein secretion systems in bacterial pathogens of animals and plants. *Microbiol. Mol. Biol. Rev.,* 62, 379-433.

Higham, C. E., Jaikaran, E. T., Fraser, P. E., Gross, M., and Clark, A. (2000). Preparation of synthetic human islet amyloid polypeptide (IAPP) in a stable conformation to enable study of conversion to amyloid-like fibrils. *FEBS Lett.*, 470, 55-60.

Hofmann, R. M., and Muir, T. W. (2002). Recent advances in the application of expressed protein ligation to protein engineering. *Current Opinion in Biotechnology,* 13, 297-303.

Holmstrom, A., Rosqvist, R., Wolf-Watz, H., and Forsberg, A. (1995). Virulence plasmid-encoded YopK is essential for *Yersinia* pseudotuberculosis to cause systemic infection in mice. *Infect Immun.* 63, 2269-76.

Hoshi, M., Sato, M., Matsumoto, S., Noguchi, A., Yasutake, K., Yoshida, N. and Sato, K. (2003). Spherical aggregates of {beta}-amyloid (amylospheroid) show high neurotoxicity and activate tau protein kinase I/glycogen synthase kinase-3{beta}. *Proc. Natl. Acad. Sci.,* 100, 6370-6375.

Hou, X., Aguilar, M. I., and Small, D. H. (2007). Transthyretin and familial amyloidotic polyneuropathy: recent progress in understanding the molecular mechanism of neurodegeneration. *FEBS J.*, 274, 1637-1650.

Howlett, D. R., Jennings, K. H., Lee, D. C., Clark, M. S. G., Brown, F., Wetzel, R., Wood, S. J., Camilleri, P. and Roberts, G. W. (1995). Aggregation state and neurotoxic properties of Alzheimer beta-amyloid peptide. *Neurodegeneration.* 4, 23-32.

Inglesby, T. V., Dennis, D. T., Henderson, D. A., Bartlett, J. G., Ascher, M. S., Eitzen, E., Fine, A. D., Friedlander, A. M., Hauer, J., Koerner, J. F., Layton, M., McDade, J., Osterholm, M. T., O'Toole, T., Parker, G., Perl, T. M., Russell, P. K., Schoch-Spana, M., and Tonat, K. (2000) Plague as a biological weapon. *American Medical Association,* 283, 2281-2290.

Irvine, G. B., El-Agnaf, O. M., Shankar, G. M., and Walsh, D. M. (2008). Protein aggregation in the brain – the molecular basis for Alzheimer's and Parkinson's diseases. *Mol. Med.* Mar 27 EPUB.

Ito, S., Ohtsuki, S., Kamiie, J., Nezu, Y. and Terasaki, T. (2007). Cerebral clearance of human amyloid-beta peptide (1-40) across the blood brain barrier is reduced by self-aggregation and formation of low-density lipoprotein receptor-related protein-1 ligand complexes. *J. Neurochem.,* 103, 2482-2490.

Ivanov, M. I., Stuckey, J. A., Schubert, H. L., Saper, M. A., and Bliska, J. B. (2005). Two substrate-targeting sites in the *Yersinia* protein tyrosine phosphatase co-operate to promote bacterial virulence. *Mol. Microbiol.* 55, 1346-1356.

Johnson, T., Quibell, M., Owen, D., and Sheppard, R. C. (1993). A reversible protecting group for the amide bond in peptides. Use in the synthesis of 'difficult sequences'. *J. Chem. Soc.; Chem. Commun.*, 369-372.

Kahn, S. E., D'Alessio, D. A., Schwartz, M. W., Fujimoto, W. Y., Ensinck, J. W., Taborsky, G. J. Jr., and Porte, D. Jr. (1990). Evidence of cosecretion of islet amyloid polypeptide and insulin by beta-cells. *Diabetes*, 39, 634-638.

Kanai, Y., and Tanuma, S. (1992). Purification of a novel B cell growth and differentiation factor associated with lupus syndrome. *Immunol. Lett.*, 32, 43-48.

Kawano, J., Kotani, T., Ogata, Y., Ohtaki, S., Takechi, S., Nakayama, T., Sawaguchi, A., Nagaike, R., Oinuma, T., Suganuma, T. (2000). CALNUC (nucleobindin) is localized in the Golgi apparatus in insect cells. *Eur. J. Cell Biol.* 79, 208-217.

Kayed, R., Head, E., Thompson, J. L., Mclntire, T. M., Milton, S. C., Cotman, C. W. and Glabe, C. G. (2003). Common structure of soluble amyloid oligomers implies common mechanism of pathogenesis. *Science,* 300, 486-489.

Kelly, J. W., Colon, W., Lai, Z., Lashuel, H. A., McCulloch, J., McCutchen, S. L., Miroy, G. J. and Peterson, S. A. (1997). Transthyretin quaternary and tertiary structural changes facilitate misassembly into amyloid. *Adv. Protein Chem.*, 50, 161–181.

Khandelwal, P., Keliikuli, K., Smith, C.L., Saper, M.A., and Zuiderweg, E.R.P. (2002). Solution Structure and Phosphopeptide Binding to the N-terminal domain of *Yersinia* YopH: comparison with a crystal structure. *Biochemistry,* 41, 11425-11437.

Klein, W. L., Kraft and Finch, C. E. (2001. Targetting small Aβ oligomers: the solution to an Alzheimer's disease conundrum? *Trends in Neurosci.,* 24, 219-224.

Knowles, T. P., Shu, W., Devlin, G. L., Meehan, S., Auer, S., Dobson, C. M., and Welland, M. E. (2007). Kinetics and thermodynamics of amyloid formation from direct measurements of fluctuations in fibril mass. *Proc. Natl. Acad. Sci. USA.*, 104, 10016-10021.

Kovacs, G. G., and Budka, H. (2008). Prion diseases: from protein to cell pathology. *Am. J. Pathol.*, 172, 555-565.

Kumar-Singh, S., Theuns, J., Van Broeck, B., Pirici, D., Vennekens, K., Corsmit, E., Cruts, M., Dermaut, B., Wang, R., and Van Broeckhoven, C. (2006). Mean age-of-onset of familial alzheimer disease caused by presenilin mutations correlates with both increased Abeta42 and decreased Abeta40. *Hum. Mutat.*, 27 686–695.

Kusumoto, Y., Lomakin, A., Teplow, D. B., and Benedek, G. B. (1998). Temperature dependence of amyloid β-protein fibrillization. *Proc. Natl. Acad. Sci. USA.*, 95, 12277–12282.

Lambert, M. P., Barlow, A. K., Chromy, B. A., Edwards, C., Freed, R., Liosatos, M., Morgan, T. E., Rozovsky, I., Trommer, B., Viola, K. L., Wals, P., Zhang, C., Finch, C. E., Krafft, G. A. and Klein, W. L. (1998). Diffusible, nonfibrillar ligands derived from Abeta 1-42 are potent central nervous system neurotoxins. *Proc. Natl. Acad. Sci.,* 95, 6448-6453.

Landschulz, W.H., Johnson, P.F., and McKnight, S.L. (1988). The leucine zipper: a hypothetical structure common to a new class of DNA-binding proteins. *Science*, 240, 1759-1764.

Lansbury, P. T. and Lashuel, H. A. (2006). A century-old debate on protein aggregation and neurodegeneration enters the clinic. *Nature,* 443, 774-779.

Larsen, K. E., Schmitz, Y., Troyer, M. D., Mosharov, E., Dietrich, P., Quazi, A. Z., Savalle, M., Nemani, V., Chaudhry, F. A., Edwards, R. H., Stefanis, L., and Sulzer, D. (2006). Alpha-synuclein overexpression in PC12 and chromaffin cells impairs catecholamine release by interfering with a late step in exocytosis. *J. Neurosci.*, 26, 11915–11922.

Lashuel, H. A., Hartley, D., Petre, B. M., Walz, T. and Lansbury, P. T. (2002). Neurodegenerative disease: amyloid pores from pathogenic mutations. *Nature,* 418, 291-292.

Lavoie, C., Meerloo, T., Linm, P., and Farquharm, M. G. (2002). Calnuc, an EF-hand Ca^{2+}-binding protein, is stored and processed in the Golgi and secreted by the constitutive-like pathway in AtT20 cells. *Mol. Endocrinol.*, 16, 2462-74.

Lemere, C. A., Blusztajn, J. K., Yamaguchi, H., Wisniewski, T., Saido, T. C. and Selkoe, D. J. (1996). Sequence of deposition of heterogeneous amyloid β-peptides and APOE in Down syndrome: implications for initial events in amyloid plaque formation. *Neurobiol. Dis.*, 3, 16-32.

Leschik, J., Welzel, A., Weissmann, C., Eckert, A., and Brandt, R. (2007). Inverse and distinct modulation of tau-dependent neurodegeneration by presenilin 1 and amyloid-beta in cultured cortical neurons: evidence that tau phosphorylation is the limiting factor in amyloid-beta-induced cell death. *J. Neurochem.*, 101, 1303–1315.

Lesné, S., Koh, M. T., Kotilinek, L., Kayed, R., Glabe, C. G., Yang, A., Gallagher, M. and Ashe, K. H. (2006). A specific amyloid-beta protein assembly in the brain impairs memory. *Nature,* 440, 352-357.

Leung, K. Y., Reisner, B. S., and Straley, S. C. (1990). YopM inhibits platelet aggregation and is necessary for virulence of *Yersinia pestis* in mice. *Infect Immun.,* 58, 3262-71.

LeVine, H., III (1999). Quantification of beta-sheet amyloid fibril structures with thioflavin T. *Methods Enzymol.* 309, 274-284.

Lewis, J., Dickson, D. W., Lin, W. L., Chisholm, L., Corral, A., Jones, G., Yen, S. H., Sahara, N., Skipper, L., Yager, D., Eckman, C., Hardy, J., Hutton, M., and McGowan, E. (2001). Enhanced neurofibrillary degeneration in transgenic mice expressing mutant tau and APP. *Science*, 293, 1487–1491.

Lin, P., Le-Niculescu, H., Hofmeister, R., McCaffery, J. M., Jin, M., Hennemann, H., McQuistan, T., De Vries, L., and Farquhar, M. G. (1998). The mammalian calcium-

binding protein, nucleobindin (CALNUC), is a Golgi resident protein. *J. Cell Biol.*, 141, 1515-1527.

Lin, P., Li, F., Zhang, Y. W., Huang, H., Tong, G., Farquhar, M. G., and Xu, H. (2007). Calnuc binds to Alzheimer's beta-amyloid precursor protein and affects its biogenesis. *J. Neurochem.*, 100, 1505-1514.

Longsdon, L.K., and Mecsas, J. (2003). Requirement of the *Yersinia* pseudotuberculosis effectors YopH and YopE in colonization and persistence in intestinal and lymph tissues. *Infect Immun.,* 71, 4595-607.

Loo, D. T., Copani, A., Pike, C. J., Whittemore, E. R., Walencewicz, A. J. and Cotman, C. W. (1993). Apoptosis is induced by ß-amyloid in cultured central nervous system neuron. *Proc. Natl. Acad. Sci.*, 90, 7951-7955.

Lorenzo, A. and Yankner, B.A. (1994). ß-amyloid neurotoxicity requires fibril formation and is inhibited by congo red. *Proc. Natl. Acad. Sci.*, 91, 12243-12247.

Lorenzo, A., Razzaboni, B., Weir, G. C. and Yankner, B. A. (1994). Pancreatic islet cell toxicity of Amylin associated with type-2 diabetes mellitus. *Nature,* 368, 756-760.

Luca, S., Yau, W. M., Leapman, R., and Tycko, R. (2007). Peptide conformation and supramolecular organization in amylin fibrils: constraints from solid-state NMR. *Biochemistry*, 46, 13505-13522.

Ludvik, B., Kautzky-Willer, A., Prager, R., Thomaseth, K., and Pacini, G. (1997). Amylin: history and overview. *Diabetes Medicine*, 14, S9-S13.

Lutz, T. A. (2006). Amylinergic control of food intake. *Physiol Behav.* 89, 465-471.

Maloy, A. L., Longnecker, D. S., and Greenbery, E. R. (1981). The relation of islet amyloid to the clinical type of diabetes. *Hum. Pathol*. 12, 917-922.

Mamikonyan, G., Necula, M., Mkrtichyan, M., Ghochikyan, A., Petrushina, I., Movsesyan, N., Mina, E., Kiyatkin, A., Glabe, C. G., Cribbs, D. H., and Agadjanyan, M. G. (2007). Anti-A beta 1-11 antibody binds to different beta-amyloid species, inhibits fibril formation, and disaggregates preformed fibrils but not the most toxic oligomers. *J. Biol. Chem.*, 282, 22376-22386.

Marr, R. A., Guan, H., Rockenstein, E., Kindy, M., Gage, F. H., Verma, I., Masliah, E. and Hersh, L. B. (2004). Neprilysin regulates amyloid beta peptide levels. *J. Mol. Neurosci.,* 22, 5-11.

Masliah, E., Rockenstein, E., Veinbergs, I., Mallory, M., Hashimoto, M., Takeda, A., Sagara, Y., Sisk, A., and Mucke, L. (2000). Dopaminergic loss and inclusion body formation in alpha-synuclein mice: implications for neurodegenerative disorders. *Science*, 287, 1265–1269.

McCutchen, S. L., Lai, Z., Miroy, G. J., Kelly, J. W. and Colon, W. (1995). Comparison of lethal and nonlethal transthyretin variants and their relationship to amyloid disease. *Biochemistry*, 34, 13527–13536.

Merlini, G., and Bellotti, V. (2003). Molecular mechanisms of amyloidosis. *N. Engl. J. Med.* 349, 583-596.

Miura, K., Titani, K., Kurosawa, Y., and Kanai, Y. (1992). Molecular cloning of nucleobindin, a novel DNA-binding protein that contains both a signal peptide and a leucine zipper structure. *Biochem. Biophys. Res. Commun.*, 187, 375-380.

Montagna, L. G., Ivanov, M. I., and Bliska, J. B. (2001). Identification of residues in the N-terminal domain of the *Yersinia* tyrosine phosphatase that is critical for substrate recognition. *J. Biol. Chem*., 276, 5005-5011.

Morgan, D., Diamond, D. M., Gottschall, P. E., Ugen, K. E., Dickey, C., Hardy, J., Duff, K., Jantzen, P., DiCarlo, G., Wilcock, D., Connor, K., Hatcher, J., Hope, C., Gordon, M.,

and Arendash, G. W. (2000). Aβ peptide vaccination prevents memory loss in an animal model of Alzheimer's disease. *Nature*, 408, 982-985.

Muir, T. W. (2003). Semisynthesis of Proteins by Expressed Protein Ligation. *Annu. Rev. Biochem.,* 72, 249-289.

Naiki, H., Higuchi, K., Hosokawa, M., and Takeda, T. (1989). Fluorometric determination of amyloid fibrils in vitro using the fluorescent dye, thioflavin T1. *Anal. Biochem.* 177, 244-249.

Neumayer, W., Groll, M., Lehmann, V., Antoneka, U., Kahler, S., Heesemann, J., and Wilharm, G. (2004). *Yersinia enterocolitica* type III secretion chaperone SycH. Recombinant expression, purification, characterization, and crystallization. *Protein Exp. Pur.* 35, 237-247.

Nordfelth, R., and Wolf-Watz, H. (2001).YopB of *Yersinia* enterocolitica is essential for YopE translocation. *Infect Immun.* 69, 3516-3518.

Oda, T., Wals, P., Osterburg, H. H., Johnson, S. A., Pasinetti, G. M., Morgan, T. E., Rozovsky, I., Stine, W. B., Snyder, S. W., Holzman, T. F., Krafft, G. A. and Finch, C. E. (1995). Clusterin (apoJ) Alters the aggregation of Amyloid β-peptide ($A\beta_{1-42}$) and forms slowly sedimenting Aβ complexes that cause oxidative stress. *Experimental Neurology,* 136, 22-31.

Oh-I, S,. Shimizu, H., Satoh, T., Okada, S., Adachi, S., Inoue, K., Eguchi, H., Yamamoto, M., Imaki, T., Hashimoto, K., Tsuchiya, T., Monden, T., Horiguchi, K., Yamada, M., and Mori, M. (2006). Identification of nesfatin-1 as a satiety molecule in the hypothalamus. *Nature*, 443, 709-712.

Ohsawa, H., Kanatsuka, A., Mizuno, Y., Tokuyama, Y., Takada, K., Mikata, A., Makino, H., and Yoshida, S. (1992). Islet amyloid polypeptide-derived amyloid deposition increases along with the duration of type 2 diabetes mellitus. *Diabetes Res. Clin. Pract.*, 15, 17-21.

Olsson, M., Herrington, M. K., Reidelberger, R. D., Permert, J., and Arnelo, U. (2007).

Opie, E.L. (1901). The relation of diabetes mellitus to lesions of the pancreas: hyaline degeneration of the islands of Langerhans. *J. Exp. Med.*, 5, 527-540.

Orgogozo, J. M., Gilman, S., Dartigues, J. F., Laurent, B., Puel, M., Kirby, L. C., and Jouanny, P. (2003). Subacute meningoencephalitis in a subset of patients with AD after Abeta42 immunization. *Neurology* 61, 46-54.

Osada, T., Hashimoto, T., Nishimura, A., Matsuo, Y., Wakabayashi, T. and Iwatsubo, T. (2005). CLAC binds to Amyloid {beta} peptides through the positively charged amino acid cluster within the collagenous domain 1 and inhibits formation of amyloid fibrils. *J. Biol. Chem.*, 280, 8596-8605.

Osto, M., Wielinga, P. Y., Alder, B., Walser, N., and Lutz, T. A. (2007). Modulation of the satiating effect of Amylin by central ghrelin, leptin and insulin. *Physiol Behav.* 91, 566-572.

Otomo, T., Ito, N., Kyogoku, Y., and Yamazaki, T. (1999). NMR observation of selected segments in a larger protein: central-segment isotope labeling through intein-mediated ligation. *Biochemistry,* 38, 16040-16044.

Padrick, S. B., and Miranker, A. D. (2002). Islet amyloid: phase partitioning and secondary nucleation are central to the mechanism of fibrillogenesis. *Biochemistry*, 41, 4694-4703.

Persson, C., Carballeira, N., Wolf-Watz, H., and Fallman, M. (1997). The PTPase YopH inhibits uptake of *Yersinia,* tyrosine phosphorylation of p130Cas and FAK, and the associated accumulation of these proteins in peripheral focal adhesions. *EMBO J.,* 16, 2307-2318.

Petersson, U., Somogyi, E., Reinholt, F. P., Karlsson, T., Sugars, R. V., and Wendel, M. (2004). Nucleobindin is produced by bone cells and secreted into the osteoid, with a potential role as a modulator of matrix maturation. *Bone*, 34, 949-60.

Petkova, A. T., Yau, W. and Tycko, R. (2006). Experimental Constraints on Quaternary Structure in Alzheimer's -Amyloid Fibrils. *Biochemistry*, *45,* 498-512.

Phillips, L. K., and Horowitz, M. (2006). Amylin. *Curr. Opin. Endocrin. and Diabetes and Obesity*, 13, 191-198.

Pike, C. J., Burdick, D., Walencewicz, A. J., Glabe, C. G. and Cotman, C. W. (1993). Neurodegeneration induced by beta-amyloid peptides in vitro: the role of peptide assembly state. *J. Neurosci.*, 13, 1676-1687.

Podlisny, M. B., Ostaszewski, B. L., Squazzo, S. L., Koo, E. H., Rydell, R. E., Teplow, D. B., and Selkoe, D. J. (1995). Aggregation of secreted amyloid beta-protein into sodium dodecyl sulfate-stable oligomers in cell culture. *J. Biol. Chem.*, 270, 9564–9570.

Portnoy, D. A., and Martinez, R. J. (1985). Role of a plasmid in the pathogenicity of *Yersinia* species. *Curr. Topics. Microbiol. Immunol.,* 118, 29-51.

Quist, A., Doudevski, I., Lin, H., Azimova, R., Ng, D., Frangione, B., Kagan, B., Ghiso, J. and Lal, R. (2005). Amyloid ion channels: A common structural link for protein-misfolding disease. *Proc. Natl. Acad. Sci.* 102, 10427-10432.

Reidelberger, R. D., Haver, A. C., Arnelo, U., Smith, D. D., Schaffert, C. S., and Permert, J. (2004). Amylin receptor blockade stimulates food intake in rats. *Am J Physiol Regul Integr Comp Physiol.* 287, R568-574.

Rochet, J. C., and Lansbury, P. T. (2000). Amyloid fibrillogenesis: themes and variations. *Curr. Opin. Struct. Biol.*, 10, 60-68.

Rocken, C., Linke, R. P., and Saeger, W. (1992). Immunohistology of islet amyloid polypeptide in diabetes mellitus: semi-quantitative studies in a post-mortem series. Virchows Arch A. *Pathol. Anat. Histopathol.*, 421, 339-344.

Rosqvist, R., Skurnik, M., and Wolf-Watz, H. (1998). Increased virulence of *Yersinia pseudotuberculosis* by two independent mutations. *Nature,* 334, 522-524.

Rymer, D. L. and Good, T. A. (2001). The role of G protein activation in the toxicity of amyloidogenic Aβ-(1-40), Aβ-(25-35), and bovine calcitonin. *J. Biol. Chem.*, 276, 2523-2530.

Ryu, J., Kanapathipillai, M., Lentzen, G., and Park, C. B. (2008). Inhibition of beta-amyloid peptide aggregation and neurotoxicity by alpha-d-mannosylglycerate, a natural extremolyte. *Peptides*, 29, 578-584.

Salyers, A. A., and Whitt, D. D. (2002). Bacterial pathogenesis - a molecular approach. 2nd ed., 202-213.

Selkoe, D. J. (1998). The cell biology of beta-amyloid precursor protein and presenilin in Alzheimer's disease. *Trends Cell Biol.,* 8, 447-453.

Selkoe, D. J. (2003). Folding proteins in fatal ways. *Nature*, 426, 900-904.

Serpell, L. C., Sunde, M., Benson, M. D., Tennent, G. A., Pepys, M. B., and Fraser, P. E. (2000). The protofilament substructure of amyloid fibrils. *J. Mol. Biol.*, 300, 1033-1039.

Shankar, G. M., Bloodgood, B. L., Townsend, M., Walsh, D. M., Selkoe, D. J., and Sabatini, B. L. (2007). Natural oligomers of the Alzheimer amyloid-beta protein induce reversible synapse loss by modulating an NMDA-type glutamate receptor-dependent signaling pathway. *J. Neurosci.*, 27, 2866–2875.

Shao, F., and Dixon, J. E. (2003). YopT is a cysteine protease cleaving Rho family GTPases. *Adv Exp Med Biol.* 529, 79-84.

Shen, Y., Joachimiak, A., Rosner, M. R. and Tang, W. (2006). Structures of human insulin-degrading enzyme reveal a new substrate recognition mechanism. *Nature,* 443, 870-874.

Shim, S. H., Strasfeld, D. B., Ling, Y. L., and Zanni, M. T. (2007). Automated 2D IR spectroscopy using a mid-IR pulse shaper and application of this technology to the human islet amyloid polypeptide. *Proc. Natl. Acad. Sci. USA*, 104, 14197-14202.

Si, K., Lindquist, S., and Kandel, E. R. (2003). A neuronal isoform of the Aplysia CPEB has prion-like properties. *Cell*, 115, 879-891.

Siemers, E. R., Dean, R. A., Friedrich, S., Ferguson-Sells, L., Gonzales, C., Farlow, M. R., and May, P. C. (2007). Safety, tolerability, and effects on plasma and cerebrospinal fluid amyloid-beta after inhibition of gamma-secretase. *Clin. Neuropharmacoli.*, 30, 317-325.

Skrzypek, E., Cowan, C., and Straley, S. C. (1998). Targeting of the Yersinia pestis YopM protein into HeLa cells and intracellular trafficking to the nucleus. *Mol. Microbiol.,* 30, 1051-1065.

Slow, E. J., Graham, R. K., Osmand, A. P., Devon, R. S., Lu, G., Deng, Y., Pearson, J., Vaid, K., Bissada, N., Wetzel, R., Leavitt, B. R., and Hayden, M. R. (2005). Absence of behavioral abnormalities and neurodegeneration in vivo despite widespread neuronal huntingtin inclusions. *Proc. Natl. Acad. Sci.*, 102, 11402-11407.

Smith, C. L., Khandelwal, P., Keliikuli, K., Zuiderweg, E. R. P., and Saper, M. A. (2001). Structure of the type-III secretion and substrate-binding domain of *Yersinia* YopH phosphatase. *Mol. Microbiol.,* 42, 967-979.

Solomon, B. (2008). Immunological approaches for amyloid-beta clearance toward treatment for Alzheimer's disease. *Rejuvenation Res.,* Epub. Mar 19.

Solomon, B., Koppel, R., Frankel, D., and Hanan-Aharon, E. (1997). Disaggregation of Alzheimer beta-amyloid by site-directed mAb. *Proc. Natl. Acad. Sci. USA*, 94, 4109-4112.

Somogyi, E., Petersson, U., Sugars, R. V., Hultenby, K., and Wendel, M. (2004). Nucleobindin--a Ca^{2+}-binding protein present in the cells and mineralized tissues of the tooth. *Calcif. Tissue Int.*, 74, 366-76.

Sousa, M. M. and Saraiva, M. J. (2003). Neurodegeneration in familial amyloid polyneuropathy: from pathology to molecular signaling. *Prog. Neurobiol.*, 71, 385–400.

Stuckey, J. A., Schubert, H. L., Fauman, E. B., Zhang, Z. Y., Dixon, J. E. and Saper, M. A. (1994). Crystal structure of *Yersinia* protein tyrosine phosphatase at 2.5A and the complex with tungstate. *Nature.* 370, 571-575.

Suehiro, S. (2007). Molecular biology of prion protein and its first homologous protein. *J. Med. Invest.*, 54, 211-223.

Sun, J. P., Wu, L., Fedorov, A. A., Almo, S. C., and Zhang, Y. Z. (2003). Crystal structure of the *Yersinia* protein-tyrosine phosphatase YopH complexed with a specific small molecule inhibitor. *The J. of Biol. Chem.,* 278, 33392-33399.

Sunde, M. Serpell, L. C., Bartlam, M., Fraser, P. E., Pepys, M. B., and Blake, C. C. F. (1997). Common core structure of amyloid fibrils by synchrotron X-ray diffraction. *J. Mol. Biol.*, 273, 729-739.

Luca, S., Yau, W., Leapman, R. and Tycko, R. (2007). Peptide Conformation and Supramolecular Organization in Amylin Fibrils: Constraints from Solid-State NMR. *Biochemistry*, 46, 13505 -13522.

Teplow D. B. (2006). Preparation of amyloid beta-protein for structural and functional studies. *Methods Enzymol.*, 413, 20-33.

Terry, R. D., Masliah, E., Salmon, D. P., Butters, N., Teresa, R. D., Hill, R., Hansen, L. A., and Katzman, R. (1991). Physical basis of cognitive alterations in Alzheimer's disease: synapse loss is the major correlate of cognitive impairment. *Ann. Neurol.*, 30, 572-580.

Turner, R. (1998). Intensive blood-glucose control with sulphonylureas or insulin compared with conventional treatment and risk of complications in patients with type 2 diabetes(UDPDS 33). UK Prospective Diabetes Study (UKPDS) Group. *Lancet*, 352, 837-853.

Uversky, V. N. and Fink, A. L. (2004). Conformational constraints for amyloid fibrillation: The importance of being unfolded. *Biochim. Biophys. Acta*, 1698, 131–153.

Walsh, D. M., Klyubin, I., Fadeeva, J. V., Cullen, W. K., Anwyl, R., Wolfe, M. S., Rowan, M. J. and Selkoe, D. J. (2002). Naturally secreted oligomers of amyloid beta protein potently inhibit hippocampal long-term potentiation in vivo. *Nature,* 416, 535-539.

Walsh, D. M., Klyubin, I., Fadeeva, J. V., Rowan, M. J., and Selkoe, D. J. (2002). Amyloid-beta oligomers: their production, toxicity and therapeutic inhibition. *Biochem. Soc. Trans.*, 30, 552–557.

Wang, Y. J., Pollard, A., Zhong, J. H., Dong, X. Y., Wu, X. B., Zhou, H. D., and Zhou, X. F. (2007). Intramuscular delivery of a single chain antibody gene reduces brain Abeta burden in a mouse model of Alzheimer's disease. *Neurobiol. Aging*, EPUB.

Westermark, P., and Wernstedt, C. (1987). Islet amyloid in type 2 human diabetes mellitus and adult diabetic cats contain a novel putative polypeptide hormone. *Am. J. Pathol.*, 127, 414-417.

White, J. A., Manelli, A. M., Holmberg, K. H., Van Eldik, L. J. and Ladu, M. J. (2005). Differential effects of oligomeric and fibrillar amyloid-β 1-42 on astrocyte-mediated inflammation. *Neurobiol. Dis.*, 18, 459-465.

Wilhelmus, M. M. M., Boelens, W. C., Otte-Holler, I., Kamps, B., Kusters, B., Maat-Schiemann, M. L. C., de Waal, R. M. W. and Verbeek, M. M. (2006). Small heat shock

protein HspB8: its distribution in Alzheimer's disease brains and its inhibition of amyloid-β protein aggregation and cerebrovascular amyloid-β toxicity. *Acta Neuropathol.,* 111, 139-149.

Wilhelmus, M. M. M., Boelens, W. C., Otte-Holler, I., Kamps, B., de Waal, R. M. W. and Verbeek, M. M. (2006). Small heat shock proteins inhibit amyloid-β protein aggregation and cerebrovascular amyloid-β protein toxicity. *Brain Research,* 1089, 67-78.

Wilhelmus, M. M. M., Boelens, W. C., Otte-Holler, I., Kamps, B., Kusters, B., Maat-Schiemann, M. L. C., de Waal, R. M. W. and Verbeek, M. M. (2006). Small heat shock protein HspB8: its distribution in Alzheimer's disease brains and its inhibition of amyloid-β protein aggregation and cerebrovascular amyloid-β toxicity. *Acta Neuropathol.,* 111, 139-149.

Williamson, J. A., and Miranker, A. D. (2007). Direct detection of transient alpha-helical states in islet amyloid polypeptide. *Protein Sci.*, 16, 110-117.

Wohr, T., Wahl, F., Nefzi, A., Rohwedder, B., Sato, T., Sun, X., and Mutter, M. (1996). Pseudo-prolines as a solubilizing, structure-disrupting protection technique in peptide synthesis. *J. Am. Chem. Soc.*, 118, 9218-9227.

Yerbury, J. J., Poon, S., Meehan, S., Thompson, B., Kumita, J. R., Dobson, C. M. and Wilson, M. R. (2007). The extracellular chaperone clusterin influences amyloid formation and toxicity by interacting with prefibrillar structures. *FASEB J.,* 21, 2312-2322.

Zhang, Z. Y., Clemens, J. C., Schubert, H. L., Stuckey, J. A., Fischer, M. W. F., Hume, D. M., Saper, M. A., and Dixon, J. E. (1992). Expression, purification and physiochemical characterization of a recombinant *Yersinia* tyrosine phosphatase. *J. Biol. Chem.,* 267, 23759-23766.

Zhang, Z. Y., Thieme-Sefler, A. M., Maclean, D., McNamara, D. J., Dobrusin, E. M., Sawyer, T. K., and Dixon, J. E. (1993). Substrate specificity of the protein tyrosine phosphatases. *Proc. Natl. Acad. Sci.* USA, 90, 4446-4450.

Zhang, Z. Y., and Dixon, J. E., (1994). Protein tyrosine phosphatases: mechanism of catalysis and substrate specificity. *Adv. Enzymol. Relat. Areas Mol. Biol.*, 68, 1-36.

Zolnierowicz, S., and Bollen, M. (2000). EMBO Conference report: protein phosphorylation and protein phosphatases – De Panne, Belgium, September 19-24, 1999. *EMBO J.,* 19, 483-488.